EXPERIMENTAL AND FINITE ELEMENT BASED INVESTIGATIONS OF SHEAR BEHAVIOR IN REINFORCED CONCRETE BOX CULVERTS

by

ANIL KUMAR GARG

Presented to the Faculty of the Graduate School of

The University of Texas at Arlington in Partial Fulfillment

of the Requirements

for the Degree of

DOCTOR OF PHILOSOPHY

THE UNIVERSITY OF TEXAS AT ARLINGTON

May 2007

DEDICATION

To my wife Bhawana, and our sons Prabhat & Tushar

ACKNOWLEDGEMENTS

I would like to express my sincere appreciation and gratitude to my advisor, Dr. Ali Abolmaali for his timely support and motivations without which completing this project was not possible. I would also like to thank Dr. John H Matthys, Dr. Guillermo Ramirez, Dr. Anand Puppala, Dr. Ernest Crosby and Dr. D. L. Hawkins for their time and invaluable suggestions.

Moreover, I would like to acknowledge the support of the Department of Civil and Environmental Engineering at UTA, especially Department Chair, Dr. Nur Yazdani, and former Chair, Dr. Siamak Ardekani. My sincere gratitude goes to all the staff, for their precious assistance during the course of this research.

My special gratitude goes to Jarrod Burns, Richard Nichols, Jeff Bethke, Francheska Seijo Montes, Winston Chan, Dobrinka Radulova, Tri Le, Anupong Kararam, Komal Patel and Vivek Gurjar for wholeheartedly assisting me during the course of laboratory experimentation thorough out this study.

A financial support of the American Concrete Pipe Association (ACPA) is greatly acknowledged.

This acknowledgment would not be complete without mentioning the support, patience, and love from my wife, Bhawana, and sons Prabhat and Tushar to whom I am indebted forever.

October 27, 2006

ABSTRACT

EXPERIMENTAL AND FINITE ELEMENT BASED INVESTIGATIONS OF SHEAR BEHAVIOR IN REINFORCED CONCRETE BOX CULVERTS

Publication No. _____

Anil Kumar Garg, Ph.D.

The University of Texas at Arlington, 2007

Supervising Professor: Ali Abolmaali

This study evaluates the shear behavior and capacity of the precast concrete box culverts subjected to HS 20 truck wheel load. The most critical culvert behavior was considered by studying culverts subjected to zero depth fill and placed on rigid laboratory floor without bedding material. Three major phases were considered to complete the study, which included: (1) experimental program; (2) finite element modeling; and (3) development of distribution width and the determination of shear capacity.

A full-scale experimental testing program was undertaken to perform tests on 24 typical precast concrete box culverts designated as per ASTM C 1433-05 with and without distribution steel (As_6) which were produced by two different precast manufacturers. The wheel load was simulated by a 25 cm x 51 cm (10 in x 20 in) load plate, which was placed, at the distance "**d**" from the tip of the haunch to the edge of the load plate. An incremental loading history was adopted to capture the culvert's nonlinear behavior. The test results include load-deflection plots as well as the step-by-step description of the events. The test results further indicated that flexure governed the behavior up to and beyond AASHTO 2005 factored load. Independent shear cracks formed before the ultimate load at approximately twice the AASHTO 2005 factored load for most of the test specimens.

Complete detailed three-dimensional finite element models (FEM) of the test specimens were developed and analyzed to simulate the experimental results. Three-dimensional shell and solid elements were used to model the culvert systems. The welded wire fabrics were modeled by using the rebar elements placed on the surface-elements provided by the ABAQUS Software. The contact surface between the outside face of the bottom slab and reaction floor was modeled by using non-linear node-to-surface contact algorithm. The analysis algorithm consisted of an incremental loading history to capture the problem non-linearity. Smeared crack model along with the Risk Algorithm were incorporated to analyze the system for micro-cracks and to stabilize the solution, respectively. The converged solution was obtained by using H-convergence coupled with the difference between the external work done and the strain energy

density of the system. The load-deflection plots obtained from the FEM analyses were compared with those obtained from the experimental results, which showed close correlation.

All the forty-two standard cases of the ASTM C 1433 were modeled using the verified FEM model developed in Chapter 3. A regression analysis was conducted to develop equations for the calibrated FEM parameters. The 3-D volumetric shear force distribution on the top slab of the boxes was obtained. The peak shear force in each of the plots was identified and a vertical plane was passed through it parallel to the box's joint length. This yielded to a 2-D shear force distribution diagram along the box joint length from which the distribution width was calculated by dividing the area under the 2-D diagram with the peak shear force.

The distribution width for the ASTM C1433 boxes were compared with those reported in the AASHTO 2005. The calculated values of the distribution width were used to calculate the critical factored shear force for all the boxes, which were then compared with the American Concrete Institute (ACI) shear capacity equations. It was shown that the shear capacity exceeded the factored critical shear force for all the ASTM C1433 boxes. This study concludes that the AASHTO 2005 provision with regard to the shear transfer device across the joint is unsupported and it needs to be revisited.

TABLE OF CONTENTS

APPENDIX

LIST OF ILLUSTRATIONS

LIST OF TABLES

CHAPTER 1

INTRODUCTION

1.1 Introduction

Culverts are mini version of bridges for conveyance of natural surface water drainage under roads, taxiways, runways or railroads. Box culverts have been used increasingly since 1965 to meet drainage requirements where the site conditions and loads acting upon them have been appropriate.

Based on the author interviewing several pipe manufacturers it is believed that 80% of single barrel culvert installations are pre-cast. They are considered to be efficient since they reduce project execution time, particularly, they are ideal when the concrete batch plant is not near the construction site. Pre-cast box culverts are not recommended for areas with excessive settlement where deep foundations are required since deep foundations would have to be placed on shorter intervals with the use of precast sections making the installation excessively expensive.

The precast concrete box culverts are manufactured in a range of span and rise combinations. A typical cross-section of box culverts is shown in Figure 1.1. Box culvert sections are typically defined by their span, rise, and design height of fill

measured from finished grade to the top of the box section. The joint or "laying" length is a function of the form equipment accessible to the individual producer. The span of the standard size culverts, as tabulated by the ASTM C1433 varies from 91 cm to 366 cm (3 ft to 12 ft), the rise varies from 61 cm to 366 cm (2 ft to 12 ft). The above standard sizes are manufactured in both in 30 cm (1 ft) increments. The minimum top and bottom slab thicknesses for the height of fill between 0 and 61 cm (0 and 2 ft) are 18 and 15 cm (7 and 6 in), respectively. While the values of minimum top and bottom slab thickness for the height of fill, greater than 61 cm (2 ft) is 10 cm (4 in). Joint lengths vary as a function of the form equipment available to the producer, but they generally vary from about 122 cm (4 ft) as a practical minimum length up to 244 cm (8 ft). Joint lengths of 366 cm (12 ft) or even 488 cm (16 ft) is available on a regional basis. The inside corners of the wall and slabs are tapered to create a haunch, which has equal horizontal and vertical dimensions (Figure 1.2). The haunch dimensions are equal to the wall thickness though some producers utilize form equipment, which yields a fixed haunch dimension (usually either 20.3 cm (8 in) or 30.5 cm (12 in)). With the exception of the special design cases, the thickness of culvert walls, top slab and bottom slab varies from 10 cm to 30 cm (4 in to 12 in) and is a function of the span. The box culverts are reinforced with the inside and the outside layers of plain/deformed steel welded wire reinforcement per ASTM A 185 (2001) and A 497 (2001). These reinforcing layers are proportioned to resist the calculated moments and thrusts in the member's sections. Inside concrete cover (C_i) and outside concrete cover (C_o) is 2.5 cm (1 in) except for the unique cases where the height of fill is less than 61 cm (24 in), C_o

is equal to 5.1 cm (2 in) per AASHTO LRFD Bridge Design Specifications (2005). Precast box sections used to be designed as per ASTM C 789 for highway loading with earth cover of 61 cm (2 ft) or more or as per ASTM C 850 for highway loading with earth cover less than 61 cm (2 ft). Since 2003, ASTM C 1433 (2003) has replaced C 789 and C 850 for both loading conditions.

Precast box sections are typically cast with batches designed to yield 34.5 N/mm^2 (5000 psi). Precast sections are produced by either the drycast or the wetcast method. Drycasting is characterized by the use of very low water/cement (w/c) ratios (0.35 or less) while wetcast uses standard mix designs yielding to slumps in the range of 10 cm (4 in) to 15 cm (6 in).

The boxes are generally joined by placing the spigot into the bell end while placing in position as shown in Figure 1.3.

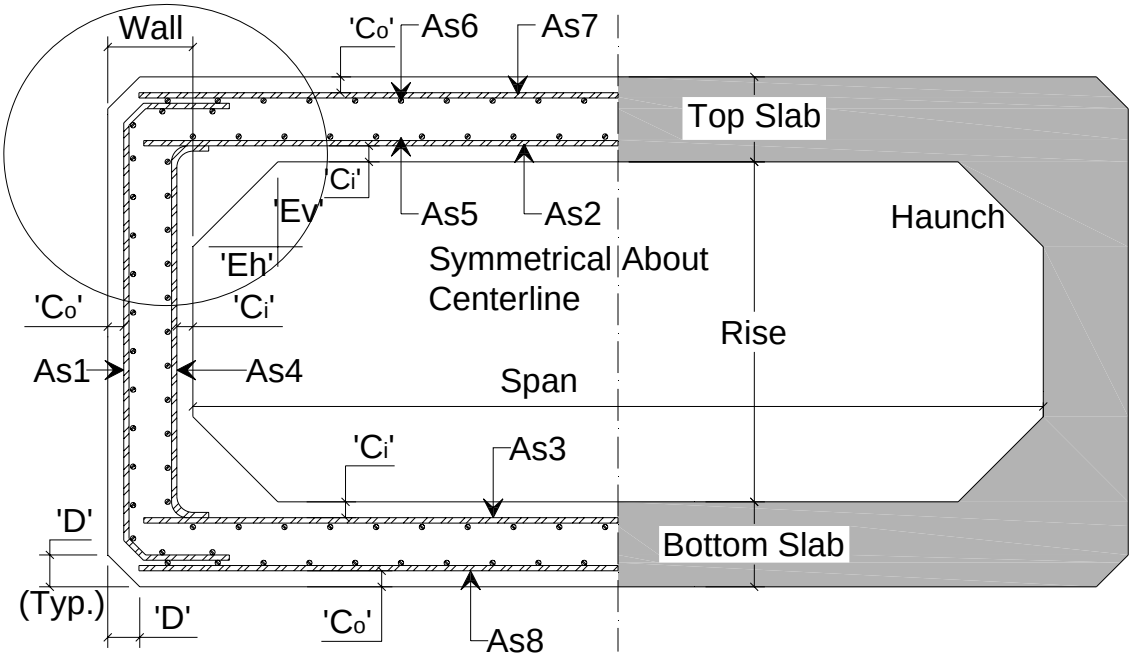

Figure 1.1 Typical Cross-Section of a Box Culvert

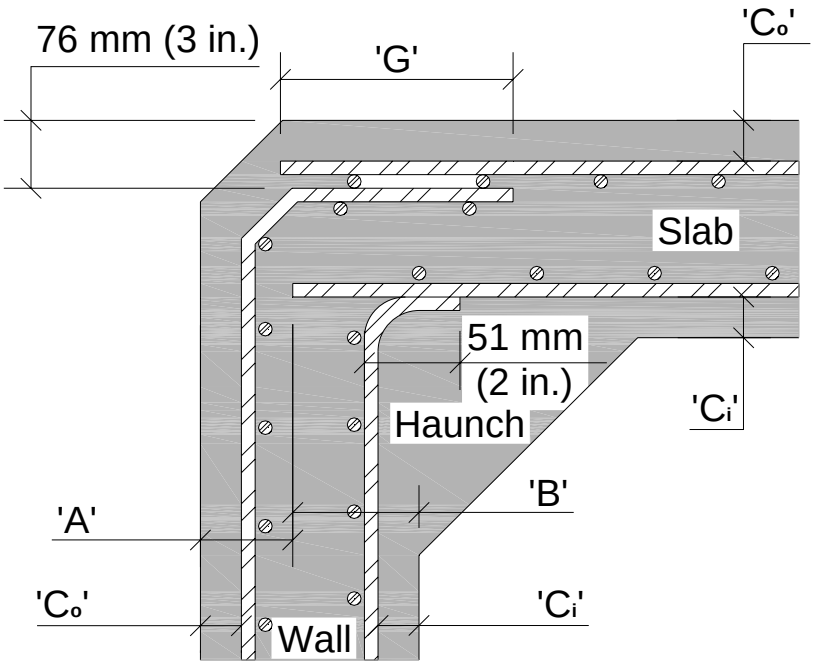

Figure 1.2 Details of Reinforcement at Haunch

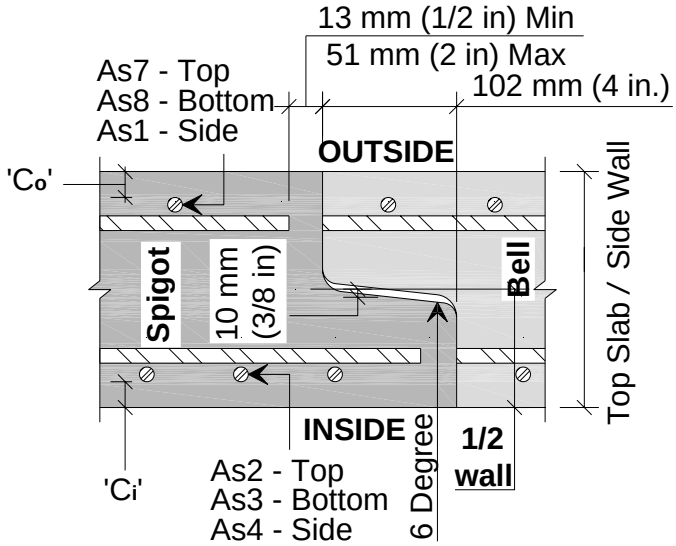

Figure 1.3 Joint Detail of the Box Culvert

1.2 Research Need

Box culverts are typically designed similar to bridges, and the new design concepts for bridges are based on the Load and Resistance Factor Design (LRFD), which were developed by the AASHTO (1998). These specifications introduced new provisions for distributing live loads to the reinforced concrete bridge decks, which also apply to the design of the reinforced concrete box culverts with depths of fill less than 61 cm (2 ft).

The AASHTO (1998) provisions introduced three separate equations for the height of fill less than 61 cm (2 ft)., based on axle load, for distributing live load to the top slab of box culverts. These equations include; one equation for spans greater than 4.6 m (15 ft) and two equations for spans less than 4.6 m (15 ft) depending on the sign of the bending moment. McGrath et al. (2004) reported that the distribution width equation for the spans greater than 4.6 m (15 ft) were developed based on the National Cooperative Highway Research Program (NCHRP) Project 12-26, while, the distribution width for the spans less than 4.6 m (15 ft) were based on the study conducted by Modjeski and Masters (2003).

The AASHTO (2002) provided a single equation for the distribution width for the height of fill less than 61 cm (2 ft), based on a single wheel load on the top slab of box culverts, which also applies to all span lengths for both positive and negative bending, and shear force. For depth of the fill, greater than 61 cm (2 ft), both the AASHTO (1998) and AASHTO (2002) employ two equations each; for one wheel as load, and two wheels as load, which are independent of the span dimension. They depend on the depth of the cover multiplied by the live load distribution factors, which are noticeably

less for the AASHTO (1998) than the AASHTO (2002) provisions. Compatible comparisons of the distribution width for depth of fill less than 61 cm (2 ft) calculated based on AASHTO (1998) and AASHTO (2002) indicate noticeable differences (McGrath et al. (2004)).

The AASHTO (1998) specifications require design check for shear at all depths of fills, while, the AASHTO (2002) specifications only require it for the depth of fill more than 61 cm (2 ft). This is due to the fact that shear strength characteristic of the box culverts with the depth of the fill less than 61 cm (2 ft) is controversial since culverts are constructed with spans as small as 91 cm (3 ft) with slabs thinner than typical bridge decks. Prior to Interim AASHTO (2005) specifications, culverts were not required to be designed with joints, to transfer direct shear across the joints. This concept was based on the research studies conducted by James (1984) and Frederick et al. (1988), which reported that shear transfer was not critical with zero fill depth across the joint due to the small deflections and strains that caused no cracks at service load. However, both the aforementioned studies placed the wheel live load at the edge of the bell or spigot-ends, at the middle of the culvert's span during their experimental testing and/or modeling. Therefore, this raised concerns that the wheel load location may not have produce the critical shear stresses since it was placed away from the vicinity of culvert's wall (support).

To address the aforementioned shortcomings, McGrath et al. (2004) used finite element method (FEM) to investigate the live load distribution widths for reinforced concrete box culverts by placing the wheel live load at a distance "**d**" (=the effective

depth of top slab) from the tip of the haunch to the edge of the load plate. Two dimensional shell elements were used to conduct linear elastic analyses of several parametric cases. This study concluded that the distribution width for shear in general was narrower than that of positive and negative bending moments, and it governed the behavior. The results of this study are implemented in the Interim AASHTO (2005) with new distribution width equations based on shear force distribution, and it was suggested that a shear transfer device should be provided across the joint, if the calculated distribution width exceeds the length between the two adjacent joints.

Since the FEM analyses conducted by McGrath et al. (2004) were linear elastic without experimental verification of the model, and the behavior of culverts subjected to shear is not known, this study was undertaken. This study reports on the findings a major and comprehensive full-scale experimental and finite element studies that considers all practical culvert span sizes with and without compression distribution steel in top slab, As6 (refer to Figure 1.1). Twenty four full-scale experimental tests were conducted on the common ASTM C1433 box culverts with varying sizes. Several tests were also conducted to identify the location of the wheel load which produces the maximum shear effects. A comprehensive nonlinear inelastic three dimensional finite element model is developed with capabilities to predict crack initiation and propagation that is validated with the conducted full-scale tests. Finally, the developed models are used to obtain the distribution width values for shear, which are then used to calculate the shear capacity of the ASTM C1433 precast box culverts.

1.3 Literature Review

1.3.1 Experimental Studies

James (1984) conducted a study to determine the safety of the precast concrete box culverts under the service and design load without the shear connectors. This study used 152 cm (5 ft) and 213 cm (7 ft) clear span boxes as per ASTM C 850 and applied load on the culvert's span centerline at the supported male end, female end, and the unsupported edge in different tests. This study measured steel stresses and deflections and compared them with analytically predicted steel stresses. It was found that the box culvert design was conservative, and the live load deflections and stresses caused by design service wheel loads are acceptable without shear connectors.

Frederick et al. (1988) conducted theoretical studies, field-testing, and model testing. They applied wheel load at center of the 366 cm (12 ft) and 305 cm (10 ft) span boxes with and without installed shear connectors. The development of a ¼-size laboratory model was reported, which was field-tested. It was determined that the shear connectors and the edge beams were not required for the ASTM C850 box culverts.

Sonnenberg et al. (2003) conducted thirty - eight concrete specimen tests. It was found that the failure load of the specimens could be predicted using the Mohr-Coulomb theory with an assumed friction angle of 35^0 provided that the normal stress was greater than 0.15 f'_c, concrete cylinder compressive strength. It was concluded that Mohr-Coulomb theory over estimated the shear capacity of the concrete, for normal stresses less than 0.15 f'_c, unless a modified cohesion value and friction angle were used.

Smeltzer et al. (2004) conducted a study to determine the safety of the precast concrete box culverts subjected to the brittle shear failures. It was recommended that additional research was required to outline the adequacy of the box culvert design for shear, and to identify the need for the shear reinforcement requirement.

1.3.2 Analytical Studies

Hillerborg et al. (1976) presented a method in which fracture mechanics is introduced into the finite element analysis by means of a model where stresses are assumed to act across a crack as long as it is narrowly opened.

Crisfield (1986) studied that the snap-through and snap-back response can also be expected with the cracking of concrete structures besides buckling of shells. Softening material is known to induce 'strain localization', which in the case softening (cracking) of a local region, adjoining material unloads elastically. This leads to a dynamic jump to a new load or displacement level, at a fixed displacement or load state, respectively.

Rots and Blaauwendraad (1989) developed numerical tools to simulate cracking in the concrete and similar materials. It was found that these materials show tensile-softening behavior normal to the crack and the shear retention parallel to the crack. It was reported that smeared cracks could introduce stress locking in a given finite element model.

Kwak and Filippou (1990) proposed a new smeared finite element model based on an improved cracking criterion. This study proposes that cracking to be concentrated

over a small region around the integration points and not over the entire finite element, which retains the objectivity of the results for very large finite elements as being small element only. This study showed that the tension stiffening is an important parameter, and it should always be included in the crack models of the reinforced concrete members.

Feenstra et al. (1991) modeled reinforced concrete with some salient features such as the stress decomposition into a stress contribution of the concrete with a strain-softening model. Also, the contribution of the reinforcing steel with an elasto-plastic model and a stress contribution owing to the interaction between the concrete and the reinforcement were considered.

Biggs et al. (2000) conducted analytical studies using the finite element software, ABAQUS, for depicting the non-linear behavior of the concrete and the reinforcing bars independent of the concrete. Three dimensional finite element models were developed to determine the structural response with reasonable accuracy, which was verified with the experimental data and certain manual calculations.

Hu and Liang (2000) employed numerical analysis using the ABAQUS finite element software to predict the failure mode and the ultimate capacity of the boiling water reactor (BWR Mark III) reinforced concrete containment at the Kuosheng Nuclear Power Plant in Taiwan. Material non-linearities.such as the concrete cracking tension stiffening, shear retention, concrete plasticity, and steel yielding were considered. The effects of temperature were also simulated with a proper constitutive model.

Marzouk et al. (2002) developed a numerical model to predict the punching load and deformations of the reinforced concrete slabs. Despite the low tensile strength of the concrete, it was shown that considerable fracture energy; therefore, the fracture process zone in front of a growing crack, contributed to the flexural concrete strength. The model provided consistent and improved results compared to the cases analyzed by using existing codes.

Mabsout et al. (2004) conducted a parametric study for the multi lane single span reinforced concrete slab bridge slabs. This paper presented the results of a parametric study related to the wheel load distribution in one-span, simply supported, and multilane reinforced concrete bridge slabs. The finite element method was used to investigate the effect of the span length, slab width (with and without shoulders) and the wheel load conditions on typical bridges. A total of 112 highway bridge cases were analyzed and studies by assuming that bridges as stand-alone structures carry one-way traffic. The FEM results of one, two, three, and four-lane bridges were presented in combination with four typical span lengths. Bridges were loaded with highway design HS20 truck load placed at the critical locations in the longitudinal direction of each lane. The FEM results for bridges subjected to edge loading showed that the AASHTO (1996) standard specifications procedure overestimates the bending moment by 30% for one lane and a span length less than 7.5 m (25 ft), but it agrees with the FEM bending moments for longer spans. The AASHTO bending moment compared well with those of the FEM when considering two or more lanes and a span length less than 10.50 m (35 ft). However, as the span length increases, AASHTO underestimates the FEM bending

moment by 15% to 30%. It was shown that the presence of the shoulders on the both sides of the bridge increases the load-carrying capacity of the bridge due to the increase in the slab width. The new AASHTO (1998) load and resistance factor design (LRFD) bridge design specifications overestimate the bending moments for normal traffic on bridges. However, the LRFD procedure gives results similar to those of the FEM edge + truck (a disabled truck at edge and another design truck in lane) loading condition.

Torres et al. (2004) conducted a study for cracked flexural concrete members using the tension-stiffening model. They presented a general strategy to select the numerical values of the coefficients defining uni-axial tensioned concrete equivalent constitutive relationships to simulate, under serviceability condition, the instantaneous and time-dependent flexural behavior of the reinforced and pre-stressed concrete members.

Yee et al. (2004) investigated and performed tests on the shear behavior of the precast reinforced concrete box culverts. This study concluded that all the designs based on the Canadian Highway and Bridge Design Code (CHBDC) and the AASHTO (2003) were conservative. Test results showed that the analysis tools used generated reasonably reliable predictions of the moment distributions.

McGrath et al. (2004) conducted a study to investigate the live load distribution widths for the reinforced concrete box culverts. It was established that equations required the distribution of the axle loads on the top slabs of the box culverts, with 0 to 61 cm (0 to 2 ft) of the fill depth, by using finite element analysis. This study compared, in details, the design equations for AASHTO LRFD with AASHTO Standard

Specifications, which concluded that the LRFD Specifications are more conservative for the box culverts, particularly with spans less than 457 cm (15 ft). Based on FEM analyses, it was reported that the distribution widths for the shear are less than the widths for the bending moment criterion. Thus, it was concluded that the shear design for box culverts bears some scrutiny.

Polak (2005) used 3D shell elements for punching and flexural analysis of the reinforced concrete slabs. The influence of the material modeling was discussed on the calculated results, and they were compared with the test results. It was found that the 3D shell finite elements are economical for studying punching shear effect analysis.

1.4 Objectives and Tasks

The main objectives of this study are:

1. To identify the behavior and mode of failure of the ASTM- C1433 precast box culverts subjected to the HS-20 shear wheel load.

2. To evaluate the shear capacity of the ASTM- C1433 precast box culverts based on the distribution width obtained from the ultimate shear force distribution in this study.

To accomplish the aforementioned objectives the following tasks are performed:

1. Twenty-four full-scale experimental tests on the typical ASTM- C1433 culverts of varying lengths and spans are conducted. In the experimental

program, the wheel load is simulated by a 25 cm x 51 cm (10 in. x 20 in.) rigid plate. The location of the wheel load is varied to identify the load plate location in which the maximum shear stresses are induced in the culvert's top slab. The crack initiation and propagation are monitored by marking the cracks during the course of experiments. The load at which each crack is initiated is recorded and compared to the AASHTO 2005 service and ultimate loads.

2. Three-dimensional FEM of the box culverts are developed by using 3-D shell and solid elements. The smeared crack model is adopted to predict crack initiation and propagation. Material, geometric and contact nonlinearities are incorporated in order to predict the culvert behavior up to the ultimate load. Several mesh configurations and densities are tested to obtain the optimum mesh. The developed finite element model and the associated algorithm are compared and verified with the results. The tension stiffening, tensile strength of concrete parameters used in the FEM for the smeared crack model is determined for each of the test cases.

3. Regression equations are obtained for the calibrated FEM parameters in terms of the geometric and force related culvert variables.

4. The verified optimized FEM is used to analyze all the sizes of the box culverts listed in the ASTM C-1433 subjected to the AASHTO 2005 ultimate design load. The distribution width for shear is obtained by calculating an equivalent width that when multiplied by the peak shear force

represents the volume under the shear force diagram, per unit of the span length under the wheel load, along the culvert joint length.

5. The distribution width for shear is then used to calculate the effective shear area, which leads to the calculation of the ultimate shear capacity of each box culvert listed in the ASTM C-1433, is obtained.

CHAPTER 2

EXPERIMENTAL PROGRAM

2.1 Introduction

A full-scale experimental testing program was undertaken to perform test on twenty-four typical box culverts designated as per ASTM C 1433-05. Several span and joint length sizes were considered to cover a variety of geometrical dimensions which included span of 91 cm (36 in), 122 cm (4 ft), 244 cm (8 ft) and 366 cm (12 ft), and joint length of 122 cm (4 ft) and 244 cm (8 ft). Boxes from two major precast manufacturers in the United States Hanson Pipe and Precast Products and Rinker Hydro-Conduit were tested.

Two UT Arlington's experimental testing facilities were used for the entire testing program: (1) Structural Engineering Laboratory located at the Engineering Lab Building, which will be referred to SEL-ELB from this point forward and (2) The pre-construction temporary UT Arlington Center for Structural Engineering Research, which will be referred to UTA-CSER.

The test set-ups and instrumentation were almost identical in the both testing locations. The test frame consisted of W12x87 columns and built-up crossbeams. The instrumentation, in general, consisted of: two laser-based optoelectronic displacement-

sensors, wire potentiometer, which was placed at almost the same location at the vicinity of the laser, for multiple displacement readings; and data acquisition system.

All the culverts were loaded similarly at 89 kN (2 kip) interval up to 178 kN (40 kip), when the load increment was changed to 22 kN (5 kip) until failure. The 178 kN (40 kip) load was selected based on the observations during the initial testing phase which indicated that the experimental load-displacement plots suffered from stiffness degradation. Also the 178 kN (40 kip) load is almost equal to the factored wheel live load of a HS 20 Truck per AASHTO (2005) (i.e. $16 \times 1.75 \times 1.33 = 37.24\ kip$).

Each test was performed with the assistance of a minimum of six researchers who identified and marked each crack in addition to scribing each event of each test. The load deflection plots, and detailed report on crack formation / initiation, and discussion of the failure mode are reported.

2.2 Specimen Preparation

To prepare the specimens, the reinforcement cages were fabricated by the manufacturer as per design/ASTM C1433-04, and they were transported to the SEL-ELB for strain gauging in a controlled environment (Figure 2.1). After proper surface preparation of the reinforcement, strain gauges were fixed, using adhesive recommended by strain gauge manufacturer, and they were cured under the recommended pressure for proper adhesion. The lead wires were soldered to the strain gage using additional terminal fixed on rebar and the stain gauge as well as lead wire connection were properly protected to withstand the heat and pressure during casting

and curing. Strain-gauged cages were transported back to the plant for dry casting. During the casting, the lead wires of the strain gauges were detoured out of the box via PVC pipes fixed at the location of the lift hole. After curing for seven days, the boxes were transported back to the laboratory.

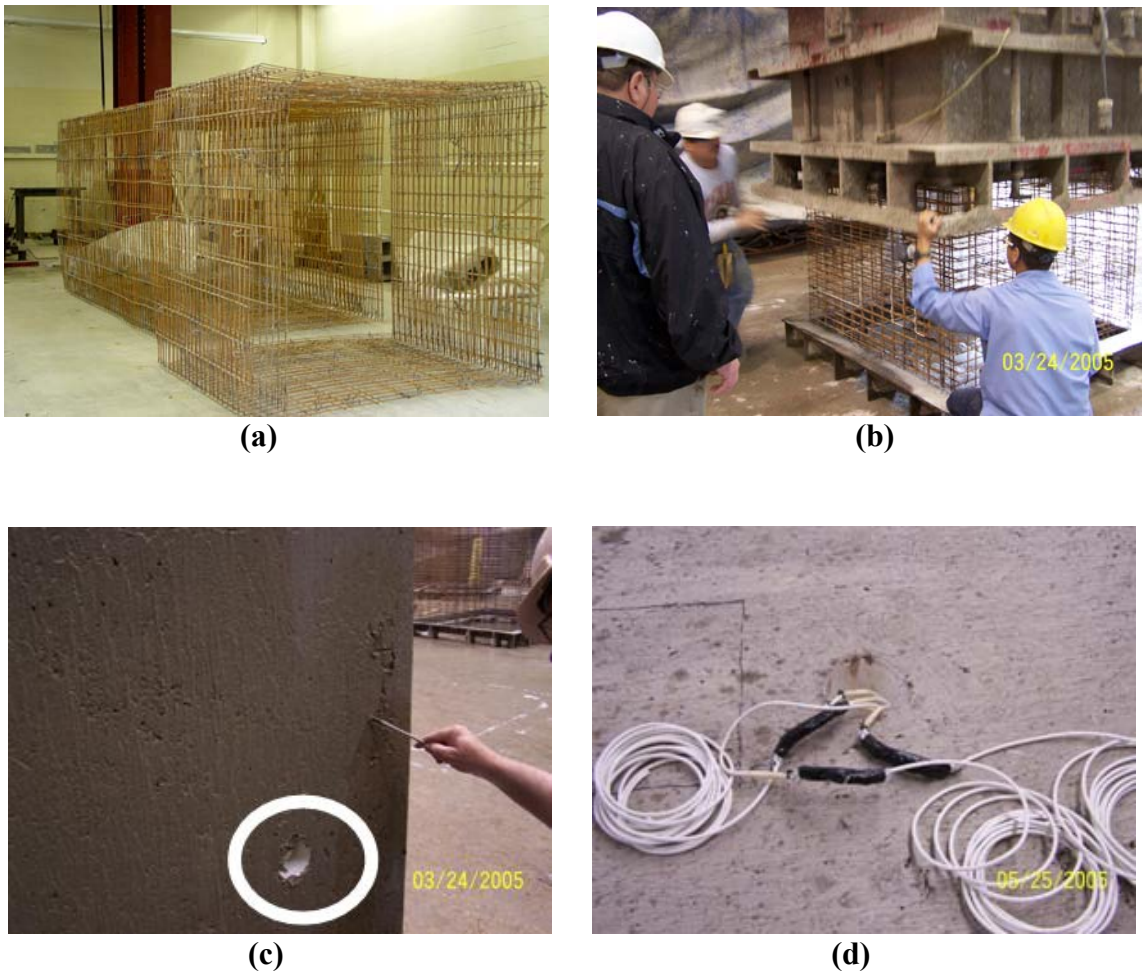

(a) (b)

(c) (d)

Figure 2.1 Specimen Preparation (a) Steel Cages Prior to Strain Gauging; (b) Placing of Form Work on Rebar Cage; (c) Location of Lead Wires after Casting; and (d) Lead Wires Extracted after Casting

2.2.1 Specimen Handling at SEL-ELB

A special A-frame was manufactured to transport the boxes from the unloading location of the laboratory to the testing frame as shown in Figure 2.2. The A-frame was constructed by having "chain and pulley" arrangement at the three adjustable locations to lift and to lower the boxes. Special hydraulic jacks were used to place the boxes in the exact location under the loading frame.

(a)

(b)

(c)

Figure 2.2 Specimen Handling at SEL-ELB (a) Transportation of Steel Cages; (b) Unloading of Box after Casting; and (c) Specimen Handling with A-frame

2.2.2 Specimen Handling at UTA-CSER

At the preconstruction UTA-CSER, a 61 cm (2 ft) thick heavily reinforced reaction floor was specially constructed for testing the large span culverts with weights up to 98 kN (22 kip) (Figure 2.8).

High capacity forklifts were used to place the specimen on the reaction floor at the desired location, under the test frame (Figure 2.3).

Figure 2.3 Specimen Handling at UTA-CSER

2.3 Test Set-Up

2.3.1 Test Set-up at SEL-ELB

The ELB test setup consisted of a reaction frame with four W12x87 steel columns welded to 90 cm x 90 cm (35 ½ in x 35 ½ in) base-plates with a thickness of 5.1 cm (2 in) (Figure 2.4). The base-plates were bolted to the heavily reinforced concrete reaction floor using 5 cm (2 in) diameter bolts. The center of each column were spaced at 244 cm (8 ft in East-West and 122 cm (4 ft) in North-South). Two cross beams were bolted to the reaction frame. A mild steel plate 61 cm x 75 cm x 5 cm (24 in x 29.5 in x 2 in) was bolted in soffit / underneath the pair of beams, and a hydraulic cylinder was bolted underneath this plate. A steel t-stub column was fixed to the bottom of the cylinder as a filler to transfer the load to the box culvert through the load cell as shown in Figure 2.4 through 2.7.

A 25 cm x 51 cm x 2.54 cm (10 in x 20 in x 1 in) mild steel load plate supported by a 1.27 cm (1/2 in) thick rubber sheet, was placed on the top of the box culvert. This was done to simulate the contact area of the wheel of a HS20 truck or tandem, having an axle load of 142 kN (32 kip) and wheel load of 71 kN (16 kip). A 890 kN (200 kip) capacity pre-calibrated load cell was placed on the top of the load plate. A load leveler was also used on the top of the load cell to ensure the application of the concentrated load to the culvert (Figure 2.10). Each test box culvert was placed directly on the top of the reaction floor, with the exception of one test, and no bedding material for the culvert was used. This was done to introduce the maximum stress state in the culvert and to consider the most conservative behavior.

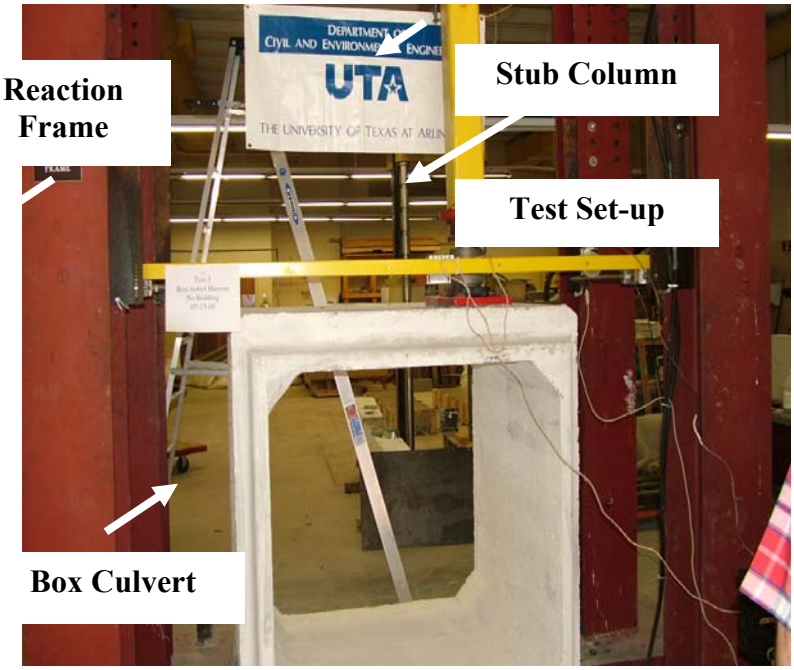

Figure 2.4 Typical Test Set-up and Instrumentation

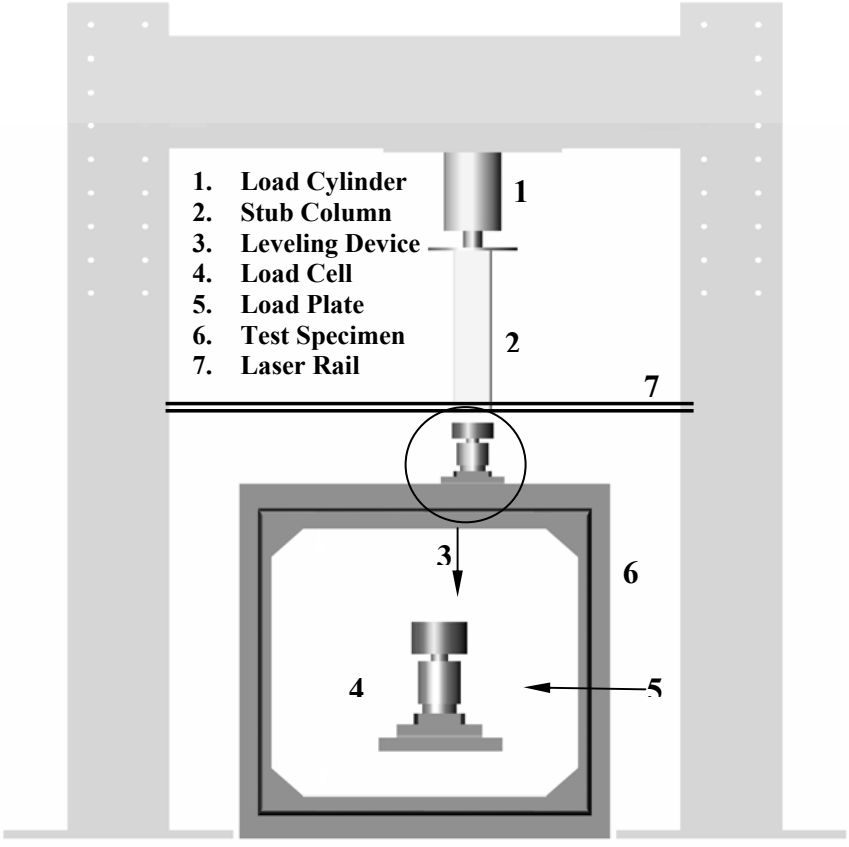

Figure 2.5 Typical Schematic Test Set-up

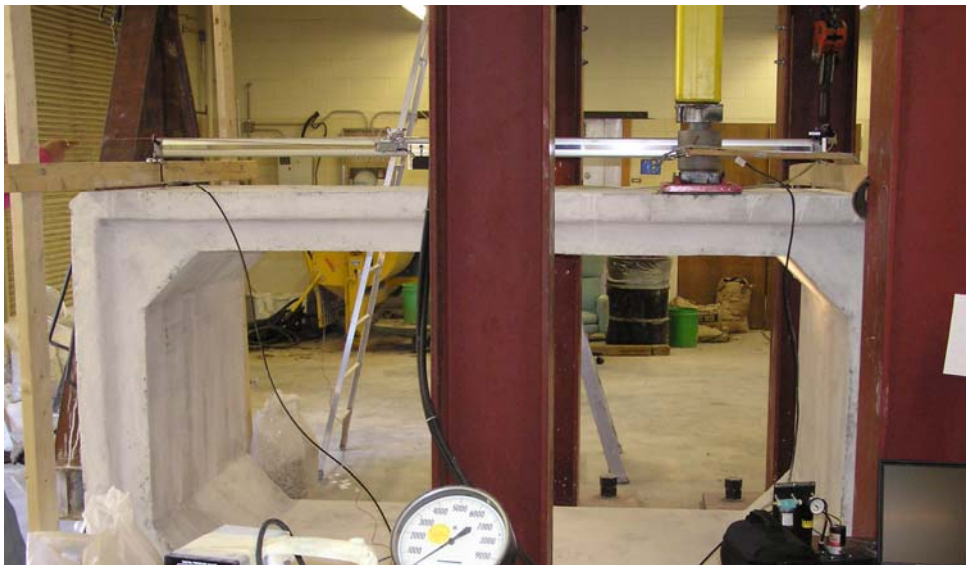

Figure 2.6 Typical Test Set-up and Instrumentation

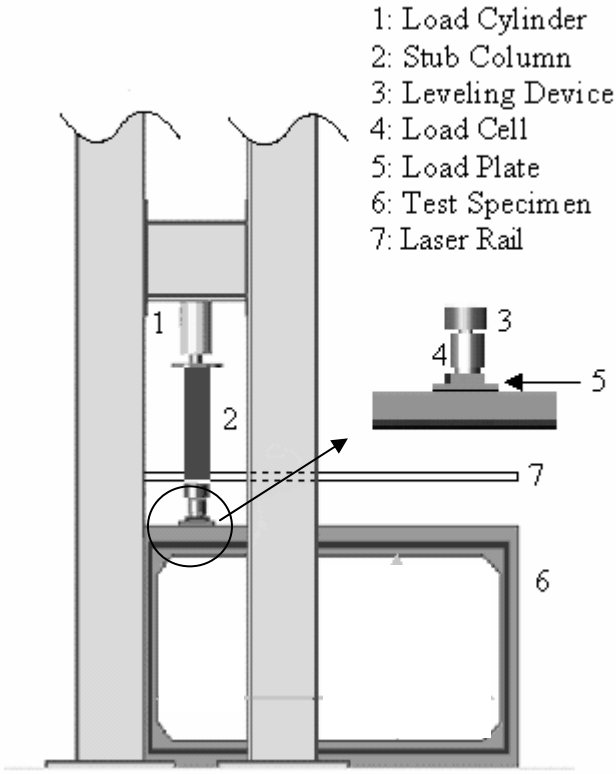

Figure 2.7 Typical Schematic Test Set-up

2.3.2 Testing Frame at Pre-construction UTA-CSER

A special testing frame was constructed at the preconstruction UTA-CSER to complete this study, as heavy and bigger size boxes were difficult to handle. The author designed a new reaction floor of size 6.4 m x 4.27 m x 0.61 m thick (21 ft x 14 ft x 2 ft thick) using reinforced concrete, to resist 1334 kN (300 kip) load. The slab was cast at a pre-existing concrete floor. Provision to hold 4 columns in tension were made in the design and execution of reaction floor. A steel testing frame was designed and fabricated to have a flexible arrangement for load position in plan and in height. Which consisted of four W12x87 steel columns spaced at 488 cm (192 in) in the East-West and 274 cm (108 in) in the North-South. The frame was fixed with 16 - 5.1 cm (2 in) dia bolts embedded in the reaction floor. A 1334 kN (300 kip) capacity pre-calibrated load cell was placed on the top of the load plate. A load leveler was also used on the top of the load cell to ensure the application of the concentrated load to the culvert (Figure 2.10).

The manufacturing of the test frame and reaction floor itself was a time and resource-demanding project. Figure 2.8 shows the reaction floor and test frame at UTA-CSER. Four various sizes of stub columns were used for different tests to fill the gap between the load cylinder and the load cell at this location.

Figure 2.8 Typical Test Set-up and Instrumentation

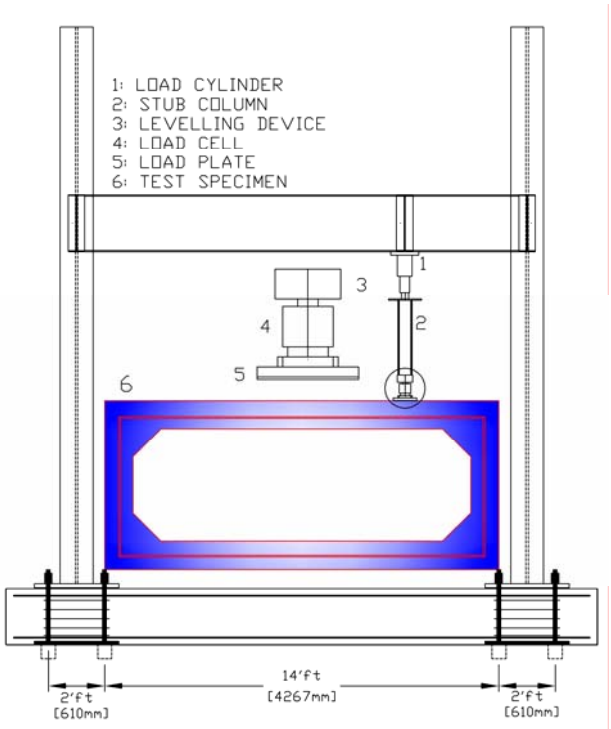

Figure 2.9 Typical Schematic Test Set-up

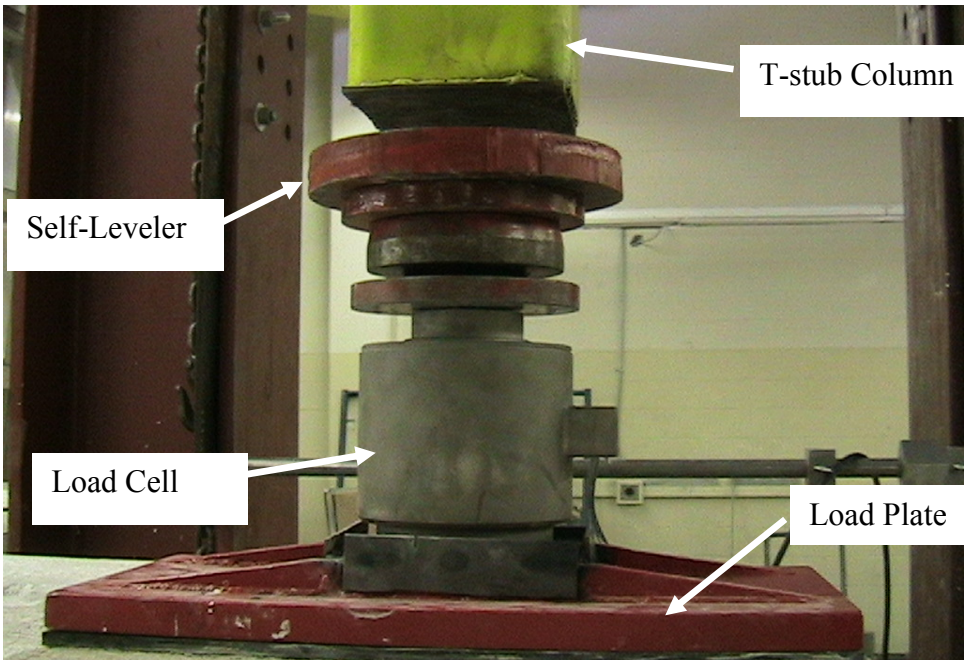

Figure 2.10 Details of Load Cell and Load Plate Assembly

2.4 Instrumentation

A computerized instrumentation and data acquisition system was custom-developed for this study. The measured variables were applied load (electronic load cell), reinforcement strains at five locations (strain gauges), and culvert top slab deflection (laser system). In addition, wire potentiometer was used to duplicate the data recorded by laser-based optoelectronic displacement sensor.

2.4.1 Load Cell

The load cells used were standard 450 Ω (single) full-bridge axial units with 890 kN (200 kip) and 735 kN (300 kip) capacities with a combined error of 0.15% of the full-scale. It featured a stainless steel housing and hermetical seal design. (Figure 2.10)

2.4.2 Strain Gauge

Culvert steel reinforcement strains were recorded with numerous general-purpose uniaxial gauges (Figure 2.11). This basic gauging configuration was selected on the expectation that reinforcements would experience a pure axial strain. The gauges have a constantan 350 Ω grid with a polyimide encapsulation and large-area copper soldering tabs. Fatigue life and operating temperature of the gauges were not important considerations for the testing conditions, and their advertised strain range of 3% was well in excess of that expected. The grid size was selected to be as large as possible for the ease of the application, while occupying a small area in the circumference of the reinforcement bar. Strain gauges are delicate instruments and require great care in their installation. This was of particular concern in the study at hand, because the gauges would experience substantial impact during the concrete pouring. Following the standard steel surface preparation practice, gauges were applied on the rebar wires. Each gauge was soldered using standard three-conductor lead wire connections.

Gauge and connections were encapsulated with a special M-COAT J-3 compound to maximize the survival during the concrete pouring and casting. Lead wires were fed to a central point in the box culvert where they would be protected from the impact of pouring concrete as shown in Figure 2.11. The strain gauge locations

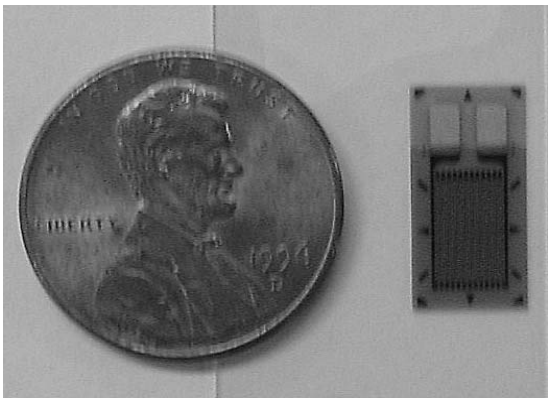

(a)

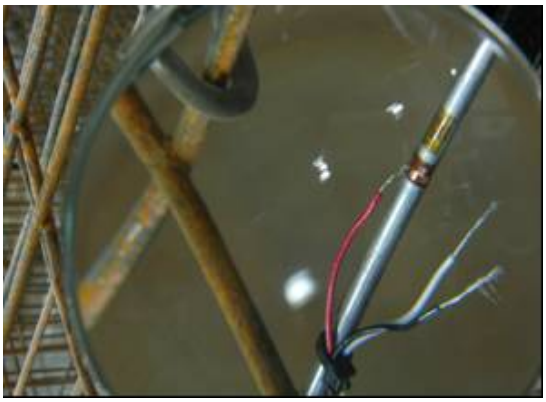

(b)

(c)

(d)

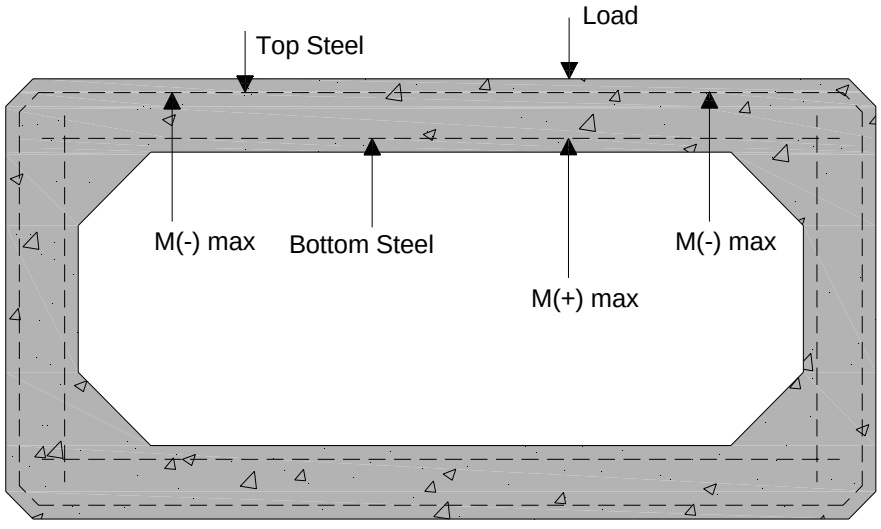

(e)

Figure 2.11 Strain Gauging (a) Strain Gauge versus Penny; (b) Strain Gauged Steel Wire; (c) Protecting Strain Gauges; (d) Protected Lead Wires; and (e) Locations of Strain Gauges

were at mid-span, directly under the load and at the position of maximum negative bending moment as shown in Figure 2.11.

Some gauges were lost and became unusable for data collection during casting and handling.

2.4.3 Laser-Based Optoelectronic Displacement Sensor

A moving laser-based optoelectronic displacement sensor (Figure 2.12) was used to accurately measure the deflection profile of the top slab of the culvert. This device measures distances within a 10 cm range (minimum standoff of 5 cm) with 20 μm resolution at 1 kHz. It operates by projecting a laser beam on the target, which is reflected and imaged on a CCD-array element such that the target distance may be computed by triangulation. Then this laser displacement unit (model MicroEpsilon IDL 1400-100) was mounted on a single-axis motorized stage powered by a Compumotor AX step motor indexer/driver, allowing it to record a continuous stream of the top slab deflection measurements along a 122 cm (4 ft) and 244 cm (8 ft) track. To ensure the minimal skewing of the span position and the deflection measurements and to minimize the acquisition system complexity, a retractable draw-wire potentiometer was attached to the track shuttle to measure the span position as an additional analog instrumentation channel as shown in Figure 2.10. Finally, the draw-wire potentiometer was directly wired into the data acquisition board as a ratio metric input channel.

Figure 2.12 Laser-Based Optoelectronic Displacement Sensor

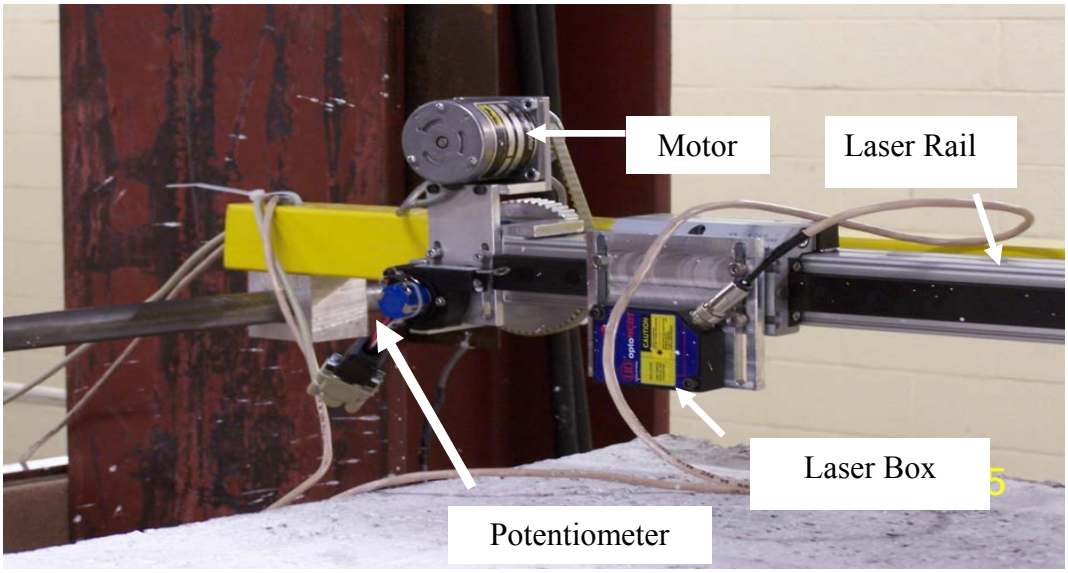

Figure 2.13 Details of Laser Instrumentation

2.4.4 Cable-Extension Displacement Sensor

A 25 cm (10 in) full scale range Cable-Extension Displacement Sensor (CDS) (Fig 2.14 - Fig 2.15) was used to measure the displacement of the inside face of the top slab of the box. The CDS was hooked to the instrumentation to get the displacement of box slab at each load step.

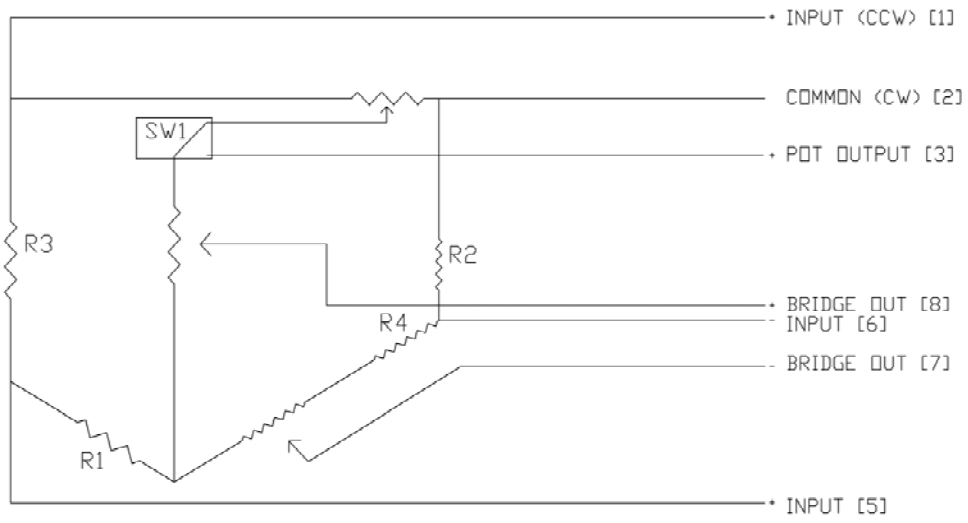

Figure 2.14 Circuit for Cable-Extension Displacement Sensor

Figure 2.15 Cable-Extension Displacement Sensor during Test Set-up

2.4.5 Data Acquisition Unit

The above sensors are connected to a signal conditioning and data acquisition unit. The load cell was connected to a precise ADMET unit and a proportional full-scale analog output ranging from 0 to 10 V was then fed into the computer data acquisition board (the use of the ADMET unit was not strictly necessary and was used for convenience). The strain gauges were directly wired into the individual quarter-bridge completion networks (model Omega BCM-1), and these were in turn connected directly to the data acquisition board—which was capable of providing the required excitation voltage. The laser displacement sensor required an external 24 V power supply and provided a 4-20 mA output proportional to the displacement, which was turned into a voltage signal and fed into the data acquisition board as well. Finally, the draw-wire

potentiometer was directly connected to the data acquisition board as a ratio metric input channel.

The data acquisition unit was an InstruNet model INET-100HC from Omega Engineering. This was a high-performance, high-precision computer-based acquisition system with the ability to interface directly to the most standard sensors. The HC version features high-current output capability, which was employed to power the strain bridges and ratio metric sensors. The software allowed the user to directly configure each channel in terms of the specific sensor used; this was particularly useful for the processing of the non-linear quarter-bridge strain gauge outputs. Other features included automatic nulling of strain channels, two-point linear calibration and engineering unit conversion, software-programmable input voltage ranges, programmable analog and digital input filtering, programmable sampling rate (nominally set at 8 Hz), and real-time visualization and acquisition of input channels.

The InstruNet software was sufficient to acquire and store the data for each test, thus no custom programming was necessary (except configuring the input channels). A separate program was written in Visual Basic to independently control the motorized shuttle carrying the laser displacement sensor. Since the position of the shuttle was simultaneously acquired at all times along with the laser displacement channel, no synchronization between the acquisition and motion programs was necessary. (Figure 2.16 and Figure 2.17)

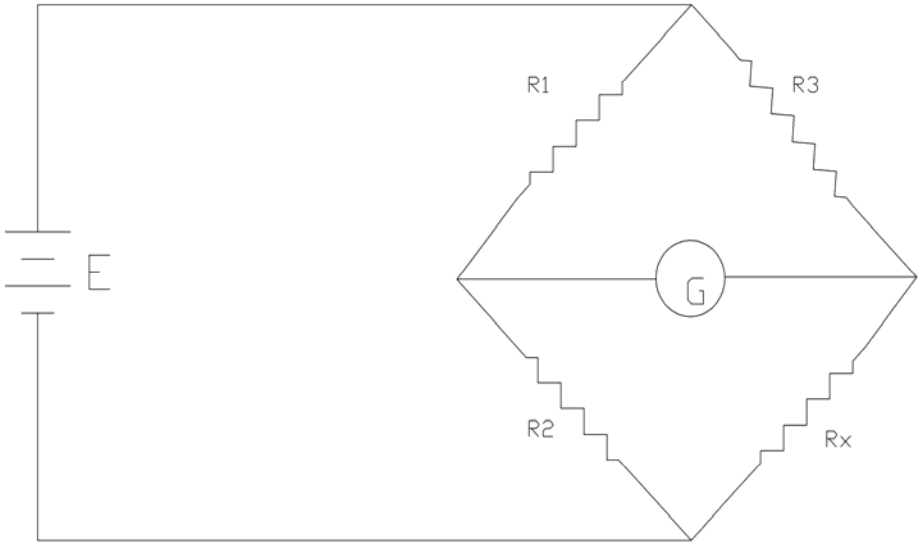

Figure 2.16 Wheatstone Bridge

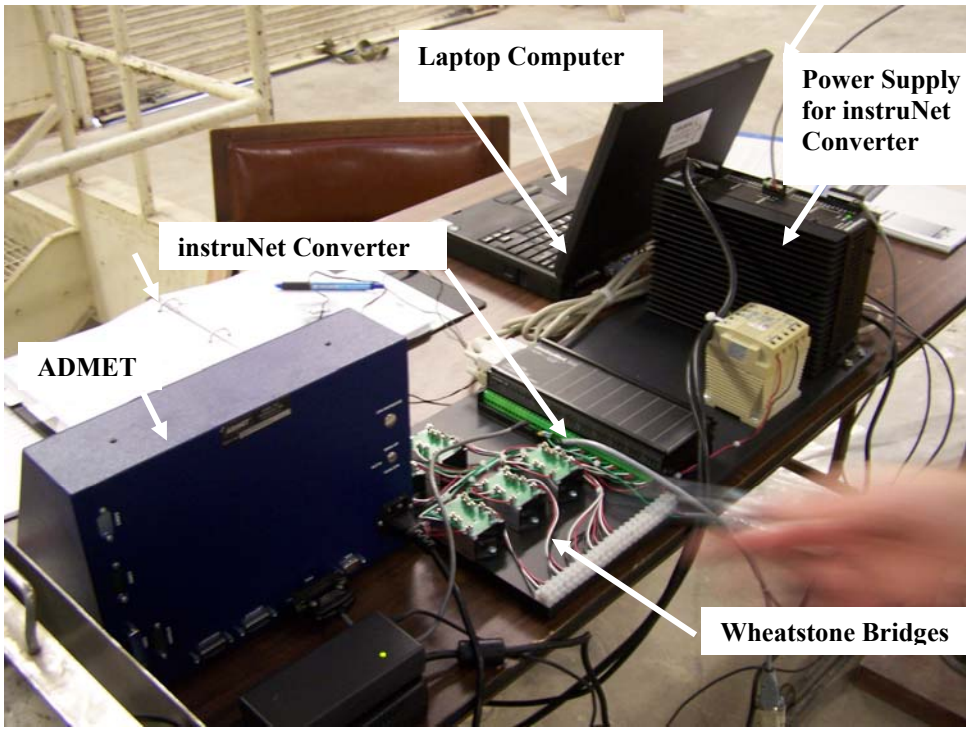

Figure 2.17 Data Collection System

2.5 Selection of Test Cases

2.5.1 Box Sizes

Test cases were selected for various spans and joint lengths. Spans of 91 cm (3 ft), 122 cm (4 ft), 244 cm (8 ft) and 366 cm (12 ft) were tested with a joint length of 122 cm (4 ft) for all the spans tested and 244 cm (8 ft) for the spans of 122 cm (4 ft) and 244 cm (8 ft).

Depending upon the span length, the thickness of the top slab varied from 17.8 cm (7 in) to 30.5 cm (12 in). The bottom slab thickness varied from 15.2 cm (6 in) to 30.5 cm (12 in), and the wall thickness varied from 12.7 cm (5 in) to 30.5 cm (12 in). The haunch dimensions also varied from 12.7 (5 in) to 30.5 cm (12 in).

The reinforcement cages consisted of plain welded wires as per ASTM A 185. The sizes of the steel wires used for the reinforcement cages were W2.0 to W8.0 with the nominal area of 12.90 mm^2 (0.02 in^2) through 51.61 mm^2 (0.08 in^2) per reinforced wire. The nominal diameter of each wire ranged from 4 mm to 8 mm (0.159 in to 0.319 in). Typical spacing of wires was 5 cm (2 in), 10 cm (4 in), and 15 cm (6 in).

2.5.2 Location of Load

The scope of the testing program was to cover culverts subjected to depth of fill less than 61 cm (2 ft). Thus, the wheel load was placed directly on the outside face of the top slab. The load plate was placed at the edge of the box, along the joint length in order to introduce the minimum distribution width. The location of the load was varied

along the span in order to identify the most critical location in which the shear capacity is minimal.

Thus, the load plate was place at **d**, 1.5**d** and 2**d** in three different tests of SP_244-122-122_Y (SP_8-4-4_Y) and the behavior of box was observed. Also in a test of SP_122-122-122_Y (SP_4-4-4_Y) box the load plate was placed at 0**d**, 0.23**d**, and **d**. Finite element analysis were also run for different load locations. It was found that the distance **d** is the most critical section. When the load plate was placed at a distance less than **d,** part of the load directly transferred to the adjoining wall without causing any shear stresses, and shear stresses were reduced in the top slab. Also, when the load plate was placed beyond the distance **d** the shear stresses on the near wall was reduced which caused less effective shear, and more bending behavior.

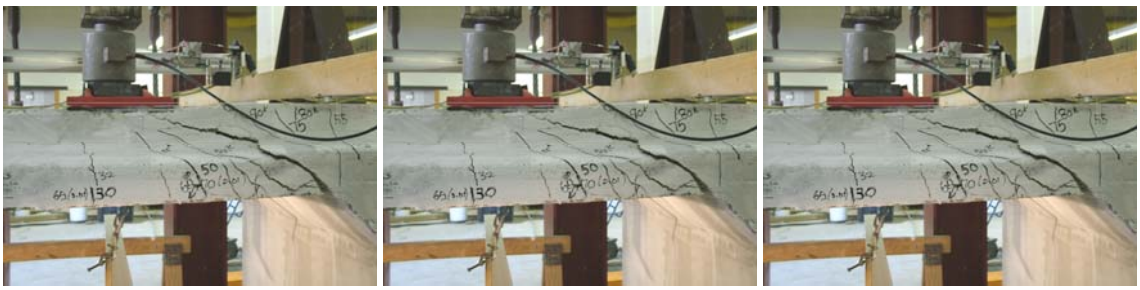

(a) **(b)** **(c)**

Figure 2.18 Location of Load Plate from Tip of the Haunch in a Spigot End Test (a) Load Plate at d; (b) Load Plate at 1.5d; and (c) Load Plate at 2d

2.6 Loading Procedure

The load was applied to the box culvert through the load plate by using a hydraulic pump. The load increment was 4.45kN (1 kip) initially up to 44.5 kN (10 kip) after which it was changed to 8.9 kN (2 kip) up to 178 kN (40 kip) where stiffness

degradation was observed for most of the test specimens. For almost all the test specimens, the load increment was 22 kN (5 kip) from the aforementioned 178 kN (40 kip) onward. The 178 kN (40 kip) was in the close range of the AASHTO factored wheel load of 166 kN ($16 \times 1.75 \times 1.33 = 37.24\ kip$)

2.7 Crack Monitoring Process

While testing, to ensure consistency between the tests, a method was used for identifying crack initiations. After a crack initiated, a black marker was used to draw a line parallel to the crack. When the crack was no longer visible in the culvert, a bar was drawn across the previously drawn line indicating the end of the crack for that load. The load was written in kips next to the line for the ease of the referencing during the testing and future evaluations (Figure 2.19).

Figure 2.19 Crack Monitoring Process

2.8 Test Nomenclature

Different loading positions were tested to examine the behavior of the box culverts. Tests were conducted on the spigot end or the bell end of each culvert. The box was either with or without top slab compression distribution steel. The following nomenclature was used to identify each test specimen. The test designations were defined as: SP or BL _ S-R-L _ N or Y _ ***l***x where designations are:

SP – Spigot end

BL – Bell end

S-R-L – Dimension of the culvert in cm (ft) (span, rise, and the joint length)

N – No distribution reinforcement (A_{S6})

lx - Distance between the tip of the haunch to the edge of the load plate in

Y – With distribution reinforcement (A_{S6}) terms of 'd'

For example SP_244-122-122_Y_d (SP_8-4-4_Y_d), identifies a spigot-end culvert test with the dimensions of: Span = 244 cm (8 ft); Rise = 122 cm (4 ft) and Joint Length = 122 cm (4 ft) with distribution steel A_{S6}. The edge of the load plate for this test was located at the distance **d** from the tip of the haunch.

2.9 Experiment Results

2.9.1 Boxes of 122 cm (4 ft) Span and 122 cm (4 ft) Joint Length

In all the tests conducted, the load plate was placed on the right side of the spigot /Bell end of the culvert. The major events recorded during the experiment are presented in Appendix A. Table 2.1 shows the main events during the experiment. All

the test specimens exhibited similar crack patterns with respect to the initiation and propagation. Generally, the initial superficial flexural cracks occurred on the inside face of the bottom slab or on the inside face of the top slab directly under the load plate near the loading (spigot/ bell) end. Flexural cracks continued to occur in these two places throughout the testing. At approximately 245 kN to 400 kN (55 kip to 90 kip), flexural cracks initiated on the sidewalls of the culverts for all the five test specimens. In most of tests the specimen failed due to the strut and tie action/ bond /flexural failure along the loading (spigot/bell) end to the left of the load plate. The failure cracks were nearly identical, extending from the left corner of the load plate diagonally to the edge of the haunch.

The load deflection plots for this series of tests are shown in Figure 2.20. As per AASHTO 2005, the permissible maximum deflection for 122 cm (4 ft) span is 1.52 mm (0.06 in) (span / 800) at the service load of 71 kN (16 kip). All the tests satisfied this criterion.

Finally, Table 2.2 presents the summary of the test results, which include the loads at which 0.25 mm (0.01 in) shear cracks occurred, the ultimate load, and the failure mode for each test specimen. This table shows that the shear cracks for all the test specimens ranged from 267 kN (60 kip) to 356 kN (80 kip) which are above the strength limit state of 166 kN ($16 \times 1.75 \times 1.33 = 37.24\ kip$) for the live load used in designing per AASHTO 2005.

Table 2.1 Crack Event Load in kN (kip) for 122 cm (4 ft) Span and 122 cm (4 ft) Joint Length Boxes

Event No.	Event	Test/Load in kN (kip)					
		# SP_122-122-122_Y_0 #(SP_4-4-4_Y_0)	SP_122-122-122_Y_0 (SP_4-4-4_Y_0)	SP_122-122-122_Y_0.23d (SP_4-4-4_Y_0.23d)	BL_122-122-122_Y_0.23d (BL_4-4-4_Y_0.23d)	*BL_122-122-122_Y_0.23d *(BL_4-4-4_Y_0.23d)	SP_122-122-122_Y_d (SP_4-4-4_Y_d)
1.	1st superficial flexure crack appeared at loading end, on the inside face of the bottom slab under the load.	156 (35)	133 (30)	107 (24)	156 (35)	200 (45)	111 (25)
2.	1st superficial flexure crack appeared at loading end, on the inside face of the top slab under the load.	178 (40)	133 (30)	156 (35)	133 (30)	133 (30)	111 (25)
3.	First flexural crack initiated on the outside face of the left wall.	-	267 (60)	267 (60)	-	-	245 (55)
4.	First flexural crack initiated on the outside face of the right wall.	-	334 (75)	311 (70)	-	334 (75)	289 (65)
5.	First serviceability flexure crack (0.01 in wide) detected.	-	-	-	245 (55)	467 (105)	289 (65)
6.	First shear crack initiated at the Loading end.	423 (95)	267 (60)	334 (75)	311 (70)	-	534 (120)
7.	First **Serviceability shear** crack detected.	578 (130)	334 (75)	601 (135)	400 (90)	-	534 (120)
8.	Ultimate failure. # With Bedding *** Double Box**	632 (142)	712 (160)	645 (145)	498 (112)	601 (135)	578 (130)

Table 2.2 Summary of Test Results for 122 cm (4 ft) Span and 122 cm (4 ft) Joint Length Boxes

Test	First Shear crack 0.25 mm (0.01 in) wide		Failure Load kN (kip)	Failure Mode
	Load kN (kip)	End Location		
#SP_122-122-122_Y_0 # (SP_4-4-4_Y_0)	578 (130)	Spigot	632 (142)	Strut & Tie /Bond/Flexural
SP_122-122-122_Y_0 (SP_4-4-4_Y_0)	267 (60)	Spigot	712 (160)	Strut & Tie /Bond/Flexural
SP_122-122-122_Y_0.23d (SP_4-4-4_Y_0.23d)	334 (75)	Spigot	645 (145)	Strut & Tie /Bond/Flexural
BL_122-122-122_Y_0.23d (BL_4-4-4_Y_0.23d)	400 (90)	Bell	498 (112)	Strut & Tie /Bond/Flexural
*BL_122-122-122_Y_0.23d *(BL_4-4-4_Y_0.23d)	-	Bell	601 (135)	Strut & Tie /Bond/Flexural
SP_122-122-122_Y_d (SP_4-4-4_Y_d)	356 (80)	Spigot	578 (130)	Strut & Tie /Bond/Flexural

With Bedding * Double Box

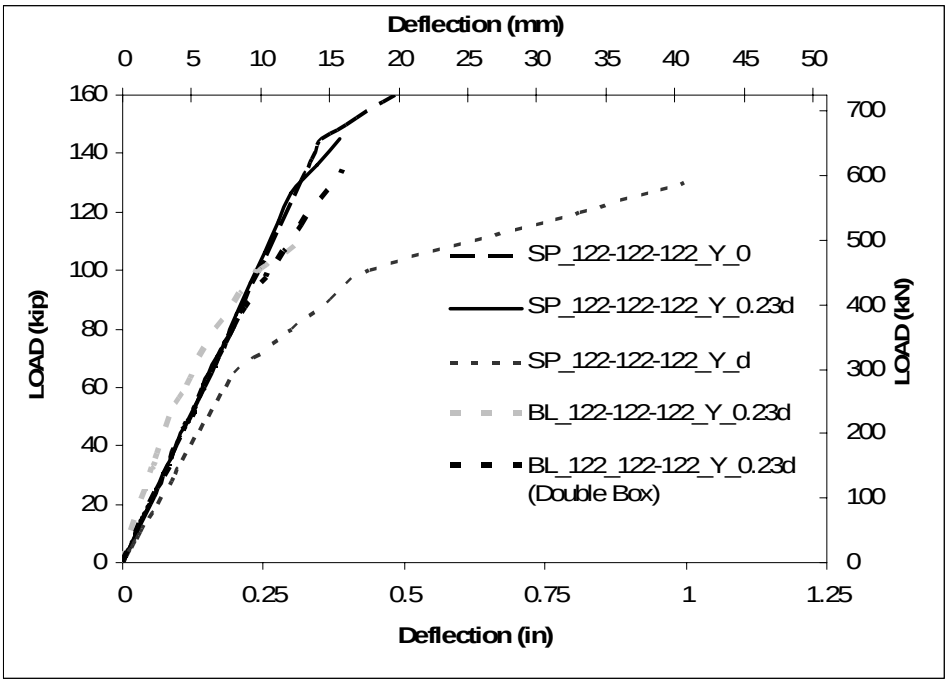

Figure 2.20 Load versus Deflection Plots for 122 cm (4 ft) Span and 122 cm (4 ft) Joint Length Boxes

2.9.1.1 Test: SP_122-122-122_Y_0 (SP_4-4-4_Y_0) (with Bedding)

This test had a bedding thickness of 7.5 cm (3 in) with nominal size of its coarse aggregate as 20 mm (0.75 in), as shown in Figure (Figure 2.21). The load plate was placed starting from the tip of the haunch, on the spigot end, to examine the effect of the maximum shear force near the support. In this test, no shear crack detected until 356 kN (80 kip) of load and the box failed at 632 kN (142 kip). The detailed events of this test are presented in Table A1 of Appendix A. The Photographs of the cracks and the associated failure are shown in Figure B1 of Appendix B.

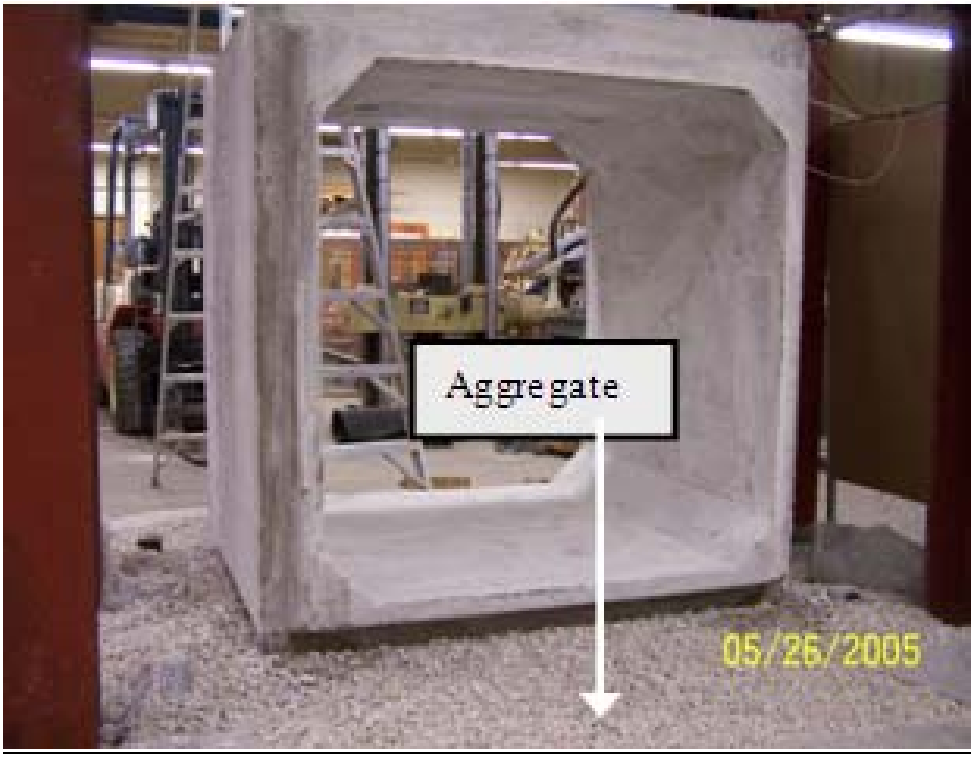

Figure 2.21 Test Specimen with Bedding

2.9.1.2 Test: SP_122-122-122_Y_0 (SP_4-4-4_Y_0)

The load plate was placed with its edge at the tip of the haunch, on the spigot end. In this test, no shear crack detected until 267 kN (60 kip) of load and the box failed at 712 kN (160 kip). The detailed events of this test are presented in Table A2 of Appendix A. The Photographs of the cracks and the associated failure are shown in Figure B2 of Appendix B. Also, the deflection of the top slab, obtained from optoelectronic displacement sensor, is shown in Figure 2.22.

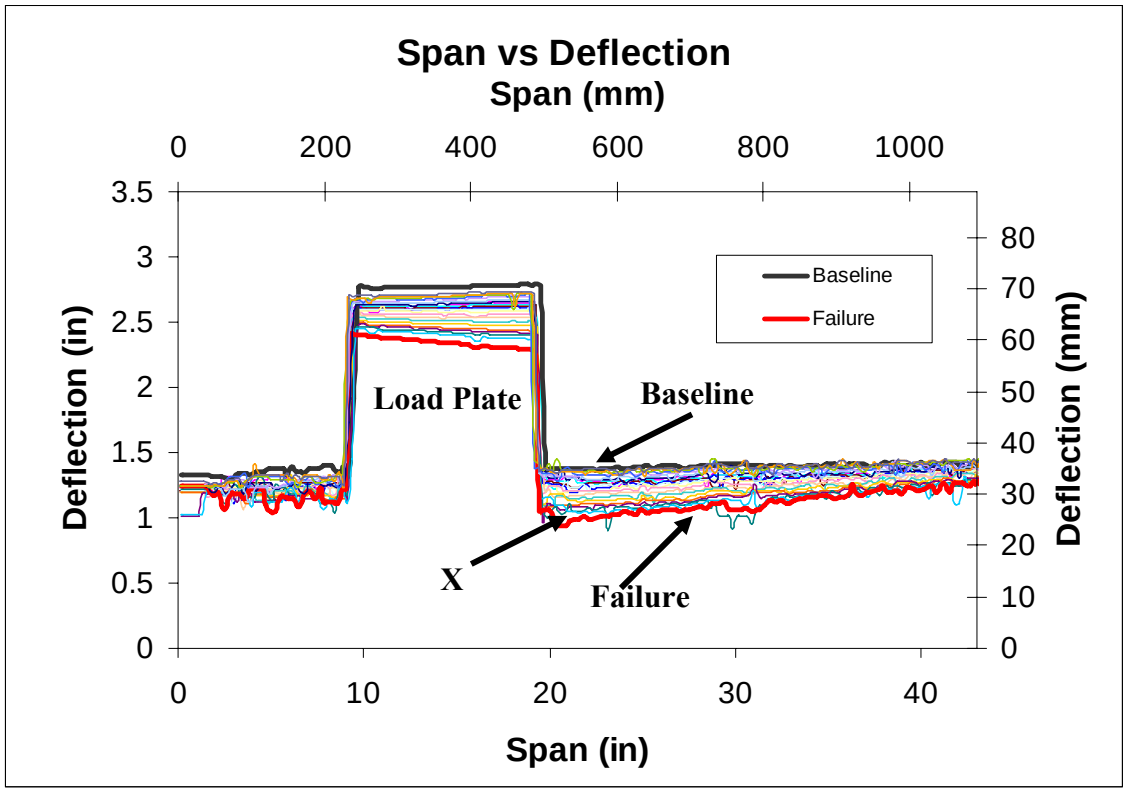

Figure 2.22 Test: SP_122-122-122_Y_0 (SP_4-4-4_Y_0) Laser Sensor Deflections

2.9.1.3 Test: SP_122-122-122_Y_0.23d (SP_4-4-4_Y_0.23d)

To examine the effect of maximum shear force, the load plate was placed on the spigot end at a distance of 3.8 cm (1.5 in) from the tip of the haunch. In this test, no shear crack detected until 334 kN (75 kip) of load and the box failed at 645 kN (145 kip). The detailed events of this test are presented in Table A3 of Appendix A. The Photographs of the set up and the observed failure are shown in Figure B3 of Appendix B.

2.9.1.4 Test: BL_122-122-122_Y_0.23d (BL_4-4-4_Y_0.23d)

The load plate was placed on the bell end at the same distance as in the previous test i.e. 3.8 cm (1.5 in) from the tip of the haunch. In this test, the first shear crack detected at approximately 311 kN (70 kip) of load and the box failed at 498 kN (112 kip). The detailed events of this test are presented in Table A4 of Appendix A. The Photographs of the set up and the failure are shown in Figure B4 of Appendix B.

2.9.1.5 Test: BL_122-122-122_Y_0.23 (BL_4-4-4_Y_0.23) (Double Box)

This was a double box test, in which, the load plate was placed at the joint, and on the bell end at the same location as in the previous test i.e. 3.8 cm (1.5 in) from the tip of the haunch. In this test, the load at which the shear crack occurred could not be recorded due to an inaccessible joint while testing. The joint was not grouted, and no shear key or any other transfer device was used. Failure of the arrangement of the boxes took place at 601 kN (135 kip). The detailed events of this test are presented in Table

A5 of Appendix A. The Photographs of the set up and the failure of the joint as well as the individual box after the unloading and separation of the boxes are shown in Figure B5 of Appendix B.

2.9.1.6 Test: SP_122-122-122_Y_d (SP_4-4-4_Y_d)

The load plate was placed on the spigot end at a distance of **d** =16.5 cm (6.5 in) from the tip of the haunch. In this test, the first shear crack detected at 534 kN (120 kip) of load and the box failed at 578 kN (130 kip). The detailed events of this test are presented in Table A6 of Appendix A. The Photographs of the set up and the failure are shown in Figure B6 of Appendix B. Also, the deflection of the top slab, obtained from optoelectronic displacement sensor, is shown in Figure 2.23.

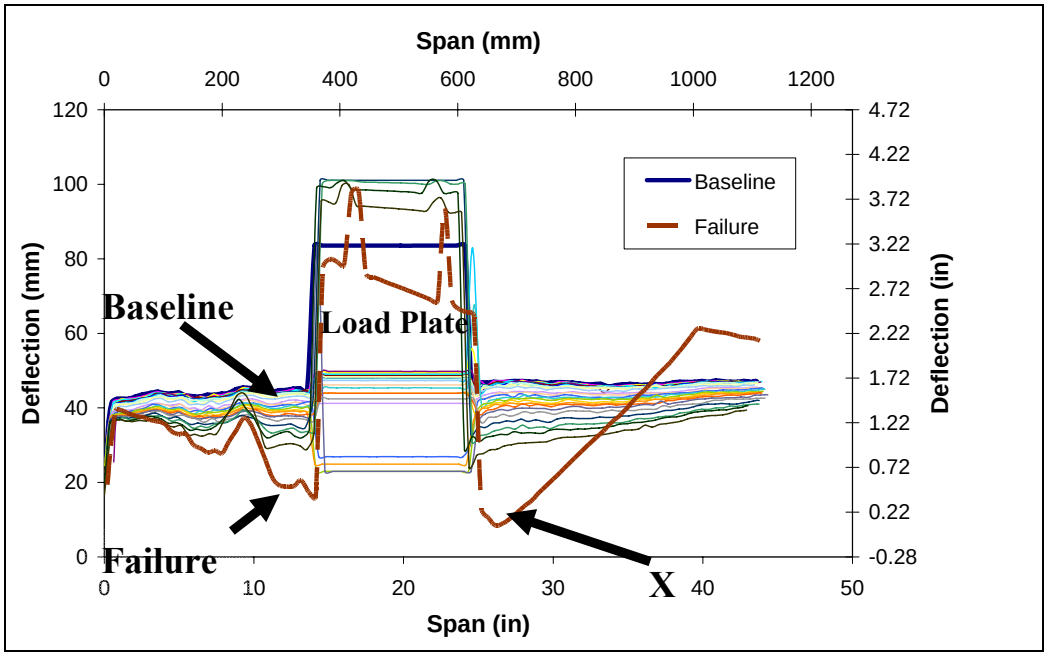

Figure 2.23 Test: SP_122-122-122_Y_d (SP_4-4-4_Y_d) Laser Sensor Deflections

2.9.2 Boxes of 122 cm (4 ft) Span and 244 cm (8 ft) Joint Length

In both the tests conducted, the load plate was placed on the right side of the spigot /Bell end of the culvert. The major events recorded during the experiment are presented in Tables A6 and A7 of Appendix A. Table 2.3 shows the main events during the experiment. Both the test specimens exhibited similar crack patterns with respect to the initiation and propagation. Generally, the initial superficial flexural cracks occurred on the inside face of the top slab, directly under the load plate near the loading (spigot/ bell) end. At approximately 200 kN to 267 kN (45 kip to 60 kip), flexural cracks initiated on the sidewalls of the culverts and the inside face of the top slab for both the test specimens. Both specimens failed due to the strut and tie action/ bond /flexural failure from the tip of haunch along the loading (spigot/bell) end to the edge of the load plate.

The load deflection plots for both the tests are shown in the Figure 2.24. Finally, Table 2.4 presents the summary of the test results, which include the loads at which 0.25 mm (0.01 in) shear cracks occurred, the ultimate load, and the failure mode for each test specimen. This table shows that the shear cracks for both the test specimens formed at 320 kN (72 kip) to 334 kN (75 kip) which are above the strength limit state of 166 kN ($16 \times 1.75 \times 1.33 = 37.24\ kip$) for the live load used per AASHTO 2005.

2.9.2.1 Test: SP_122-122-244_Y_d (SP_4-4-8_Y_d)

The load plate was placed on the spigot end at a distance of '**d**', 16.5 cm (6.5 in) from the tip of the haunch. The first shear crack detected at 311 kN (70 kip) of load, and the

box failed at 578 kN (130 kip). The detailed events of this test are presented in Table A7 of Appendix A. The Photographs of the set up and the failure are shown in Figure B7 of Appendix B.

2.9.2.2 Test: BL_122-122-244_Y_d (BL_4-4-8_Y_d)

The load plate was placed on the bell end at a distance of **d**=16.5 cm (6.5 in) from the tip of the haunch. In this test, no shear crack detected until failure and the box failed at 320 kN (72 kip). The detailed events of this test are presented in Table A8 of Appendix A. The Photographs of the set up and the failure are shown in Figure B8 of Appendix B.

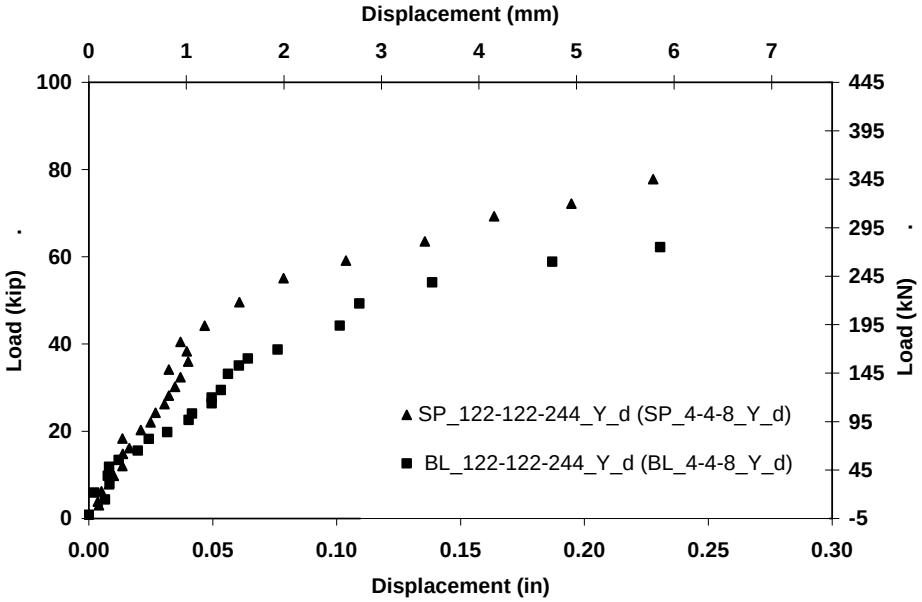

Figure 2.24 Load versus Deflection Plots for 122 cm (4 ft) Span 244 cm (8 ft) Joint Length Boxes

Table 2.3 Crack Event Load in kN (kip) for 122 cm (4 ft) Span and 244 cm (8 ft) Joint Length Boxes

Event No.	Event	Test/Load in kN (kip)	
		SP_122-122-244_Y_d (SP_4-4-8_Y_d)	BL_122-122-244_Y_d (BL_4-4-8_Y_d)
1.	1st superficial flexure crack appeared at loading end, on the inside face of the top slab under the load.	142 (32)	133 (30)
2.	1st superficial flexure crack appeared at loading end, on the inside face of the bottom slab under the load.	267 (60)	245 (55)
3.	First flexural crack initiated on the outside face of the left wall.	289 (65)	245 (55)
4.	First flexural crack initiated on the outside face of the right wall.	245 (55)	200 (45)
5.	First serviceability flexure crack (0.01 in wide) detected.	311 (70)	220 (50)
6.	First shear crack initiated at the Loading end.	334 (75)	-
7.	First **Serviceability shear** crack detected.	-	-
8.	Ultimate failure.	578 (130)	320 (72)

Table 2.4 Summary of Test Results for 122 cm (4 ft) Span and 244 cm (8 ft) Joint Length Boxes

Test	First Shear crack 0.25 mm (0.01 in) wide		Failure Load kN (kip)	Failure Mode
	Load kN (kip)	End Location		
SP_122-122-244_Y_d (SP_4-4-8_Y_d)	334 (75)	Spigot	578 (130)	Strut & Tie /Bond/Flexural
BL_122-122-244_Y_d (BL_4-4-8_Y_d)	320 (72)	Spigot	320 (72)	Strut & Tie /Bond/Flexural

2.9.3 Test Results for 244 cm (8 ft) Span and 122 cm (4 ft) Joint Length Boxes

In all the tests conducted, the load plate was placed on the right side of the spigot / Bell end of the culvert. The major events recorded during the experiment are presented in Appendix A. Table 2.5 shows the main events during the experiment. All the test specimens exhibited similar crack patterns with respect to the initiation and propagation. Generally, the initial superficial flexural cracks occurred on the inside face of the bottom slab or on the inside face of the top slab directly under the load plate near the loading (spigot/ bell) end. Flexural cracks continued to occur in these two places throughout testing. At approximately 187 kN to 334 kN (42 kip to 75 kip), some flexural cracks initiated on the sidewalls of the culverts for all the six test specimens. In most of the tests, the specimen failed due to shear/ bond / flexural failure along the loading (spigot / bell) end to the right of the load plate. The failure cracks were nearly identical, extending from the right corner of the load plate and diagonally to the edge of the haunch.

The load deflection plot for all the tests are shown in the graph of Figure 2.25. As per AASHTO 2005, the permissible maximum deflection for 244 cm (8 ft) span is 3.05 mm (0.12 in) (span / 800) at the service load of 71 kN (16 kip). All the tests satisfied this parameter.

Finally, Table 2.6 presents the summary of the test results, which include the loads at which 0.25 mm (0.01 in) shear cracks occurred, the ultimate load, and the failure mode for each test specimen. This table shows that the shear cracks for all the test specimens formed at 311 kN (70 kip) to 423 kN (95 kip) which are above the strength limit state of 166 kN ($16 \times 1.75 \times 1.33 = 37.24\ kip$) for the live load used in design per AASHTO 2005. The loaded failure Photographs for all the six tests are shown in Figure 2.26.

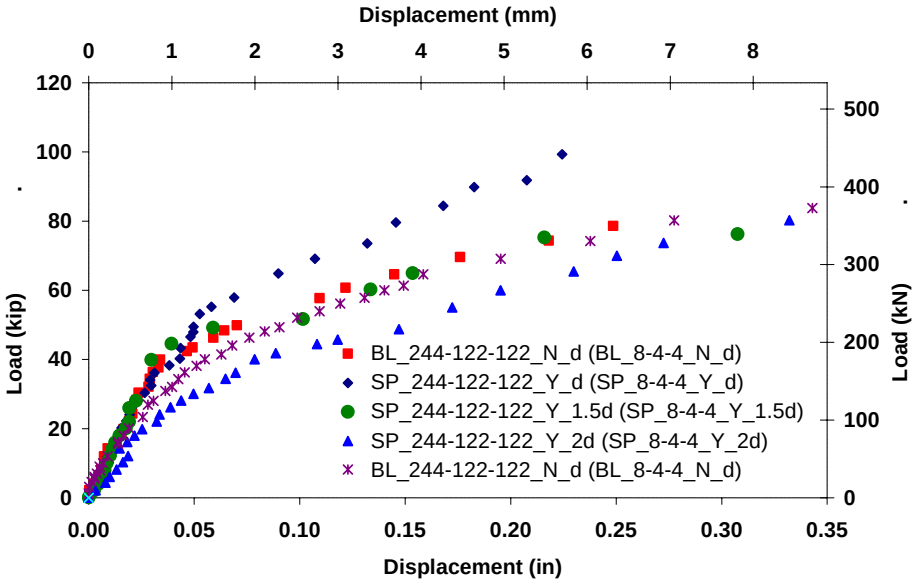

Figure 2.25 Load versus Center-Load Plate-Deflection Plots for 244 cm (8 ft) Span 122 cm (4 ft) Joint Length Boxes

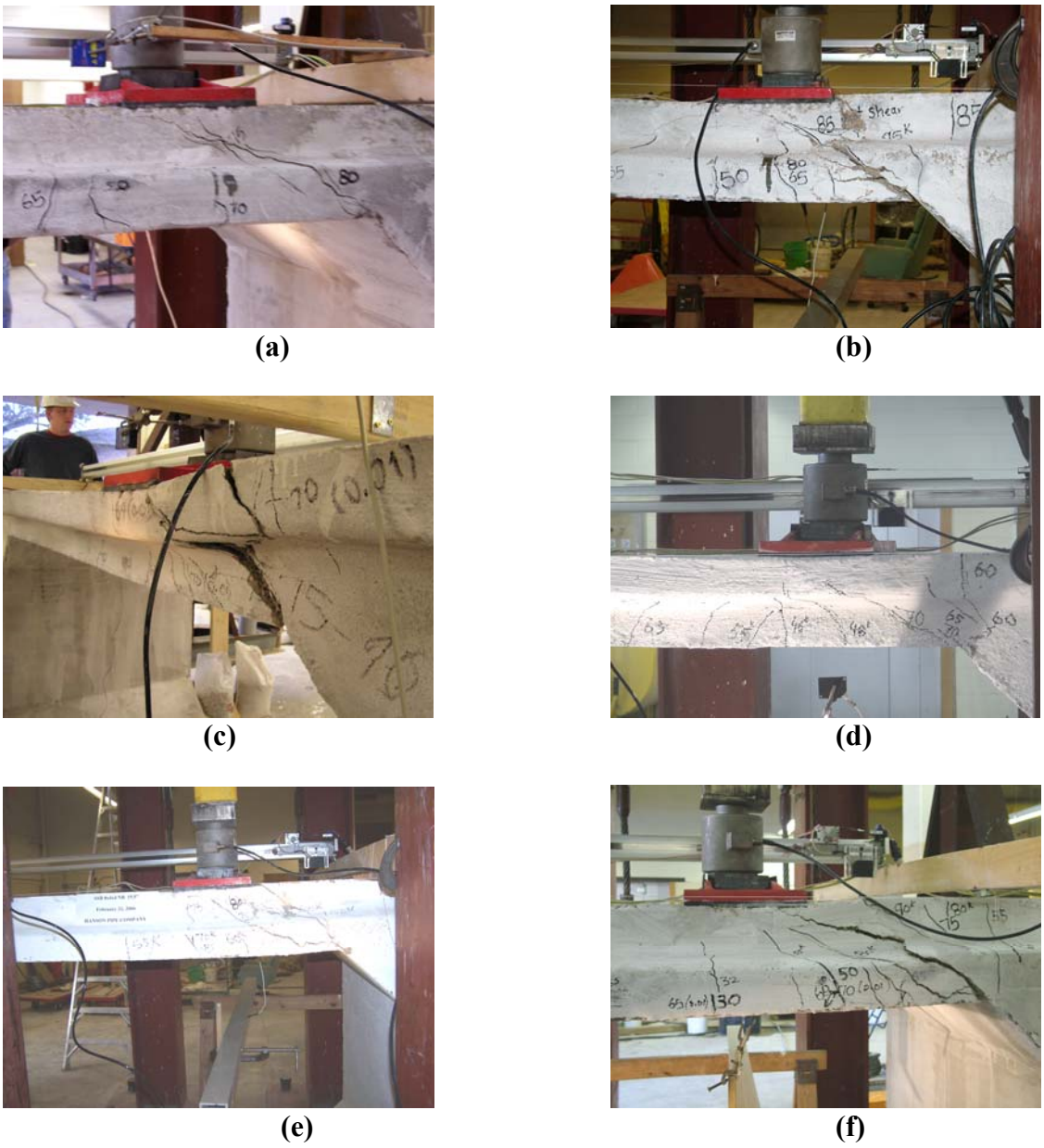

Figure 2.26 Photographs of the 244 cm (8 ft) Span and 122 cm (4 ft) Joint Length Specimens at Failure (a) SP_244-122-122_N_d (SP_8-4-4_N_d); (b) SP_244-122-122_Y_d (SP_8-4-4_Y_d); (c) BL_244-122-122_N_d (BL_8-4-4_N_d); (d) BL_244-122-122_Y_d (BL_8-4-4_Y_d); (e) SP_244-122-122_Y_1.5d (SP_8-4-4_Y_1.5d); and (f) SP_244-122-122_Y_2d (SP_8-4-4_Y_2d)

Table 2.5 Crack Event Load in kN (kip) for 244 cm (8 ft) Span and 122 cm (4 ft) Joint Length Test Boxes

Event No.	Event	Test/Load in kN (kip)					
		SP_244-122-122_N_d (SP_8-4-4_N_d)	SP_244-122-122_Y_d (SP_8-4-4_Y_d)	BL_244-122-122_N_d (BL_8-4-4_N_d)	BL_244-122-122_Y_d (BL_8-4-4_Y_d)	SP_244-122-122_Y_1.5d (SP_8-4-4_Y_1.5d)	SP_244-122-122_Y_2d (SP_8-4-4_Y_2d)
1.	First non-measurable flexural crack detected on the inside face of the top slab under the load plate.	187 (42)	160 (36)	125 (28)	116 (26)	133 (30)	107 (24)
2.	First negative flexural crack detected on the outside face of the top slab.	231 (52)	245 (55)	205 (46)	214 (48)	200 (45)	187 (42)
3.	First flexural crack initiated on the outside face of the wall.	222 (50)	334 (75)	311 (70)	214 (48)	200 (45)	187 (42)
4.	Flexural crack detected at left haunch on the inside face of the bottom slab.	231 (52)	289 (65)	311 (70)	267 (60)	245 (55)	222 (50)
5.	First serviceability crack detected (0.25 mm (0.01 in) wide).	334 (75)	356 (80)		311 (70)	311 (70)	267 (60)
6.	First shear crack initiated at the Loading end.	334 (75)	378 (85)	334 (75)	312 (70)	356 (80)	356 (80)
7.	First **Serviceability shear** crack detected.	334 (75)	423 (95)	400 (90)	334 (75)	356 (80)	311 (70)
8.	Ultimate failure.	543 (122)	480 (108)	400 (90)	391 (88)	480 (108)	445 (100)

Table 2.6 Summary of Test Results for 122 cm (4 ft) Span and 122 cm (4 ft) Joint Length Boxes

Test	First Shear crack 0.25 mm (0.01 in) wide		Failure Load kN (kip)	Failure Mode
	Load kN (kip)	Location		
SP_244-122-122_N_d (SP_8-4-4_N_d)	334 (75)	Spigot-end	543 (122)	Shear/flexure/bond
SP_244-122-122_Y_d (SP_8-4-4_Y_d)	423 (95)	Spigot-end	480 (108)	Shear/flexure/bond
BL_244-122-122_N_d (BL_8-4-4_N_d)	400 (90)	Bell-end	400 (90)	Shear/flexure/bond
BL_244-122-122_Y_d (BL_8-4-4_Y_d)	334 (75)	Bell-end	391 (88)	Shear/flexure/bond
SP_244-122-122_Y_1.5d (SP_8-4-4_Y_1.5d)	356 (80)	Spigot-end	480 (108)	Shear/flexure/bond
SP_244-122-122_Y_2d (SP_8-4-4_Y_2d)	311 (70)	Spigot-end	445 (100)	Shear/flexure/bond

2.9.3.1 Test: SP_244-122-122_N_d (SP_8-4-4_N_d)

The load plate was placed at a distance of '**d**' starting from the tip of the haunch, on the spigot end of the box, being the critical location of the shear as verified by FEM model. This specimen was lacking A_{S6}, distribution steel in compression, in top slab. In this test, no shear crack detected until 334 kN (75 kip) of load and the box failed at 543 kN (122 kip). The detailed events of this test are presented in Table A9 of Appendix A.

The Photographs of cracks on all the faces after unloading are shown in Figure B9 of Appendix B.

2.9.3.2 Test: SP_244-122-122_Y_d (SP_8-4-4_Y_d)

The load plate was also placed at the distance **d** from the tip of the haunch, on the spigot end of the box. This specimen was having compression distribution steel in the top slab. The first shear crack detected at 378 kN (85 kip) of load and the box failed at 480 kN (108 kip). The detailed events of this test are presented in Table A10 of Appendix A. The Photographs of the cracks on all the faces are shown in Figure B10 of Appendix B.

2.9.3.3 Test: BL_244-122-122_N_d (BL_8-4-4_N_d)

The load plate was placed at the distance **d** from the tip of the haunch, on the bell end. This specimen was lacking A_{S6}, compression distribution steel, in the top slab. The first shear crack detected at 334 kN (75 kip) of load and the box failed at 400 kN (90 kip). The detailed events of this test are presented in Table A11 of Appendix A. The Photographs of the cracks on all the faces are shown in B11 of Appendix B.

2.9.3.4 Test: BL_244-122-122_Y_d (BL_8-4-4_Y_d)

The load plate was placed at the distance **d** from the tip of haunch, on the bell end. This specimen was having compression distribution steel in the top slab. The first shear crack detected at 312 kN (70 kip) of load and box failed at 391 kN (88 kip). The detailed events of this test are presented in Table A12 of Appendix A. The Photographs of the cracks on all the faces after unloading are shown in B12 of Appendix B.

2.9.3.5 Test: SP_244-122-122_Y_1.5d (SP_8-4-4_Y_1.5d)

The load plate was placed at the distance 1.5**d** from the tip of the haunch, on the spigot end of the box. This specimen had A_{S6}, compression distribution steel, in top slab. The first shear crack detected at 356 kN (80 kip) of load and the box failed at 480 kN (108 kip). The detailed events of this test are presented in Table A13 of Appendix A. The Photographs of cracks on all faces after unloading are shown in B13 of Appendix B

2.9.3.6 Test: SP_244-122-122_Y_2d (SP_8-4-4_Y_2d)

The load plate was placed at the distance 2**d** from the tip of the haunch to the edge of the load plate on the spigot end. This specimen was having A_{S6}, compression distribution steel, in the top slab. The first shear crack detected at 356 kN (80 kip) of load and the box failed at 445 kN (100 kip). The detailed events of this test are presented in Table A14 of Appendix A. The Photographs of the cracks on all the faces are shown in B14 of Appendix B.

2.9.4 Test Result for 244 cm (8 ft) Span and 244 cm (8 ft) Joint Length Boxes

In all the tests conducted, the load plate was placed on the right side of the spigot / Bell end of the culvert. The major events recorded during the experiment are presented in Table A15 through Table A18 of Appendix A. Table 2.7 shows the main events during the experiment. All the test specimens exhibited similar crack patterns with respect to the initiation and propagation. Generally, the initial superficial flexural

cracks occurred on the inside face of the bottom slab or on the inside face of the top slab directly under the load plate near the loading (spigot/ bell) end. Flexural cracks continued to occur in these two places throughout testing. At approximately 200 kN to 289 kN (45 kip to 65 kip), some flexural cracks initiated on the sidewalls of the culverts for all the four test specimens. In most tests, the specimen failed due to a shear / bond / flexural failure along the loading (spigot / bell) end to the right of the load plate. The failure cracks were extending from the right corner of the load plate and diagonally to the edge of the haunch or at the joint of top right haunch and right wall.

The load deflection plots for all the tests are shown in Figure 2.27. The data for one test was corrupted due to the power failure. Finally, Table 2.8 presents the summary of the test results, which include the loads at which 0.25 mm (0.01 in) shear cracks occurred, the ultimate load, and the failure mode for each test specimen. This table shows that the shear cracks for all the test specimens formed at 298 kN (67 kip) to 400 kN (90 kip) which are above the strength limit state of 166 kN ($16 \times 1.75 \times 1.33 = 37.24\ kip$) for the live load used in design per AASHTO 2005.

Table 2.7 Crack Event Load in kN (kip) for 244 cm (8 ft) Span and 244 cm (8 ft) Joint Length Boxes

Event No.	Event	Test/Load in kN (kip)			
		SP_244-122-244_Y_d (SP_8-4-8_Y_d)	SP_244-122-244_N_d (SP_8-4-8_N_d)	BL_244-122-244_Y_d (BL_8-4-8_Y_d)	BL_244-122-244_N_d (BL_8-4-8_N_d)
1.	First non-measurable flexural crack detected on the inside face of the top slab under the load plate.	178 (40)	142 (32)	169 (38)	142 (32)
2.	First negative flexural crack detected on the outside face of the top slab.	267 (60)	334 (75)	222 (50)	200 (45)
3.	First flexural crack initiated on the outside face of the wall.	200 (45)	245 (55)	245 (55)	289 (65)
4.	Flexural crack detected at left haunch on the inside face of the bottom slab.	-	151 (34)	220 (50)	-
5.	First serviceability crack detected (0.25 mm (0.01 in) wide).	400 (90)	178 (40)	267 (60)	311 (70)
6.	First shear crack initiated at the Loading end.	423 (95)	400 (90)	298 (67)	311 (70)
7.	First **Serviceability shear** crack detected.	525 (118)	525 (118)	334 (75)	334 (75)
8.	Ultimate failure.	618 (139)	592 (133)	378 (85)	387 (87)

Table 2.8 Summary of Test Results for 244 cm (8 ft) Span and 244 cm (8 ft) Joint Length Test Boxes

Test	First Shear crack (0.01 in) wide		Failure Load kN (kip)	Failure Mode
	Load kN (kip)	Location		
SP_244-122-244_Y_d (SP_8-4-8_Y_d)	525 (118)	Spigot-end	618 (139)	Shear/flexure/bond
SP_244-122-244_N_d (SP_8-4-8_N_d)	525 (118)	Spigot-end	592 (133)	Shear/flexure/bond
BL_244-122-244_Y_d (BL_8-4-8_Y_d)	334 (75)	Bell-end	378 (85)	Shear/flexure/bond
BL_244-122-244_N_d (BL_8-4-8_N_d)	334 (75)	Bell-end	387 (87)	Shear/flexure/bond

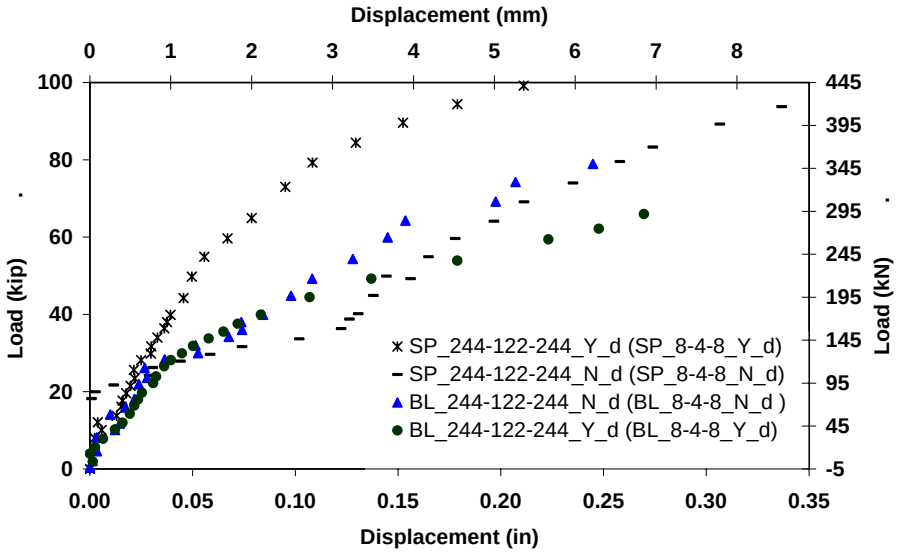

Figure 2.27 Load versus Center-Load Plate-Deflection Plots for 244 cm (8 ft) Span and 244 cm (8 ft) Joint Length Boxes

2.9.4.1 Test: SP_244-122-244_Y_d (SP_8-4-8_Y_d)

The load plate was placed at the distance **d** from the tip of the haunch, on the spigot end of the box, being the critical location. This specimen was having distribution steel in the compression region of the top slab. The first shear crack detected at 525 kN (118 kip) of load, and the box failed at 618 kN (139 kip). The detailed events of this test are presented in Table A15 of Appendix A. The Photographs of the cracks on all the faces are shown in Figure B15 of Appendix B.

2.9.4.2 Test: SP_244-122-244_N_d (SP_8-4-8_N_d)

The load plate was placed at the distance **d** from the tip of the haunch, on the spigot end of the box. This specimen was without A_{S6}, compression distribution steel in the top slab. The first shear crack formed at 525 kN (118 kip) of load and the box failed at 592 kN (133 kip). The detailed events of this test are presented in Table A16 of Appendix A. The Photographs of cracks on all the faces after unloading are shown in Figure B16 of Appendix B

2.9.4.3 Test: BL_244-122-244_Y_d (BL_8-4-8_Y_d)

The load plate was also placed at the distance **d** from the tip of haunch being the critical location. This specimen was having compression distribution steel in the top slab. The first shear crack detected at 334 kN (75 kip) of load and the box failed at 378 kN (85 kip). The detailed events of this test are presented in Table A17 of Appendix A. The Photographs of the cracks on all the faces are shown in Figure B17 of Appendix B.

2.9.4.4 Test: BL_244-122-244_N_d (BL_8-4-8_N_d)

The load plate was placed at the distance **d** from the tip of the haunch, on the bell end. This specimen was without A_{S6}, compression distribution steel in the top slab. In this test, no shear crack detected until 334 kN (75 kip) of load and the box failed at 387 kN (87 kip). The detailed events of this test are presented in Table A18 of Appendix A. The Photographs of the cracks on all the faces after unloading are shown in Figure B18 of Appendix B.

2.9.5 Test Result for 366 cm (12 ft) Span and 122 cm (4 ft) Joint Length Boxes

In all the tests conducted, the load plate was placed on the right side of the spigot / Bell end of the culvert. The major events recorded during the experiment are presented in Appendix A. Table 2.9 shows the main events during the experiment. All the test specimens exhibited similar crack patterns with respect to the initiation and propagation. Generally, the initial superficial flexural cracks occurred on the inside face of the top slab directly under the load plate near the loading (spigot/ bell) end. Flexural cracks continued to occur in this place throughout testing. At approximately 151 kN to 222 kN (34 kip to 50 kip), some flexural cracks initiated on the sidewalls of the culverts for all the four test specimens. In these tests, the specimen failed due to a shear / bond / flexural failure along the bell end to the right of the load plate and at mid span. During the test in which spigot end was loaded, the boxes did not fail until 667 kN (150 kip) of load. The failure cracks were extending from the right corner of the load plate and diagonally to the edge of the haunch or at the left edge of the load plate to the mid span.

All the tests are shown in the graph of Figure 2.28. Finally, Table 2.9 presents the summary of the test results, which include the loads at which 0.25 mm (0.01 in) shear cracks occurred, the ultimate load, and the failure mode for each test specimen. This table shows that the shear cracks for all the test specimens formed at 334 kN (75 kip) to 578 kN (130 kip) which are above the strength limit state of 166 kN ($16 \times 1.75 \times 1.33 = 37.24$ *kip*) for the live load used in design per AASHTO 2005.

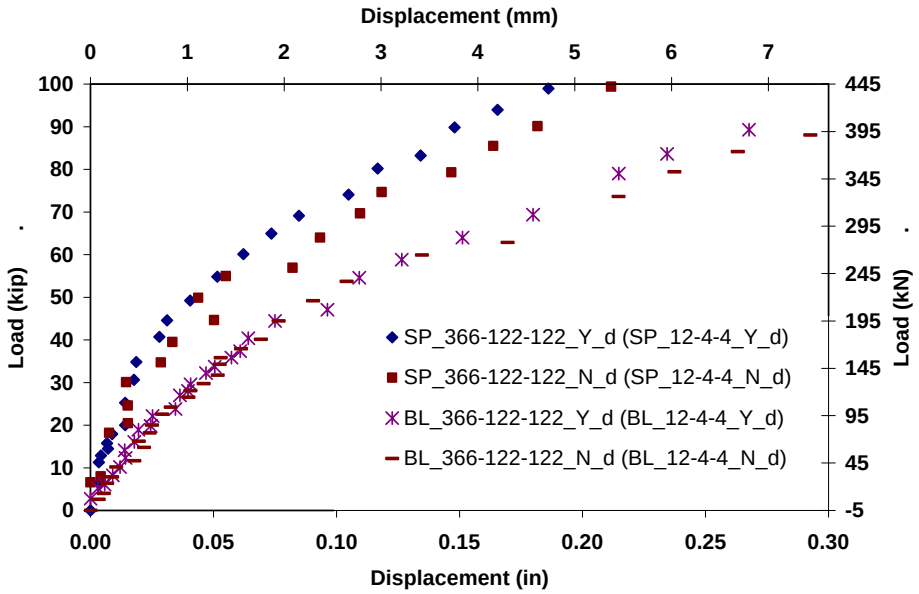

Figure 2.28 Load versus Center-Load Plate-Deflection Plots for 366 cm (12 ft) Span and 122 cm (4 ft) Joint Length Boxes

Table 2.9 Crack Event Load in kN (kip) for 366 cm (12 ft) Span and 122 cm (4 ft) Joint Length Boxes

Event No.	Event	Test/Load in kN (kip)			
		SP_366-122-122_Y_d (SP_12-4-4_Y_d)	SP_366-122-122_N_d (SP_12-4-4_N_d)	BL_366-122-122_Y_d (BL_12-4-4_Y_d)	BL_366-122-122_N_d (BL_12-4-4_N_d)
1.	First non-measurable flexural crack detected on the inside face of the top slab under the load plate.	178 (40)	200 (45)	133 (30)	98 (22)
2.	First negative flexural crack detected on the outside face of the top slab.	445 (100)	267 (60)	245 (55)	222 (50)
3.	First flexural crack initiated on the outside face of the wall.	178 (40)	222 (50)	169 (38)	151 (34)
4.	Flexural crack detected at left haunch on the inside face of the bottom slab.	423 (95)	267 (60)	245 (55)	245 (55)
5.	First serviceability crack detected (0.25 mm (0.01 in) wide).	445 (100)	400 (90)	311 (70)	311 (70)
6.	First shear crack initiated at the Loading end.	578 (130)	445 (100)	467 (105)	334 (75)
7.	First **Serviceability shear** crack detected.	578 (130)	623 (140)	489 (110)	334 (75)
8.	Ultimate load* /failure. * Box did not fail	618* (139)	645* (145)	498 (112)	525 (118)

Table 2.10 Summary of Test Results for 366 cm (12 ft) Span and 122 cm (4 ft) Joint Length Test Boxes

Test	First Shear crack (0.01 in) wide		Max* / Failure Load kN (kip)	Failure Mode
	Load kN (kip)	Location		
SP_366-122-122_Y_d (SP_12-4-4_Y_d)	578 (130)	Spigot -end	618* (139)	Shear/flexure/bond
SP_366-122-122_N_d (SP_12-4-4_N_d)	445 (100)	Spigot -end	645* (145)	Shear/flexure/bond
BL_366-122-122_Y_d (BL_12-4-4_Y_d)	467 (105)	Bell-end	498 (112)	Shear/flexure/bond
BL_366-122-122_N_d (BL_12-4-4_N_d)	334 (75)	Bell-end	525 (118)	Shear/flexure/bond

2.9.5.1 Test: SP_366-122-122_Y_d (SP_12-4-4_Y_d)

The load plate was placed at the distance **d** from the tip of the haunch, on the spigot end. This specimen was with compression distribution steel in the top slab. The first shear crack detected at 578 kN (130 kip) of load and failure was not observed until 618 kN (139 kip). The detailed events of this test are presented in Table A19 of Appendix A. The Photographs of the cracks on all the faces are shown in Figure B19 of Appendix B.

2.9.5.2 Test: SP_366-122-122_N_d (SP_12-4-4_N_d)

The load plate was placed at the distance **d** from the tip of the haunch, on the spigot end of the box. This specimen was without A_{S6}, compression distribution steel in the top slab. The first shear crack detected at 445 kN (100 kip) of load and the box did not fail up to 645 kN (145 kip). The detailed events of this test are presented in Table A20 of Appendix A. The Photographs of cracks on all the faces after unloading are shown in Figure B20 of Appendix B.

2.9.5.3 Test: BL_366-122-122_Y_d (BL_12-4-4_Y_d)

The load plate was placed at the distance **d** from tip of haunch, on the bell end. This specimen was with compression distribution steel in the top slab. The first shear crack detected at 467 kN (105 kip) and the box failed at 498 kN (112 kip). The detailed events of this test are presented in Table A21 of Appendix A. The Photographs of the cracks on all the faces are shown in Figure B21 of Appendix B.

2.9.5.4 Test: BL_366-122-122_N_d (BL_12-4-4_N_d)

The load plate was placed at the distance **d** from the tip of the haunch, on the bell end. This specimen was without A_{S6}, compression distribution steel in the top slab. The first shear crack detected at 334 kN (75 kip) of load and the box failed at 525 kN (118 kip). The detailed events of this test are presented in Table A22 of Appendix A. The Photographs of the cracks on all the faces are shown in Figure B22 of Appendix B.

2.9.6 Boxes of 91 cm (3 ft) Span, 61 cm (2 ft) Rise and 145 cm (4.75 ft) Joint Length

The load plate was placed on the right side of the spigot end of the culvert and at the center of box. This is due to short span which caused the distance **d** to place the load plate beyond the culvert's mid-span. The major events recorded during the experiment are presented in Appendix A. Table 2.11 shows the main events during the experiment. Both the test specimens exhibited similar crack initiation and propagation patterns. Generally, the initial superficial flexural cracks initiated on the inside face of the top slab, directly under the load plate near the loading (spigot) end. At approximately 200 kN to 267 kN (45 kip to 60 kip), the flexural cracks initiated on the sidewalls of the culverts and inside face of top slab, for both test specimens. In both the tests, the failure was not observed until 658 kN (148 kip). (Ref. Figure B23 and B24 of Appendix B)

Both the load deflection plots for these tests are shown in Figure 2.29. Finally, Table 2.11 presents the summary of the test results, which include the 0.25 mm (0.01 in) wide cracks load, the ultimate load, and the failure mode for each test specimen. This table shows that the shear cracks for both the test specimens formed at 320 kN (72 kip) to 334 kN (75 kip) which are above the strength limit state of 166 kN ($16 \times 1.75 \times 1.33 = 37.24\ kip$) for the live load used in designing per AASHTO 2005.

Table 2.11 Crack Event Load in kN (kip) for 91 cm (3 ft) Span, 61 cm (2 ft) Rise and 145 cm (4.75 ft) Joint Length Boxes

Event No.	Event	Test/Load in kN (kip)	
		SP_91-61-145_Y_0 (SP_3-2-4.75_Y_0)	SP_91-61-145_Y_0.83d (SP_3-2-4.75_Y_0.83d)
1.	1st superficial flexure crack appeared at loading end, on the inside face of the top slab under the load.	178 (40)	289 (65)
2.	1st superficial flexure crack appeared at loading end, on the inside face of the bottom slab under the load.	289 (65)	267 (60)
3.	First flexural crack initiated on the outside face of the left wall.	334 (75)	334 (75)
4.	First flexural crack initiated on the outside face of the right wall.	245 (55)	311 (70)
5.	First serviceability flexure crack (0.01 in wide) detected.	445 (100)	-
6.	First shear crack initiated at the Loading end.	525 (118)	-
7.	First **Serviceability shear** crack detected.	623 (140)	645 (145)
8.	Ultimate Load*/ failure. * Box did not fail	663* (149)	658* (148)

Table 2.12 Summary of Test Results for 91 cm (3 ft) Span, 61 cm (2 ft) rise and 145 cm (4.75 ft) Joint Length Boxes

Test	First Shear crack 0.25 mm (0.01 in) wide		Max* / Failure Load kN (kip)	Failure Mode
	Load kN (kip)	End Location		
SP_91-61-145_Y_0 (SP_3-2-4.75_Y_0)	-	Spigot	663* (149)	-
SP_91-61-145_Y_0.83d (SP_3-2-4.75_Y_0.83d)	-	Spigot	658* (148)	-

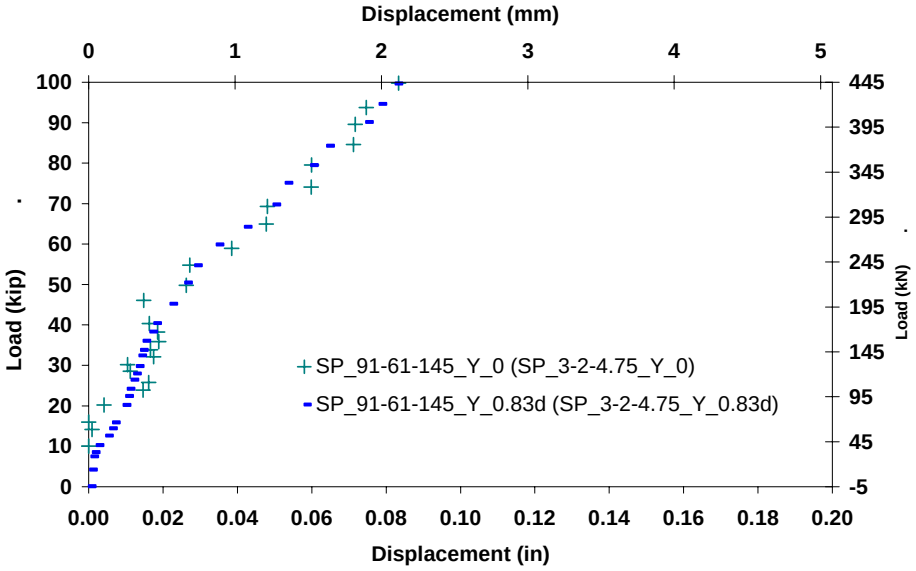

Figure 2.29 Load versus Deflection Plots for 91 cm (3 ft) Span, 61 cm (2 ft) Rise and 145 cm (4.75 ft) Joint Length Boxes

2.9.6.1 Test: SP_91-61-145_Y_0 (SP_3-2-4.75_Y_0)

The edge of the load plate was placed on the spigot at the tip of the haunch. The first shear crack detected at 311 kN (70 kip) of load, and the box failed at 623 kN (140

kip). The detailed events of this test are presented in Table A23 of Appendix A. The Photographs of the set up and the failure are shown in Figure B23 of Appendix B.

2.9.6.2 Test: SP_91-61-145_Y_0.83d (SP_3-2-4.75_Y_0.83d)

Due to the short span the load plate was placed on the spigot end at the mid span. In this test, no shear crack detected until 663 kN (149 kip) of applied load. The detailed events of this test are presented in Table A24 of Appendix A. The photographs of the set up and the failure are shown in Figure B24 of Appendix B.

2.10 Cored Samples

Three cored samples were taken from each tested box in order to perform compressive strength tests. The compressive strength test results are listed in Table D1 of Appendix D.

2.11 Cylinder Testing with Strain Gauge

Ten 15 cm x 30 cm (6 in x 12 in) concrete cylinders were strain gauged using 10 cm (4 in) long strain gauges in order to identify the modulus of elasticity of the concrete in the boxes being tested. First, the surface of cylinders as prepared and filled with adhesive and cured for 24 hours. After removing the extra adhesive using recommended procedure for EA-00-40CBY-120 strain gauge were glued using adhesive. The gauges were covered with cardboard and wrapped with tape along with concrete cylinder to protect the gauge. The concrete cylinders were then loaded in horizontal position to put

the gauge with adhesive under pressure for curing. After curing for 24 hours the gauges were connected to the data acquisition unit and the cylinders were tested for compression until failure (Figure 2.30). The load displacement plots are shown in Figure 2.31, which indicates that the concrete modulus of elasticity varies from 17.2 $kN.mm^2$ to 29.4 kN/mm^2 (2500 ksi to 4260 ksi). The standard value per ACI 318-05 is 27.6 kN/mm^2 (4000 ksi) for a compressive strength of 34.5 N/mm^2 (5000 psi) concrete.

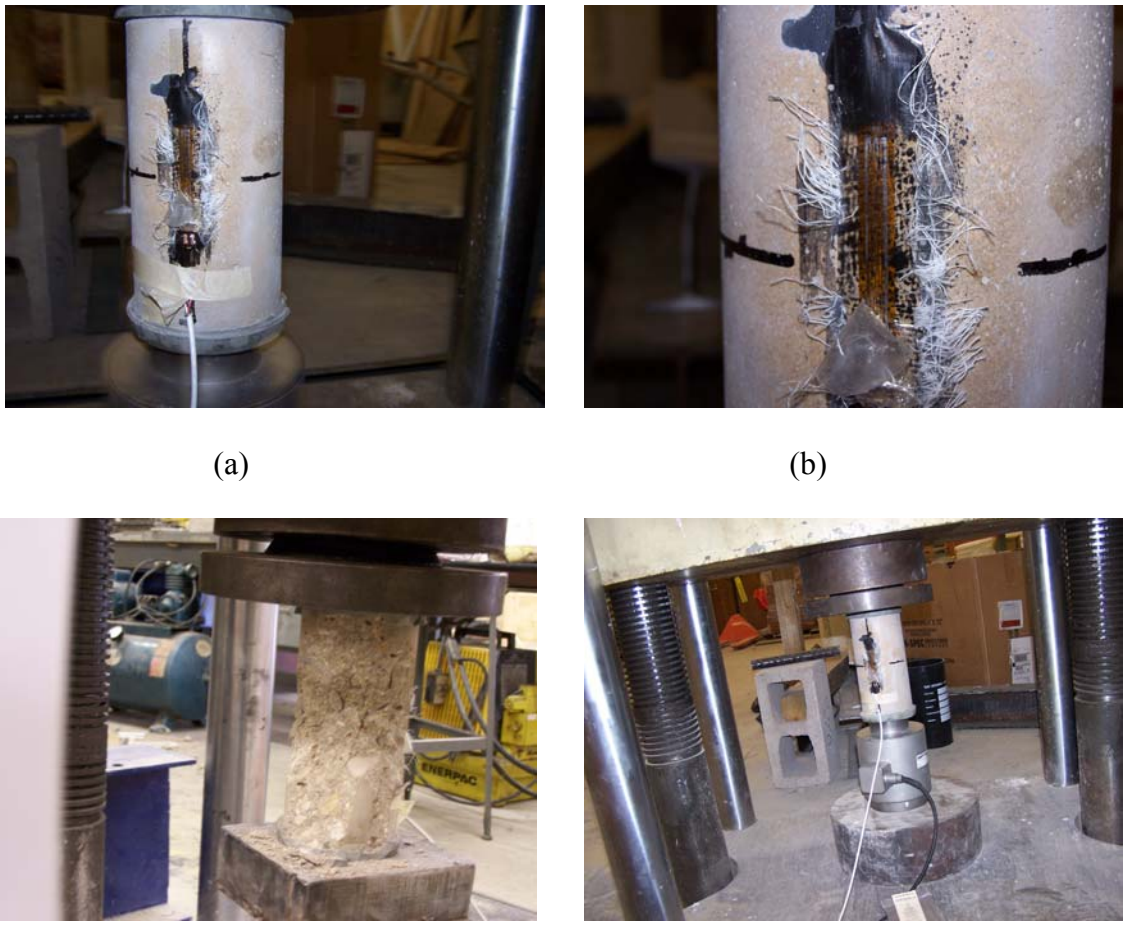

(a) (b)

(c) (d)

Figure 2.30 Concrete Cylinder Compression Test with Strain Gauge (a) Concrete Cylinder with Strain Gauge; (b) Strain Gauge in Close up; (c) Concrete Cylinder after Failure; and (d) Test Set up for concrete Cylinder Testing

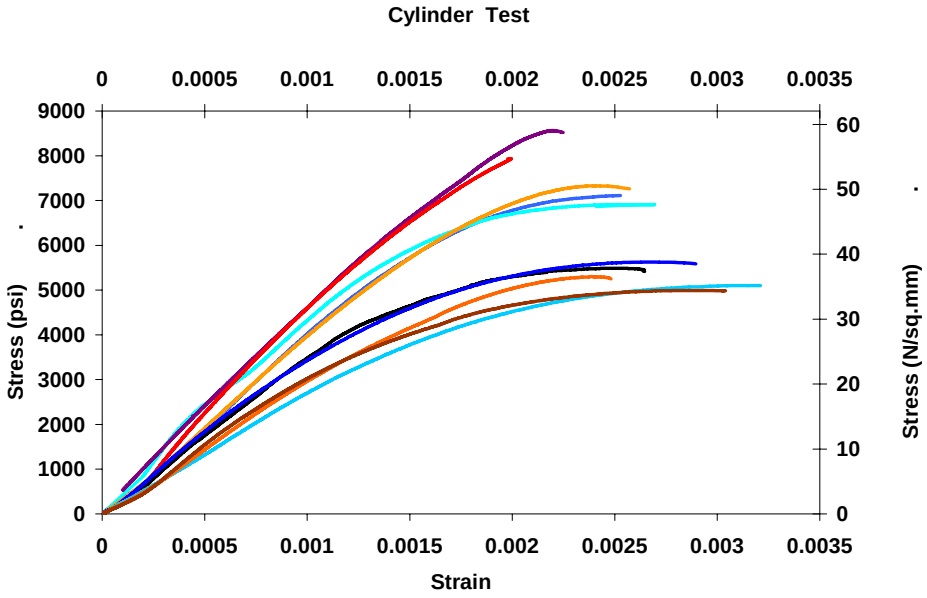

Figure 2.31 Stress Strain Plot for Concrete Cylinders using Strain Gauges

CHAPTER 3

FINITE ELEMENT ANALYSIS

3.1 Introduction

To study the behavior of all the possible standard box culverts three-dimensional finite element models were prepared for all the standard sizes of box culverts per ASTM C 1433-04. The models included 3-D solid and 3-D shell elements having geometric and material non-linearities. The reinforcement was modeled as rebar elements embedded in the surface element. The base support (strong reaction floor) was also modeled by modeling a rectangular block with a high value of stiffness. The contact between the box and the reaction floor was modeled using node-to-surface contact elements. The boxes were loaded on an area equal to the wheel load plate 30 cm x 51 cm (10 in x 20 in). The incremental wheel load was applied using Riks method up to 445 kN (100 kip), the load at which most of the test specimens failed during the experimental testing (refer to Chapter 2). The cracking strains were studied for all the load steps for all the 11 size of boxes tested using brick (C3D8R) elements in ABAQUS software. The amount of plastic strain needed to reduce the stresses to zero at crack, known as tension stiffening was used in controlling the stiffness of the model. The elements cracked at specified load levels were identified by using the cracking strain value.

3.2 Elements

3.2.1 Solid Element

Solid elements are volume elements, which are composed of a single homogeneous material, or can include several layers of different materials. Even though tetrahedral elements are relatively easy to model and cost effective when compared to , hexahedral elements, hexahedral elements are shown to yield accurate results for linear and non-linear analysis involving contact, plasticity, and large deformations. The First order (linear) interpolation element such as hexahedral (brick) exhibit stiff behavior with slow convergence rate but prevents "mesh locking" when the material response is approximately incompressible, whereas second order elements provides higher accuracy than first order for problems not involving compact contact conditions. Thus, first order elements were used in this study to accommodate the non-linear contact problem present.

3.2.2 Thick Shell Element

The 8-noded quadrilateral in-plane general purpose continuum shell, reduced integration, (SC8R), finite membrane strains, elements were used. This element is capable of presenting results for the distribution of shear force and bending moments at various load levels in the models. These elements are capable of accommodating rebar layers at the specified locations in the given part known as rebar elements. The stiffness of the rebar is transferred to the nearest nodes of the shell element. The bond slippage model is not considered, and perfect bond between the concrete and rebar is presumed.

Thus, even after concrete cracking stiffness is available at the nodes due to availability of steel at those nodes having reinforcement in their vicinity till the failure rebar stress is reached. Shell element needs to be defined by using stacking and orientation direction. While meshing each and every partition of the model needs to be defined in the direction outside the box using sweep mesh technique to have correct model behavior. Since the haunch dimension is such that the width of the haunch varies (i.e., triangular shape), The 'haunch' was modeled by using hexahedral brick elements.

3.2.3 Brick Element

Thick shell elements show only inside and outside extreme surfaces of the top / bottom slab, and walls in visualization mode for depicting stresses and strains. Thus, viewing of stresses and strains in the thickness of the wall and slab was not possible. Therefore, a separate model with reduced integration 8-noded linear brick elements (C3D8R) were used for predicting the cracking strain at various load levels in the model. These elements have a limitation of predicting shear force and bending moment due to having only translational degree of freedom, whereas shell elements have rotational degree of freedom.

3.2.4 Surface Element

Three-dimensional 4-node surface element (SFM3D4) was used on which the rebars are placed. The stiffness and mass of the rebar layers are added to the surface elements. These reinforced surface elements were embedded in the brick (C3D8R) and

thick shell (SC8R) “host” elements. Surface parts are generated as inner rebar cage and outer rebar cage for the box at the location of rebar in the actual box. These parts are meshed using surface elements after embedding in concrete. Surface element have inbuilt option of modeling of the box culvert’s welded wire fabrics with area, spacing and direction of each rebar.

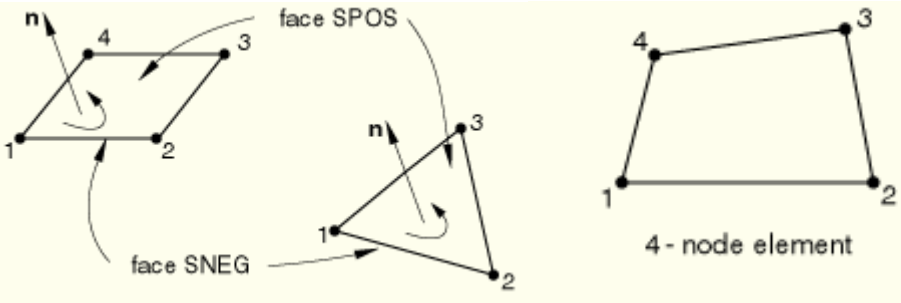

Figure 3.1 Surface Element (Ref: ABAQUS (2006) Version 6.6)

3.2.5 Embedded Element

This is a technique used to have embedded node(s) at desired locations with the constraints on translational degrees-of-freedom on the embedded element by the host element. Both the rebar cages are modeled as embedded region in concrete using constraints in interaction module, and making the concrete the host. Thus, rebar element can only have translations/ rotations equal to those of the host elements surrounding them.

3.3 Contact Modeling

The box was placed on strong reaction floor. During the application of the load on the top slab, the outside face of the bottom slab moves in horizontal as well as vertical direction at places. Friction behavior in the horizontal and the variation of reactions in the vertical directions require contact modeling. To model this behavior, non linear-contact algorithm was used in the modeling the contact between the box and strong reaction floor. These two surfaces form as contact pairs. The strong reaction floor was made as master surface and outside face of the bottom slab of box was assigned to be the slave surface. The node-to-surface contact with small sliding algorithm was used during analysis.

The typical parts used in the FEM of this study are presented in Figure 3.2, which consist of inner cage, outer cage, concrete, and reaction floor.

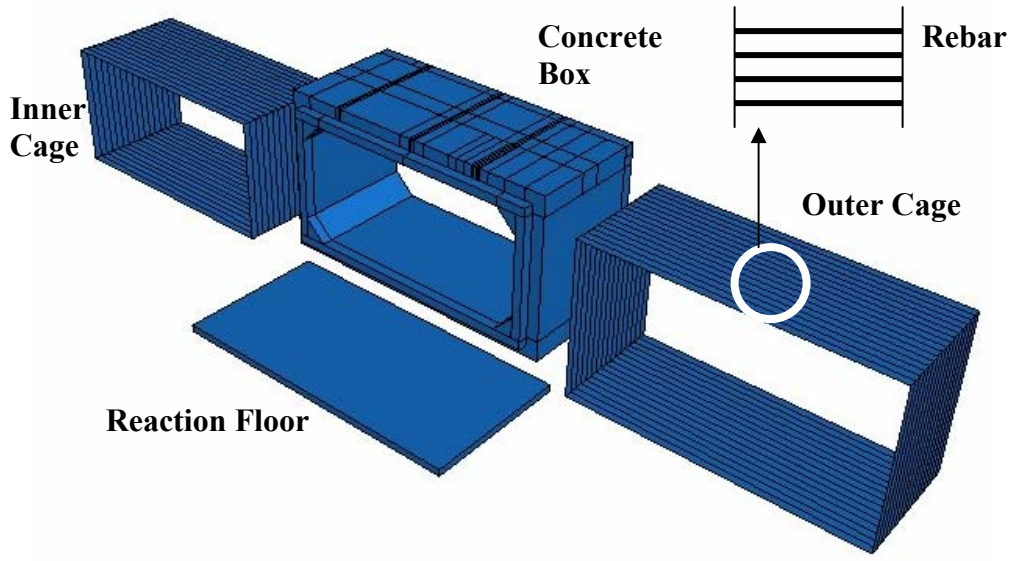

Figure 3.2 Parts Showing Inner Cage, Outer Cage of Rebar with Concrete Box and Strong Reaction Floor

3.4 Material

Material properties of concrete and steel were defined using standard properties. Density, Modulus of elasticity, Poisson's ratio, elastic strain, and plastic strain of concrete and steel were incorporated. For concrete a density of 2400 kg/m^3 (150 pcf), Modulus of Elasticity of 27579 MPa (4000 ksi), Poisson's ratio 0.17, total strain 0.003 were used. For steel a density 7850 kg/m^3 (490.0 pcf), Modulus of Elasticity 200,000 MPa (29000 ksi), Poisson's ratio 0.3 were used.

Reaction Floor

3.5 Smeared Crack Model

This model is chosen to represent the discontinuous micro crack brittle behavior of concrete. This model does not track individual macro cracks, rather constitutive calculations are performed independently at each integration point of the finite element model, and the presence of crack enters into these calculations by the way that the cracks affects the stresses and material stiffness associated with the model. This modeling approach inherently introduces mesh sensitivity in the solutions, resulting in non-convergence to a unique result. Presence of rebar helps the model to converge as the element does not loose entire stiffness of the element, on cracking due to presence of rebar.

The responses of concrete in compression and cracking, incorporated in the model are illustrated by the uniaxial response of a specimen shown in Figure 3.3.

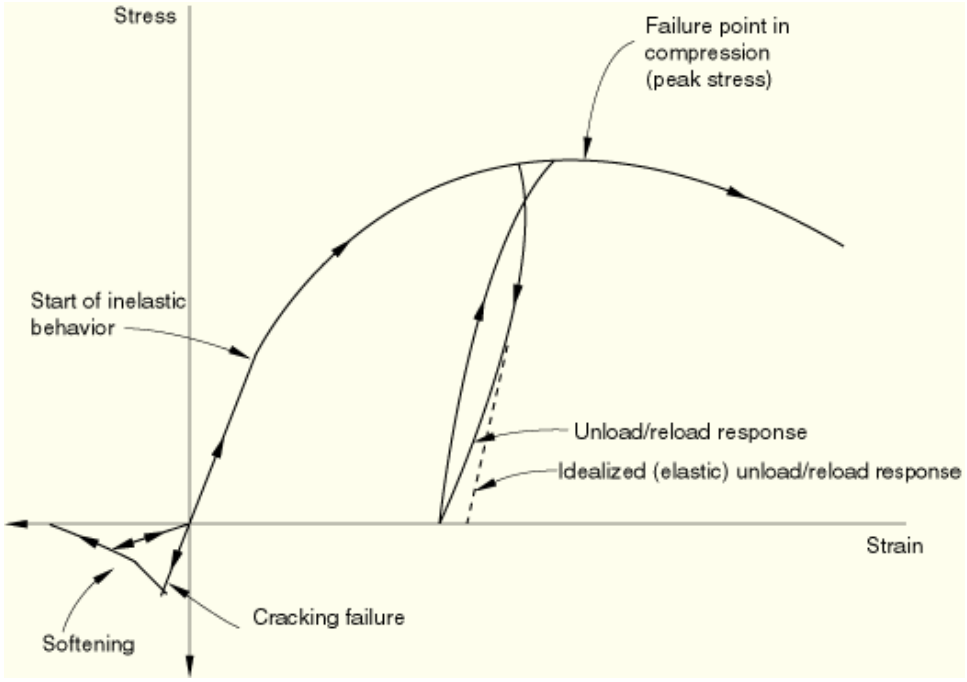

Figure 3.3 Uniaxial Behavior of Plain Concrete
(Ref: ABAQUS (2006) Version 6.6)

The concrete, on loading in compression, exhibits elastic response initially. As the stress is increased, some non-recoverable (inelastic) straining occurs, and the response of the material softens. An ultimate stress is reached, after which the material softens until it can no longer carry any stress. If the load is removed at some point after inelastic straining has occurred, the unloading response is softer than the initial elastic response: this effect is ignored in the model. When a uniaxial specimen is loaded into tension, it responds elastically until, the tensile strength of concrete, (typically 7–10% of the ultimate compressive strength), and than cracks abruptly, causing very difficult to observe/ record the actual behavior of concrete while tensile failure in comparison to compression failure.

3.6 Tension Stiffening

It is assumed that the material loses strength through a softening mechanism and that this is dominantly a damage effect. Alternatively opening of cracks can be represented by the loss of elastic stiffness. The model neglects any permanent strain associated with cracking; that is, we assume that the cracks can close completely when the stress across them becomes compressive.

Tension stiffening (refer ABAQUS (2006) version 6.6) is required in the concrete smeared cracking model. It is specified by means of a post-failure stress-strain relation.

Tension stiffening is defined as plastic strain at which the cracking stresses causing tensile failure of the concrete reduces to zero. The stresses remain as tensile cracking stresses, until it is defined as, at which plastic strain the cracking stress reduces to zero. This reduction of tensile cracking stresses with plastic strain, can be linear or multi-linear. Faster the drop in stresses, faster will be the degradation in the stiffness of the model (Figure 3.4).

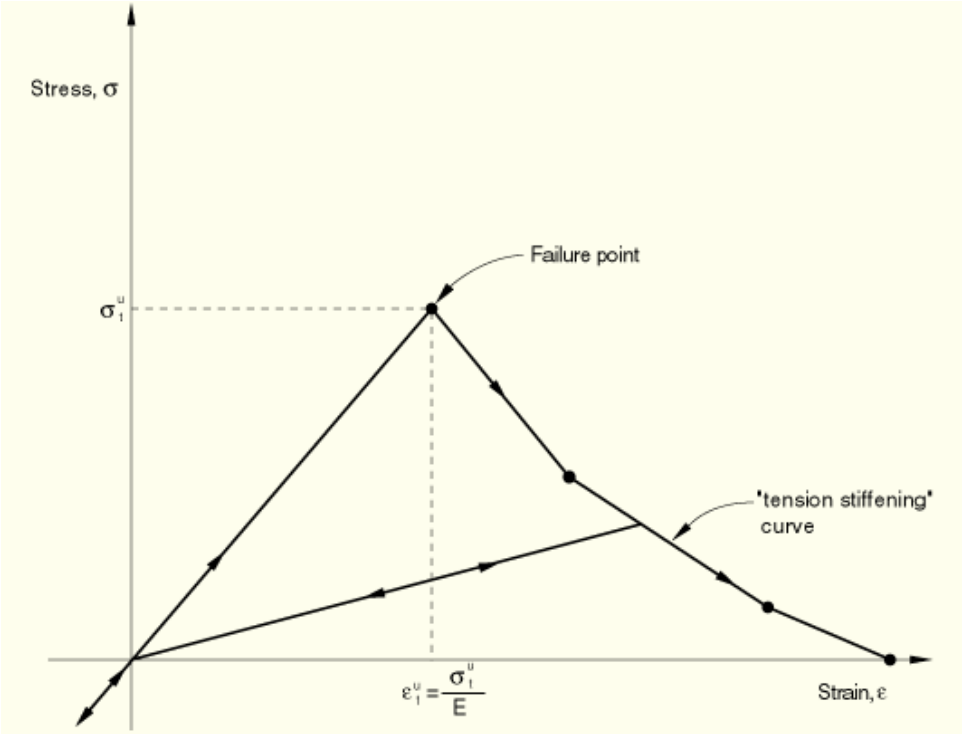

Figure 3.4 "Tension Stiffening" Model (Re: ABAQUS (2006) Version 6.6)

In ABAQUS (2006), the failure stress, σ_t^u, occurs at a failure strain (defined by the failure stress divided by the Young's modulus); however, the stress goes to zero at an ultimate strain (ε^{max}). The gap between failure strain and ultimate strain controls the stiffness of the model. This was played with for calibration of the models, which was found by varying tension stiffening from 0.001 to 0.005 for the thick shell element models having experimental results. For brick models tension stiffening was 0.05 to 0.07 for the models having experimental results. This vanishing of stresses at crack / failure is done in linear or bilinear arrangements.

3.7 Shear Retention

With the initiation of cracks in concrete, it loses shear stiffness. This effect is defined by specifying the reduction in the shear modulus as a function of the opening strain across the crack. The finite element model does not reduce the shear modulus, and it gives higher strength. One can also specify a reduced shear modulus for closed cracks. This reduced shear modulus will also have an effect when the normal stress across a crack becomes compressive. The new shear stiffness will have been degraded by the presence of the crack.

The modulus for shearing of cracks is defined as ρG, where G is the elastic shear modulus of the un-cracked concrete and ρ is a multiplying factor. The shear retention model assumes that the shear stiffness of open cracks reduces linearly to zero as the crack opening increases:

$$\rho = (1- \varepsilon / \varepsilon^{max}) \quad \text{for} \quad \varepsilon < \varepsilon^{max}, \quad \rho = 0 \quad \text{for} \quad \varepsilon \geq \varepsilon^{max} \tag{3.1}$$

where ε is the direct strain across the crack and ε^{max} is a user-specified value.

3.8 Failure Ration

To define the concrete smeared crack model the following rations was defined

1. Ratio of the ultimate biaxial compressive stress to the uniaxial compressive ultimate stress. A value of 1.16 was used.

2. Absolute value of the ratio of uniaxial tensile stress at failure to the uniaxial compressive stress at failure. A value of 0.085 was used initially, but calibrated later.
3. Ratio of the magnitude of a principal component of plastic strain at ultimate stress in biaxial compression to the plastic strain at ultimate stress in uniaxial compression. A value of 1.28 was used.
4. Ratio of the tensile principal stress value at cracking in plane stress, when the other nonzero principal stress component is at the ultimate compressive stress value, to the tensile cracking stress under uniaxial tension. A value of 0.333 was used.

3.9 Modified Riks Algorithm

During cracking of concrete, a local region softens while the adjoining material unloads elastically. These local effects may be accompanied by sudden change in load keeping displacement constant or sudden change in displacement keeping load constant (Figure 3.5). To obtain nonlinear static equilibrium solutions for unstable problems, where the load-displacement response can exhibit this type of behavior, the modified Riks method (refer ABAQUS (2006) version 6.6) is used which is an algorithm that allows effective solution of such cases.

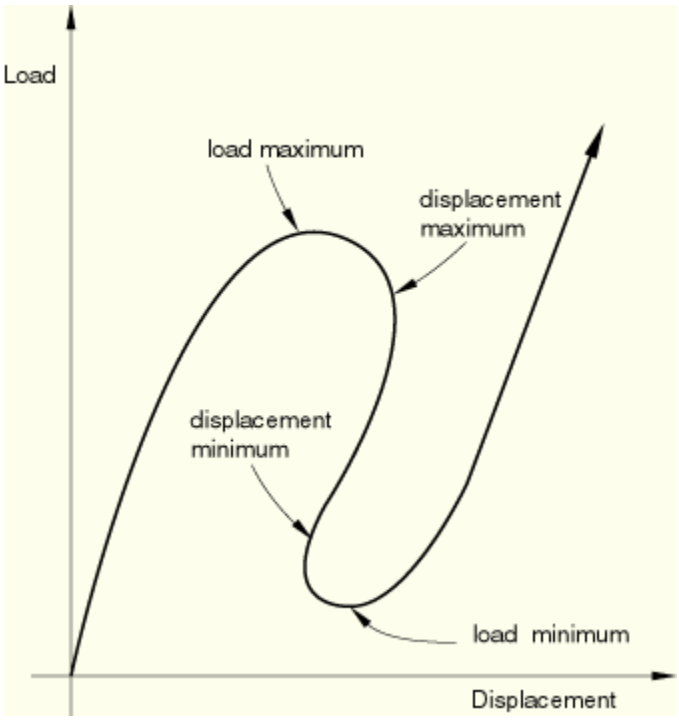

Figure 3.5 Typical Unstable Static Response (Re: ABAQUS (2006) Version 6.6)

In this method using Newton method, automatic load increment is given, if the solution does not converge then the increment is reduced by a certain predetermined ratio. Again, the solution is checked and if convergence is not achieved, the process is repeated for a number of predefined iterations or until the solution convergences, whichever is earlier (Figure 3.6).

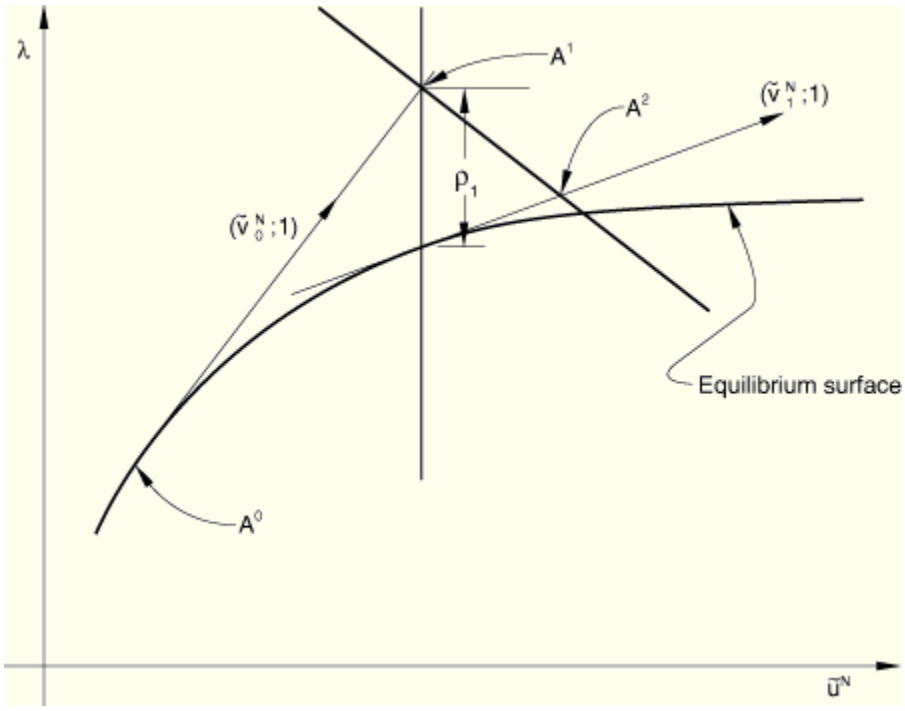

Figure 3.6 Modified Riks Algorithm (Ref: ABAQUS (2006) Version 6.6)

3.10 Model Convergence

Various mesh sizes are shown in Figures 3.7 and 3.8 for a SP_244-244-122_N_d (SP_8-4-4_N_d) model. These figures show number of elements and nodes in a given model. Element size is decreasing from first to the last photograph. The number of elements in the coarsest and finest models were 1055 and 16166, respectively. Energy convergence was sought due to the non-linear nature of the problem and the fact that monotonic convergence of non-linear problems based on mesh density refinement alone is not guaranteed (Razavi (2004)). The error in energy (external work done – strain energy density) is plotted against the number of elements in the typical boxes SP_244-122-122_N_d (SP_8-4-4_N_d) and SP_366_122-122_N_d (SP_12-4-4_N_d)

(Figure 3.9 and 3.10). The coarsest model, in which the error in energy is insignificant in the subsequent mesh with increased element number, is selected for the further analysis. Thus, Mesh with 1427 elements of Figure 3.7 (b) was selected.

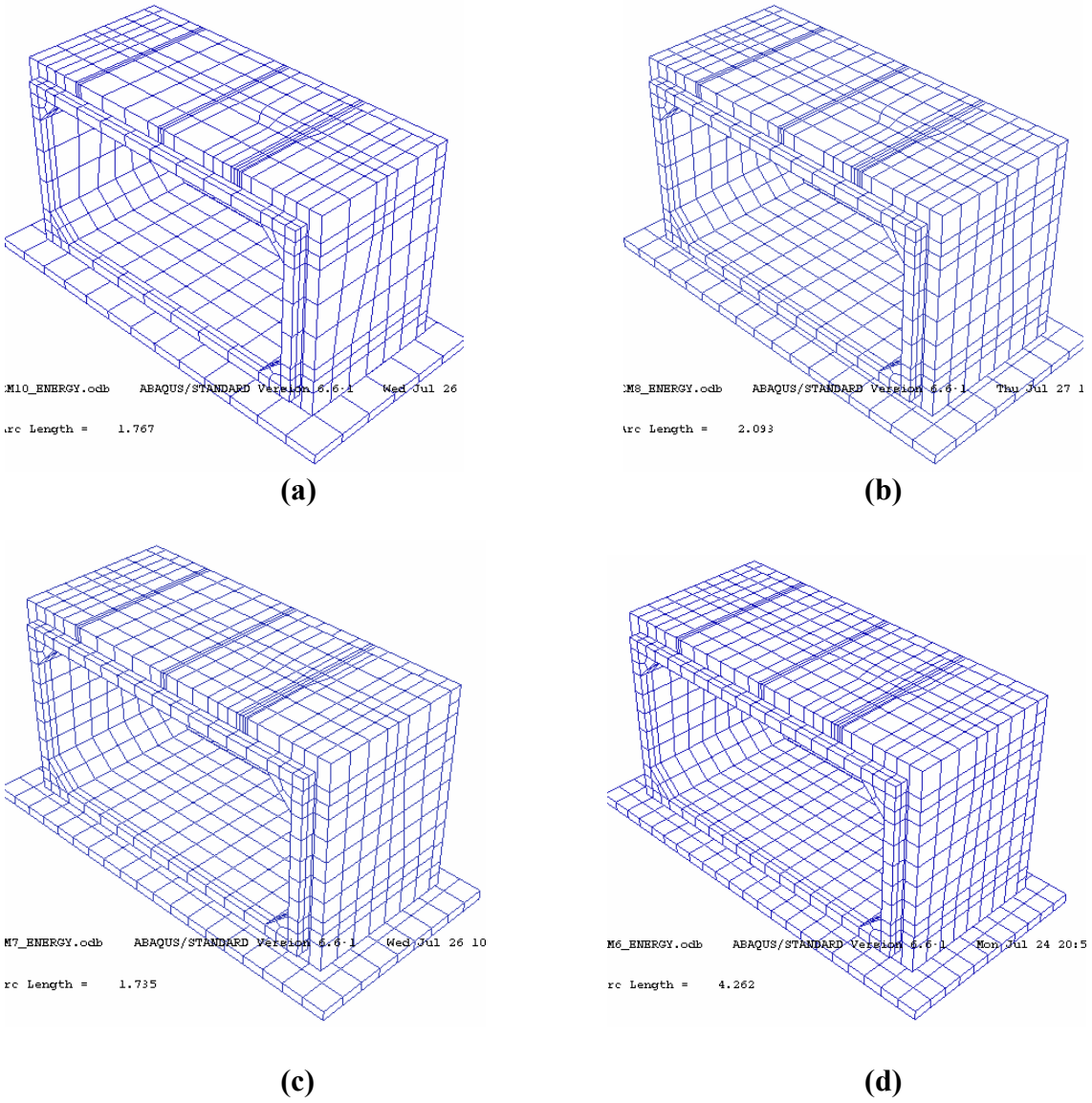

Figure 3.7 Various Coarser Meshes for SP_244-122-122_N_d (SP_8-4-4_N_d) Box; (a) Mesh 1: 1055 Elements & 1990 Nodes; (b) Mesh 2: 1427 Elements & 2596 Nodes; (c) Mesh 3: 1684 Elements & 2982 Nodes; and (d) Mesh 4: 2077 Elements & 3590 Nodes

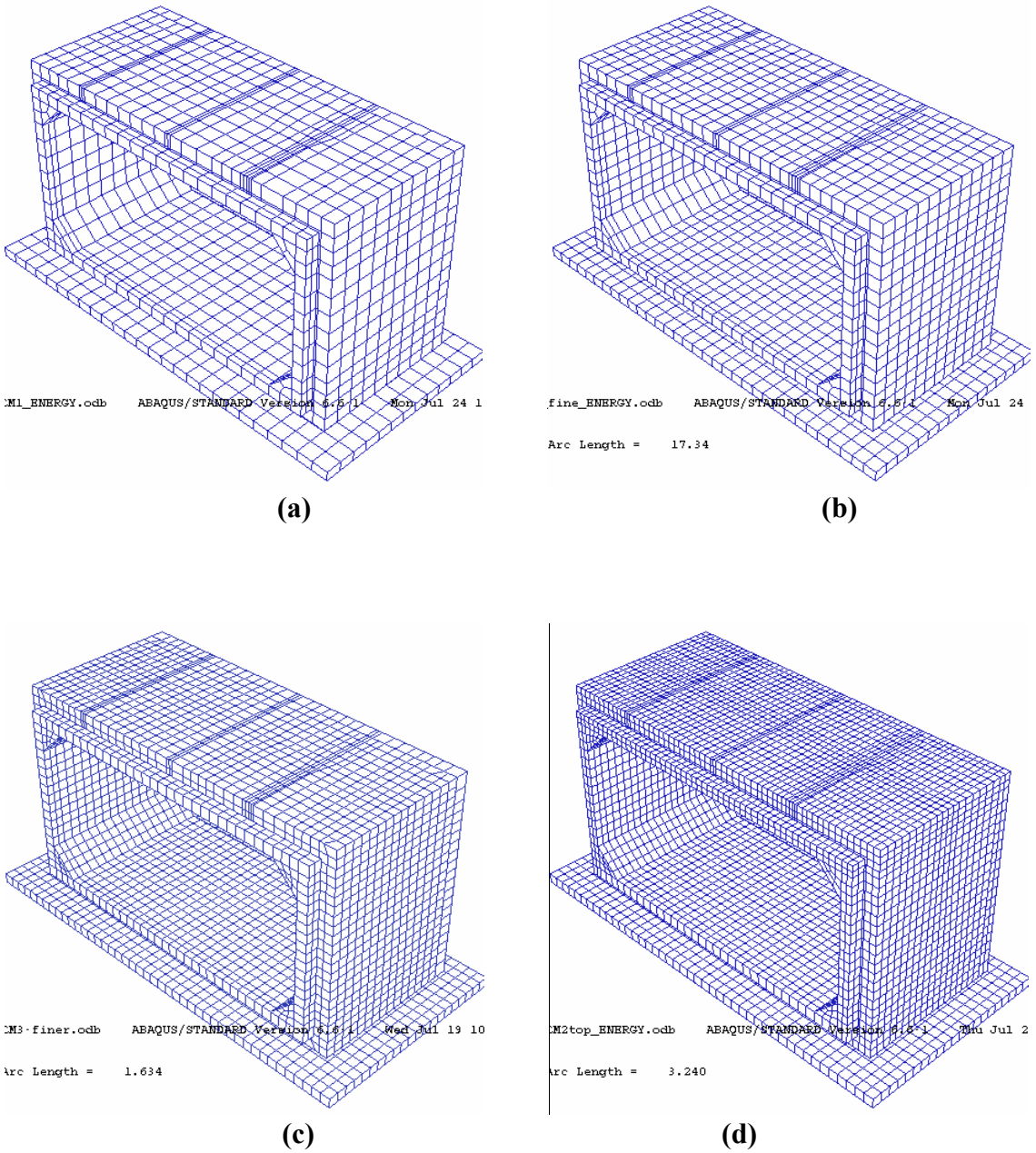

Figure 3.8 Various Finer Meshes for SP_244-122-122_N_d (SP_8-4-4_N_d) Box (a) Mesh 5: 3193 Elements & 5104 Nodes; (b) Mesh 6: 4783 Elements & 7326 Nodes; (c) Mesh 7: 10216 Elements & 14426 Nodes; and (d) Mesh 8: 16166 Elements & 21713 Nodes

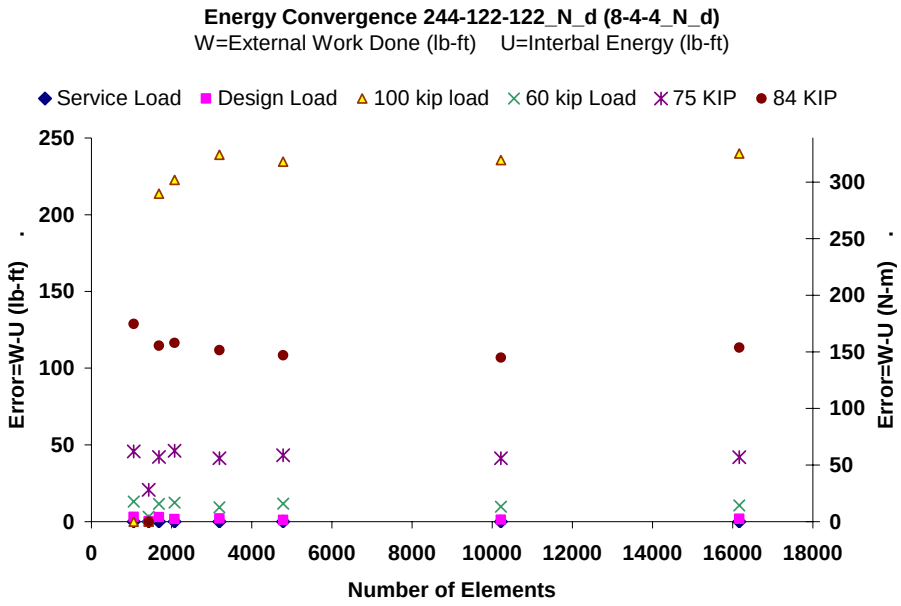

Figure 3.9 Energy Convergence Study for SP_244-122-122_N_d (SP_8-4-4_N_d)

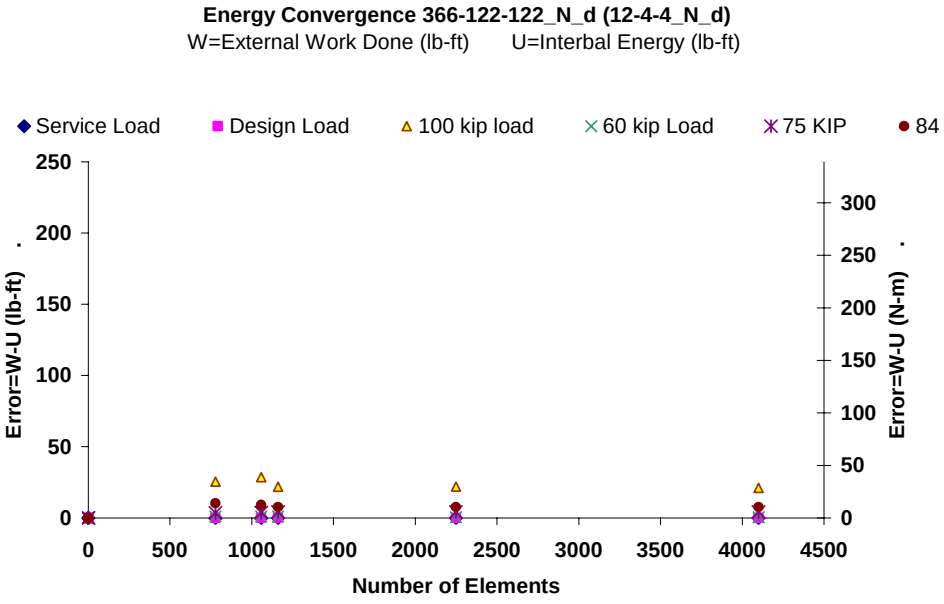

Figure 3.10 Energy Convergence Study for SP_366_122-122_N_d (SP_12-4-4_N_d)

3.11 Typical Finite Element Results

The output database files in ABAQUS were read by visualization module to create contour plots, animations, XY plots, and tabular output of the results. Crack is not supported by visualization mode so it is read in data file, which identifies the cracked elements and the level of stress at that point. Alternatively, strain contour is plotted in the visualization mode with the limits of cracking: compressive and tensile strains.

3.12 Deflected Shape

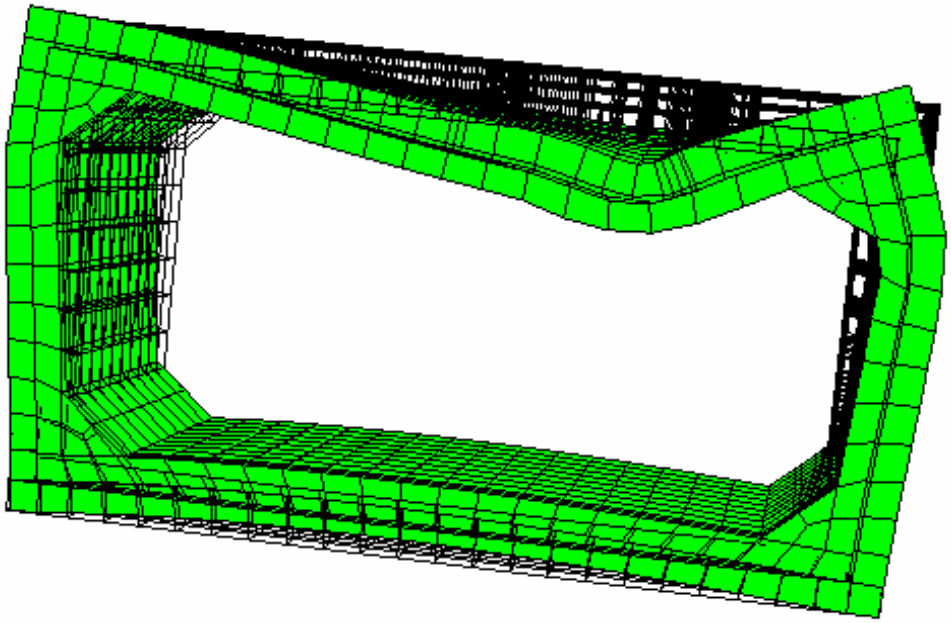

Figure 3.11 Typical Deflection Shape of the Box (Solid – Deformed, and Wireframe – Undeformed)

Upon the application of the load, through the load plate, on the outside face of the top slab at the distance, **d** from the tip of haunch, the box undergoes deflection. The top and bottom slabs deflect inside of the box and side walls deflect outside of the box.

Figure 3.11 shows the deformed shape (solid) compared to the un-deformed shape (wire frame) of SP_244-122-122_N_d (SP_8-4-4_N_d) box, at the load of 356 kN (80 kip). The deformation is magnified 50 times.

3.13 Crack Strain Contours

The contours of the cracking strain on the SP_244-122-122_N_d (SP_8-4-4_N_d) box surface are shown in the Figure 3.12 at a load of 356 kN (80 kip). Once again, the deformation is magnified 50 times. The limit to strains in compression as well as in tension is provided, so that the part of the box having strains beyond these limits are identified as cracked in compression and tension. This figure shows that cracking at locations of the maximum sagging and hogging moments on the top slab, bottom slab, and both walls, which cause tensile cracks. The cracked and intact portions are shown in grey and red colors, respectively.

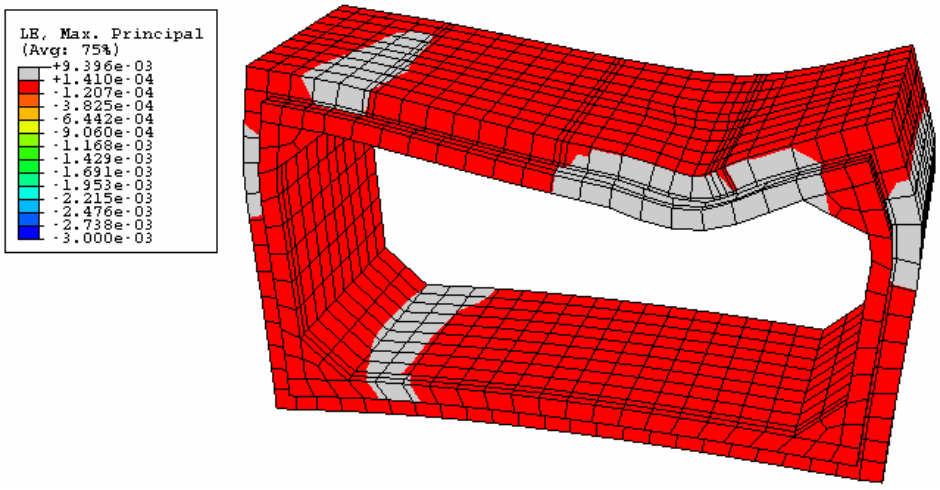

Figure 3.12 Typical Contours for Cracking Strain (Cracked Region: Grey Color)

3.14 Bending Moment Contours

The contours of moment for a typical box surface are shown in Figure 3.13 at a load of 178 kN (40 kip) with the magnification factor of 50. The maximum moments shown are 572 N-m (5060 lb-in) and -1105 N-m (-9779 lb-in). This figure shows that the maximum sagging moment under the load plate and maximum hogging moment near to left haunch are located on the loading end. With these contours, the values and location of moments at every load steps were known and studied to understand the behavior of box at every load step.

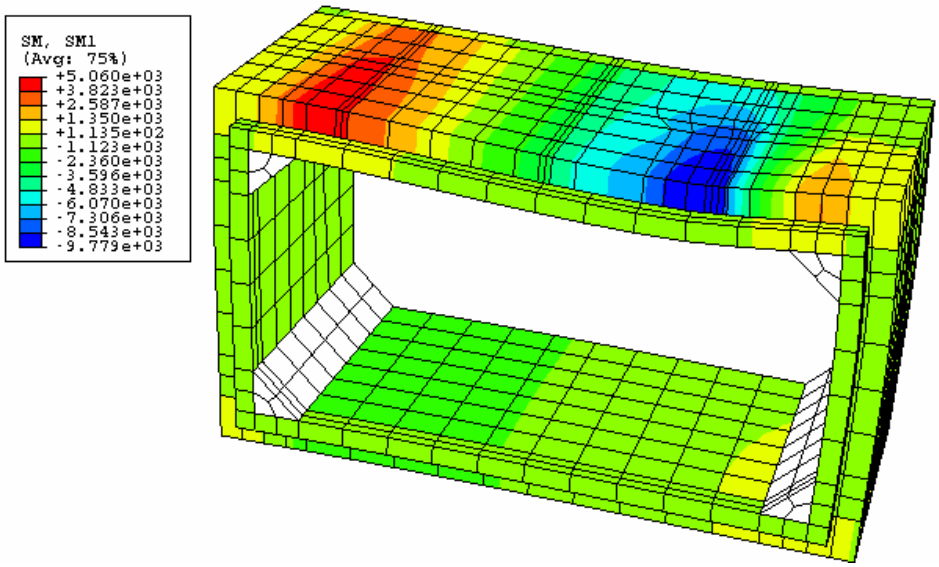

Figure 3.13 Typical Contours for Moment

3.15 Shear Force Contours

The contours of shear force for a typical box surface are shown in Figure 3.14 at a load of 178 kN (40 kip) with the magnification factor of 50. The maximum absolute

value of shear force is 7575 N (1703 lb). It shows that maximum shear force is detected between the load plate and the tip of the haunch at the loading end.

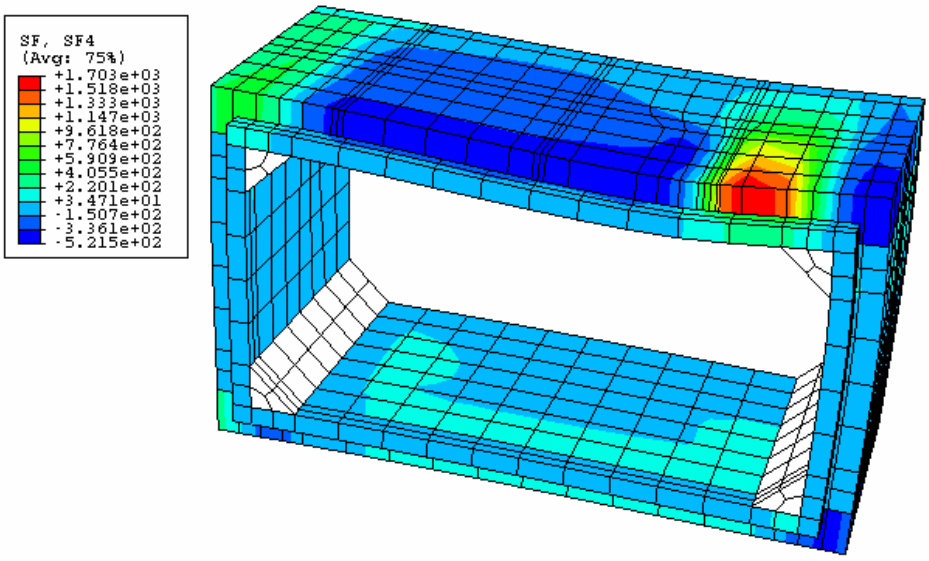

Figure 3.14 Typical Contours for Shear Force

Using the developed FEM model, an investigation was conducted to identify the location of the maximum shear force in the culverts when the wheel load is placed at the distance "**d**" from the tip of the haunch (refer to Chapter 2). Table 3.1 presents the location of the maximum shear force obtained from the FEM analyses measured from the tip of the haunch for different span sizes of the ASTM C1433 boxes. From the values presented in the table, it is concluded that the maximum shear force falls between the tip of the haunch and the load plate. It is interesting to note that in 70% of the cases the maximum shear force falls at ½ the distance between the tip of the haunch

and the edge of the load plate. In only one of the cases (122C cm (4 ft) span), the maximum shear force is under the load plate.

Table 3.1 Location of Peak Shear along Span, When Load at 'd' from the Tip of the Haunch

S cm (ft)	**e/d**
91 (3)	1.05
122 (4)	1.20
152 (5)	0.50
182 (6)	0.50
213 (7)	0.50
244 (8)	0.50
274 (9)	0.38
305 (10)	0.50
335 (11)	0.50
366 (12)	0.50

Load Location: '**d**' from tip of haunch

d: Effective depth of top slab

e: Distance of peak shear from tip of haunch

3.16 Model Calibration

The experimentally obtained load-deflection plots are compared with the FEM analysis for model calibration. The parameters calibrated were: modulus of elasticity of concrete, E, the absolute value of the ratio of uniaxial tensile stress at failure to the uniaxial compressive stress at failure, f_t / f'_c, and the tension stiffening parameter, TS.

Table 3.2 Model Calibration Parameters

Test	Modulus of Elasticity kN/mm^2 (ksi)	Absolute Value of the ratio of uniaxial tensile stress at failure to the uniaxial compressive stress at failure (f_t / f'_c)	Tension Stiffening (TS)
SP_122-122-244_Y_d (SP_4-4-8_Y_d)	20.7 (3000)	0.0340	0.0015
BL_122-122-244_Y_d (BL_4-4-8_Y_d)		0.0425	0.0010
SP_244-122-122_Y/N_d (SP_8-4-4_Y/N_d)		0.0850	0.0015
BL_244-122-122_Y/N_d (BL_8-4-4_Y/N_d)		0.0640	0.0015
SP_244-122-244_Y_d (SP_8-4-8_Y_d)		0.0510	0.0020
BL_244-122-244_Y/N_d (BL_8-4-8_Y/N_d)		0.0340	0.0020
SP_366-122-122_Y/N_d (SP_12-4-4_Y/N_d)		0.0340	0.0025
BL_366-122-122_Y/N_d (BL_12-4-4_Y/N_d)		0.0170	0.0050
SP_91-61-145_Y_0 (SP_3-2-4.75_Y_0)		0.0425	0.0015
SP_91-61-145_Y_0.85d (SP_3-2-4.75_0.85_Y_0.85d)		0.0340	0.0015

Table 3.2 shows the values of the aforementioned parameters used for the calibration of the models. The calibrated parameters is compared with the standard parameters of modulus of elasticity (E) = 27.6 kN/mm^2 (4000 ksi), and absolute value of the ratio of uniaxial tensile stress at failure to the uniaxial compressive stress at failure = 0.085. The necessity for model calibration was due to the fact that displacement-based finite element was used which in the case of crack modeling yields

to stress locking ((Rots and Blaauwendraad (1989). This would yield to stiffer finite element solution. Thus, calibrating the above coefficient is necessary to soften the solution in order to represent the true behavior.

3.17 Comparison of Experimental and FEM Results

The comparison of the calibrated FEM and the experimental results for crack initiation and propagation of cracks showed close correlation. The crack predictions by the FEM analyses were similar to those observed in the experiments for the particular load level and crack location. The crack prediction obtained from the FEM analyses for all the boxes tested is presented in Appendix C.

The FEM analysis generally predicts cracks initially on the inside face of the top slab at the loading end and with the increase in load the cracks are detected on the outside face of the side walls. With further increase of load, cracks are predicted on the outside face of the top slab. Similar behavior was observed in 24 full-scale tests. For the test designated SP_244-122-122_N_d (SP_8-4-4_N_d) tested on spigot end, per FEM Figure C14, Appendix C, FEM predicts crack on the inside face of the top slab at a load of 169 kN (38 kip), which is confirmed in test as tabulated in Table A9 of Appendix A as 187 kN (42 kip) and also presented in experimental Figure B9 of Appendix B.

Next, the FEM predicted the crack at the out side face of the top slab on the top of haunch and outside face of the right wall near to load plate at 222 kN (50 kip), which was documented experimentally in Table A9 of Appendix A at 222 kN (50 kip) for side wall and 231 kN (52 kip) for the top slab as shown in Figure B9 of Appendix B.

The FEM continued predicting crack at the outside face of the left wall at 276 kN (62 kip) (Figure C15) which was similar to the experimentally observed crack at 289 kN (65 kip) as shown in Figure B9 of Appendix B. Also, FEM predicted crack at the joint between the bottom slab and the left haunch at 383 kN (86 (kip) (Figure C17). The same phenomenon was observed during the experiment at 289 kN (65 kip) (Figure B9 of Appendix B). Thus, it was found that the crack prediction was similar in location and load levels.

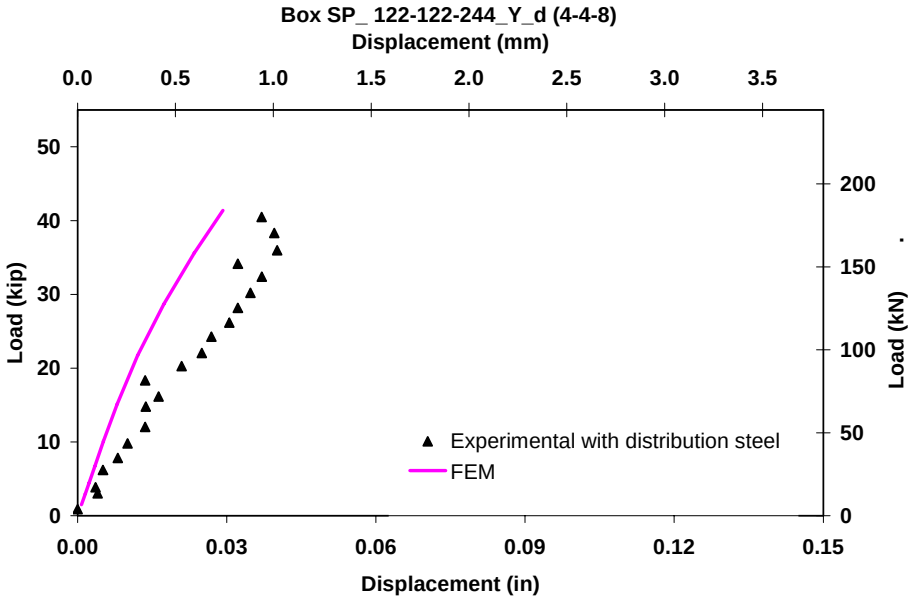

Figure 3.15 Comparison of FEM with Experimental Data for SP_122-122-244_Y_d (SP_4-4-8_Y_d)

Comparisons of FEM versus experimental data are shown through the load deflection plots of Figures 3.15 though 3.24. For SP_122-122-122_Y_d (SP_4-4-4_Y_d) due to moving optoelectronic displacement sensor the displacement recorded under the load plate were not reliable and were not used for calibration. In these figures,

the experimental load deflection plots are presented for the AASHTO factored load. These figures show close relationship between the FEM and experimental results.

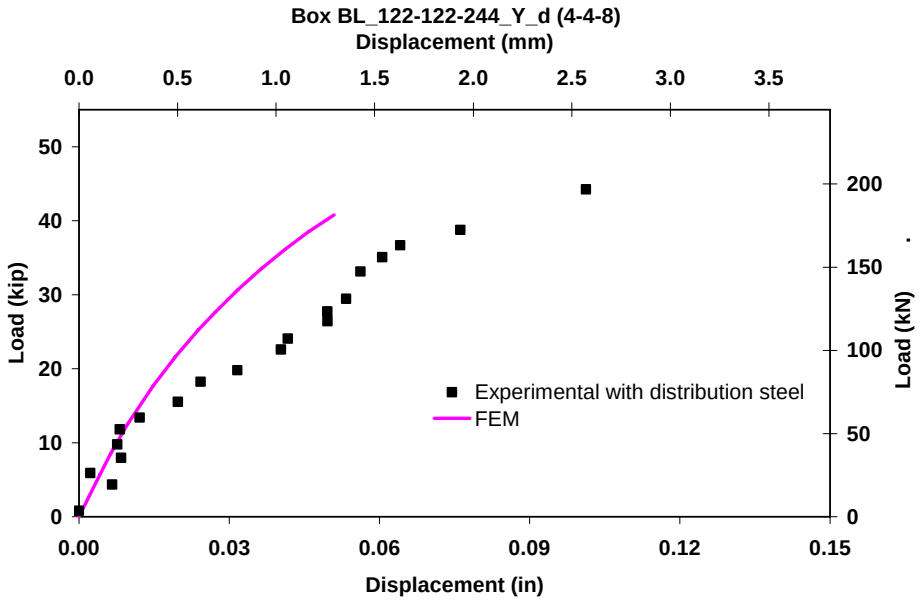

Figure 3.16 Comparison of FEM with Experimental Data for BL_122-122-244_Y_d (BL_4-4-8_Y_d)

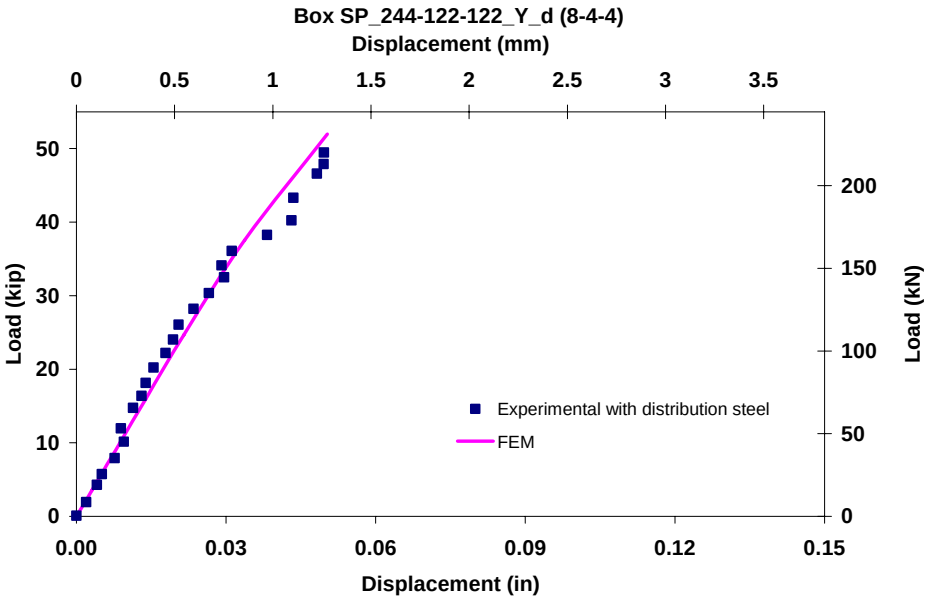

Figure 3.17 Comparison of FEM with Experimental Data for SP_244-122-122_Y_d (SP_8-4-4_Y_d)

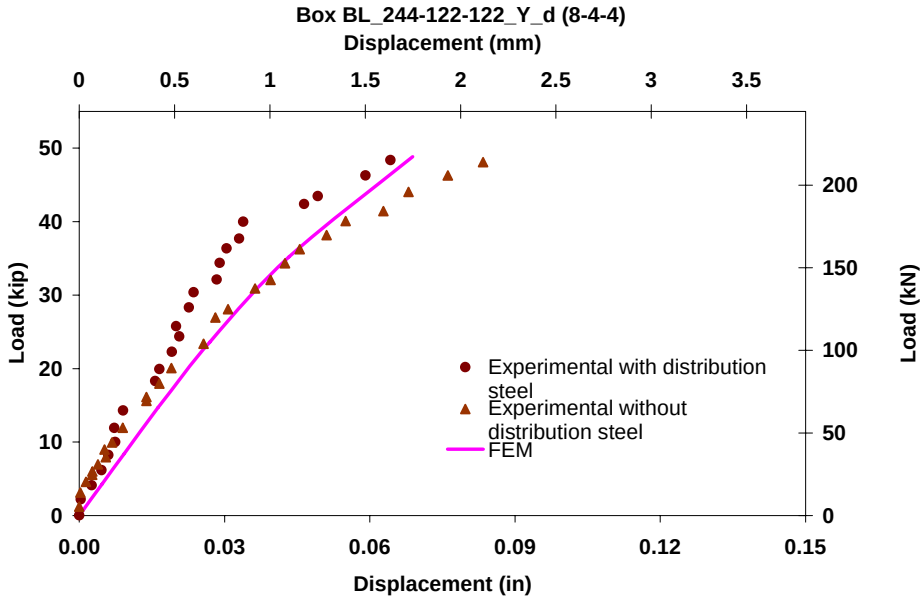

Figure 3.18 Comparison of FEM with Experimental Data for BL_244-122-122_Y/N_d (BL_8-4-4_Y/N_d)

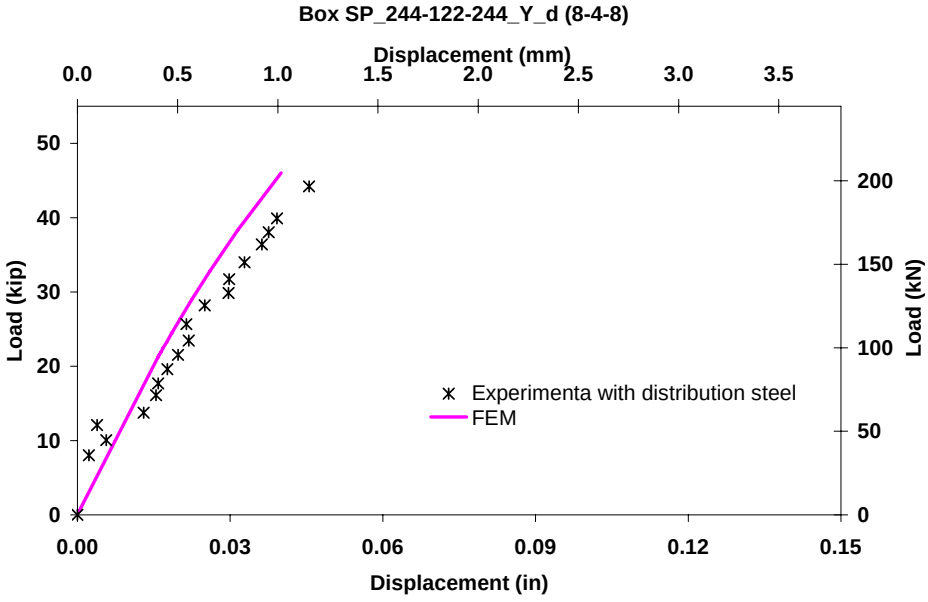

Figure 3.19 Comparison of FEM with Experimental Data for SP_244-122-244_Y_d (SP_8-4-8_Y_d)

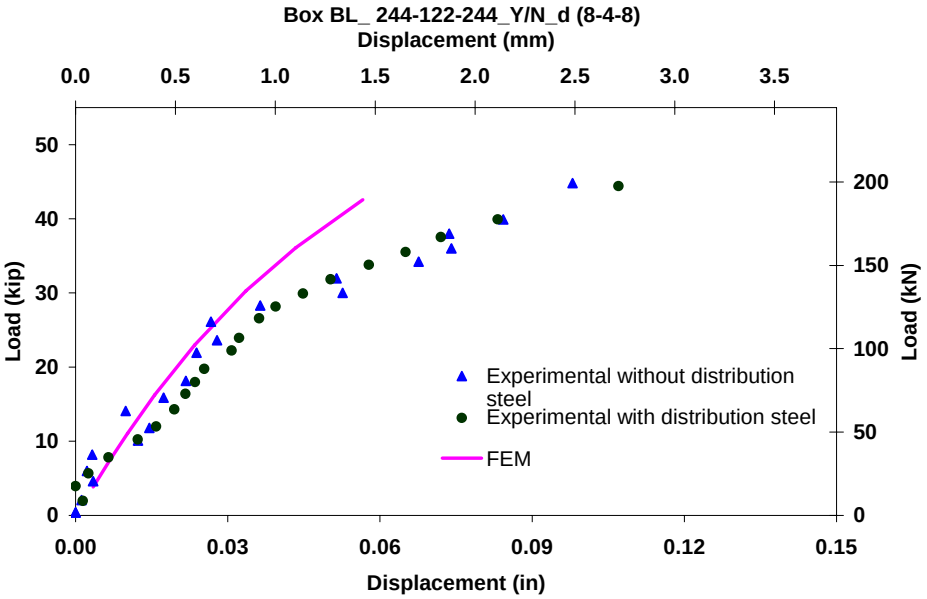

Figure 3.20 Comparison of FEM with Experimental Data for BL_244-122-244_Y/N_d (BL_8-4-8_Y/N_d)

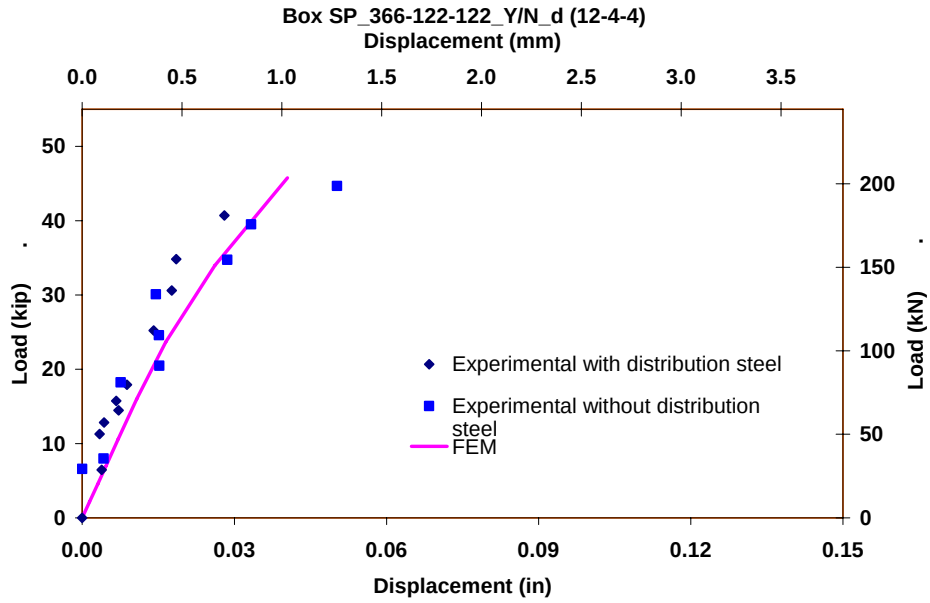

Figure 3.21 Comparison of FEM with Experimental Data for SP_366-122-122_Y/N_d (SP_12-4-4_Y/N_d)

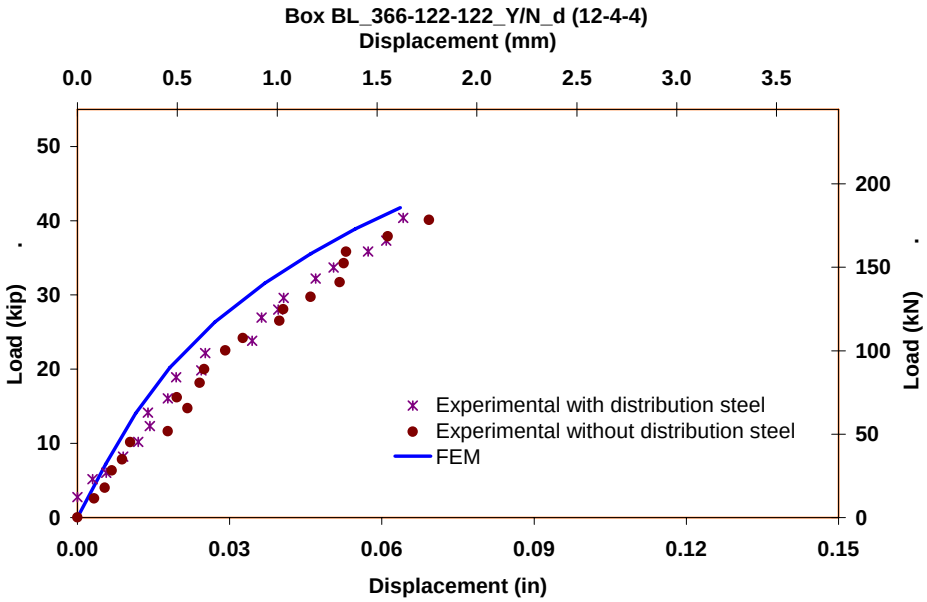

Figure 3.22 Comparison of FEM with Experimental Data for BL_366-122-122_Y/N_d (BL_12-4-4_Y/N_d)

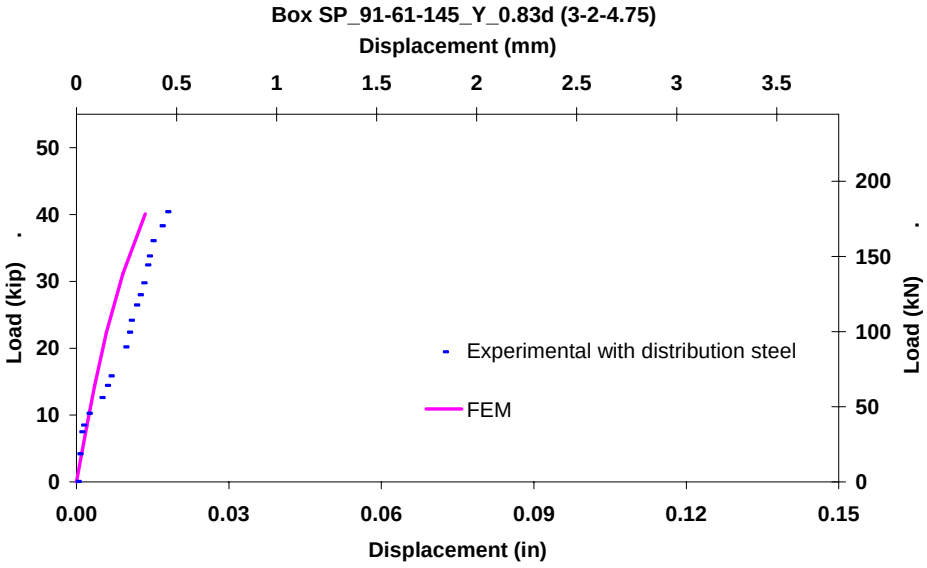

Figure 3.23 Comparison of FEM with Experimental Data for SP_91-61-145_Y_0.83d (SP_3-2-4.75_Y_0.83d)

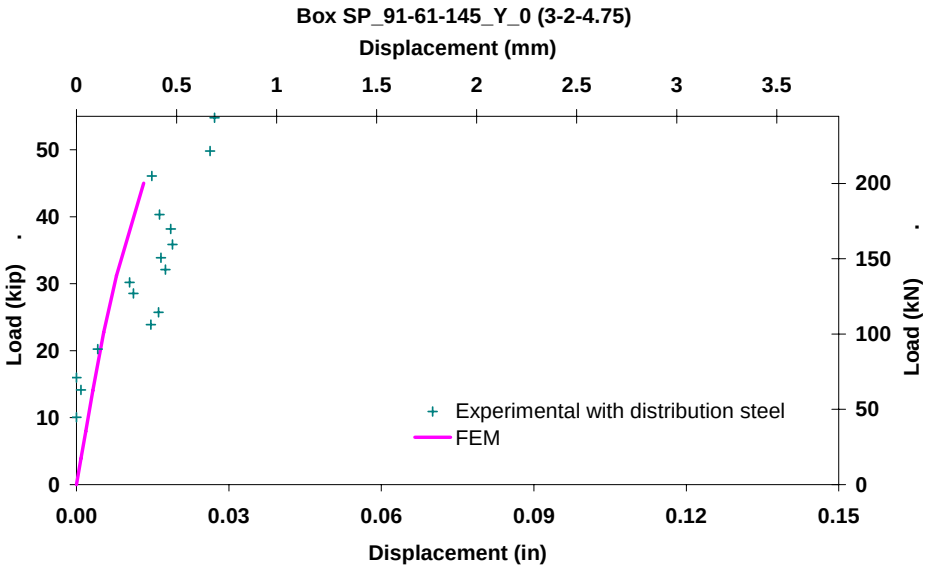

Figure 3.24 Comparison of FEM with Experimental Data for SP_91-61-145_Y_0 (SP_3-2-4.75_Y_0)

CHAPTER 4

DETERMINATION OF SHEAR CAPACITY OF PRECAST BOX CULVERTS

4.1 Introduction

All the forty-two standard cases of the ASTM C 1433 were modeled using the verified FEM model developed in Chapter 3. A regression analysis was conducted to develop equations for the calibrated FEM parameters identified in Chapter 3 in terms of the geometric parameters of the box culverts. These equations were used to obtain the calibration model parameters for all the aforementioned boxes based on their geometric parameters. The verified model and the calibration parameters were used to perform complete 3-D FEM analyses of the ASTM-C1433 boxes by placing the load plate at the distance "**d**" from the tip of the haunch to the edge of the load plate.

The FEM model analyses were used to plot the 3-D volumetric shear force distribution on the top slab of the boxes analyzed. The peak shear force in each of the plots was identified and a vertical plane was passed through it parallel to the box's joint length. This yielded to a 2-D shear force distribution diagram along the box joint length from which the distribution width was calculated by dividing the area under the 2-D diagram with the peak shear force.

The distribution width for the ASTM C1433 boxes were compared with those reported in the AASHTO 2005. The calculated distribution widths were used to calculate the critical factored shear force for all the boxes, which were compared with the American Concrete Institute (ACI) shear capacity equations. It was shown that the shear capacity exceeded the factored critical shear force for all the ASTM C1433 boxes.

4.2 Regression Analysis Concept

In statistics, regression equations are developed from sample data collected from numerous experiments conducted to determine the values of the dependent parameters for predetermined values of independent parameters, to use them to predict the values of dependent parameters by varying independent parameters. To perform the regression analysis, it is a common procedure to represent the response of dependent parameter as functions of the independent parameters. In this parametric study, the two parameters of the boxes are the response measured as functions of the independent parameters. These independent parameters for the 15 experimentally calibrated models were listed in Tables 4.1. The regression equations were solved for the tensile strength coefficient and tension stiffening of concrete. Thus, the objective of the regression analysis was to develop equations for parameters defining tensile strength coefficient and tension stiffening of concrete for the boxes as functions of geometric and force-related parameters of the box. For example, the following would be the form of the equation, which is a function of certain parameters:

$$K = f(S, L, d, b)$$

(4.1)

Determination of the function f is discussed in general terms as follows. Let

$$x = f(X_1, X_2, X_3, ...X_n) \tag{4.2}$$

be a function of n independent parameters, intended to fit data collected from a study. A linear (or summation) regression model for the function is written as

$$x = C_0 + C_1X_1 + C_2\ X_2 + C_3X_3 + ... + C_nX_n + C_{12}X_1X_2$$

$$+ C_{23}X_2X_3 + ... + C_{n1}X_nX_1 + C_{123}X_1X_2X_3 + ...$$

$$+ C_{123.....n}(X_1X_2X_3 .....X_n) \tag{4.3}$$

This techniques yield information on the relative significance of not only the main parameters $X_1, X_2, ..., X_n$, but also the interactions between these same parameters $X_1X_2X_3, ..., (X_1X_2...X_n)$. However, in most practical problems, such as the one studied, many of the higher-order interactions may be eliminated on the basis of physical and intuitive considerations. Probable interactions must, however, be included in the model. The behavior of the pole seems to be a simple solution considering the cantilever profile of the member, but there are many more parameters that can be considered in an analytical study and regression analysis. For example, bolt diameter, base diameter, base condition and connection, yield stress, plate thickness, and tapering can be factors contributing to the outcome. This possibility makes this type of an analytical study and regression analysis a complex and interesting study, but does not facilitate the complete defining of all the interactions.

If a linear regression model is not found satisfactory, an alternative method is the product regression model of the form:

$$x = C_0 X_1^{C_1} X_2^{C_2} \ldots X_n^{C_n} \tag{4.4}$$

This nonlinear regression method was used in this project because of the complexity of the interactions involved. This may be reduced to a linear regression model if logarithms are taken of both sides as shown below:

$$\ln x = \ln C_0 + C_1 \ln X_1 + C_2 \ln X_2 + \ldots + C_n \ln X_n \tag{4.5}$$

Denoting the logarithms of the various parameters by prime superscripts, Equation 4.5 becomes

$$x' = C_0' + C_1 X_1' + C_2 X_2' + \ldots + C_n X_n' \tag{4.6}$$

This is similar to the first group of terms in Equation 4.2. It should be noted that in Equation 4.6 product terms of the form $X_1', X_2', X_3', \ldots X_n$ do not occur, so no interactions are present.

In this study, the coefficient C_0' and the exponents $C_1, C_2, \ldots, C_n$ in Equation 4.5 are determined by multiple regression analysis, so as to obtain the best least square fit to the data. With this method, the best-fit regression equation is taken as the one, which minimizes the sum of the squares of the deviations of the data points from the equation fitted to the data. To demonstrate the basic principles, say that the value of the dependent variable predicted from the best-fit equation is x_i', for any particular set of

values, $X_{li}^{'}, X_{2i}^{'}, X_{3i}^{'}, ..., X_{ni}^{'}$ while it is measured (or directly determined) value is $\overline{x}_i$. Deviation of the predicted value from the measured value is given by

$$\overline{x}_i - x_i^{'} = \overline{x}_i - \left(C_0^{'} + C_1 x_{1i}^{'} + C_2 x_{2i}^{'} + ... + C_n x_{ni}^{'}\right) \tag{4.7}$$

The sum of the squares, S for m number of data is given by

$$S = \sum_{i=1}^{m} \left(\overline{x}_i^{'} - x_i^{'}\right)^2 \tag{4.8}$$

The unknown coefficients $C_0^{'}, C_1, C_2, ..., C_n$ are determined by minimizing the quality S with respect to each coefficient, in other words by setting it equal to zero as shown below.

$$\frac{\partial S}{\partial C_0^{'}} = \frac{\partial S}{\partial C_1} = \frac{\partial S}{\partial C_2} = ... = \frac{\partial S}{\partial C_n} = 0 \tag{4.9}$$

This will result in $(n+1)$ linear simultaneous equations from which the coefficients $C_0^{'}, C_1, C_2, ..., C_n$ can be determined. To determine C_0 the anti-logarithm of C_0' must be found.

A "goodness of fit" of the prediction equation is a comparison of S, the sum of the squares, and the deviations for the constant term C_0 above. The constant term model is

$$S = C_0^{'} \tag{4.10}$$

and the sum of the squares of this model can be written as

$$S_0 = \sum_{i=1}^{m} \left(\bar{x}_i' - x_0' \right)^2 \tag{4.11}$$

in which x_0' is the mean. The difference between S_0 and S is called as "sum of squares due to regression" and the ratio $\frac{(S_0 - S)}{S_0}$ is called as "coefficient of multiple determinations", R^2 which can also be written:

$$R^2 = 1 - \frac{S}{S_0} \tag{4.12}$$

A value of $R^2 = 1$ implies that S is zero and the regression prediction equation passes through all the data points. A value of $R^2 = 0.80$ means that 80 % of the sum of squares of the deviations of the observed (or directly determined) $\bar{x}_i'$ values about their x_0' can be explained by the prediction equation obtained.

4.3 Regression Equations for FEM Calibration

Using the above concept, the calibration parameters obtained from the experimental data (Table 4.1) were used to conduct nonlinear regression analyses. Table 4.2 presents the values of the calibration parameters obtained from regression analysis. Equations for dependent variables; f (the ratio of tensile to compressive strength) and t (tension stiffening parameter) in terms of the independent variables (span, length, effective depth, and spigot/bell test) were obtained (Equations 4.13 and 4.14).

Table 4.1 FEM Calibration Parameters Obtained from Experimental Data

Independent Variable				Dependent Variable	
Span cm (in)	Length cm (in)	Eff. Depth cm (in)	Spigot / Bell End	Tensile Strength / Compressive Strength	Tension Stiffening
S	L	d	b	f_t / f'_c	TS
366 (144)	122 (48)	28 (11)	1	0.034	0.0025
366 (144)	122 (48)	28 (11)	1	0.034	0.0025
366 (144)	122 (48)	28 (11)	2	0.017	0.005
366 (144)	122 (48)	28 (11)	2	0.017	0.005
244 (96)	244 (96)	18 (7)	1	0.051	0.002
244 (96)	244 (96)	18 (7)	2	0.034	0.002
244 (96)	244 (96)	18 (7)	2	0.034	0.002
244 (96)	244 (96)	18 (7)	1	0.085	0.0015
244 (96)	122 (48)	18 (7)	1	0.085	0.0015
244 (96)	122 (48)	18 (7)	2	0.064	0.0015
244 (96)	122 (48)	18 (7)	2	0.064	0.0015
122 (48)	244 (96)	16.5 (6.5)	1	0.034	0.001
122 (48)	244 (96)	16.5 (6.5)	2	0.0425	0.003
91 (36)	145 (57)	15 (6)	3	0.0425	0.0015
91 (36)	145 (57)	15 (6)	4	0.034	0.0015

Table 4.2 Data Obtained from Regression Analysis for Model Calibration

Independent Variable			Dependent Variable		
Span cm (in)	**Length cm (in)**	**Eff. Depth cm (in)**	**Spigot / Bell End**	**Tensile Strength / Compressive Strength**	**Tension Stiffening**
S	**L**	**d**	**b**	**f_t / f'_c**	**TS**
366 (144)	122 (48)	28 (11)	1	.02903	0.00302
335 (132)	122 (48)	25 (10)	1	0.0367	0.0025
305 (120)	122 (48)	23 (9)	1	0.04756	0.00203
274 (108)	122 (48)	20 (8)	1	0.06359	0.00161
244 (96)	122 (48)	18 (7)	1	0.08847	0.00124
213 (84)	122 (48)	18 (7)	1	0.08305	0.00122
183 (72)	122 (48)	18 (7)	1	0.0772	0.0012
152 (60)	122 (48)	18 (7)	1	0.07082	0.00117
122 (48)	122 (48)	16.5 (6.5)	1	0.07893	0.00099
91 (36)	122 (48)	15 (6)	1	0.08681	0.00083

*R^2 = 1.0 corresponds to a perfect fitting

R^2 = 0.91035143 for Tensile Strength /Compressive Strength
R^2 = 0.77630541 for Tension Stiffening

Tensile Strength (f_t):

$$f_t = 5000\left[(e^{(4.17)}(S)^{(0.473)}(L)^{(-0.809)}(d)^{(-2.89)}(b)^{(-0.542)})\right] \tag{4.13}$$

Tension Stiffening:

$$TS = e^{(-12.6)}(S)^{(0.120)}(L)^{(0.444)}(d)^{(1.86)}(b)^{(0.468)} \tag{4.14}$$

4.4 Distribution Width Concept

Distribution width is a concept used in design of slabs in which the strength of a specified width is required to resist the bending moment developed due to any standard loading, which is commonly adopted by the AASHTO specifications for designing the bridge decks. In AASHTO (2005), same concept is utilized by McGrath et al. (2004) to conclude that since shear distribution width was reported to be small, a shear transfer device may be needed across the joint of the connected culverts. Since the experimental testing program of this study indicted that the shear behavior was not the governing factor in any of the box culverts tested until the loads up to at least twice the factored design load (Chapter 2), it led the investigators to believe that the relationship between the magnitude of the distribution width and the actual box behavior as presented in the AASHTO 2005 is misleading. Thus, the distribution width for all the boxes of ASTM 1433 was calculated and compared with the ACI shear strength equations.

To calculate the shear distribution width the volumetric shear force distribution for the top slab is plotted as shown in Figure 4.1 (a). A vertical plane is passed through the location at which the shear force is maximum along the joint length. To obtain the distribution width the area under the shear force diagram obtained from the vertical cut (Figure 4.1 (b)) is calculated and then divided by the value of maximum shear force. This basically means that by multiplying the distribution width with the peak shear force, an equivalent rectangular area representing the area under the 2-D shear force distribution is obtained.

Plots of the 2-D shear force distributions are presented in Figure 4.2 for various culvert span lengths, which show that the area under the shear distribution increases as the span length increases. It should be noted that the wheel load plate is placed at a distance "d" from the tip of the haunch to the edge of the load plate, and since the span length increases in a larger magnitude (3 ft to 12 ft) compared to the increase in "**d**" (7 in. to 12 in.), the "**d**"/span ratio is smaller for the larger span boxes. This means that for the shorter span boxes, the load plate is closer to the center of the span, which forces the bending rather than shear behavior.

Figures 4.3 through 4.12 show the 2-D shear distribution for 91 cm (3 ft) to 366 cm (12 ft) span boxes. These figures indicate that the shear distribution is entirely dependent on the span length and independent of the rise and joint length dimensions.

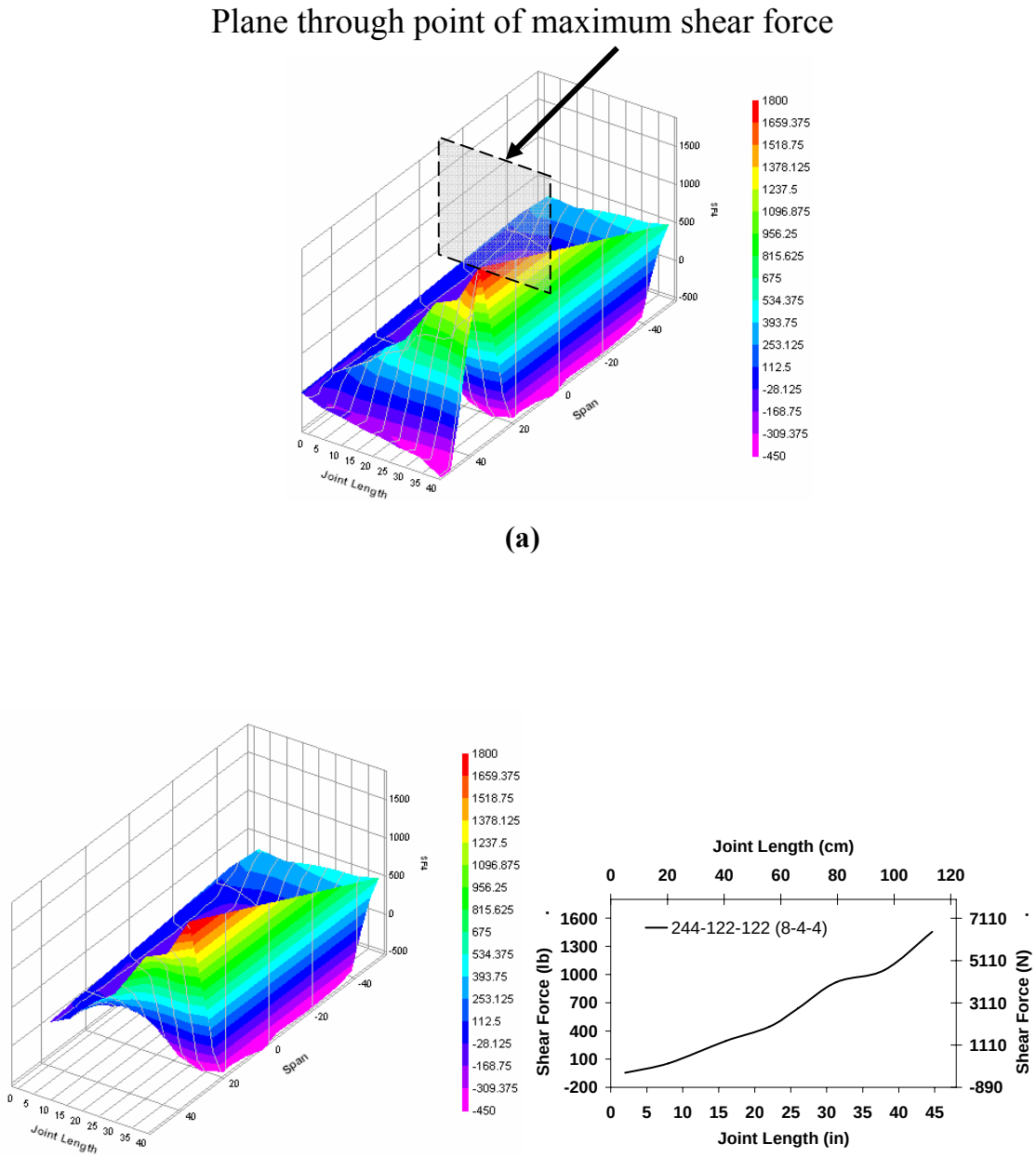

Figure 4.1 Typical Shear Force Plot on the Top Slab of the Box (a) Typical Volumetric Shear Force Plot Showing a Cutting Plane at the Point of Maximum Shear Force; and (b) Shear Force Plot in Volume and in Area at the Point of Maximum Shear Force

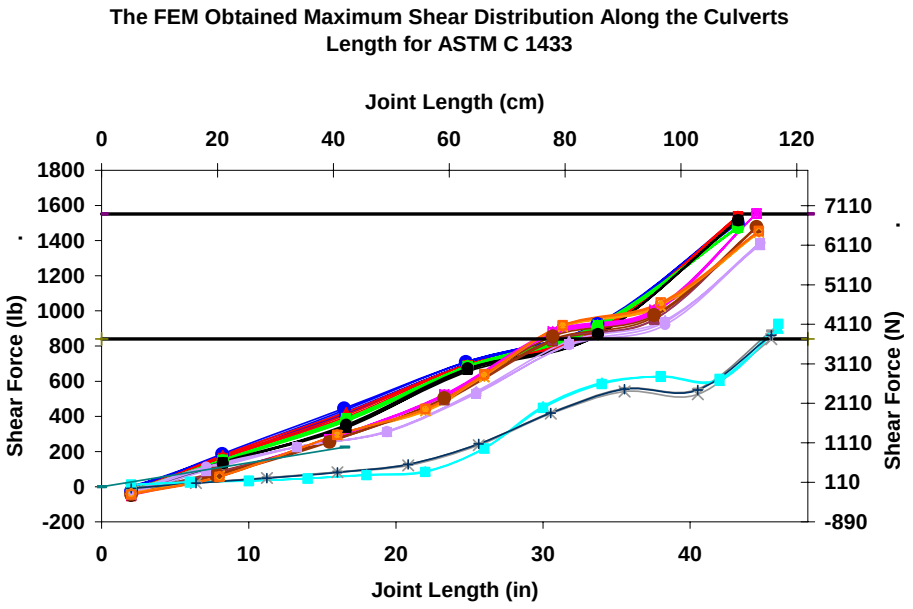

Figure 4.2 Shear Force Plot Along Joint Length at Peak Shear Location on Span

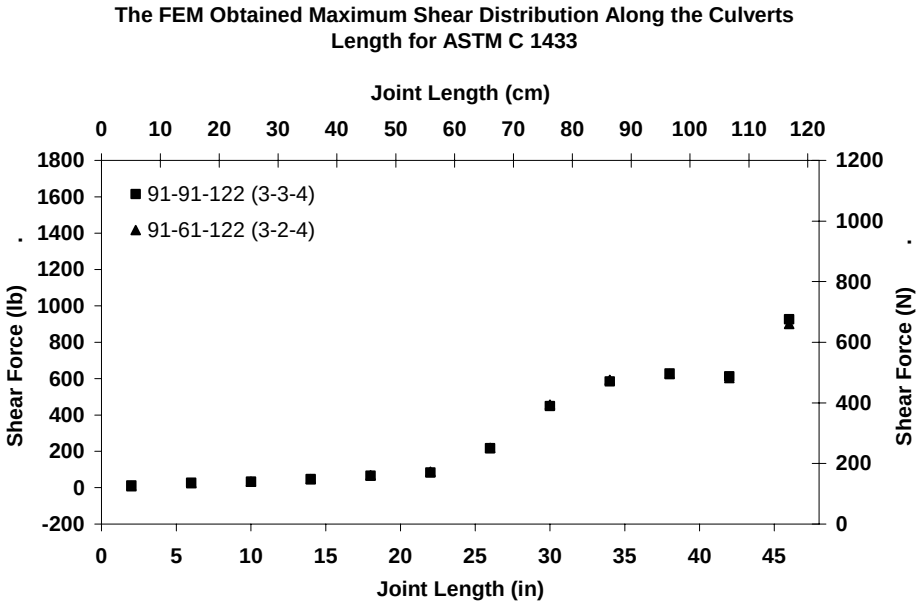

Figure 4.3 Shear Force Plot Along Joint Length at Peak Shear Location on 91 cm (3 ft) Span Boxes

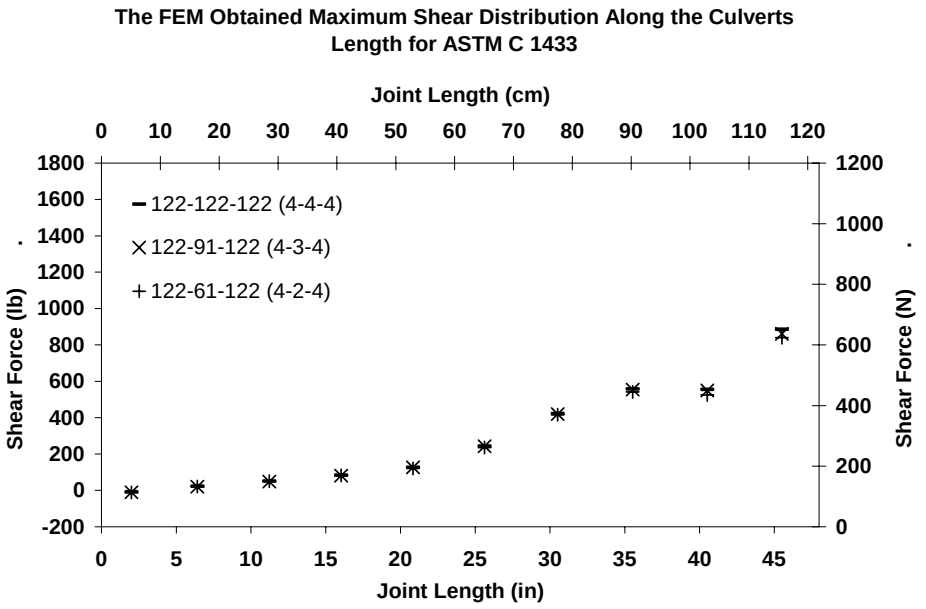

Figure 4.4 Shear Force Plot Along Joint Length at Peak Shear Location on 122 cm (4 ft) Span Boxes

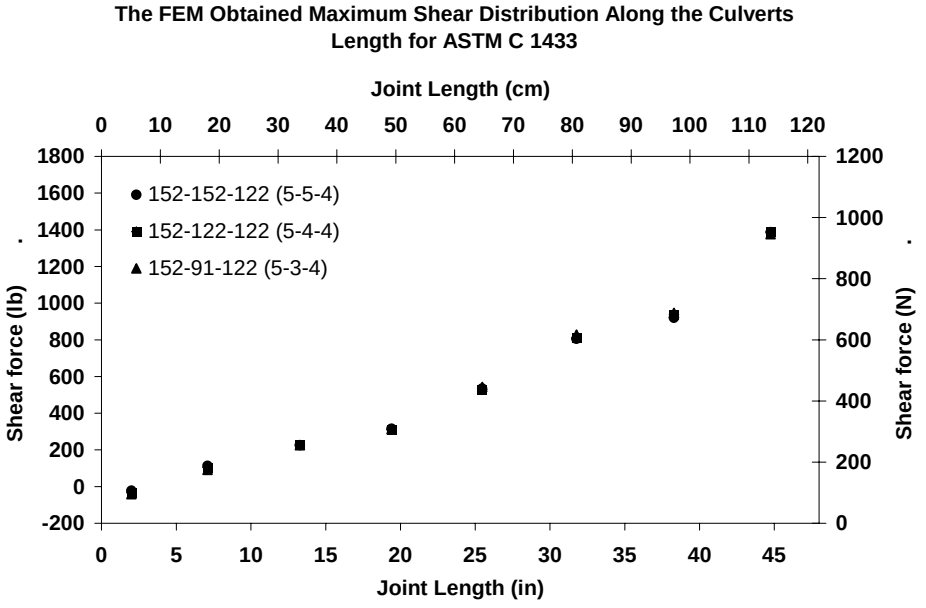

Figure 4.5 Shear Force Plot Along Joint Length at Peak Shear Location on 152 cm (5 ft) Span Boxes

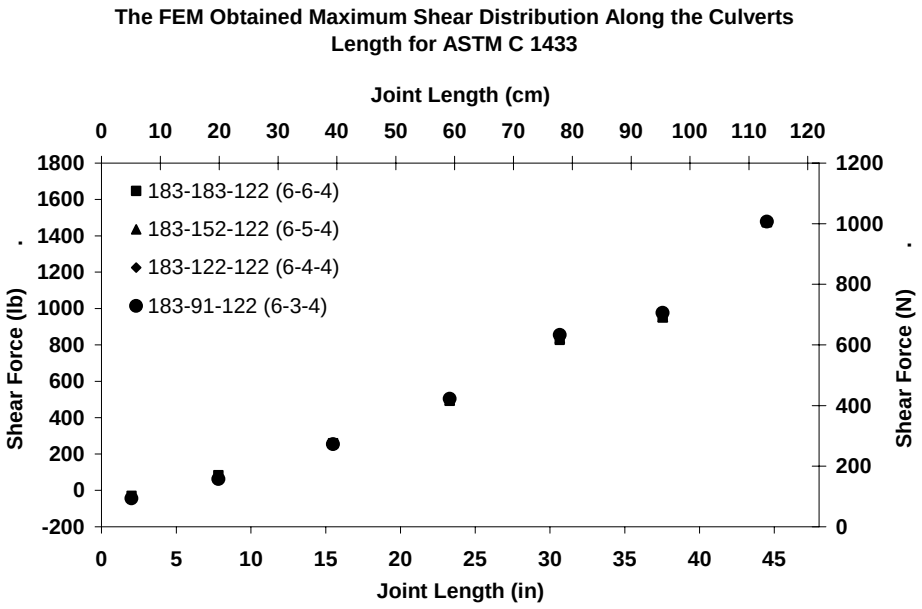

Figure 4.6 Shear Force Plot Along Joint Length at Peak Shear Location on 183 cm (6 ft) Span Boxes

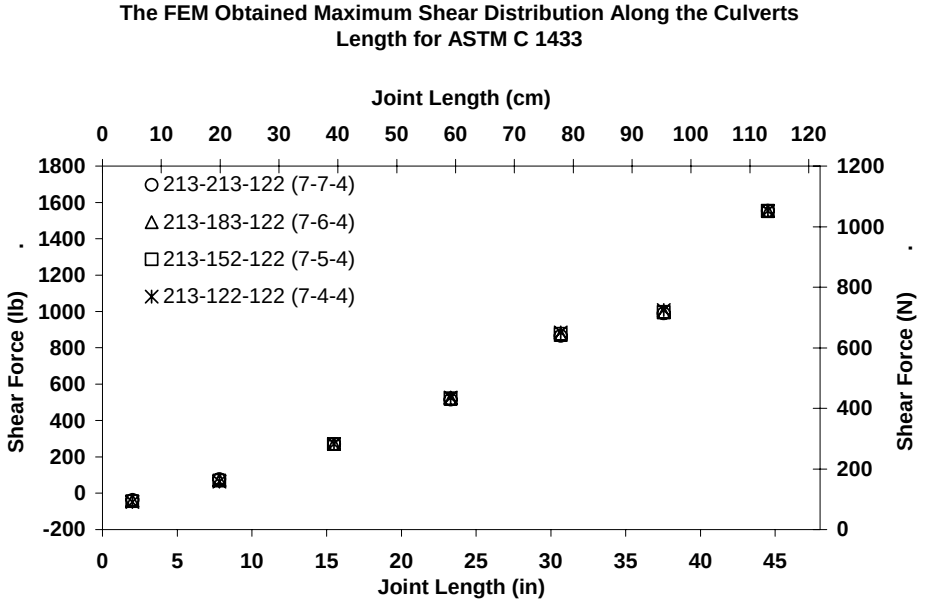

Figure 4.7 Shear Force Plot Along Joint Length at Peak Shear Location on 213 cm (7 ft) Span Boxes

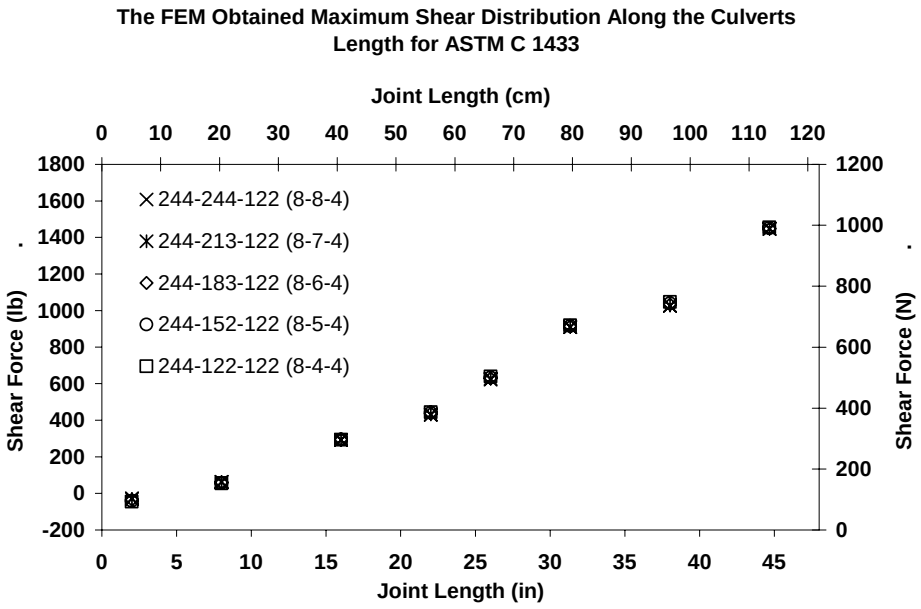

Figure 4.8 Shear Force Plot Along Joint Length at Peak Shear Location on 244 cm (8 ft) Span Boxes

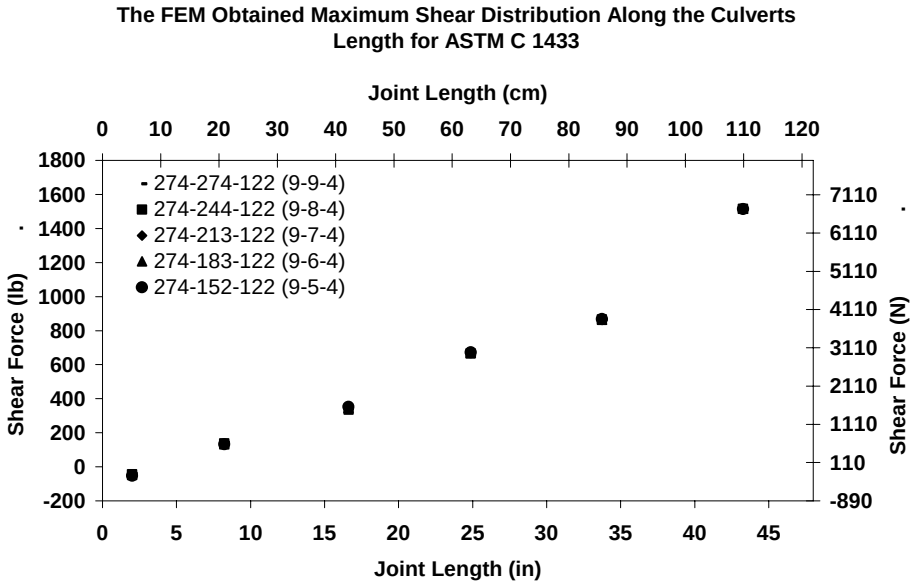

Figure 4.9 Shear Force Plot Along Joint Length at Peak Shear Location on 274 cm (9 ft) Span Boxes

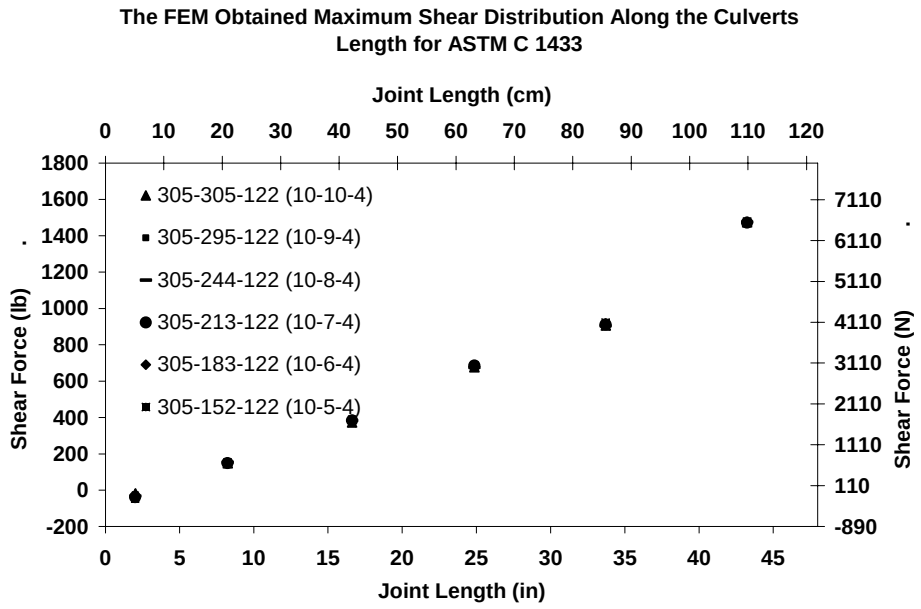

Figure 4.10 Shear Force Plot Along Joint Length at Peak Shear Location on 305 cm (10 ft) Span Boxes

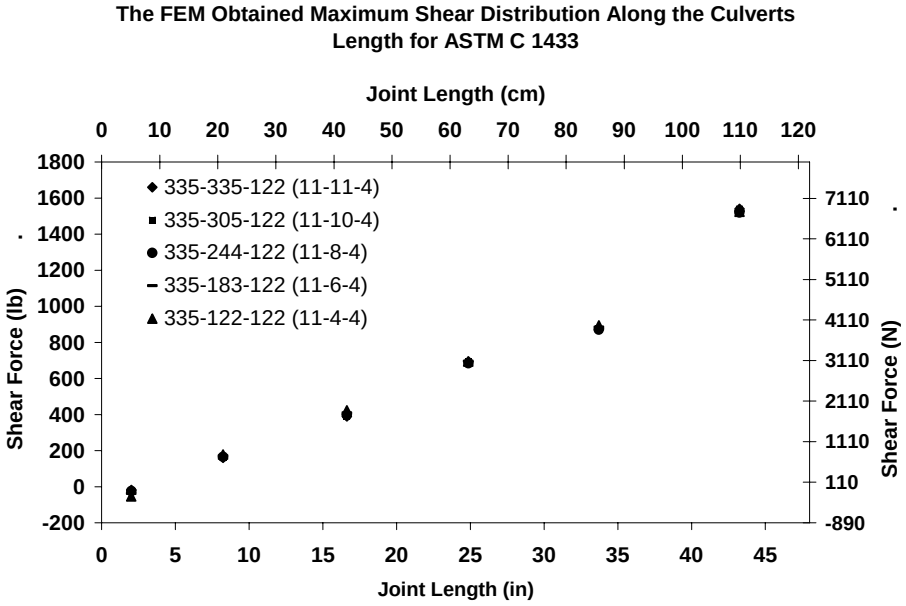

Figure 4.11 Shear Force Plot along Joint Length at Peak Shear Location on 335 cm (11 ft) Span Boxes

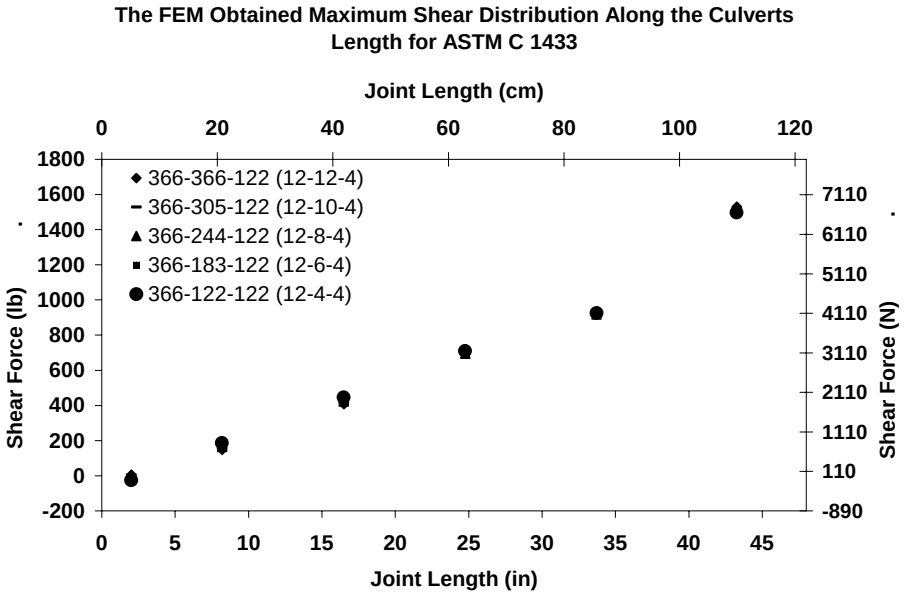

Figure 4.12 Shear Force Plot Along Joint Length at Peak Shear Location on 366 cm (12 ft) Span Boxes

4.5 Shear Capacity

Table 4.3 presents the values of distribution width for the ASTM C1433 boxes calculated in this study based on the factored load, which are less than those calculated per AASHTO 2005. Indeed, the AASHTO distribution width is at least three to four times of those calculated in this study for the ASTM C1433 box geometry (Table 4.3). Furthermore, the distribution width values were used to calculate the critical factored shear force values as presented in Column 3 of Table 4.4, which was compared with the two ACI shear capacity equations: $2b_w d\sqrt{f'_c}$ (referred from this point forward as lower bound shear strength equation) and $3.5b_w d\sqrt{f'_c}$ (referred to from this point forward as upper bound shear strength equation). It should be noted that the former is used for scenarios in which shear cracks form at the tip of existing flexural cracks while

the latter is used for cases in which shear cracks initiates at a 45-degree angle independent of flexural cracks. All the experimental testing (Chapter 2) indicated that the shear cracks initiated independently at the tip of the haunch at approximately twice the factor loads with nearly 45 degree angles, which indicate that the $3.5b_w d\sqrt{f'_c}$ is the applicable shear strength equation for the precast box culverts.

Referring back to Table 4.4, the ratio between the aforementioned lower and upper bound strength equations and the critical factored shear force is calculated and presented in Columns 5 and 6, respectively. Column 5 shows that the range of these ratios varies from 0.64 to 1.04 with 60% of them between 0.90 and 1.04, and the remaining 40% falls between 0.64 and 0.90. Also, Column 6 shows that 100% of the calculated ratios are above 1.0 with their range varying from 1.10 to 1.80 from which over 50% of the ratios are above 1.50. Thus, it is shown that the shear strength of the ASTM C1433 box culverts is more than adequate with the upper bound shear (applicable) strength equation. When comparing with the lower bound shear strength equation, 60% of the ASTM C1433 boxes are considered adequate.

It should be noted that the lower bound shear strength equation is not applicable to the precast box culverts based on the experimental observations (Chapter 2), and it is only presented here for the comparison purposes. However, since this study was conducted based on the culverts subjected to the most critical stresses (no bedding materials and zero depth of the fill), it is anticipated that for the less severe loading condition when bedding material, depth of fill, and lateral soil are accounted for, the majority of the boxes will satisfy the lower bound shear strength equation.

Table 4.4 also shows that the minimum calculated ratios of strength to critical shear force are obtained for the 183 cm (6 ft), 213 (7 ft), and 244 cm (8 ft) span box culverts. This is due to the fact that there is negligible difference between the peak shear force for boxes with spans 183 cm (6 ft), 213 (7 ft), 244 cm (8 ft), 274 (9ft), 305 (10 ft), 335 (11 ft), and 366 (12 ft) (refer to Figure 4.2) while the top slab thickness for the 183 cm (6 ft), 213 (7 ft), and 244 cm (8 ft) span boxes are 18 cm (7 in), 20 cm (8 in), 20 cm (8 in), respectively, which are considerably less that the slab thickness of 23 cm (9 in), 25 cm (10 in), 28 (11 in), and 30 cm (12 in) for the 274 (9ft), 305 (10 ft), 335 (11 ft), and 366 (12 ft) span boxes, respectively.

The above observations further contradicted the relationship between the distribution width and shear capacity presented in AASHTO 2005, which was based on the study conducted by McGrath et al. (2004). While distribution width values calculated in this study were less than those calculated based on AASHTO 2005, it was shown that the shear capacity of the ASTM C1433 boxes were more than adequate. This conclusion is drawn based on the experimental observation and analytical studies conducted in this research. Thus, it is concluded that the distribution width equations presented in AASHTO 2005 for the box culverts is subject to criticism and should not be relied on. This statement is particularly supported since the study presented by McGrath et al. (2004) was based on 2-D linear elastic finite element analyses on 3-D geometry, which was neither supported nor validated by experimental observations. Moreover, since linear elastic analyses were conducted, they were unable to establish a relationship between the distribution width and the box culvert failure mode. Thus, they

compared the distribution width for shear to the distribution width for bending moment, and they concluded that the lesser distribution width controls the failure mechanism.

This study disputes the McGrath et al. findings and argues that the small distribution width for shear is due to two scenarios: small shear force and large shear force. We believe that the former is true in the case of box culverts subjected to shear loading since the governing mode of failure is flexure rather than shear even though the wheel load is placed at the distance "**d**" from the tip of the haunch. This behavior was observed during the extensive experimental testing and analytical investigations of this research, which led us to believe that the behavior of the box culverts is typically different from the bridge slabs due to the additional joint rotation induced during loading. The aforementioned joint rotation will introduce additional bending moment in the culvert's top slab which causes the flexural cracks to govern the behavior up to and beyond the AASHTO factored wheel load.

Table 4.3 Shear Load and Shear Strength of Concrete Boxes

Span-Rise-Length_with/without Dist. Steel_L_w cm (ft)	Shear Force			AASHTO 2005 Distribution Width cm (in)	$(b_w)_{AASHTO}$ / $(b_w)_{Calculated}$
	Maximum kN (kip)	Factored Critical Shear cm-kN/cm (in-kip/in)	Distribut-ion Width cm (in)		(5)/(4)
(1)	(2)	(3)	(4)	(5)	(6)
SP_366-366-122_N_d	2.68	133	50	166	3
(SP_12-12-4_N_d)	(1.53)	(30.00)	(19.59)	(65.28)	3
SP_366-305-122_N_d	2.66	133	50	166	3
(SP_12-10-4_N_d)	(1.52)	(29.93)	(19.67)	(65.28)	3
SP_366-244-122_N_d	2.65	133	50	166	3
(SP_12-8-4_N_d)	(1.52)	(30.00)	(19.80)	(65.28)	3
SP_366-183-122_N_d	2.66	135	51	166	3
(SP_12-6-4_ N_d)	(1.52)	(30.44)	(20.03)	(65.28)	3
SP_366-122-122_N_d	2.62	136	52	166	3
(SP_12-4-4_ N_d)	(1.50)	(30.53)	(20.39)	(65.28)	3
SP_335-335-122_ N_d	2.70	131	49	162	3
(SP_11-11-4_ N_d)	(1.54)	(29.46)	(19.12)	(63.84)	3
SP_335-305-122_ N_d	2.69	131	49	162	3
(SP_11-10-4_ N_ N_d)	(1.54)	(29.51)	(19.18)	(63.84)	3
SP_335-244-122_ N_d	2.66	130	49	162	3
(SP_11-8-4_ N_d)	(1.52)	(29.30)	(19.29)	(63.84)	3
SP_335-183-122_ N_d	2.68	133	50	162	3
(SP_11-6-4_ N_d)	(1.53)	(29.80)	(19.51)	(63.84)	3
SP_335-122-122_ N_d	2.67	134	50	162	3
(SP_11-4-4_ N_d)	(1.52)	(30.09)	(19.75)	(63.84)	3

Table 4.3 - *continued*

Span-Rise-Length_with/without Dist. Steel_ l_w cm (ft)	Shear Force			AASHTO 2005 Distribution Width cm (in)	$(b_w)_{AASHTO}/(b_w)_{Calculated}$
	Maximum kN (kip)	Factored Critical Shear cm-kN/cm (in-kip/in)	Distribut-ion Width cm (in)		(5)/(4)
(1)	(2)	(3)	(4)	(5)	(6)
SP_305-305-122_ N_d	2.58	128	50	158	3
(SP_10-10-4_ N_d)	(1.47)	(28.88)	(19.59)	(62.40)	3
SP_305-274-122_ N_d	2.58	129	50	158	3
(SP_10-9-4_ N_ N_d)	(1.47)	(28.96)	(19.64)	(62.40)	3
SP_305-244-122_ N_d	2.58	129	50	158	3
(SP_10-8-4_ N_d)	(1.48)	(29.06)	(19.69)	(62.40)	3
SP_305-213-122_ N_d	2.58	130	50	158	3
(SP_10-7-4_ N_d)	(1.47)	(29.21)	(19.84)	(62.40)	3
SP_305-183-122_ N_d	2.59	130	50	158	3
(SP_10-6-4_ N_d)	(1.48)	(29.28)	(19.83)	(62.40)	3
SP_305-152-122_ N_d	2.59	131	51	158	3
(SP_10-5-4_ N_d)	(1.48)	(29.44)	(19.92)	(62.40)	3
SP_274-274-122_ N_d	2.65	126	48	155	3
(SP_9-9-4_ N_d)	(1.51)	(28.38)	(18.76)	(60.96)	3
SP_274-244-122_ N_d	2.66	127	48	155	3
(SP_9-8-4_ N_ N_d)	(1.52)	(28.44)	(18.75)	(60.96)	3
SP_274-213-122_ N_d	2.65	127	48	155	3
(SP_9-7-4_ N_ N_d)	(1.51)	(28.49)	(18.83)	(60.96)	3
SP_274-183-122_ N_d	2.66	127	48	155	3
(SP_9-6-4_ N_ N_d)	(1.52)	(28.55)	(18.83)	(60.96)	3
SP_274-152-122_ N_d	2.65	128	48	155	3
(SP_9-5-4_ N_d)	(1.52)	(28.67)	(18.92)	(60.96)	3

Table 4.3 - *continued*

Span-Rise-Length_with/without Dist. Steel_ ℓ_w cm (ft)	Shear Force			AASHTO 2005 Distribution Width cm (in)	$(b_w)_{AASHTO}/(b_w)_{Calculated}$
	Maximum kN (kip)	Factored Critical Shear cm-kN/cm (in-kip/in)	Distribut-ion Width cm (in)		(5)/(4)
(1)	(2)	(3)	(4)	(5)	(6)
SP_244-244-122_ N_d	2.53	121	48	151	3
(SP_8-8-4_ N_d)	(1.45)	(27.15)	(18.77)	(59.52)	3
SP_244-213-122_ N_d	2.54	121	48	151	3
(SP_8-7-4_ N_d)	(1.45)	(27.25)	(18.82)	(59.52)	3
SP_244-183-122_ N_d	2.54	122	46	151	3
(SP_8-6-4_ N_d)	(1.45)	(27.35)	(18.88)	(59.52)	3
SP_244-152-122_ N_d	2.54	122	48	151	3
(SP_8-5-4_ N_ d)	(1.45)	(27.46)	(18.92)	(59.52)	3
SP_244-122-122_ N_d	2.55	123	48	151	3
(SP_8-4-4_ N_d)	(1.46)	(27.60)	(18.97)	(59.52)	3
SP_213-213-122_ N_d	2.72	124	45	148	3
(SP_7-7-4_ N_d)	(1.55)	(27.79)	(17.88)	(58.08)	3
SP_213-183-122_ N_d	2.72	124	46	148	3
(SP_7-6-4_ N_d)	(1.55)	(27.88)	(17.96)	(58.08)	3
SP_213-152-122_ N_d	2.72	124	46	148	3
(SP_7-5-4_ N_d)	(1.55)	(27.97)	(18.00)	(58.08)	3
SP_213-122-122_ N_d	2.72	125	46	148	3
(SP_7-4-4_ N_d)	(1.55)	(28.12)	(18.09)	(58.08)	3

Table 4.3 - *continued*

Span-Rise-Length_with/without Dist. Steel_ l_w cm (ft)	Shear Force			AASHTO 2005 Distribution Width cm (in)	$(b_w)_{AASHTO}/(b_w)_{Calculated}$
	Maximum kN (kip)	Factored Critical Shear cm-kN/cm (in-kip/in)	Distribution Width cm (in)		(5)/(4)
(1)	(2)	(3)	(4)	(5)	(6)
SP_183-183-122_ N_d	2.58	118	46	144	3
(SP_6-6-4_ N_d)	(1.47)	(26.60)	(18.04)	(56.64)	3
SP_183-152-122_ N_d	2.58	119	46	144	3
(SP_6-5-4_ N_d)	(1.48)	(26.68)	(18.08)	(56.64)	3
SP_183-122-122_ N_d	2.58	119	46	144	3
(SP_6-4-4_ N_d)	(1.47)	(26.80)	(18.18)	(56.64)	3
SP_183-91-122_ N_d	2.59	120	46	144	3
(SP_6-3-4_ N_d)	(1.48)	(26.96)	(18.24)	(56.64)	3
SP_152-152-122_ N_d	2.43	112	46	140	3
(SP_5-5-4_ N_d)	(1.39)	(25.23)	(18.19)	(55.20)	3
SP_152-122-122_ N_d	2.43	113	46	140	3
(SP_5-4-4_ N_d)	(1.39)	(25.29)	(18.23)	(55.20)	3
SP_152-91-122_ N_d	2.41	113	47	140	3
(SP_5-3-4_ N_d)	(1.38)	(25.46)	(18.50)	(55.20)	3
SP_122-122-122_ N_d	1.55	60	39	137	4
(SP_4-4-4_ N_d)	(0.89)	(13.52)	(15.27)	(53.76)	4
SP_122-91-122_ N_d	1.51	59	39	137	3
(SP_4-3-4_ N_d)	(0.86)	(13.35)	(15.50)	(53.76)	3
SP_122-61-122_ N_d	1.47	58	39	137	3
(SP_4-2-4_ N_d)	(0.84)	(13.02)	(15.51)	(53.76)	3
SP_91-91-122_ N_d	1.62	61	38	133	4
(SP_3-3-4_ N_d)	(0.93)	(13.81)	(14.90)	(52.32)	4
SP_91-61-122_ N_d	1.58	59	38	133	4
(SP_3-2-4_ N_d)	(0.90)	(13.32)	(14.79)	(52.32)	4

Table 4.4 Shear Strength versus Shear Load on Box Culvert at Factored Load per AASHTO 2005

Span-Rise-Length_with/without Dist. Steel_ L_w cm (ft)	Factored Critical Shear cm-kN/cm (in-kip/in)	Shear Strength kN (kip)		Shear Strength / Shear Force	
		$b_w d\sqrt{f'_c}/6$	$0.3 b_w d\sqrt{f'_c}$		
		$2 b_w d\sqrt{f'_c}$	$3.5 b_w d\sqrt{f'_c}$	(3)/(2)	(4)/(2)
(1)	(2)	(3)	(4)	(5)	(6)
SP_366-366-122_N_d (SP_12-12-4_N_d)	133 (30.00)	136 (30.48)	237 (53.34)	1.02	1.78
SP_366-305-122_N_d (SP_12-10-4_N_d)	133 (29.93)	136 (30.60)	238 (53.56)	1.02	1.79
SP_366-244-122_N_d (SP_12-8-4_N_d)	133 (30.00)	137 (30.80)	240 (53.89)	1.03	1.80
SP_366-183-122_N_d (SP_12-6-4_ N_d)	135 (30.44)	139 (31.16)	243 (54.53)	1.02	1.79
SP_366-122-122_N_d (SP_12-4-4_ N_d)	136 (30.53)	141 (31.72)	247 (55.50)	1.04	1.82
SP_335-335-122_ N_d (SP_11-11-4_ N_d)	131 (29.46)	120 (27.04)	210 (47.32)	0.92	1.61
SP_335-305-122_ N_d (SP_11-10-4_ N_ N_d)	131 (29.51)	121 (27.13)	211 (47.47)	0.92	1.61
SP_335-244-122_ N_d (SP_11-8-4_ N_d)	130 (29.30)	121 (27.28)	212 (47.73)	0.93	1.63
SP_335-183-122_ N_d (SP_11-6-4_ N_d)	133 (29.80)	123 (27.58)	215 (48.27)	0.93	1.62
SP_335-122-122_ N_d (SP_11-4-4_ N_d)	134 (30.09)	124 (27.94)	217 (48.89)	0.93	1.62

Table 4.4 - *continued*

Span-Rise-Length_with/without Dist. Steel_ ℓ_w cm (ft)	Factored Critical Shear cm-kN/cm (in-kip/in)	Shear Strength kN (kip)		Shear Strength / Shear Force	
		$b_w d\sqrt{f'_c}/6$	$0.3b_w d\sqrt{f'_c}$		
		$2b_w d\sqrt{f'_c}$	$3.5b_w d\sqrt{f'_c}$	(3)/(2)	(4)/(2)
(1)	(2)	(3)	(4)	(5)	(6)
SP_305-305-122_ N_d (SP_10-10-4_ N_d)	128 (28.88)	111 (24.93)	194 (43.63)	0.86	1.51
SP_305-274-122_ N_d (SP_10-9-4_ N_ N_d)	129 (28.96)	111 (25.00)	195 (43.75)	0.86	1.51
SP_305-244-122_ N_d (SP_10-8-4_ N_d)	129 (29.06)	112 (25.07)	195 (43.87)	0.86	1.51
SP_305-213-122_ N_d (SP_10-7-4_ N_d)	130 (29.21)	112 (25.25)	197 (44.19)	0.86	1.51
SP_305-183-122_ N_d (SP_10-6-4_ N_d)	130 (29.28)	112 (25.23)	196 (44.16)	0.86	1.51
SP_305-152-122_ N_d (SP_10-5-4_ N_d)	131 (29.44)	113 (25.35)	197 (44.37)	0.86	1.51
SP_274-274-122_ N_d (SP_9-9-4_ N_d)	126 (28.38)	94 (21.23)	165 (37.15)	0.75	1.31
SP_274-244-122_ N_d (SP_9-8-4_ N_ N_d)	127 (28.44)	94 (21.22)	165 (37.13)	0.75	1.31
SP_274-213-122_ N_d (SP_9-7-4_ N_ N_d)	127 (28.49)	95 (21.30)	166 (37.28)	0.75	1.31
SP_274-183-122_ N_d (SP_9-6-4_ N_ N_d)	127 (28.55)	95 (21.30)	166 (37.28)	0.75	1.31
SP_274-152-122_ N_d (SP_9-5-4_ N_d)	128 (28.67)	95 (21.41)	167 (37.47)	0.75	1.31

Table 4.4 – *continued*

Span-Rise-Length_with/without Dist. Steel_ ℓ_w cm (ft)	Factored Critical Shear cm-kN/cm (in-kip/in)	Shear Strength kN (kip)		Shear Strength / Shear Force	
		$b_w d\sqrt{f'_c}/6$	$0.3b_w d\sqrt{f'_c}$		
		$2b_w d\sqrt{f'_c}$	$3.5b_w d\sqrt{f'_c}$	(3)/(2)	(4)/(2)
(1)	(2)	(3)	(4)	(5)	(6)
SP_244-244-122_ N_d (SP_8-8-4_ N_d)	121 (27.15)	83 (18.59)	145 (32.52)	0.68	1.20
SP_244-213-122_ N_d (SP_8-7-4_ N_d)	121 (27.25)	83 (18.63)	145 (32.60)	0.68	1.20
SP_244-183-122_ N_d (SP_8-6-4_ N_d)	122 (27.35)	83 (18.69)	145 (32.71)	0.68	1.20
SP_244-152-122_ N_d (SP_8-5-4_ N_ d)	122 (27.46)	83 (18.73)	146 (32.78)	0.68	1.19
SP_244-122-122_ N_d (SP_8-4-4_ N_d)	123 (27.60)	84 (18.78)	146 (32.86)	0.68	1.19
SP_213-213-122_ N_d (SP_7-7-4_ N_d)	124 (27.79)	79 (17.70)	138 (30.97)	0.64	1.11
SP_213-183-122_ N_d (7-6-4_ N_d)	124 (27.88)	79 (17.78)	138 (31.11)	0.64	1.12
SP_213-152-122_ N_d (SP_7-5-4_ N_d)	124 (27.97)	79 (17.82)	139 (31.18)	0.64	1.11
SP_213-122-122_ N_d (SP_7-4-4_ N_d)	125 (28.12)	80 (17.90)	139 (31.33)	0.64	1.11

Table 4.4 – *continued*

Span-Rise-Length_with/without Dist. Steel_ ℓ_w cm (ft)	Factored Critical Shear cm-kN/cm (in-kip/in)	Shear Strength kN (kip) $2b_w d\sqrt{f'_c}$	Shear Strength kN (kip) $0.3b_w d\sqrt{f'_c}$	Shear Strength / Shear Force	
		$b_w d\sqrt{f'_c}/6$	$3.5b_w d\sqrt{f'_c}$	(3)/(2)	(4)/(2)
(1)	(2)	(3)	(4)	(5)	(6)
SP_183-183-122_ N_d (SP_6-6-4_ N_d)	118 (26.60)	79 (17.86)	139 (31.25)	0.67	1.17
SP_183-152-122_ N_d (SP_6-5-4_ N_d)	119 (26.68)	80 (17.90)	139 (31.32)	0.67	1.17
SP_183-122-122_ N_d (SP_6-4-4_ N_d)	119 (26.80)	80 (18.00)	140 (31.50)	0.67	1.18
SP_183-91-122_ N_d (SP_6-3-4_ N_d)	120 (26.96)	80 (18.06)	141 (31.60)	0.67	1.17
SP_152-152-122_ N_d (SP_5-5-4_ N_d)	112 (25.23)	80 (18.01)	140 (31.52)	0.71	1.25
SP_152-122-122_ N_d (SP_5-4-4_ N_d)	113 (25.29)	80 (18.04)	140 (31.58)	0.71	1.25
SP_152-91-122_ N_d (SP_5-3-4_ N_d)	113 (25.46)	81 (18.31)	143 (32.05)	0.72	1.26
SP_122-122-122_ N_d (SP_4-4-4_ N_d)	60 (13.52)	62 (14.04)	109 (24.56)	1.04	1.82
SP_122-91-122_ N_d (SP_4-3-4_ N_d)	59 (13.35)	63 (14.25)	111 (24.94)	1.07	1.87
SP_122-61-122_ N_d (SP_4-2-4_ N_d)	58 (13.02)	63 (14.26)	111 (24.95)	1.09	1.92
SP_91-91-122_ N_d (SP_3-3-4_ N_d)	61 (13.81)	56 (12.64)	98 (22.13)	0.92	1.60
SP_91-61-122_ N_d (SP_3-2-4_ N_d)	59 (13.32)	56 (12.55)	98 (21.96)	0.94	1.65

CHAPTER 5

SUMMARY, CONCLUSIONS, AND RECOMMEDATIONS

5.1 Summary

This study evaluated the shear behavior and capacity of the precast concrete box culverts subjected to HS 20 truck wheel load. The most critical culvert behavior was considered by studying culverts subjected to zero depth of the fill and placed on a rigid bedding material. Three major phases were considered to complete the study, which included: (1) experimental program; (2) finite element modeling; and (3) development of distribution width and the determination of shear capacity.

5.1.1 Phase 1 - Experimental Program

A full-scale experimental testing program, presented in Chapter 2, was undertaken to perform tests on 24 typical box culverts designated as per ASTM C 1433-05 with and without distribution steel (As_6). Several span and joint length sizes were considered to cover a variety of geometrical dimensions. To consider variable casting process, boxes from two major precast manufacturers in the United States, were tested.

Two UT Arlington's experimental testing facilities were used for the entire testing program: (1) Structural Engineering Laboratory located at the Engineering Lab Building, which will be referred to SEL-ELB from this point forward and (2) The pre-construction temporary UT Arlington Center for Structural Engineering Research, which will be referred to UTA-CSER.

The test set-ups and instrumentation were almost identical in the both testing locations. The test frame consisted of W12x87 columns and built-up crossbeams. The instrumentation, in general, consisted of laser-based optoelectronic displacement sensors, to measure vertical displacements; displacement transducers, which was placed at almost the same location as the laser for multiple displacement reading; and data acquisition system.

A 25 cm x 51 cm (10 in x 20 in) load plate was placed, at the distance "**d**" from the tip of the haunch to the edge of the load plate, on the outside face of the top slab to transfer the load from the load cylinder and the load cell to each test culvert. All the culverts were loaded similarly at 89 kN (2 kip) intervals up to 178 kN (40 kip), when the load increment was changed to 22 kN (5 kip) until failure. The 178 kN (40 kip) load was selected based on the observations during the initial testing phase which indicated that the experimental load displacement plots suffered significantly from stiffness degradation. Also the 178 kN (40 kip) load is almost equal to the factored wheel live load of a HS 20 Truck per AASHTO (2005) (i.e. $16 \times 1.75 \times 1.33 = 37.24\ kip$) 166 kN.

Each test was conducted with the assistance from the team of at least five researchers in which crack initiation and propagation were marked. The load-deflection plots for each of the test specimens are presented in Chapter 2. The step-by-step test events were recorded and are presented in the Appendix A for each test specimen. Photographs of the test specimens including crack marks are presented in the Appendix B.

5.1.2 Phase 2 - Finite Element Modeling

Complete detailed three-dimensional finite element models (FEM) of the test specimens were developed and analyzed to simulate the experimental results, which are presented in Chapter 3. Three- dimensional shell and solid elements were used to model the culvert systems. The models shell elements were used to obtain the values of the bending moment and shear forces while the models with solid elements were developed for crack detection. The welded wire fabrics were modeled by using the rebar elements placed on the surface-elements provided by the ABAQUS Software. The contact surface between the outside face of the bottom slab and reaction floor was modeled by using non-linear node-to-surface contact algorithm.

The analysis algorithm consisted of an incremental loading history to capture the problem non-linearity. Smeared crack model along with the Riks Algorithm were incorporated to analyze the system after micro-cracks and to stabilize the solution, respectively. The converged solution was obtained by using H-convergence coupled with the difference between the external work done and the strain energy density of the system. Three critical parameters were calibrated based on the experimental results to treat the stress locking inherent to the displacement-based-only finite element algorithm. These parameters were: tension stiffening; concrete modulus of elasticity; and the ratio of tensile to compressive strength.

The load-deflection obtained from the FEM analyses were compared with those obtained from the experimental results which are presented in Chapter 3. The crack initiation and propagation obtained from FEM at different load levels are presented in

the Appendix C. Finally, the FEM was used to locate the location of the maximum shear force on the outside face of the top slab when the culvert is subjected to the wheel load placed at the distance "**d**" from the tip of the haunch.

5.1.3 Phase 3 - Distribution Width and Shear Capacity

All the forty-two standard cases of the ASTM C 1433 were modeled using the verified FEM model developed in Chapter 3. A regression analysis was conducted to develop equations for the calibrated FEM parameters identified in Chapter 3 in terms of the geometric parameters of the box culverts. These equations were used to obtain the calibration model parameters for all the aforementioned boxes based on their geometric parameters. The verified model and the calibration parameters were used to perform complete 3-D FEM analyses of the ASTM-C1433 boxes by placing the load plate at the distance "**d**" from the tip of the haunch to the edge of the load plate.

The FEM model analyses were used to plot the 3-D volumetric shear force distribution on the top slab of the boxes analyzed. The peak shear force in each of the plots was identified and a vertical plane was passed through it parallel to the box's joint length. This yielded to a 2-D shear force distribution diagram along the box joint length from which the distribution width was calculated by dividing the area under the 2-D diagram with the peak shear force.

The distribution width for the ASTM C1433 boxes were compared with those reported in the AASHTO 2005. The calculated distribution widths were used to calculate the critical factored shear force for all the boxes which were compared with

the American Concrete Institute (ACI) shear capacity equations. It was shown that the shear capacity exceeded the factored critical shear force for all the ASTM C1433 boxes.

5.2 Conclusion

The conclusion of this study advances in the following forefronts:

- The full-scale experimental tests indicated that flexure governed the behavior for all the test specimens up to and beyond the AASHTO factor live load. For all the test specimens the flexural cracks formed initially on the inside face of the top or bottom slab, which extended to the spigot or bell toward the middle of the load plate. No flexural cracks were observed at loads below the AASHTO service load,

- The second series of cracks, for all the test specimens, were negative moment cracks which formed on the wall closest to the load plate along the joint length at a distance equal to approximately one-third from the top slab. These cracks normally extended to the spigot and bell ends.

- The third series of cracks were noticed to be the negative moment cracks which initiated at both walls and extended to the outside face of the top slab. In some tests, these cracks extended along the span on the outside face of top slab.

- The shear cracks were among the final cracks observed. For all of the test specimens shear cracks formed at approximately 320 kN (72 kip) of load

(almost twice the AASHTO factored load). These cracks initiated independently from the tip of the haunch (on the testing end (spigot or bell)) and extended toward the edge of the load plate. By independent shear crack, we mean that it did not initiate at the tip of the flexural cracks. No shear crack was observed before flexural cracks in any of the specimens tested.

- Even though the load plate was place at the distance "**d**" from the tip of the haunch to the edge of the load plate, the culverts behavior governed by flexural cracks during the experiment up to high load levels. This is due to culvert's joint rotation, which contributes significantly to culvert's bending moment. Thus, it was concluded that the behavior of the box culverts is different than that of the bridge slabs. Furthermore, the AASHTO bridge design concept for the distribution width is not justifiable for culverts.

- The comparison of the test results, for with and without top slab distribution steel showed that the effect of the compression distribution steel (As_6) in the top slab is insignificant. This comparison was made with respect to crack initiation and propagation as well as the load-deflection plots. The overall culverts behaviors during the course of experiments were almost identical for the specimens with and without top slab compression distribution steel.

- The final failure for all the test specimens was due to shear/bond failure at loads ranging from 320 kN (72 kip) to 712 kN (160 kip) or above for all the box culverts tested.

- The finite element model exhibited close correlation with the experimental results for load-deflection and crack prediction for all the test specimens. The calibration parameters identified to defuse the stress locking inherent in the displacement-based-only finite element were identified as: modulus of elasticity; the ratio of tensile to compressive strength; and the tension stiffening parameter.

- The FEM analyses showed that when the load plate was placed at the distance "**d**" from the tip of the haunch to the edge of the load plate, the value of the maximum shear force was located between the edge of the haunch and the edge of the load plate for all the culverts' geometry used in the experimental program. Indeed, for 70% of the culvert's tested, the maximum shear force value was at one-half the distance between the tip of the haunch and edge of the load-plate.

- It was shown that the maximum value of the shear force increased as the culvert's span increased for the same load. This counter intuitive finding is due to the fact that the wheel load plate is placed at a distance "**d**" from the

tip of the haunch to the edge of the load plate, and since the span increases in a larger magnitude 91 cm (3 ft) to 366 cm (12 ft) compared to the increase in "**d**" 15 cm (6 in.) to 30 cm (12 in.), the **span /"d"** ratio is larger for the larger span boxes. This implies that for the shorter span boxes the load plate is closer to the center of the span which forces more bending rather than shear behavior.

- The values of the distribution width calculated based on the validated FEM analyses in this study were between one-fourth and one-third of those calculated based on the AASHTO 2005. Since experimental testing of twenty four test specimens and FEM analyses of forty two ASTM C1433 box culvert geometries confirmed that shear was not governing the behavioral mode (particularly at service and factored AASHTO loads), it is concluded that there are no relations between the AASHTO 2005 distribution width equations and the culvert's behavior. It should be noted that AASHTO 2005 distribution width equations are based on the McGrath et al. (2004) study which compared the values of distribution width for shear and moment and concluded that the smaller of the two governs the behavior. This study disputes McGrath et al. (2004) conclusion that small values of distribution width are indicative of cases with induced critical shear.

- This study concludes that small distribution width is the result of two scenarios: (1) large shear forces and (2) small shear forces. In the case of the box culverts in which the joints undergo rotations and increase the bending moment in the top slab, the latter is the case and shear forces are not the governing mode of the failure.

- The critical factored shear force for all the ASTM C1433 precast box culverts were calculated and were compared with the two ACI shear capacity equations: $2b_w d\sqrt{f'_c}$ (lower bound) and $3.5b_w d\sqrt{f'_c}$ (upper bound) . It was shown that the shear capacity exceeds the critical shear force for all the aforementioned cases considered.

- This study concludes that the behavior of the box culverts is significantly different than that of bridge slab. Thus, the AASHTO provisions for box culverts, which are obtained from McGrath et al. (2004) study based on linear elastic finite element analysis, which is not capable of predicting culvert's behavior and failure modes should be revisited.

- This study concludes that the AASHTO 2005 provisions that states "shear transfer device should be provided across the joint, if the calculated distribution width exceeds the length between the two adjacent joints" is not justified and not scientifically supported. The authors are aware that the

AASHTO 2005 provisions also applies to non ASTM C 1433 culverts in which relatively thin slab thicknesses are used for special cases. However, there are no indications from the McGrath et al. (2004) research report that they incorporated thin slab thicknesses in their study. Thus the merit of AASHTO shear provisions for box culverts based on McGrath et al. study remain questionable.

5.3 Recommendations

This study recommends the following future research studies to complement the work presented here:

- This study investigated the shear capacity of all the ASTM C1433 precast box culverts with minimum slab thickness of 18 cm (7 in) which are fabricated with standard forms. Thus, special design cases with thinner top slab thickness and varying lengths need to be studied.

- The finite element modeling and analysis presented in this study considers smeared crack model only which can successfully model the crack widths less than 0.10 in. It is recommended that coupled smeared crack and discrete crack models to be employed in order to predict culvert's behavior with more accuracy when crack width exceeds 0.10 in. across which stresses do not transfer.

- This study recommends that the AASHTO 2005 distribution width for the box culverts needs to be revisited. It is highly recommended the following statement “shear transfer device should be provided across the joint, if the calculated distribution width exceeds the length between the two adjacent joints” be eliminated from the AASHTO 2005 provisions.

APPENDIX A

REPORTS OF EXPERIMENTS CONDUCTED

Table A1 Test: SP_122-122-122_Y_0 (SP_4-4-4_Y_0) (with bedding)

Manufacturer: Hanson Pipe & Products

Load kN (kip)	Events
156 (35)	The 1st superficial flexural crack detected on the inside face of the bottom slab under the load.
178 (40)	The 1st superficial flexural crack detected on the inside face of the top slab under the load.
200 (45)	The 2nd superficial flexural crack detected on the inside face of the top slab under the load.
222 (50)	The 2nd superficial flexural crack detected on the inside face of the bottom slab under the load.
289 (65)	The 1st and 2nd superficial flexural cracks, on the inside face of the top slab, extended further and became visible at spigot face and bell face.
289 (65)	The 1st and 2nd superficial flexural cracks on the inside face of the top slab extended further in the full joint length.
289 (65)	The 1st and 2nd superficial flexural cracks on the inside face of the bottom slab extended further.
356 (80)	The 1st superficial flexural crack on the inside face of the top slab extended further in the full joint length.
356 (80)	A shear crack at the tip of the right haunch detected on the spigot end.
400 (90)	The cracks in the left sidewall propagated and moved up around the load plate.
400 (90)	The cracks in the right sidewall propagated in the full joint length.
400 (90)	A crack appeared on the bell face.
423 (95)	An inclined crack (towards the load plate) in the center of the spigot face in the top slab developed.
423 (95)	Near the right haunch, a crack detected on the inside face of the bottom slab in the full joint length.
445 (100)	The shear crack moved up towards the center of the load plate.
534 (120)	At the Bell end, a new crack detected on the inside face of the bottom slab.
534 (120)	The new cracks in the right sidewall and the left sidewall widened in the full joint length.
534 (120)	Another inclined shear crack from the left edge of the load plate towards the left side wall detected and reached the inside face of the top slab at 31
578 (130)	The shear crack appeared at 356 kN (80 kip) widened at the top slab on the right haunch.
632 (142)	Ultimate failure.

Table A2 Test: SP_122-122-122_Y_0 (SP_4-4-4_Y_0)
Manufacturer: Hanson Pipe & Products

Load kN (kip)	Events
133 (30)	The 1st superficial flexural crack detected at the spigot end on the inside face of the bottom slab, under the load.
133 (30)	The 1st superficial flexural crack, at the spigot end on the inside face of the top slab extended in the joint length.
200 (45)	The 2nd superficial flexural crack detected at the spigot end face at the top slab.
222 (50)	The 3rd superficial flexural crack detected at the spigot end face at the top slab.
267 (60)	A non measurable shear crack at the tip of the right haunch detected on the spigot face.
267 (60)	The cracks in the left sidewall propagated and moved up around the load plate.
334 (75)	The shear crack at the tip of the right haunch widened on the spigot face.
334 (75)	The new cracks in the right sidewall and the left sidewall propagated in the full joint length.
512 (115)	The new cracks in the right sidewall and the left sidewall propagated in the full joint length.
512 (115)	An inclined crack (towards the load plate) detected in the center of the spigot face on the top slab.
645 (145)	An inclined crack (towards the load plate) detected in the center of the spigot face on the top slab.
645 (145)	The new cracks detected on the right and the left sidewalls.
712 (160)	Ultimate failure.

Table A3 Test: SP_122-122-122_Y_0.23d (SP_4-4-4_Y_0.23d)

Manufacturer: Hanson Pipe & Products

Load kN (kip)	Event
107 (24)	The 1st superficial flexural crack detected at the spigot end on the inside face of the bottom slab, under the load.
156 (35)	The 1st superficial flexural crack detected at the spigot end on the inside face of the bottom slab at 61 cm (24 in) extended in joint length.
156 (35)	The 1st superficial flexural crack detected at the spigot end on the inside face of the top slab, under the load.
178 (40)	The 2nd superficial flexural crack detected at the spigot end on the inside face of the top slab, under the load.
222 (50)	The 2nd superficial flexural crack detected at the bell end, on the inside face of the bottom slab.
267 (60)	The 2nd superficial flexural crack, on the inside face of the top slab, extended to the bell end.
267 (60)	The 1st superficial flexural crack detected at the spigot end on the outside face of the left sidewall near the load plate (31 cm (12 in) below the top slab).
289 (65)	The 3rd superficial flexural crack detected at the spigot end, on the inside face of the top slab.
289 (65)	The 2nd superficial flexural crack at the bell end in the inside face of the bottom slab, extended further.
311 (70)	The 1st superficial flexural crack detected at the spigot end, in the right side wall near the load plate (31 cm (12 in) below the top slab and 76 cm
334 (75)	A shear crack developed at the west haunch (far from the load) in the full joint length at the top slab.
334 (75)	The 1st superficial flexural crack detected at the spigot end on the outside face of the left sidewall near the load plate (31 cm (12 in) below the top
378 (85)	Another shear crack detected at the west haunch (far from the load) in the line of the haunch at the bell end, at the top slab.
423 (95)	The 1st superficial crack at the spigot end, on the right side wall near the load plate propagated in the full joint length.
423 (95)	Another flexural crack detected on the outside face of the right side wall in the full joint length.
423 (95)	The 3rd flexural crack at the spigot end, on the inside face of the top slab, extended upwards.
423 (95)	On the spigot end of the top slab, a new small crack detected.

Table A3 – *continued*

467 (105)	On the spigot end of the top slab, two new small cracks detected.
467 (105)	On the inside face of the bottom slab, cracks detected at 245 kN (55 kip) and 289 kN (65 kip) connected by a new crack in the span direction.
467 (105)	A new crack detected on the outside face of the right side wall at the both ends.
512 (115)	A shear crack joining the left haunch & the load plate detected.
512 (115)	The two new full joint length cracks detected on the outside face of the east wall.
512 (115)	A new crack detected at the bell end near the left wall on the top slab.
512 (115)	A new crack on the inside face of the bottom slab, 61 cm (24 in) long 38 cm (15 in), detected from the left wall.
512 (115)	A new crack on the outside face of the right wall of 41 cm (16 in) detected at the spigot end.
512 (115)	A new crack on the right wall of 41 cm (16 in) detected in the center of the joint length.
556 (125)	The cracks on the outside face of the right side wall detected at 467 kN (105 kip) propagated from the both sides and join.
601 (135)	A new crack detected on the outside face of the west wall.
601 (135)	A shear crack detected at the spigot end.
645 (145)	Ultimate failure.

Table A4 Test: BL_122-122-122_Y_0.23d (BL_4-4-4_Y_0.23d)

Manufacturer: Hanson Pipe & Products

Load kN (kip)	Event
133 (30)	A superficial flexure crack detected on the bell end on the inside face of the top slab.
156 (35)	A superficial flexural crack detected on the bell end on the inside face of the bottom slab.
200 (45)	The 1st flexural crack became visible on the bell end on the inside face of the top slab.
222 (50)	The 1st visible flexural crack, on the bell end on the inside face of the top slab, propagated towards the spigot end.
245 (55)	The 1st superficial flexural crack transformed to the **1st serviceability flexural crack**, wider than 0.25 mm (0.01 in), on the bell end on the inside face of the top slab.
311 (70)	The 2nd superficial flexural crack detected at the center on the bell end on the inside face of the top slab.
311 (70)	The 3rd superficial flexural crack detected at the center between the center of the box and the edge of the load plate on the bell end on the inside face of the top slab and extended in the full joint length.
311 (70)	A superficial shear crack detected at the edge of the haunch (near the load) on the bell end.
311 (70)	A shear crack on the right wall (close to the load) detected first moving towards the spigot end and then going upwards rounding the load plate.
356 (80)	The 1st superficial shear crack widened, however, less than 0.25 mm (0.01 in), on the bell end at the edge of the haunch (near the load).
400 (90)	A visible shear crack, not wider than 0.25 mm (0.01 in), detected on the left wall running through the joint length near the top slab.
400 (90)	The 1st superficial shear crack transformed to the **1st serviceability shear crack** wider than 0.25 mm (0.01 in) on the bell end at the edge of the haunch (near the load).
400 (90)	A superficial shear crack detected at the edge of the haunch (near the load) on the spigot end. It seems that this was an extension of the crack from the bell end.
445 (100)	A **serviceability shear crack** wider than 0.25 mm (0.01 in) detected on the bell end starting from the left edge of the load plate and moving towards the center of the box.

Table A4 – *continued*

445 (100)	A visible shear crack, on the left wall running through the joint length near the top slab, transformed to the **serviceability shear crack** wider than 0.25 mm (0.01 in).
489 (110)	All cracks widened.
498 (112)	Ultimate failure.

Table A5 Test: BL_122-122-122_Y_0.23d (BL_4-4-4_Y_0.23d) (Double Box)
Manufacturer: Hanson Pipe & Products

Load kN (kip)	Event
133 (30)	A superficial flexural crack detected on the bell box at the bell end, under the load on the inside face of the top slab.
200 (45)	A superficial flexural crack detected on the bell box at the bell end, under the load on the inside face of the bottom slab.
200 (45)	The superficial flexural crack on the bell box at the bell end, under the load, on the inside face of the top slab extended further.
289 (65)	The 2nd superficial flexural crack detected on the bell box at the bell end, under the load, on the inside face of the top slab.
289 (65)	The 1st superficial flexural crack on the bell box at the bell end, on the inside face of the top slab extended further.
289 (65)	The 3rd superficial flexural crack detected on the bell box at the bell end, near the haunch, on the inside face of the top slab.
334 (75)	The 1st superficial crack on the bell box on the outside face of the right side wall (near the load) detected.
378 (85)	The 1st superficial flexural crack on the bell box at the bell end, on the inside face of the top slab extended up to the spigot end.
467 (105)	The 1st superficial flexural crack in the bell box at the bell end on the inside face of the top slab transformed to the **1st serviceability flexural**
467 (105)	A crack detected on the bell box at the spigot end on the inside face of the bottom slab.
467 (105)	A crack on the side of the bell box detected and moved towards the outside face of the top slab, moving around the load plate.
556 (125)	The crack, on the bell box at the spigot end on the inside face of the bottom slab, transformed to the **2nd serviceability flexural crack** and
556 (125)	All cracks widened.
601 (135)	Ultimate failure.
Note	The load of the appearance of the cracks at the joint could not be recorded being not accessible.

Table A6 Test: SP_122-122-122_Y_d (SP_4-4-4_Y_d)

Manufacturer: Hanson Pipe & Products

Load kN (kip)	Event
111 (25)	The 1st superficial flexural crack detected on the spigot end on the inside face of the top slab under the load.
111 (25)	The 1st superficial flexural crack detected on the spigot end on the inside face of the bottom slab under the load.
133 (30)	The 1st superficial flexural crack on the spigot end on the inside face of the top slab extended further.
133 (30)	The 1st superficial flexural crack on the spigot end on the inside face of the bottom slab extended further.
156 (35)	The 1st superficial flexural crack on the spigot end on the inside face of the top slab extended further.
156 (35)	The 1st superficial flexural crack on the spigot end on the inside face of the bottom slab extended further.
178 (40)	The 1st superficial flexural crack on the spigot end on the inside face of the top slab extended further.
178 (40)	The 1st superficial flexural crack on the spigot end on the inside face of the bottom slab extended further.
178 (40)	The 2nd superficial flexural crack detected on the spigot end on the inside face of the top slab under the load.
200 (45)	The 2nd superficial flexural crack on the spigot end on the inside face of the top slab extended further.
200 (45)	The 1st superficial flexural crack on the spigot end on the inside face of the bottom slab extended further.
245 (55)	A crack on the outside face of the left wall detected at the spigot end.
289 (65)	A crack on the outside face of the right wall detected at the spigot end.
289 (65)	The 1st superficial flexural crack transformed to the **1st serviceability flexural crack** wider than 0.25 mm (0.01 in) on the bell end on the inside
356 (80)	Another crack on the outside face of the right wall detected at the spigot end.
400 (90)	A layer peeled off right under the load plate.
534 (120)	A shear crack detected on the haunch at the spigot end.
534 (120)	The **shear crack** developed wider than 0.25 mm (0.01 in).
534 (120)	All cracks widened.
578 (130)	Ultimate failure.

Table A7 Test: SP_122-122-244_Y_d (SP_4-4-8_Y_d)

Manufacturer: Rinker Materials

Load kN (kip)	Event
142 (32)	The first superficial crack initiated at the inside face of the top slab under the load plate.
173 (39)	The first non-measurable flexural crack detected on the spigot end and extended towards the mid of the load plate.
178 (40)	The second non-flexural crack detected on spigot end extended towards the left edge of the load plate.
222 (50)	The third flexural crack detected under spigot extended towards the inside face of the top slab under the left edge of load plate.
245 (55)	A flexure crack initiated on spigot end about the right edge of load plate extended vertically toward the middle of the load plate at an angle.
245 (55)	The crack initiated at 173 kN (39 kip) load extended towards the inside face of the top slab towards the lift-hole.
245 (55)	A negative moment flexural crack initiated at right wall about 1/3 rise from top and extended towards the outside face of the top slab.
267 (60)	The flexural crack on right wall initiated at the 245 kN (55 kip) load further extended towards the outside face of the top slab.
267 (60)	The flexural crack initiated on the spigot just to the left of the load plate and extended at an angle towards the load plate.
267 (60)	The first superficial crack seen at the inside face of bottom slab under the load extended about half of the joint length from the edge.
289 (65)	The flexural crack initiated on the spigot about the left of load plate and extended at an angle towards load plate at 267 KN (60 kip) further extended to the left edge of load plate.
289 (65)	A negative superficial flexural crack detected on the left wall.
289 (65)	The negative flexural crack initiated at 245 kN (55 kip) load on right wall extended across the top slab towards the left wall.
311 (70)	The flexural crack occurred at 267 kN (60 kip) load on spigot end on left of load plate widened to a serviceability crack [0.25 mm (0.01 in) wide].
334 (75)	The first shear crack initiated at the right edge of load plate extended towards the right haunch.
356 (80)	The shear crack initiated at 334 KN (75 kip) load became a serviceability crack [0.25 mm (0.01 in) wide].
356 (80)	All instrumentation removed.
578 (130)	Failure load. The failure crack was inclined from the right edge of the load plate to the right wall through the right haunch.

Table A8 Test: BL_122-122-244_Y_d (BL_4-4-8_Y_d)

Manufacturer: Rinker Materials

Load kN (kip)	Event
116 (26)	The first superficial flexural crack initiated at the bell end towards the left edge of the load plate.
133 (30)	The crack initiated at 116 kN (26 kip) extended towards the inside face of the top slab.
146 (33)	A superficial flexural crack detected at the bell end approximately towards middle of the load plate.
177 (40)	The crack initiated at 133 kN (30 kip) extended towards the right lift hole.
200 (45)	A flexural crack initiated at the bell end at the right edge of load plate and extended towards the inside face of the top slab. On the other direction it extended at an angle towards the middle of the load plate.
200 (45)	First negative flexural crack detected at right wall and extended towards the outside face of top slab and towards load plate.
200 (45)	A negative flexural crack detected on the bell end at the left haunch and extended towards the outside face of the top slab.
222 (50)	A negative moment flexural crack initiated at the right wall and extended along the joint length about 2/3 rise from bottom.
222 (50)	The crack initiated at 200 kN (45 kip) on the left haunch widened to be a serviceability crack [0.25 mm (0.01 in) wide].
245 (55)	A superficial flexural crack detected at the intersection of the left haunch and the inside face of the bottom slab.
245 (55)	The crack detected on the right wall approximately 1/3rd of the rise from the top extended towards the lift hole on the outside face of top slab.
245 (55)	The crack detected at 50 kip on the wall widened to become a serviceability crack [0.575 mm (0.023 in) wide].
245 (55)	The crack initiated at the bell end towards the right edge of load plate extended at an angle towards the centre of the load plate.
245 (55)	A crack initiated on the left wall about 1/3 rise from the top and extended towards the outside face of top slab near the load plate.
245 (55)	The crack initiated at 222 kN (50 kip) on the right wall extended towards the top slab.
245 (55)	A superficial flexural crack initiated at the top edge near the left wall and extended across the top slab towards the right wall.
267 (60)	A serviceability crack [0.25 mm (0.01 in) wide] detected from the left edge of load plate in an inclined fashion on bell end.

Table A8 - *continued*

289 (65)	The inclined crack initiated at 222 kN (50 kip) from centre of load plate towards left of the load plate widened to serviceability crack [0.6 mm (0.024 in) wide].
289 (65)	The inclined crack at 200 kN (45 kip) towards the right haunch and widened to become a serviceability crack [0.6 mm (0.024 in) wide].
289 (65)	All instrumentation was removed.
320 (72)	Failure load. The failure crack extended from the left haunch to the tip of the left edge of the load plate, and failed in shear and bond. Also, the top reinforcement of the top slab from the left haunch to center of the load plate failed in bond.

Table A9 Test: SP_244-122-122_N_d (SP_8-4-4_N_d)

Manufacturer: Hanson Pipe & Products

Load kN (kip)	Event
187 (42)	First non-measurable crack detected at the inside face of the top slab, directly under the load place.
214 (48)	The first crack extended to the bell end, this crack was still non-measurable.
222 (50)	Non-measurable crack propagated around the side wall near the load plate.
222 (50)	The crack detected at 187 kN (42 kip) extended to the spigot end.
222 (50)	A crack detected in the inside face of the bottom slab.
231 (52)	A crack detected at the top of the haunch at the far side of the load and extended to the top of the slab and then, to the bell end.
267 (60)	The crack, on the outside face of the wall close to the load plate, extended to the bell end.
289 (65)	A non-measurable crack detected on the outside face of the wall near to the load plate extended to the far joint, the bottom of the haunch.
289 (65)	A crack initiated and extended at the inside face of the bottom slab at the intersection at the bottom tip of the haunch in all the joint length.
289 (65)	A non-measurable crack detected at the inside face of the top slab and extended to the spigot end, 15 cm (6 in) to the left of the edge of the load plate.
311 (70)	A crack detected at 214 kN (48 kip) extended to the bell end side at the tip of the haunch (non-measurable).
334 (75)	A non-measurable superficial shear crack detected at the center of the load place and 45 degree at the spigot end.
334 (75)	A crack, initially detected at the inside face of the top slab, widened to 0.2 mm (0.008 in).
334 (75)	A crack on the outside face of the top slab detected at 231 kN (52 kip) widened to 0.25 mm (0.01 in).
356 (80)	The shear crack detected at 334 kN (75 kip) extended to the tip of the haunch and widened to 0.15 mm (0.006 in).
400 (90)	The shear crack widened to **serviceability crack**.
445 (100)	The shear crack widened to 0.63 mm (0.25 in).
543 (122)	Ultimate failure.

Table A10 Test: SP_244-122-122_Y_d (SP_8-4-4_Y_d)

Manufacturer: Hanson Pipe & Products

Load kN (kip)	Event
160 (36)	The first non-measurable flexural crack detected at the center of the load plate on the spigot end.
169 (38)	The first crack detected at 160 kN (36 kip) extended further to the spigot end.
169 (38)	The first crack detected at 160 kN (36 kip) extended further to the inside face of the top slab towards the lift hole.
222 (50)	The first crack detected at 160 kN (36 kip) widened but was still less than 0.25 mm (0.01 in).
245 (55)	The second flexural crack started from the inside face of the top slab on the left of the load plate and extended to the half joint length.
245 (55)	The third flexural crack started from the inside face of the top slab on the left of the load plate and extended to the half joint length.
245 (55)	The first negative flexural crack in the left side of the top slab (near the wall) detected on the spigot end and extended to the outside face of the top slab.
289 (65)	The fourth flexural crack detected on the inside face of the top slab at the center of the load plate.
289 (65)	The negative moment crack detected at 245 kN (55 kip) extended to the spigot end.
289 (65)	The first flexural crack extended to the full joint length at the inside face of the top slab.
289 (65)	Two flexural cracks detected at the bell end opposite to the load plate in the top slab.
289 (65)	A crack detected at the joint of the bottom slab and the left haunch.
311 (70)	The **first serviceability flexural crack** detected at the negative moment near the left wall on the top slab.
311 (70)	The crack at the left haunch or the bottom slab, detected at 289 kN (65 kip), extended further.
334 (75)	The crack at the left haunch or the bottom slab, detected at 289 kN (65 kip), extended to the full joint length.
334 (75)	A flexural crack detected on the left wall in the half joint length from the spigot end.
356 (80)	The third **flexural crack at the spigot end developed to 0.25 mm (0.01 in).**
356 (80)	The flexural crack in the left wall, detected at 334 kN (75 kip), extended to the full joint length on the bell end.

Table A10 - *continued*

356 (80)	A flexural crack detected at the mid span on the spigot end.
378 (85)	The first shear crack, initiated at the spigot end at the mid of the load plate, extended towards the tip of the haunch (not 0.25 mm (0.01 in) long).
378 (85)	A negative moment crack detected on the top slab on the right side of the load plate.
423(95)	The second shear crack detected at the right of the first shear crack.
445 (100)	The first shear crack became the **serviceability shear crack**.
445 (100)	The laser was removed from the inside of the box.
480 (108)	Ultimate failure (it is holding 267 kN (60 kip) load after failure).

Table A11 Test: BL_244-122-122_N_d (BL_8-4-4_N_d)

Manufacturer: Hanson Pipe & Products

Load kN (kip)	Event
125 (28)	The first non-measurable flexural crack detected at the center of the load plate on the bell.
151 (34)	The first crack detected at 125 kN (28 kip) extended further to the inside face of the top slab.
178 (40)	The first crack detected at 125 kN (28 kip) extended further to the inside face of the top slab, but still remained less than 0.254 mm (0.01 in).
187 (42)	The first crack detected at 125 kN (28 kip) extended further to the inside face of the top slab, measured 0.05 mm (0.002 in).
196 (44)	The second flexural crack detected at the bell end at the edge of the load plate and extended to the center of the inside face of the top slab.
196 (44)	The first crack detected at 125 kN (28 kip) extended further to the inside face of the top slab, measured 0.76 mm (0.003 in).
196 (44)	The first flexural crack detected in the wall 46 cm (18 in) below the top slab.
205 (46)	The first negative flexural crack detected on the right side of the (near) wall, in the top slab.
222 (50)	The first crack detected at 125 kN (28 kip) extended further to the inside face of the top slab, measured 0.15 mm (0.006 in).
222 (50)	A negative flexural crack detected at the far end of the top slab and continued to the outside face of the top slab.
240 (54)	The first crack detected at 125 kN (28 kip) extended further to the inside face of the top slab, measured 0.22 mm (0.009 in).
249 (56)	The negative flexural crack detected at 222 kN (50 kip) at the far end of the top slab extended to the outside face of the top slab and in the full joint length.
249 (56)	A perpendicular crack joins two cracks on the inside face of the top slab.
276 (62)	The third flexural crack detected under the load plate on the inside face of the top slab.
285 (64)	A flexural crack detected on the inside face of the top slab at far end, extended to center of the top slab.
311 (70)	A flexural crack detected at the mid span at the inside face of the top slab extended to the bell end.
311 (70)	A crack detected at the tip of the haunch at the inside face of the top slab.
311 (70)	A flexural crack detected in the wall at the far end in the full joint length.

Table A11 – *continued*

334 (75)	The first non measurable shear crack detected at the bell end at 15.2 cm (6 in) from the tip of the haunch and extended to the mid of the load plate.
334 (75)	A crack extended from the hole 1 to the hole 2 in the top slab.
400 (90)	Ultimate failure in shear.

Table A12 Test: BL_244-122-122_Y_d (BL_8-4-4_Y_d)

Manufacturer: Hanson Pipe & Products

Load kN (kip)	Event
116 (26)	Non-measurable-flexural crack at the inside face of the top slab under the load plate.
133 (30)	The first crack 116 kN (26 kip) extended to the bell-end
160 (36)	The first crack 116 kN (26 kip) extended; still, it is less than 0.25 mm (0.01 in).
187 (42)	The second non-measurable-flexural crack at the inside face of the top slab on the right of the first crack and expanded toward the bell-end under the load plate.
214 (48)	The third non-measurable crack on the outside face of the right wall
214 (48)	The fourth crack on the outside face of the top slab near the load plate
222 (50)	The third 214 kN (48 kip) crack extended toward the bell end
245 (55)	The fifth non-measurable-flexural crack on the left of the first crack at the inside face of the top slab (near load plate) extended towards bell end
245 (55)	The first 116 kN (26 kip) and second 187 kN (42 kip) cracks expanded; still, they are less than 0.01”
245 (55)	The sixth non-measurable crack on outside of top slab
267 (60)	The seventh at inside of bottom slab at edge of slab and haunch
267 (60)	The sixth crack 245 kN (55 kip) extended full length of the outside face of the top slab (left)
267 (60)	The eighth crack on outside face of the top slab close to the load plate and extended down to the inside face of top slab at edge of haunch
267 (60)	The third crack (48 kip) on the outside face of the right side wall extended on full length of the wall
289 (65)	The ninth crack on outside face of left wall extended on full length of the wall, towards spigot end and bell end
289 (65)	The tenth crack at inside of top slab extends to the bell end (non-measurable-flexural)
311 (70)	The sixth crack 245 kN (55 kip) on the outside face of the top slab (left edge) widened to 0.01”
311 (70)	The first shear crack at tip of the haunch (45 degrees) at bell end under load plate
311 (70)	The fourth crack 214 kN (48 kip) on the outside face of top slab extended on the middle of the top slab through the left lift hole toward the second lift hole.

Table A12 - *continued*

334 (75)	The first shear crack 311 kN (70 kip) widens from 0.25 mm (0.01 in) to 0.635 mm (0.25 in).
334 (75)	The eighth 267 kN (60 kip) crack widened to 0.25 mm (0.01 in).
334 (75)	The eleventh crack on the outside face of right wall
351 (79)	Laser removed
391 (88)	Ultimate Failure

Table A13 Test: SP_244-122-122_Y_1.5d (SP_8-4-4_Y_1.5d)

Manufacturer: Hanson Pipe & Products

Load kN (kip)	Event
133 (30)	The first non-measurable flexural crack detected at the center of the load plate on the spigot end.
160 (36)	The first crack detected at133 kN (30 kip) extended further to the inside face of the top slab.
178 (40)	The first crack detected at 133 kN (30 kip) extended further on the inside face of the top slab, but was still less than 0.25 mm (0.01 in).
200 (45)	The first negative flexural crack on the outside face of the right side (near) the wall, near the load, at 406 mm (16 in) down of the top slab.
200 (45)	The first crack detected at 133 kN (30 kip) extended further on the inside face of the top slab, but was still less than 0.25 mm (0.01 in).
222 (50)	The second flexural crack detected at the right edge of the load plate on the spigot.
222 (50)	The first flexural crack detected at 133 kN (30 kip) extended further on the inside face of the top slab, and joined “lift hole”.
222 (50)	The first side wall crack detected at 200 kN (45 kip) extended further towards the spigot end.
245 (55)	A crack detected on the inside face of the bottom slab along the tip of the haunch on the left side (far side).
245 (55)	A negative flexural crack detected on the spigot end on the left of the load (far side) and extended to the outside face of the top slab.
245 (55)	The third flexural crack detected on the spigot end on the left of the load plate.
267 (60)	The fourth flexural crack detected on the top the spigot end.
267 (60)	The second crack detected at 222 kN (50 kip) extended further on the inside face of the top slab, up to the center of the load plate.
267 (60)	The crack in the bottom slab at tip of haunch detected at 245 kN (55 kip) extended to the full joint length.
267 (60)	The side wall crack detected at 200 kN (45 kip) extended towards the haunch.
311 (70)	The second flexural crack detected at 222 kN (50 kip) widened to 0.25 mm (0.01 in) as **the first serviceability crack in flexure.**
334 (75)	The flexural crack in the right wall developed in the full joint length.
334 (75)	The negative flexural crack of 200 kN (45 kip) extended toward the load plate.

Table A13 – *continued*

334 (75)	The crack detected at 222 kN (50 kip) extended toward the center of the load plate.
334 (75)	The negative flexural crack detected at 245 kN (55 kip) extended in the full joint length.
	The second flexural crack detected at 222 kN (50 kip) extended to the outside face of the top slab.
356 (80)	**The first serviceability shear crack developed on the spigot end at the tip of haunch to the right of the load plate.**
356 (80)	The bottom laser was removed.
480 (108)	Ultimate failure in shear flexure and bond.

Table A14 Test: SP_244-122-122_Y_2d (SP_8-4-4_Y_2d)

Manufacturer: Hanson Pipe & Products

Load kN (kip)	Event
107 (24)	The first non-measurable flexural crack detected at the left of the load plate on the spigot end.
133 (30)	An undetectable crack detected at the right wall.
142 (32)	The second flexural crack surface at the right edge of the load plate on the spigot end.
178 (40)	The second crack, on the inside face of the top slab under the load, extended to the bell end and the spigot end.
178 (40)	The second flexural crack detected at 142 kN (32 kip) was now visible but not measurable.
187 (42)	The first negative flexural crack, in the left side of the top slab (near) the wall, detected on the spigot end and extended to the center of the outside face of the top slab.
187 (42)	The first flexural crack detected on the right wall.
196 (44)	The first negative crack detected on the top slab at 187 kN (42 kip) extended to the spigot end.
205 (46)	The second flexural crack detected on the right wall above the crack detected at 187 kN (42 kip).
205 (46)	The first negative moment crack detected on the top slab at 187 kN (42 kip) extended to the full joint length on the bell end.
222 (50)	The negative moment crack detected at 187 kN (42 kip) widened but was still less than 0.25 mm (0.01 in).
222 (50)	A non-measurable crack detected at the intersection of the left haunch and the inside face the bottom slab.
222 (50)	The first left wall flexural crack detected near the spigot end.
222 (50)	The first non measurable inclined crack detected at the right edge of the load plate forming an angle of 60 degree.
245 (55)	The inclined crack detected at 222 kN (50 kip) extended to the bottom of the center of the load plate.
267 (60)	**The left negative moment crack in the top slab detected at 187 kN (42 kip) widened to 0.25 mm (0.01 in).**

Table A14 - *continued*

289 (65)	The first flexural crack in the top slab, detected at 107 kN (24 kip), widened to 0.25 mm (0.01 in).
289 (65)	The right wall cracks, detected at 187 kN (42 kip) and 205 kN (46 kip), extended to the full joint length.
311 (70)	The inclined crack at the spigot end, detected at 222 kN (50 kip), widened to 0.25 mm (0.01 in).
311 (70)	The crack detected at 222 kN (50 kip) at the joint of the left haunch at the bottom slab widened to 0.25 mm (0.01 in).
334 (75)	A non measurable inclined crack detected on the spigot end.
356 (80)	The first 45 degree inclined shear crack detected at the right of the load plate.
356 (80)	The laser was removed from the inside.
356 (80)	A negative moment crack detected on the right of the load plate in the top slab and extended towards the load plate.
400 (90)	The second 45 degree crack detected at the spigot end and extended towards the load plate on the outside face of the top slab.
445 (100)	Ultimate failure in bond and shear.

Table A15 Test: SP_244-122-244_Y_d (SP_8-4-8_Y_d)

Manufacturer: Rinker Materials

Load kN (kip)	Event
89 (20)	First superficial flexural crack detected on the spigot end towards the left edge of the load plate.
98 (22)	First superficial flexural crack detected on the spigot end at the left edge of the load plate extended further towards the load plate.
178 (40)	Second superficial flexural crack detected on the spigot end at the center of load plate extended towards the inside face of top slab.
200 (45)	The crack detected at 178 kN (40 kip) on the spigot end below the center of load plate further extended towards the middle of load plate.
200 (45)	A superficial flexural crack detected on the right wall about 1/3rd rise from top extending along the joint length.
222 (50)	The crack detected at 200 kN (45 kip) on the right wall extended further towards joint length.
267 (60)	The first negative moment flexural crack detected on the tip of right haunch extended towards the outside face of top slab.
267 (60)	A superficial flexural crack detected on the spigot end at the right edge of load plate and extended towards the inside face of the top slab.
267 (60)	The crack detected at 178 kN (40 kip) on the spigot end extended to the inside face of the top slab towards the lift hole.
267 (60)	The crack found at 267 kN (60 kip) on the spigot end extended to the inside face of the top slab towards the lift hole.
311 (70)	A superficial flexural crack detected on the right wall at mid height
334 (75)	A superficial flexural crack detected on spigot end at the left edge of load plate extended towards the inside face of top slab.
334 (75)	A superficial flexural crack detected at spigot end extending towards the inside face of the top slab along the entire joint length.
334 (75)	The crack formed at 311 kN (70 kip) on spigot end at left edge of load plate extended further towards the inside face of top slab and ended into the lift hole.
356 (80)	First negative moment flexural crack detected on the left haunch at spigot end in the top slab.
356 (80)	A superficial flexural crack detected at the right edge of load plate and extended towards tip of right haunch.
356 (80)	A superficial flexural crack detected 10 cm (4 in) left of the left edge of load plate on spigot end and extended towards inside face of top slab.

Table A15 - *continued*

378 (85)	A superficial flexural crack detected on the right wall at 1/3rd rise from top.
378 (85)	A superficial negative flexural crack detected at mid of right haunch and extended towards outside face of top slab.
378 (85)	A superficial negative flexural crack appeared 1/3rd span from left wall of inside face of bottom slab extending along joint length.
378 (85)	The crack detected on the left wall at 1/3rd rise from top extended along joint length.
400 (90)	The crack formed at 356 kN (80 kip) near the left edge of the load plate, extended towards the right edge of load plate.
400 (90)	The crack formed at 378 kN (85 kip) on the left wall at 1/3rd rise from top extended towards the outside face of top slab and curved around the load plate.
400 (90)	The crack formed at 200 kN (45 kip) widened to become a serviceability crack [0.25 mm (0.01 in) wide].
423 (95)	The crack detected at 400 kN (90 kip) on the right edge of load plate widened to become a serviceability crack [0.25mm (0.01 in) wide].
423 (95)	The first shear crack detected on the spigot end starting from right edge of load plate and extended towards the tip of right haunch.
445 (100)	Instrumentation removed.
618 (139)	Failure load. The failure cracks were at the joint of the right haunch and right wall in shear, and under the load plate in top slab in flexure.

Table A16: Test: SP_244-122-244_N_d (SP_8-4-8_N_d)

Manufacturer: Rinker Materials

Load kN (kip)	Event
116 (26)	First superficial flexural crack detected on spigot end at the middle of the load plate
142 (32)	A superficial flexural crack initiated on the spigot end at the left edge of load plate and extended towards the inside face of the top slab and ended
151 (34)	Flexural cracks initiated at the middle on the inside face of the bottom slab and branched along the joint length.
151 (34)	A flexural crack detected on the left half of the inside face of bottom slab and extended in an inclined fashion towards the intersection of left
160 (36)	A flexural crack detected on the right half of the inside face of bottom slab.
160 (36)	A superficial flexural crack detected on the spigot end on the left side of the crack initiated at 142 kN (32 kip).
169 (38)	Crack detected at 116 kN (26 kip) at the middle of load plate on the spigot end extended towards the load plate.
169 (38)	Crack initiated at 151 kN (34 kip) and 160 kN (36 kip) on the inside face of bottom slab extended further along the joint length.
178 (40)	A superficial flexural crack detected on spigot end on right edge of load plate.
178 (40)	The crack detected on middle of inside face of bottom slab at 151 kN (34 kip) widened to become a serviceability crack [0.25 mm (0.01 in) wide].
222 (50)	The crack detected at 116 kN (26 kip) at the middle of load plate on the spigot end branched and extended to the inside face of top slab.
245 (55)	A superficial negative flexural crack initiated on spigot end at the tip of left haunch.
245 (55)	The crack detected at 178 kN (40 kip) extended further towards the middle of the load plate.
245 (55)	First invisible negative moment flexural crack detected on the right wall at 1/3rd rise from the top.
245 (55)	A superficial flexural crack detected 15 cm (6 in) left from the left edge of load plate and extended towards the inside face of top slab.
289 (65)	A flexural crack detected on the lower spigot face and extended to the spigot top going towards the middle of load plate.
289 (65)	An invisible flexural crack detected on left wall at 1/3rd rise from the top.
311 (70)	A negative moment flexural crack detected on upper spigot face at the location of the right haunch.

Table A16 - *continued*

311 (70)	The crack detected at 289 kN (65 kip) on the lower spigot face extended all the way towards the middle of load plate.
311 (70)	The crack formed at 245 kN (55 kip) on the right wall at 1/3rd rise from the top extended towards mid height of right wall.
334 (75)	A superficial flexural crack detected on lower spigot face at the left edge of load plate.
334 (75)	The crack formed at 290 kN (65 kip) on lower spigot face widened to become a serviceability crack [0.25 mm (0.01 in) wide].
334 (75)	The crack formed at 290 kN (55 kip) on tip of left haunch on upper spigot face extended to the outside face of top slab.
356 (80)	The second negative moment flexural crack detected on the right wall above the crack formed at 245 kN (55 kip) and extended towards the outside face of top slab.
356 (80)	The crack formed at 245 kN (55 kip) on the tip of left haunch widened to become a 0.25 mm (0.01 in) thick crack.
400 (90)	First shear crack detected at 15 cm (6 in) left from the left edge of load plate in an inclined fashion towards the load plate.
423 (95)	Crack detected on the lower spigot face and extended towards inside face of top slab.
423 (95)	The crack formed at 289 kN (65 kip) on the lower spigot face widened to become a serviceability crack [0.25 mm (0.01 in) wide].
423 (95)	The negative moment flexural crack formed on the right wall at 356 kN (80 kip) extended towards the right haunch.
445 (100)	Instrumentation removed.
592 (133)	Failure load. Failure crack was at the joint of right haunch and right wall including right wall. The flexural failure crack formed under the load plate.

Table A17: Test: BL_244-122-244-Y_d (BL_8-4-8_Y_d)

Manufacturer: Rinker Materials

Load kN (kip)	Event
89 (20)	A superficial flexural cracks detected on the inside face of bottom slab near the right haunch and extended along joint length.
107 (24)	Crack formed at 89 kN (20 kip) on the inside face of bottom slab extended further towards the bell end.
151 (34)	A superficial flexural crack detected on the bottom face of bell end at right edge of load plate.
151 (34)	A superficial flexural crack detected on the bottom face of bell end and extended towards the top face of bell end at middle of the load plate.
169 (38)	The crack detected at 151 kN (34 kip) on the bottom face of bell end extended to the inside face of top slab.
200 (45)	The crack formed at 89 kN (20 kip) on the inside face of bottom slab branched along the joint length and widened to become a serviceability crack [0.25 mm (0.01 in) wide].
200 (45)	The crack formed at 151 kN (34 kip) on the left edge of load plate extended towards the inside face of top slab.
222 (50)	The first negative moment flexural crack detected at the middle of right haunch on the load plate and curved around the load plate towards the outside face of top slab.
245 (55)	The crack formed at 151 KN (55 kip) on the bell end extended towards the centre of the load plate and further towards the right haunch on the inside face of top slab.
245 (55)	A superficial flexural crack detected on the right wall about 1/3rd rise from the top and extended towards the outside face of top slab curving around the load plate.
267 (60)	The crack formed at center of load plate at 151 kN (34 kip) widened to become a serviceability crack [0.25 mm (0.01 in) wide].
267 (60)	A flexural crack detected on the right wall at 1/3rd rise from bottom.
267 (60)	A flexural crack initiated on the top face of bell end and extended towards the outside face of top slab and curving around the load plate.
298 (67)	A flexural crack detected with a cracking sound at the tip of right haunch on the top face of bell end.
298 (67)	The first shear crack formed at the tip of right haunch and extending towards the right edge of load plate
298 (67)	The crack formed at 151 kN (34 kip) at the center of load plate became a serviceability flexural crack.

Table A17 - *continued*

298 (67)	Instrumentation removed
334 (75)	Serviceability shear.
378 (85)	Failure Load. The failure took place on the left side of the load plate as a shear crack and extended towards mid span as bond failure.

Table A18 Test: BL_244-122-244_N_d (BL_8-4-8_N_d)

Manufacturer: Rinker Materials

Load kN (kip)	Event
116 (26)	First superficial flexural crack detected on the bell end at the middle of the load plate.
116 (26)	A superficial flexural crack detected on the inside face of the bottom slab under the loading and branched along the joint length.
133 (30)	The crack detected on the inside face of bottom slab under the loading at 116 kN (26 kip) extended further along the joint length.
142 (32)	The crack formed at 116 kN (26 kip) on the bell end extended further towards the inside face of top slab.
151 (34)	A superficial flexural crack detected at 15 cm (6 in) toward the left to the crack formed at 116 kN (26 kip) on the inside face of the bottom slab.
160 (36)	A superficial flexural crack detected on the lower face of bell end at the left edge of load plate and extended towards the inside face of top slab.
200 (45)	A flexural crack detected on the top face of bell end at the tip of right haunch and extended towards outside face of top slab.
200 (45)	The crack detected at 160 kN (36 kip) on the bottom face of bell end extended towards left edge of load plate.
222 (50)	An invisible flexural crack detected on the bottom face of bell end and extended towards the inside face of bottom slab.
245 (55)	A diagonal crack initiated at the center of box under the load and extended towards the inside face of bottom slab.
267 (60)	A superficial flexural crack detected on the right haunch and extended towards the outside face of top slab and curved around the load plate.
289 (65)	The first serviceability flexural crack found on the middle of the load plate on the upper face of bell end.
289 (65)	A superficial flexural crack detected on the right wall extending towards the outside face of top slab at about 1/3rd rise from the top.
311 (70)	The first shear crack detected on bell end joining the right edge of load plate and the tip of right haunch.
311 (70)	The crack detected at 116 kN (26 kip) at the middle of load plate on the bell end widened to become a serviceability crack [0.25 mm (0.01 in) wide].
311 (70)	Second shear crack detected on the upper face of bell end and at the tip of left haunch.
311 (70)	On the outer face of the top slab, flexural cracks curved around the load plate.

Table A18 - *continued*

334 (75)	All cracks on the bell end widened.
334 (75)	First shear crack detected at 311 kN (70 kip) widened to become a serviceability crack [0.25 mm (0.01 in) wide].
334 (75)	A superficial negative moment flexural crack detected on the top face of bell end on the left haunch.
356 (80)	All instrumentation removed.
387 (87)	Shear failure of the specimen joining the right edge of the load plate and the tip of the right haunch. Another pair of diagonal shear cracks detected at mid span on the bell end.

Table A19 Test: SP_366-122-122_Y_d (SP_12-4-4_Y_d)

Manufacturer: Hanson Pipe & Products

Load kN (kip)	Event
178 (40)	The first flexural crack detected on the inside face of the top slab under the load plate and extended towards the spigot end.
178 (40)	The flexural crack detected on the left wall at 2/3rd rise and extended towards the spigot end.
222 (50)	Second superficial flexural crack detected on the left wall at 1/3rd rise and extended towards the spigot end.
245 (55)	A superficial flexural crack seen directly under the load plate on the inside face of the top slab.
245 (55)	A superficial flexural crack detected on the inside face of the top slab near the left edge of the load plate.
289 (65)	The first flexural crack seen on the right wall at 2/3rd rise and extended towards the spigot end.
289 (65)	The flexural crack initiated at 245 kN (55 kip) directly on the inside face of top slab under the load plate extended further and merged into the lift hole.
334 (75)	A flexural crack initiated at an angle under the left side of load plate on the spigot end.
334 (75)	The flexural crack initiated at 245 kN (55 kip) under the left side of load plate extended further towards the spigot end.
334 (75)	The flexural crack detected on the left edge of the load plate and extended towards the spigot end and than on the inside face of the top slab.
356 (80)	The crack detected at 334 kN (75 kip) on the left edge of the load plate extended further towards the right edge of the load plate.
400 (90)	A flexural crack initiated at the Bell end and extended towards the lift hole on the outside face of the top slab.
423 (95)	First distinct crack seen on the inside face of bottom slab at left haunch.
445 (100)	First serviceability flexural crack measuring 0.25 mm (0.01 in) detected on the outside face of right wall.
445 (100)	First negative moment crack detected on the top left haunch wall on the outside face of the top slab.
534 (120)	All Instrumentation removed.
623 (140)	Several non-serviceability shear cracks on right edge of load on the spigot end detected.

Table A20 Test: SP_366-122-122_N_d (SP_12-4-4_N_d)

Manufacturer: Hanson Pipe & Products

Load kN (kip)	Event
0 (0)	Pre existing crack on the inside face of bottom slab along the joint length.
0 (0)	Pre-existing crack on the right wall along joint length at distance 1/3rd rise on the outside face of right wall.
0 (0)	Pre-existing crack at the bell end about 2/3rd of span from loaded edge.
111 (25)	The first flexural crack detected on the inside face of the top slab at 2/3rd of span from right wall on the spigot end.
178 (40)	The first superficial flexural crack detected on the spigot end at the middle of the load plate.
200 (45)	The flexural crack at spigot end that detected at 178kN (40kip) extended to the inside face of top slab and upwards towards the load plate.
200 (45)	The flexural crack that detected at 111kN (25 kip), extended towards the spigot end.
222 (50)	The pre-existing crack on the outside face of the right wall detected extended towards the bell end.
267 (60)	A superficial crack initiated on the inside face of bottom slab along the haunch along the joint length.
267 (60)	The first negative flexural crack initiated on the spigot end on left haunch and extended on outside face of the top slab.
289 (65)	Second non-measurable flexural crack initiated on spigot end just at the left of the load plate.
311 (70)	The negative flexural crack initiated at 267kN (60 kip) on the left spigot end extended to the outside face of top slab and extended at bell end.
311 (70)	Five superficial flexural cracks detected on right wall.
334 (75)	There were no serviceability cracks [0.25mm (0.01 in) wide cracks up to 334 kN (75 kip)].
378 (85)	An inclined superficial crack detected on spigot end under the load plate.
378 (85)	A Negative flexural crack on right haunch detected and moved to the outside face of the top slab.
400 (90)	The flexural crack seen at 178 kN (40 kip) on right wall widened to a serviceability crack [0.25 mm (0.01 in) wide].

Table A20 - *continued*

445 (100)	The first shear flexural crack initiated on the spigot on the right side of the load plate and extended towards center of load plate.
467 (105)	The flexural crack seen at 289 kN (65 kip) extended towards the inside face of the top slab.
467 (105)	A flexural crack detected on the spigot end.
467 (105)	All instrumentation removed.
645 (145)	A shear crack detected at the tip of the haunch toward the center of the load plate.

Table A21 Test: BL_366-122-122_Y_d (BL_12-4-4_Y_d)

Manufacturer: Hanson Pipe & Products

Load kN (kip)	Event
107 (24)	The first non-measurable superficial flexural crack initiated at the bell end at the middle of load plate. There was a pre-existing damage at the end of crack.
125 (28)	The crack formed at 107 kN (24 kip) extended towards the center of load plate.
133 (30)	The crack formed at 107 kN and 125 kN (24 kip and 28 kip) extended towards the inside face of the top slab.
142 (32)	The crack formed at 107 kN (24 kip) became visible.
169 (38)	The first visible negative moment crack was initiated on the right wall about 1/3rd rise from the top slab.
169 (38)	The first invisible crack occurred at the spigot end to the left of load plate.
222 (50)	The second flexural crack occurred on the bell end to the left of load plate.
222 (50)	The crack formed at 107 kN (24 kip) extended to the inside face of the top slab.
222 (50)	The second negative moment flexural crack occurred on the right wall above the negative moment crack occurred at 169 kN (38 kip). This crack extended to the right wall toward the bell end.
222 (50)	The crack detected on 222 kN (50 kip) on the right wall extended on the spigot end.
222 (50)	The flexural crack formed at 169 kN (38 kip) on the spigot end extended towards the inside face of the top slab.
245 (55)	The first negative moment crack appeared on the left wall about 1/3rd rise from the top.
245 (55)	The first flexural crack formed on the bell end of the left haunch. This crack was extended toward the outside face of the top slab.
245 (55)	The flexural crack that detected at 222 kN (50 kip) extended towards the inside face of the bell end.
245 (55)	The flexural crack that detected at 107 kN (24 kip) extended to the inside face on the top slab and extended to the left wall.
245 (55)	The third negative moment flexural crack occurred at the mid height on the right wall extending the entire joint length.

Table A21 - *continued*

267 (60)	A flexural crack formed at the bell end at the middle of the haunch region and extended to the outside face of the top slab along the joint length.
267 (60)	The fourth negative moment flexural crack was formed on the right wall.
267 (60)	A non-measurable crack occurred at the inside face of bottom slab on left wall.
267 (60)	Another flexural crack detected on the bell end about 1 feet to the left of load plate.
267 (60)	The first negative moment crack on the right wall extended toward the joint length to the spigot end.
267 (60)	The crack that detected at 222 kN (50 kip) extended across the left wall.
289 (65)	A superficial flexural crack initiated on spigot end and extended towards the inside face of the top slab.
289 (65)	Crack formed at 267 kN (60 kip) extended across the joint of inside face of bottom slab and the left haunch.
311 (70)	The flexural crack that detected at 267 kN (60 kip) extended vertically towards haunch.
311 (70)	The initial flexural crack that detected at 107 kN (24 kip) widened to become a serviceability crack [0.25mm (0.01 in) wide].
311 (70)	The first visible shear crack occurred at tip of haunch moving towards the center of load plate.
356 (80)	Most of the flexural cracks widened to become serviceability cracks [0.25mm (0.01 in) wide].
378 (85)	First negative moment flexural crack formed at bell end at tip of haunch.
378 (85)	The crack formed at 267 kN (60 kip) extended at outside face of top slab and widened to become a serviceability crack [0.25mm (0.01 in) wide] and moved around the load plate.
378 (85)	The crack formed at 245 kN (55 kip) on tip of left haunch widened to become a serviceability crack [0.05mm (0.02 in) wide].
378 (85)	The crack formed at the front of the inside face of bottom slab and haunch widened to become a serviceability crack [0.25mm (0.01in) wide].

Table A21 - *continued*

400 (90)	A flexural crack occurred parallel to the crack seen at 267 kN (60 kip) at the intersection of inside face of bottom slab and the left haunch.
400 (90)	All instrumentation removed.
467 (105)	Shear crack formed below the load plate.
498 (112)	Failure load

Table A22 Test: BL_366-122-122_N_d (BL_12-4-4_N_d)

Manufacturer: Hanson Pipe & Products

Load kN (kip)	Event
98 (22)	The first superficial flexural crack detected on bell end at middle of load plate and extended towards inside face of top slab.
133 (30)	The crack which detected at 98 kN (22 kip) extended towards the middle of the load plate on the bell end.
151 (34)	An invisible flexural crack occurred on the bell end at 15 cm (6 in) to the left of load plate and extended towards the inside face of the top slab.
169 (38)	The crack formed at 98 kN (22 kip) extended towards inside face of the top slab.
178 (40)	The crack formed at 98kN (22 kip) became visible.
178 (40)	The crack formed at 169 kN (34 kip) extended towards the inside face of the top slab.
178 (40)	A flexural crack detected on the top edge of right wall.
178 (40)	An invisible flexural crack detected at midspan of the inside face of bottom slab.
200 (45)	The second flexural crack formed on bell end at right side of the load plate.
200 (45)	An invisible flexural crack detected at the top edge of left wall.
200 (45)	The first invisible negative moment flexural crack detected on right wall at 1/3rd of the height from the top.
222 (50)	A flexural invisible crack detected on inside face of bottom slab at mid-span.
222 (50)	The first negative moment flexural crack occurred on outside face of the top slab on the bell end at right haunch
245 (55)	The second negative moment flexural crack formed on right wall and extended along the joint length.
245 (55)	An invisible flexural crack detected at the intersection of the inside face of bottom slab and the left haunch.
245 (55)	A negative moment flexural crack formed on bell end at tip of left haunch and extended to the outside face of top slab across the joint length and ended on spigot end.
245 (55)	The crack formed on the right wall at 222 kN (50 kip) at mid-height became a serviceability crack [0.25mm (0.01 in) wide].

Table A22 – *continued*

245 (55)	A flexural crack detected on bell end on right edge of the load plate.
245 (55)	The crack detected at 200 kN (45 kip) extended towards inside face of top slab and ended in the lift hole.
267 (60)	The first 98 kN (22 kip) flexural crack extended on bell end towards middle of load plate.
267 (60)	A negative moment flexural crack occurred on bell end at the edge of the right haunch.
289 (65)	A flexural crack detected on bell end at the left edge of load plate and extended towards the inside face of top slab.
289 (65)	The negative moment flexural crack detected at 222 kN (50 kip) extended towards the right edge of right haunch.
289 (65)	A flexural crack occurred on the left wall at 1/3rd rise from top across the left wall.
311 (70)	The flexural crack on the top of haunch widened to become a serviceability crack [0.25mm (0.01 in) wide].
334 (75)	The crack which detected at 245 kN (55 kip) widened to become a serviceability crack [0.25mm (0.01 in) wide].
334 (75)	The crack formed at 290 kN (65 kip) at left edge of load plate extended towards inside face of top slab along the joint length.
334 (75)	The first shear crack formed at the tip of the right haunch.
334 (75)	The crack formed at 290 kN (65 kip) at joint of left haunch and inside of bottom slab widened to become a serviceability crack [0.25mm (0.01 in) wide] and it also extended towards the bell end and the spigot end.
334 (75)	Bond failure occurred both on the bell end and on the right wall.
400 (90)	All negative moment flexural cracks widened to become more than 0.25mm (0.01 in) thick cracks
400 (90)	A flexural crack detected on bell end towards left to the mid span.
400 (90)	All instrumentation removed.
489 (110)	Numerous shear cracks appeared
525 (118)	Failure Load

Table A23 Test: SP_91-61-145_Y_0 (SP_3-2-4.75_Y_0)

Manufacturer: Rinker Materials

Load kN (kip)	Event
151 (34)	An invisible flexural crack formed on spigot end approximately at the middle of the load plate.
169 (38)	The second invisible flexural crack formed on the spigot end at the middle of the load plate.
178 (40)	The crack formed at 151 kN (34 kip) extended towards inside face of the top slab.
245 (55)	The crack detected at 169 kN (38 kip) extended more towards the load plate.
267 (60)	The second invisible flexural crack formed on spigot end at left edge of the load plate.
267 (60)	A superficial flexural crack detected on the inside face of top slab starting from spigot end and extending towards the lift hole.
289 (65)	The third flexural crack formed on spigot end extending towards right edge of the load plate.
311 (70)	A negative moment flexural crack detected on right wall at mid-height and extended towards mid length of the joint length.
311 (70)	The second negative moment flexural crack detected at the intersection of right haunch and inside face of the bottom slab.
334 (75)	A flexural crack detected on the left wall at mid height.
334 (75)	The crack formed at 267 kN (60 kip) on left edge of load plate and extended further towards load plate on spigot end.
334 (75)	The negative moment flexural crack formed on right wall extended towards joint length.
356 (80)	A flexural crack formed on spigot end which was inclined towards the left edge of the load plate.
356 (80)	The crack formed at 334 kN (75 kip) on left wall extended along entire joint length.
356 (80)	Superficial flexural crack detected at the joint of left haunch and inside face of bottom slab.
378 (85)	There were no serviceability cracks [0.25mm (0.01 in) wide].
378 (85)	No crack found on outside face of top slab at this load.

Table A23 **- *continued***

445 (100)	Negative flexural crack on the right wall widened to become a serviceability crack [0.25mm (0.01 in) wide].
445 (100)	A superficial flexural crack detected on the middle of bell end and extended towards the inside face of top slab.
467 (105)	A flexural crack formed at the tip of the haunch going up straight towards the load plate.
489 (110)	A flexural crack formed on spigot end on tip of haunch and extended towards the outside face of top slab.
489 (110)	All instrumentation removed.
663 (149)	Specimen didn't fail at this load.

Table A24 Table: SP_91-61-145_Y_0.83d (SP_3-2-4.75_Y_083d)

Manufacturer: Rinker Materials

Load kN (Kip)	Event
245 (55)	First superficial flexural crack detected on right wall at mid height.
289 (65)	A superficial flexural crack detected at the intersection of left haunch and the inside face of the bottom slab.
289 (65)	A superficial flexural crack detected on the inside face of top slab starting near the middle of the load plate and extending along the entire joint length.
334 (75)	First Negative moment flexural crack detected at mid height on the left wall.
378 (85)	Crack formed on the right wall at 245 kN (55 kip) extended along the joint length.
378 (85)	Instrumentation removed
658 (148)	Specimen didn't fail at this load.

APPENDIX B

EXPERIMENTAL PHOTOGRAPHS

(a)

(b)

(c)

(d)

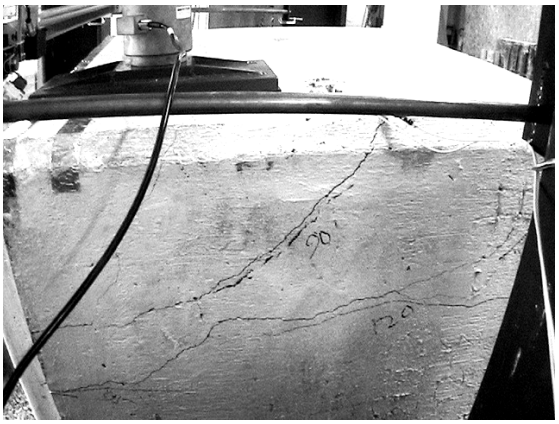

(e)

(f)

Figure B1 Experimental Photograph for SP_122-122-122_Y_0 (SP_4-4-4_Y_0) (with bedding): (a) Spigot End; (b) Bell End; (c) Inside Face of Bottom Slab; (d) Inside Face of Top Slab; (e) Outside Face of Right Wall; and (f) Outside Face of Left Wall.

(a)

(b)

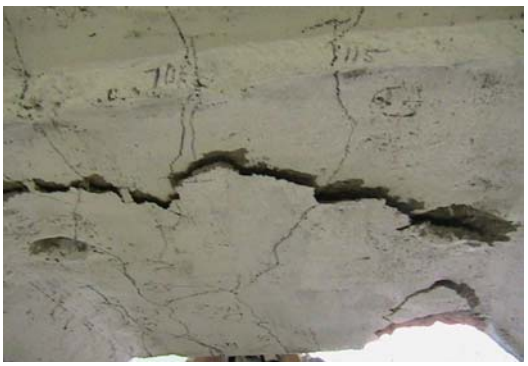

(c)

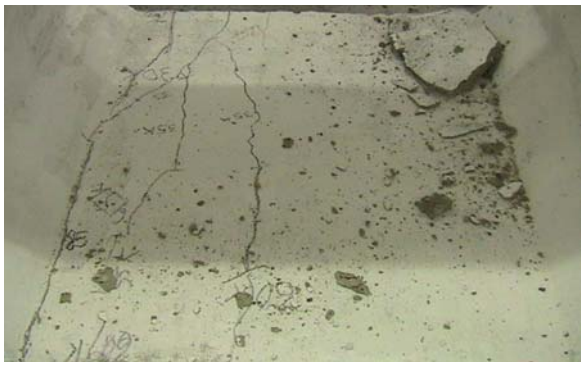

(d)

(e)

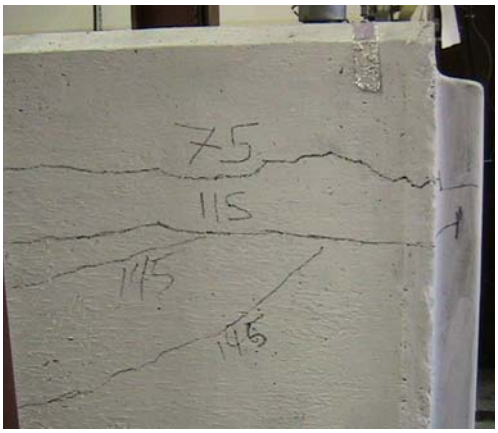

(f)

Figure B2 Experimental Photograph for SP_122-122-122_Y_0 (SP_4-4-4_Y_0): (a) Spigot end; (b) Spigot end in Close-up; (c) Inside Face of Top Slab; (d) Inside Face of Bottom Slab; (e) Outside Face of Right Wall; and (f) Outside Face of Left Wall

(a)

(b)

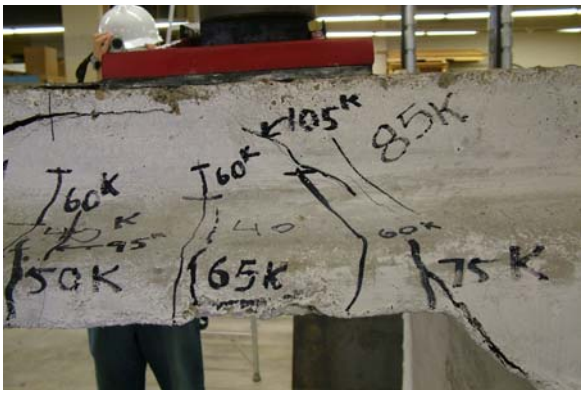

(c)

(d)

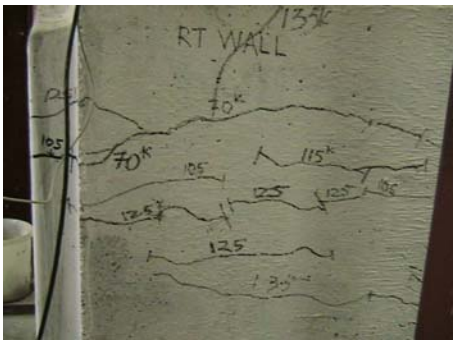

(e)

(f)

Figure B3 Experimental Photograph for Test: SP_122-122-122_Y_0.23d (SP_4-4-4_Y_0.23d) (a) Spigot End; (b) Inside Face of Bottom Slab; (c) Spigot End in Close up; (d) Spigot End; (e) Outside Face of Right Wall; and (f) Inside Face of Bottom Slab

(a)

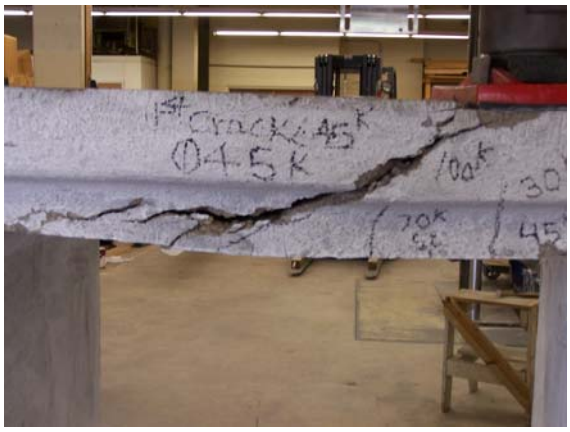

(b)

(c)

Figure B4 Experimental Photograph for Test: BL_122-122-122_Y_0.23d (BL_4-4-4_Y_0.23d) (a) Test Set-up; (b) Ultimate Failure; and (c) Inside Face of Top Slab

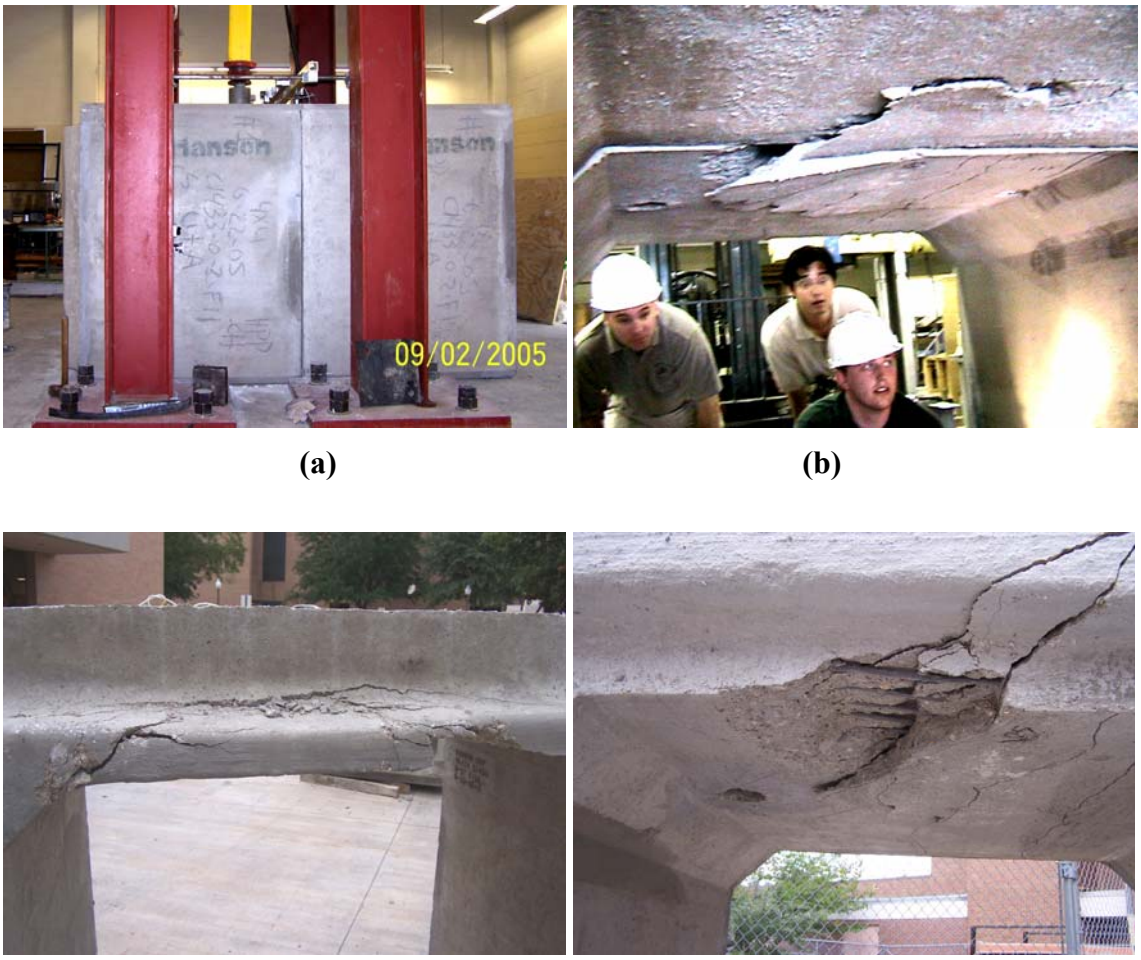

(a) **(b)**

(c) **(d)**

Figure B5 Experimental Photograph for Test: BL_122-122-122_Y_0.23d (BL_4-4-4_Y_0.23d) (Double Box) (a) Test Set up; (b) Failure (Double Box); (c) Failure (Spigot Box); and (d) Failure Bell Box

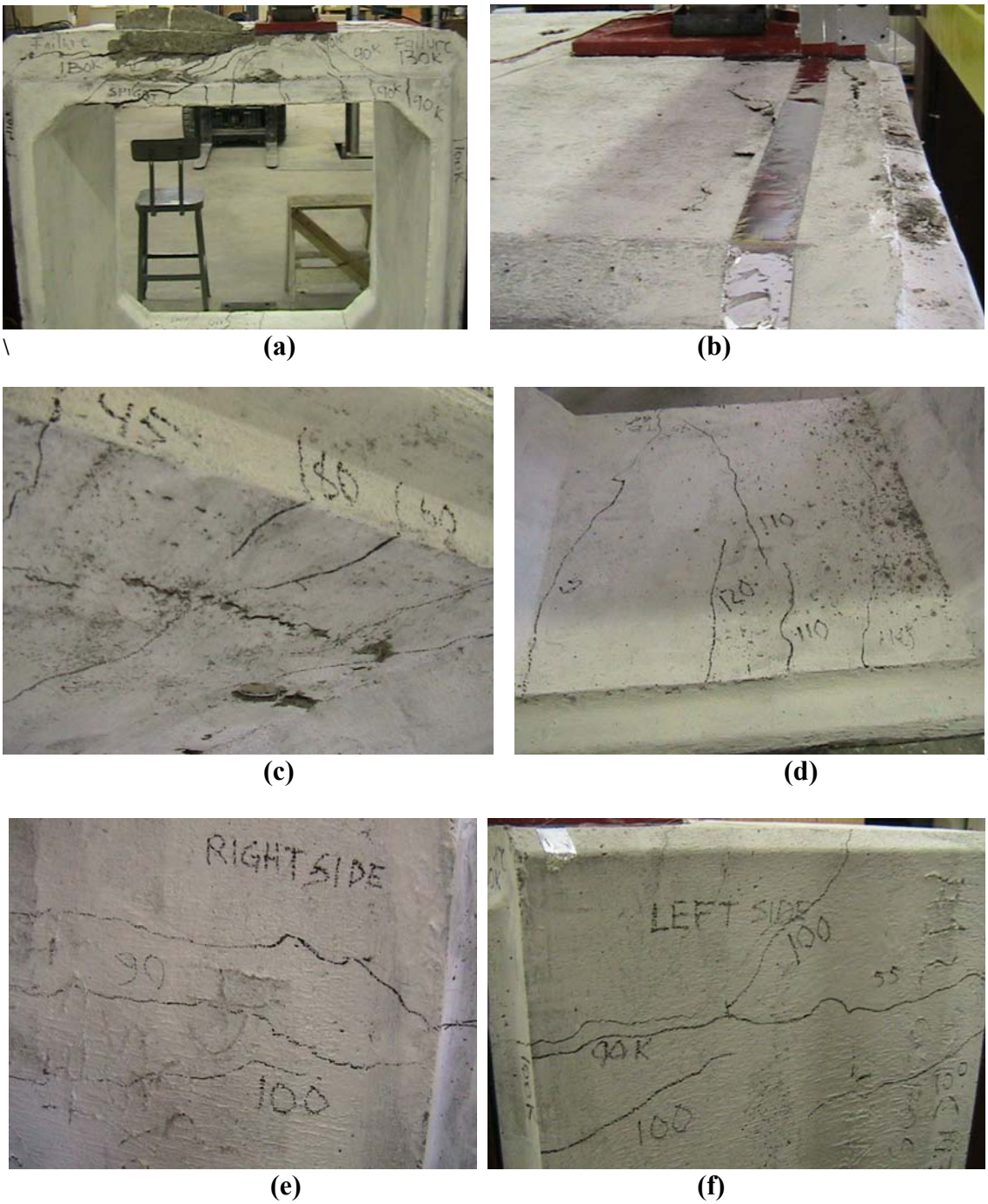

\ **(a)** **(b)**

(c) **(d)**

(e) **(f)**

Figure B6 Experimental Photograph for Test: SP_122-122-122_Y_d (SP_4-4-4_Y_d) (a) Spigot End ((b) Outside Faced of Top Slab; (c) Inside Face of Top Slab; (d) Inside Face of Bottom Slab; (e) Outside face of Right Wall; and (f) Outside face of Left Wall

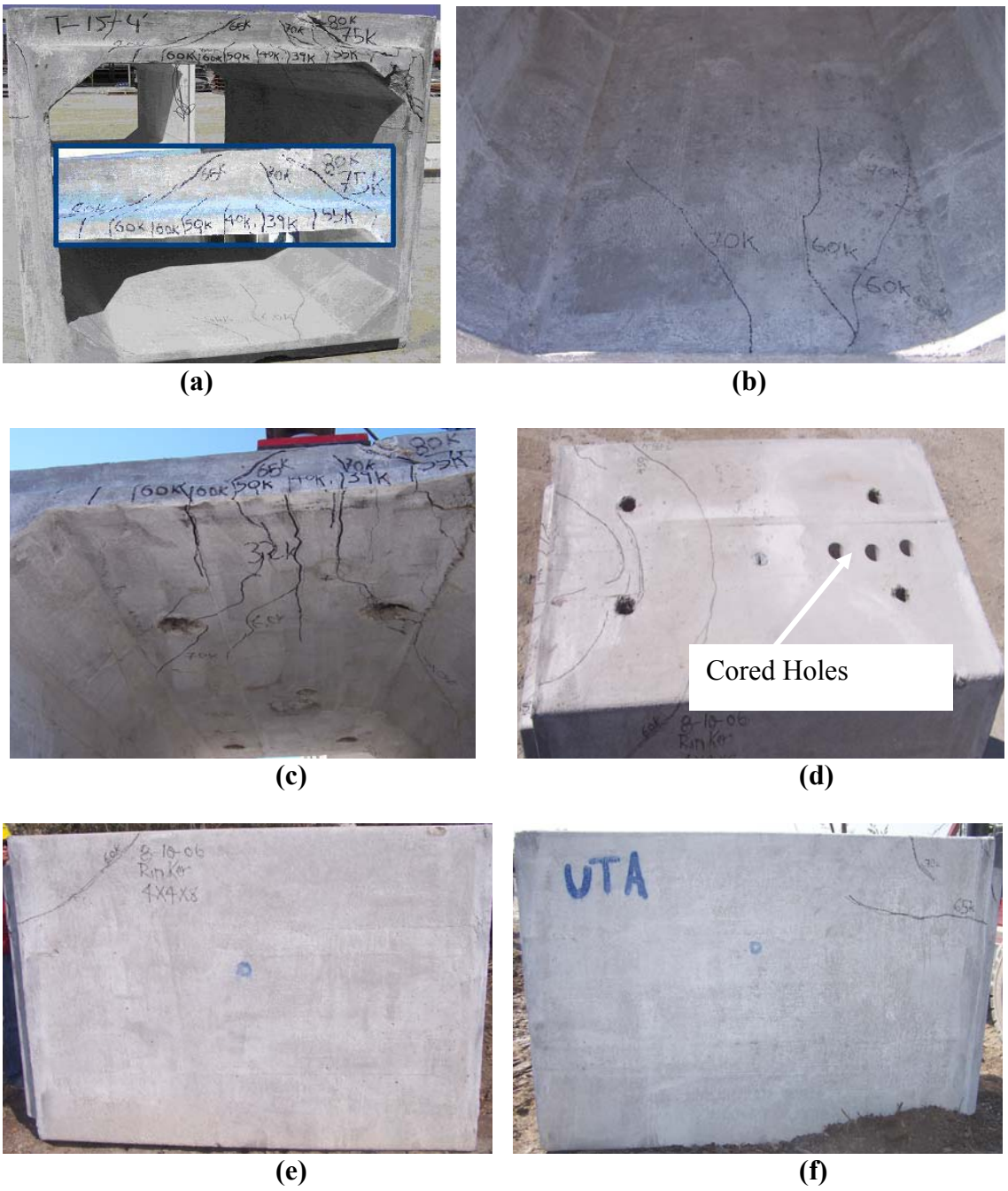

(a) (b) (c) (d) (e) (f)

Figure B7 Experimental Photograph for Test: SP_122-122-244_Y_d (SP-4-4-8_Y_d) (a) Spigot End; (b) Inside Face of Bottom Slab; (c) Inside Face of Top Slab; (d) Outside Face of Top Slab (e) Outside Face of Right Wall; and (f) Outside Face of Left Wall

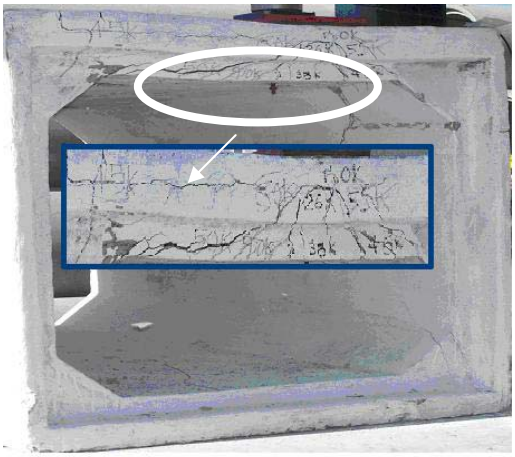

(a)

(b)

(c)

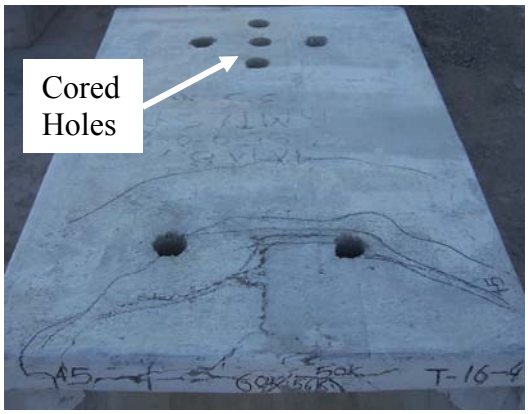

(d) b

(e)

(f) l

Figure B8 Experimental Photograph for Test: BL_122-122-244_Y_d. (BL-4-4-8_Y_d) (a) Bell End; (b) Inside Face of Bottom Slab; (c) Inside Face of Top Slab; (d) Outside Face of Top Slab; (e) Outside Face of Right Wall; and (f) Outside Face of Left Wall

(a)

(b)

(c)

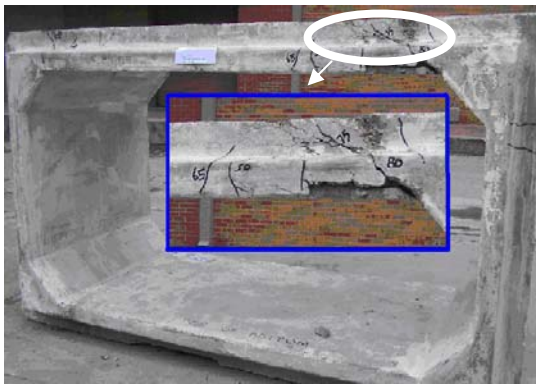

(d)

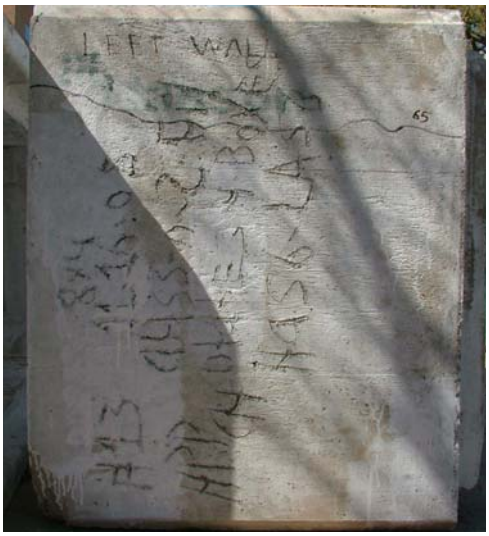

(e)

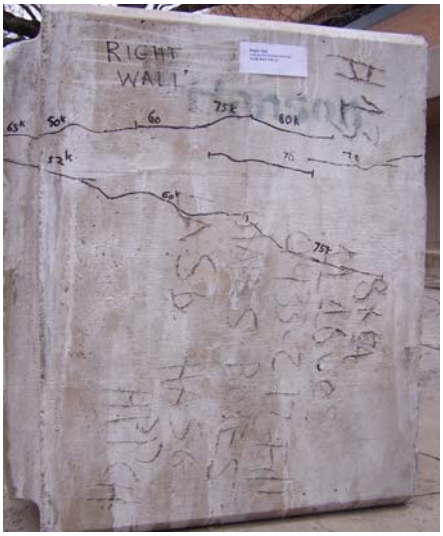

(f)

Figure B9 Experimental Photograph for Test: SP_244-122-122_N_d (SP-8-4-4_N_d) (a) Outside Face of Top Slab; (b) Inside Face of Top Slab; (c) Inside Face of Bottom Slab; (d) Spigot End; (e) Outside Face of Left Wall; and (f) Outside Face of Right Wall

(a)

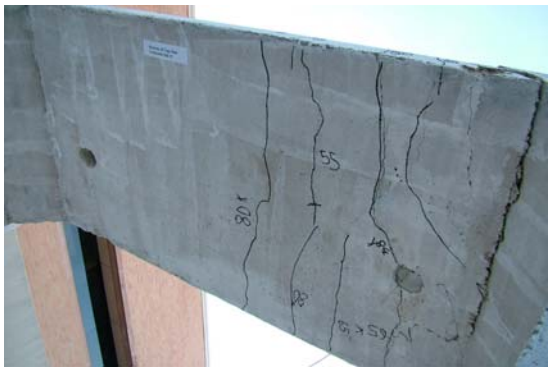

(b)

(c)

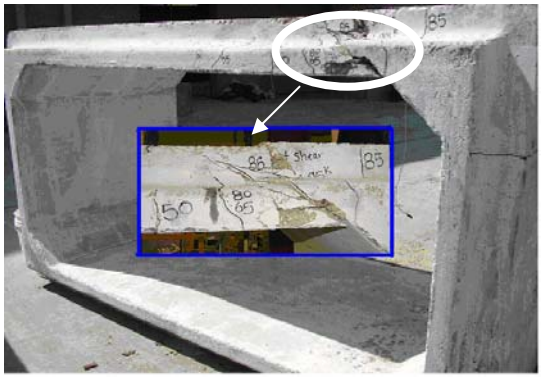

(d)

(e)

(f) l

Figure B10 Experimental Photograph for: Test: SP_244-122-122_Y_d (SP-8-4-4_Y_d) (a) Outside Face of Top Slab; (b) Inside Face of Top Slab; (c) Inside Face of Bottom Slab; (d) Spigot End; (e) Outside Face of Left Wall; and (f) Outside Face of Right Wall

(a)

(b)

(c)

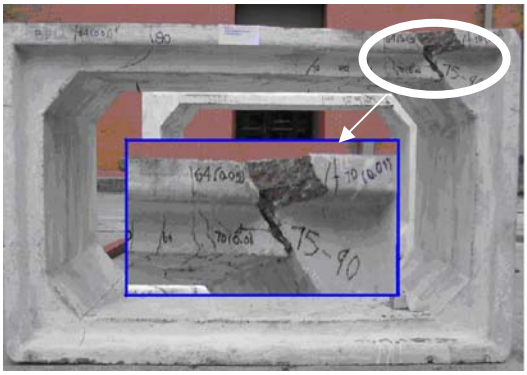

(d)

(e)

(f)

Figure B11 Experimental Photograph for Test: BL_244-122-122_N_d (BL-8-4-4_N_d) (a) Outside Face of Top Slab; (b) Inside Face of Top Slab; (c) Inside Face of Bottom Slab; (d) Bell End; (e) Outside Face of Left Wall; and (f) Outside Face of Right Wall

(a)

(b)

(c)

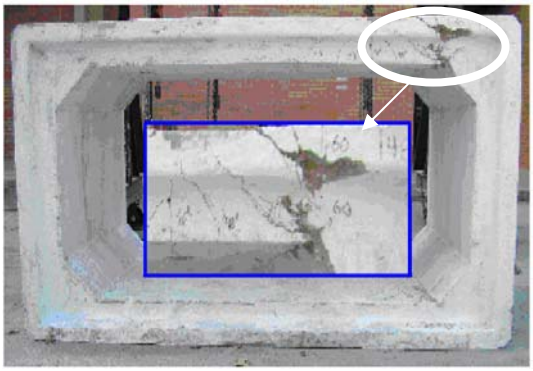

(d)

(e)

(f)

Figure B12 Experimental Photograph for Test: BL_244-122-122_Y_d (BL-8-4-4_Y_d) (a) Outside Face of Top Slab; (b) Inside Face of Top Slab; (c) Inside Face of Bottom Slab; (d) Bell End; (e) Outside Face of Left Wall; and (f) Outside Face of Right Wall

(a)

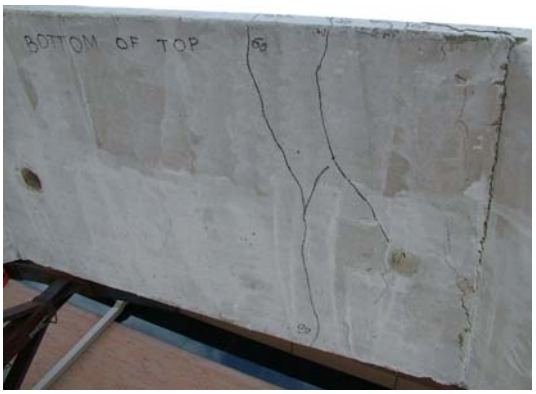

(b)

(c)

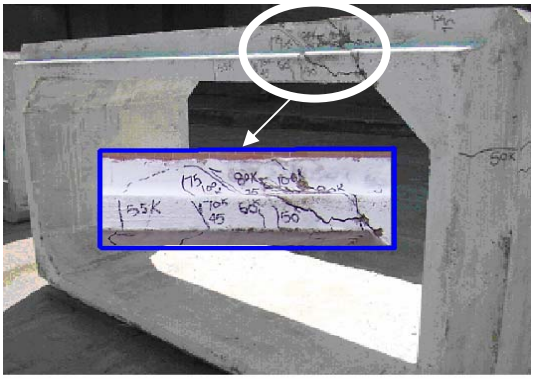

(d)

(e)

(f)

Figure B13 Experimental Photograph for Test: SP_244-122-122_Y_1.5d(SP-8-4-4_Y_1.5d) (a) Outside Face of Top Slab; (b) Inside Face of Top Slab; (c) Inside Face of Bottom Slab; (d) Spigot End; (e) Outside Face of Left Wall; and (f) Outside Face of Right Wall

(a)

(b)

(c)

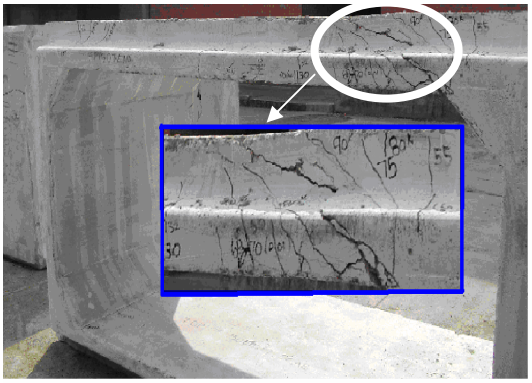

(d)

(e)

(f) l

Figure B14 Experimental Photograph for Test: SP_244-122-122_Y_2d (SP-8-4-4_Y_2d) (a) Outside Face of Top Slab; (b) Inside Face of Top Slab; (c) Inside Face of Bottom Slab; (d) Spigot End; (e) Outside Face of Left Wall; and (f) Outside Face of Right Wall

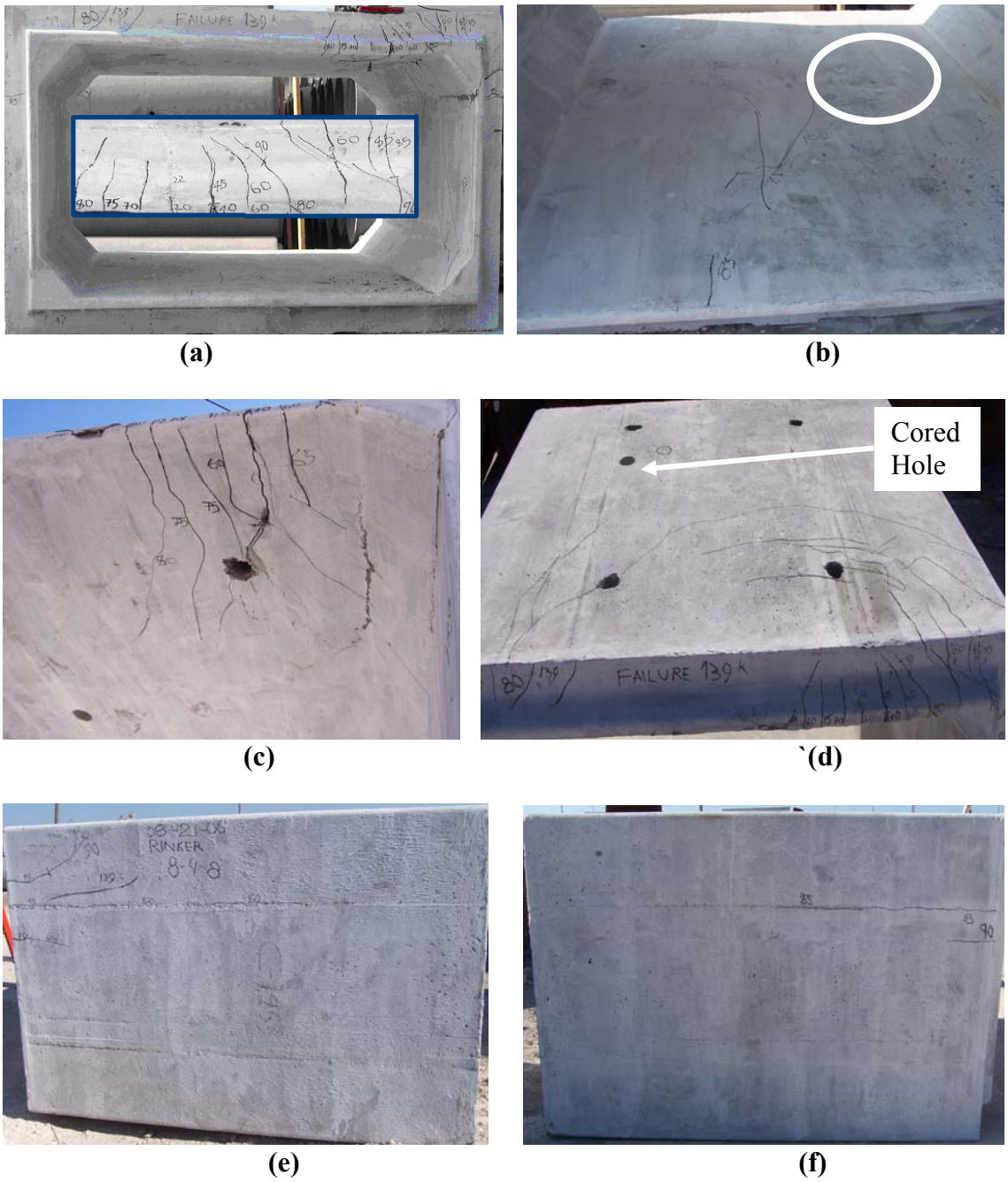

(a) (b)

(c) `(d)

(e) (f)

Figure B15 Experimental Photograph for Test: SP_244-122-244_Y_d (SP_8-4-8_Y_d) (a) Spigot End; (b) Inside Face of Bottom Slab; (c) Inside Face of Top Slab; (d) Outside Face of Top Slab; (e) Outside Face of Right Wall; and (f) Outside Face of Left Wall

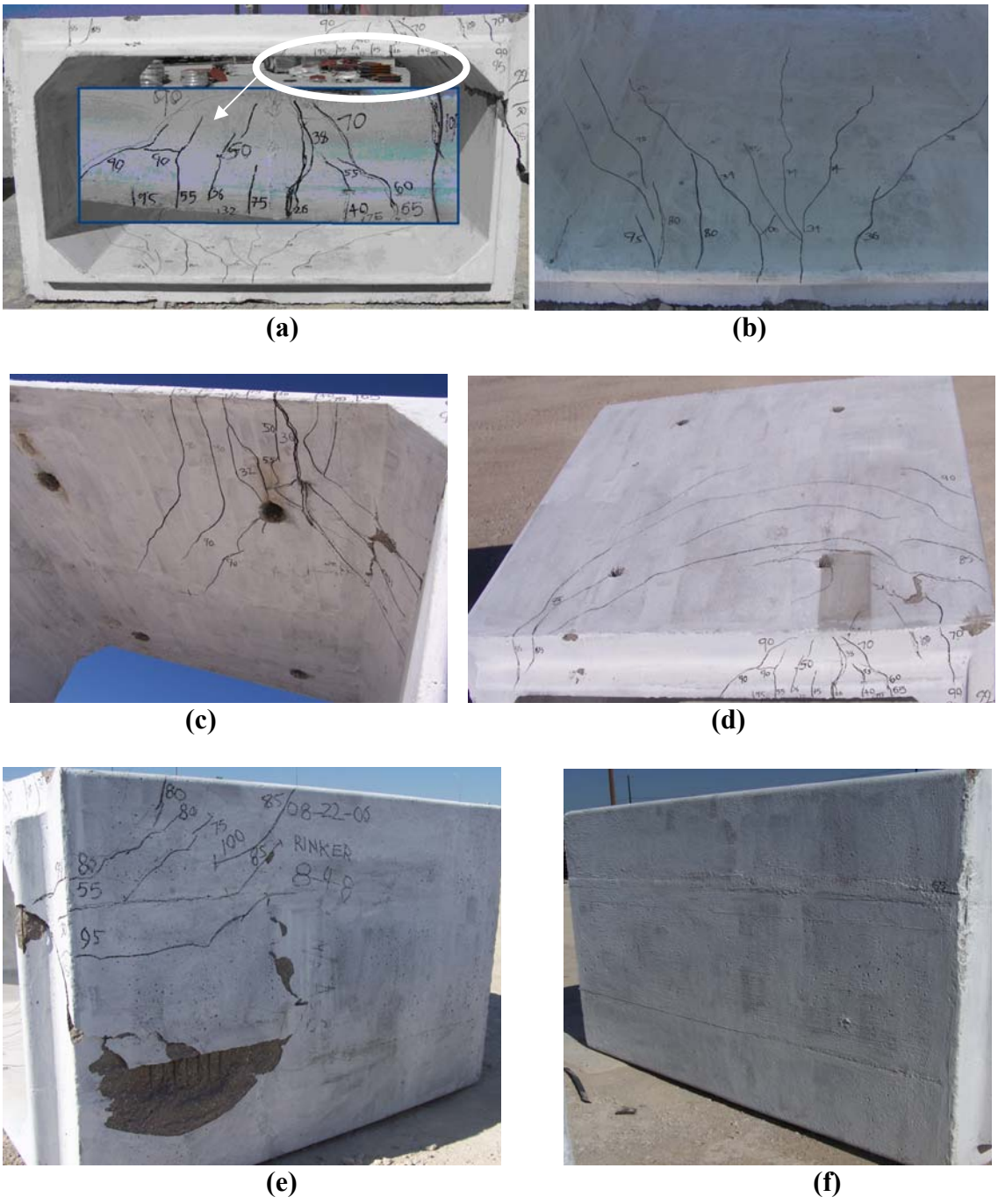

(a) (b) (c) (d) (e) (f)

Figure B16 Experimental Photograph for Test: SP_244-122-244_N_d (SP_8-4-8_N_d) (a) Spigot End; (b) Inside Face of Bottom Slab; (c) Inside Face of Top Slab; (d) Outside Face of Top Slab; (e) Outside Face of Right Wall; and (f) Outside Face of Left Wall

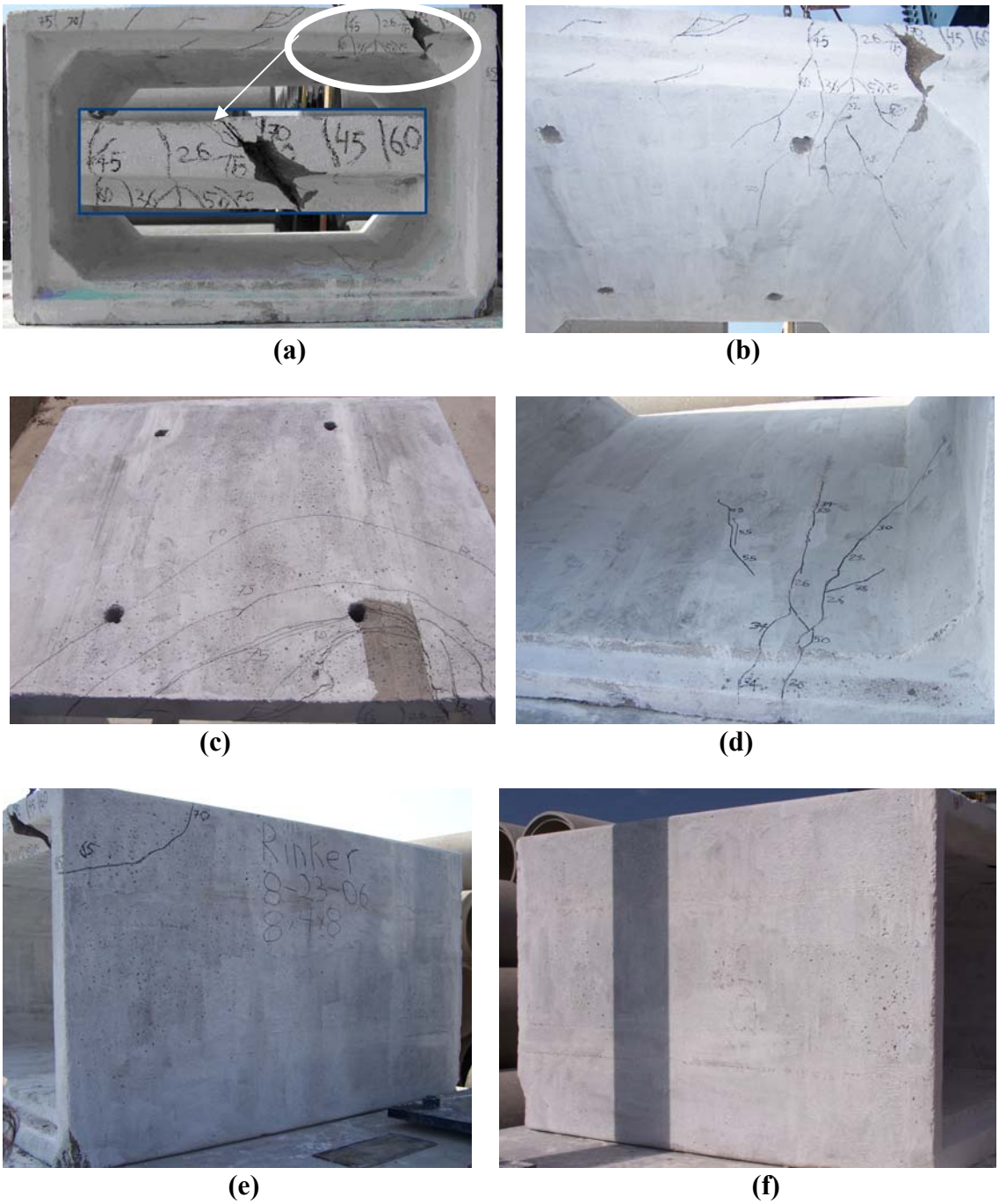

Figure B17 Experimental Photograph for Test: BL_244-122-244_N_d (BL_8-4-8_N_d) (a) Bell End; (b) Inside Face of Top Slab; (c) Outside Face of Top Slab; (d) Inside Face of Bottom Slab; (e) Outside Face of Right Wall; and (f) Outside Face of Left Wall

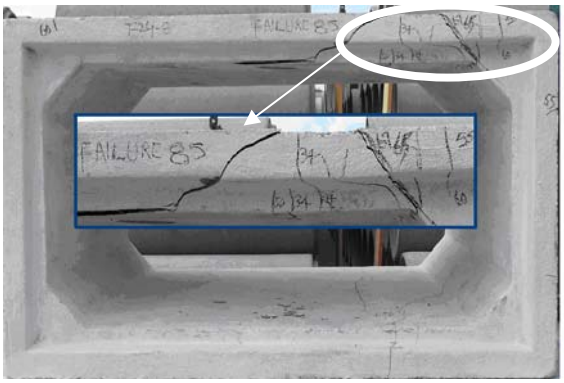

(a)

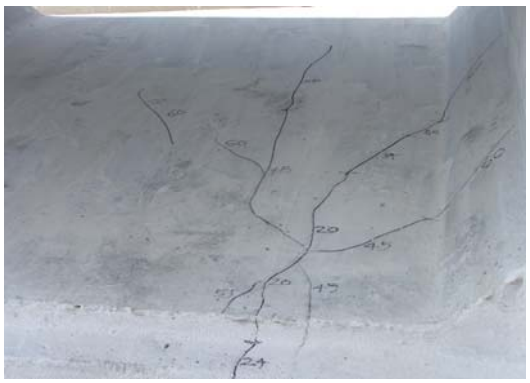

(b)

(c)

(d)

(e)

(f)

Figure B18 Experimental Photograph for Test: BL_244-122-244_Y_d (BL_8-4-8_Y_d) (a) Bell End; (b) Inside Face of Bottom Slab; (c) Inside Face of Top Slab; (d) Outside Face of Top Slab; (e) Outside Face of Right Wall; and (f) Outside Face of Left Wall

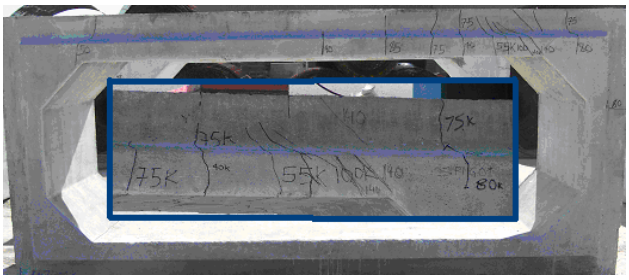

(a)

(b)

(c)

(d)

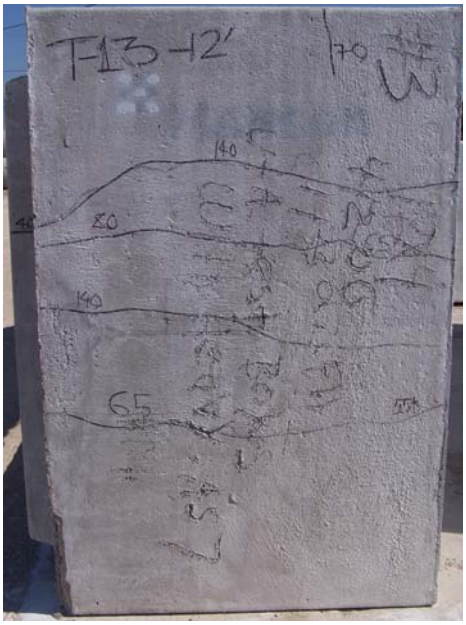

(e)

(f)

Figure B19 Experimental Photograph for Test: SP_366-122-122_Y_d (SP_12-4-4_Y_d) (a) Spigot End; (b) Inside Face of Bottom Slab; (c) Inside Face of Top Slab; (d) Outside Face of Top Slab ; (e) Outside Face of Right Wall; and (f) Outside Face of Left Wall

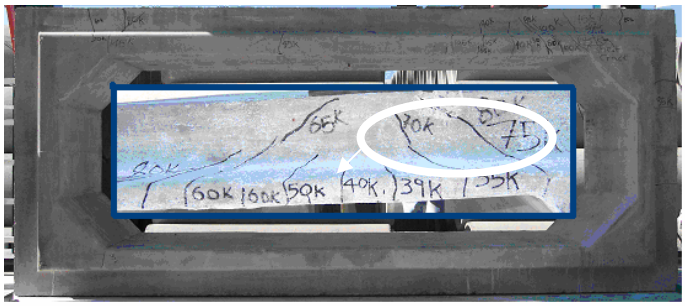

(a)

(b)

(c)

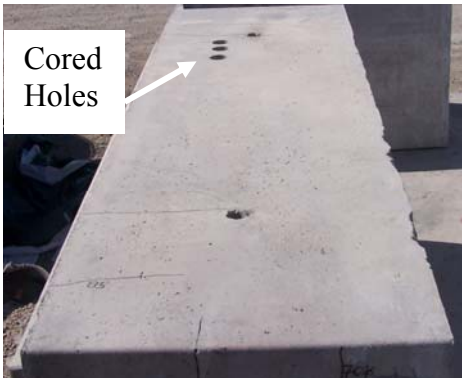

(d)

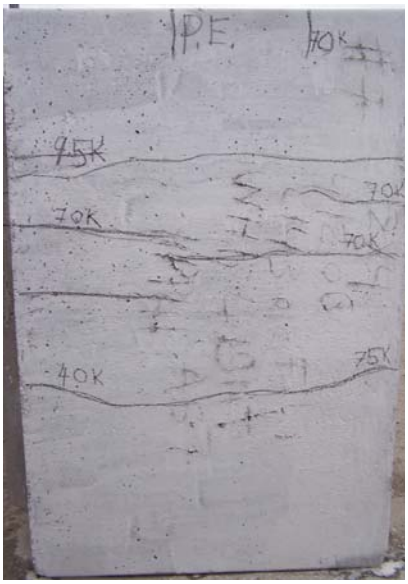

(e)

(f)

Figure B20 Experimental Photograph for Test: SP_366-122-122_N_d (SP_12-4-4_N_d) (a) Spigot End; (b) Inside Face of Bottom Slab; (c) Inside Face of Top Slab; (d) Outside Face of Top Slab; (e) Outside Face of Right Wall; and (f) Outside Face of Left Wall

(a)

(b)

(c)

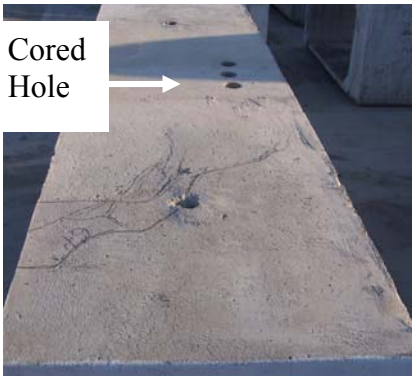

(d)

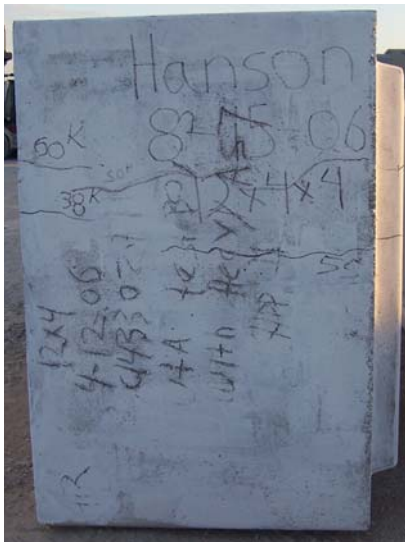

(e)

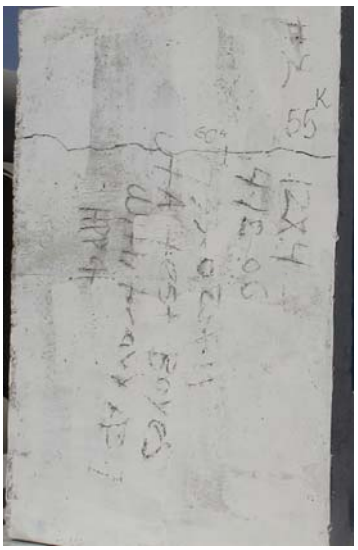

(f)

Figure B21 Experimental Photograph for Test: BL_366-122-122_Y_d (BL_12-4-4_Y_d) (a) Bell End; (b) Inside Face of Bottom Slab; (c) Inside Face of Top Slab; (d) Outside Face of Top Slab; (e) Outside Face of Right Wall; and (f) Outside Face of Left Wall

(a)

(b)

(c)

(d)

(e)

(f)

Figure B22 Experimental Photograph for Test: BL_366-122-122_N_d (BL_12-4-4_N_d) (a) Bell End; (b) Inside face of Bottom Slab; (c) Inside Face of Top Slab; (d) Outside Face of Top Slab(e) Outside Face of Right Wall; and (f) Outside Face of Left Wall

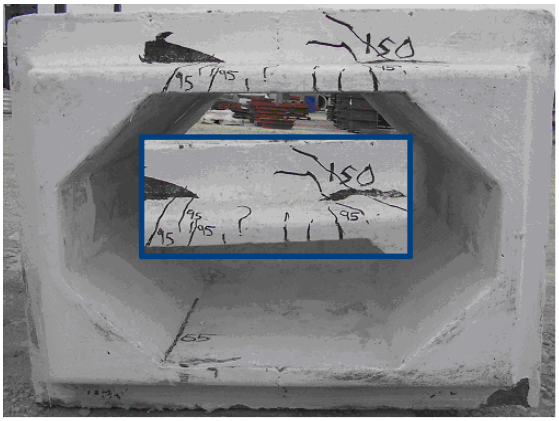

(a)

(b)

(c)

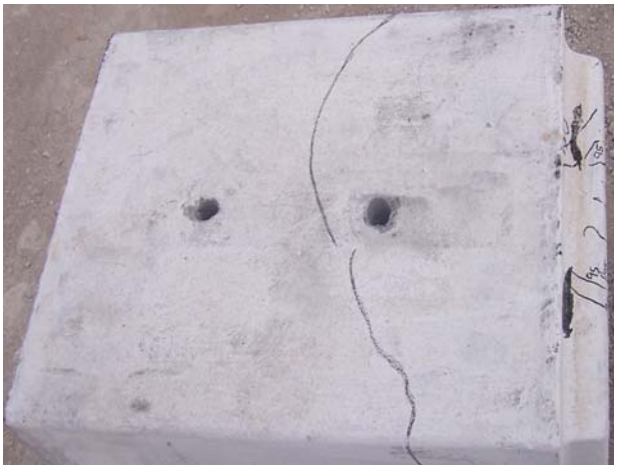

(d)

(e)

(f)

Figure B23 Experimental Photograph for SP_91-61-145_Y_0 (SP_3-2-4.75_Y_0) (a) Spigot End; (b) Inside Face of Bottom Slab; (c) Inside Face of Top Slab; (d) Outside Face of Top Slab; (e) Outside Face of Right Wall; and (f) Outside Face of Left Wall

(a)

(b)

(c)

(d)

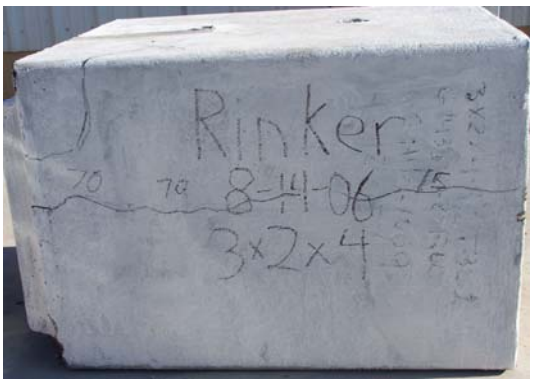

(e)

(f)

Figure B24 Experimental Photograph for Test: SP_91-61-145_Y_0.83d (SP_3-2-4.75_Y_0.83d) (a) Spigot end; (b) Inside Face of Bottom Slab; (c) Inside Face of Top Slab; (d) Outside Face of Top Slab; (e) Outside Face of Right Wall; and (f) Outside Face of Left Wall

APPENDIX C

FINITE ELEMENT MODEL CRACK PREDICTION

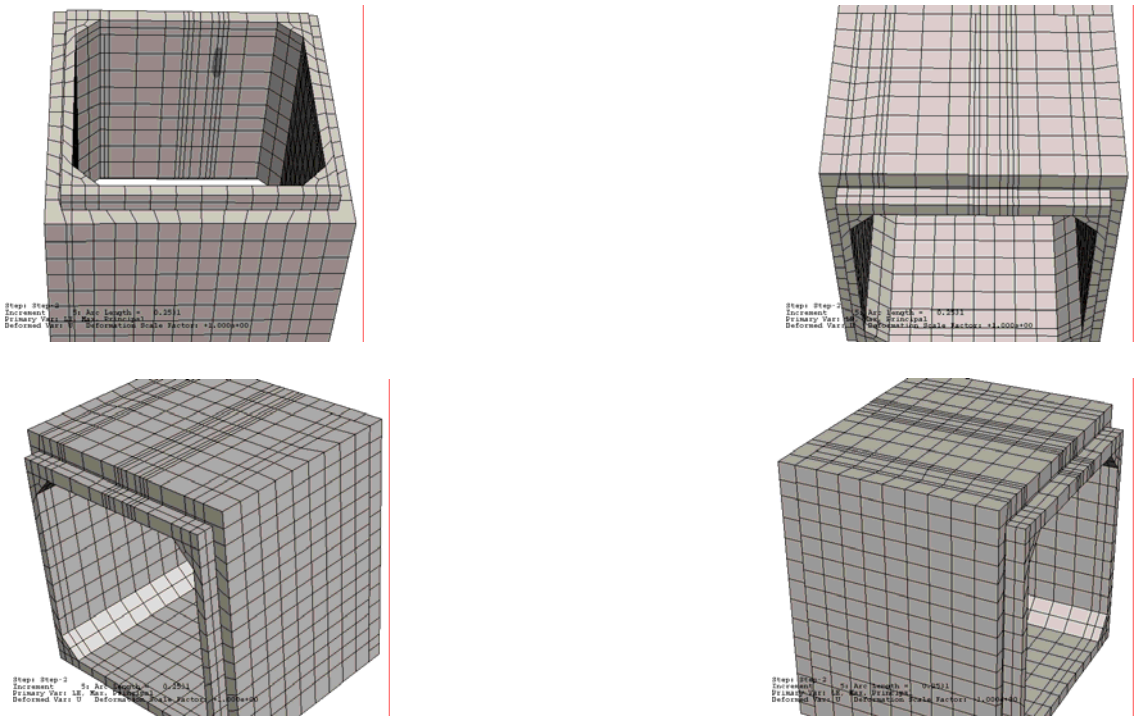

At 116 kN (26 kip) Load

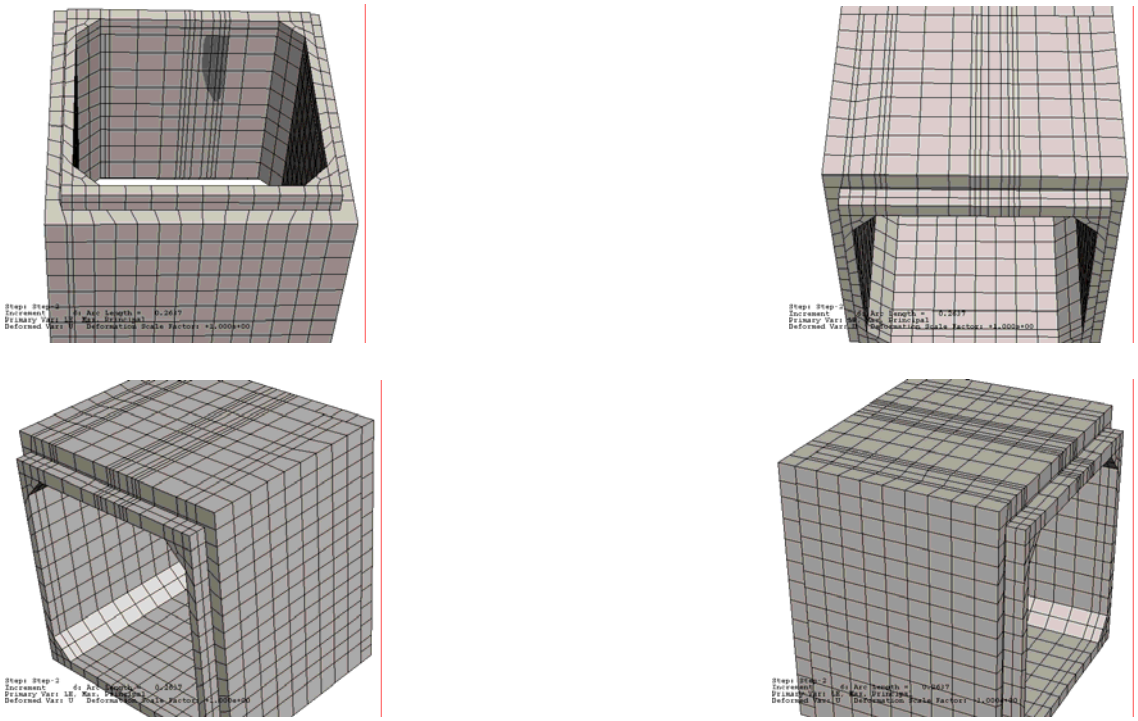

At 125 kN (28 kip) Load

Figure C1 FEM Crack Prediction of Model SP_122-122-122_N_d (SP_4-4-4_N_d)

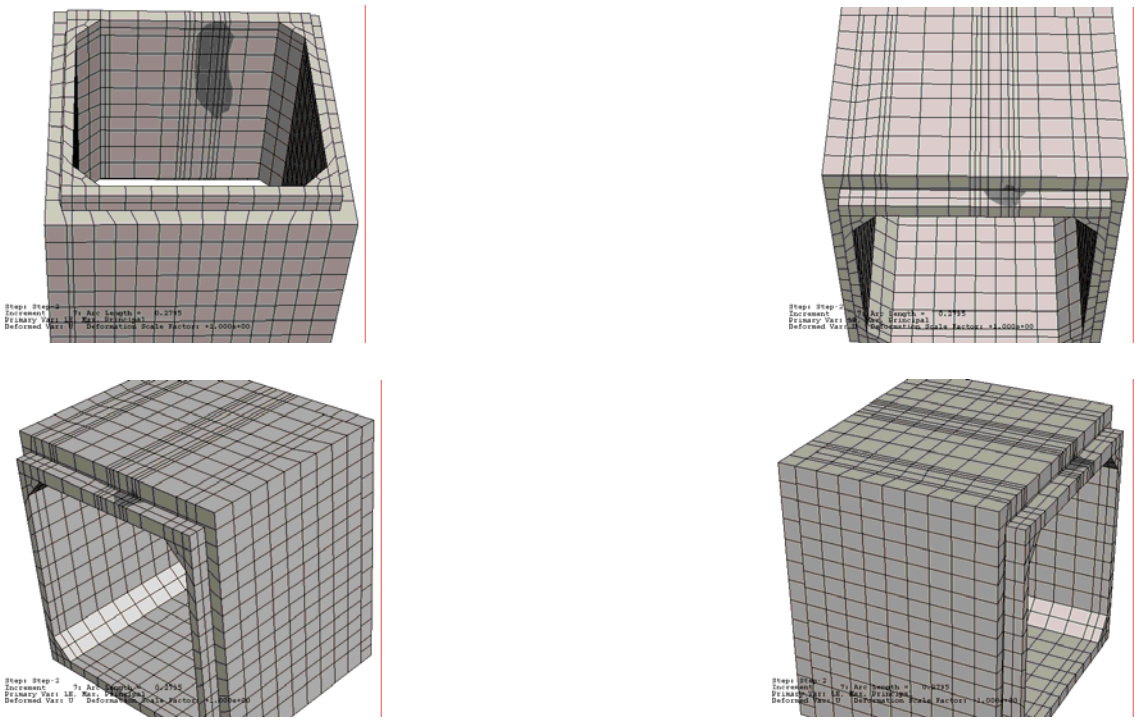

At 138 kN (31 kip) Load

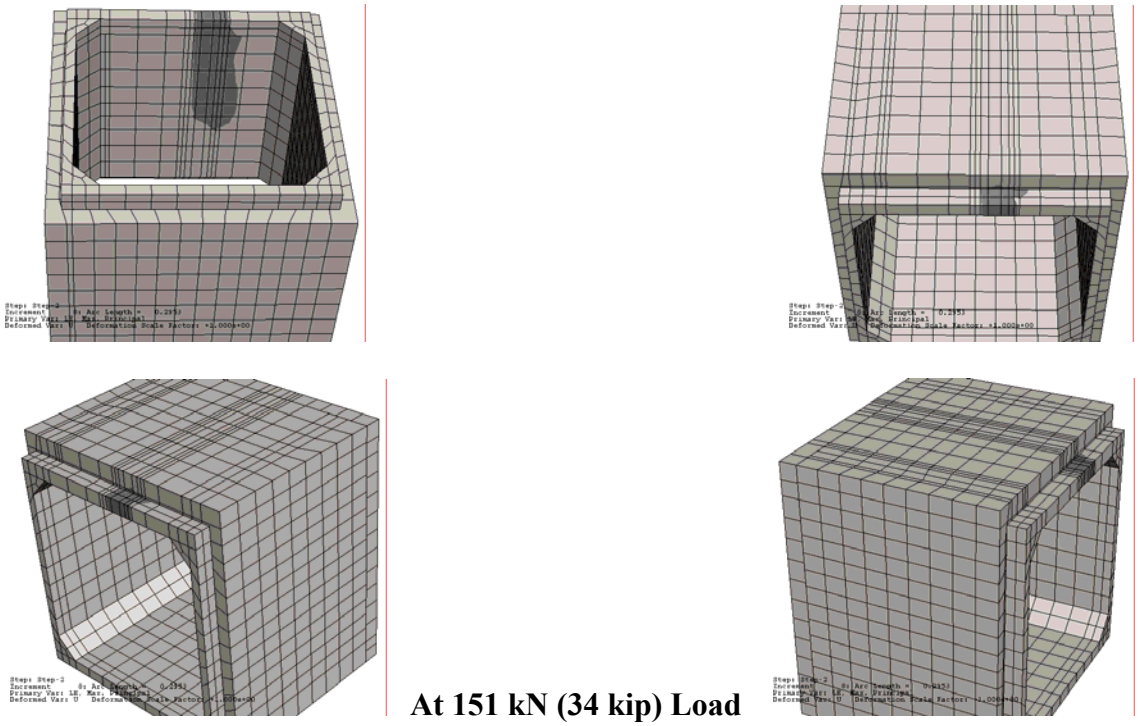

At 151 kN (34 kip) Load

Figure C2 FEM Crack Prediction of Model SP_122-122-122_N_d (SP_4-4-4_N_d)

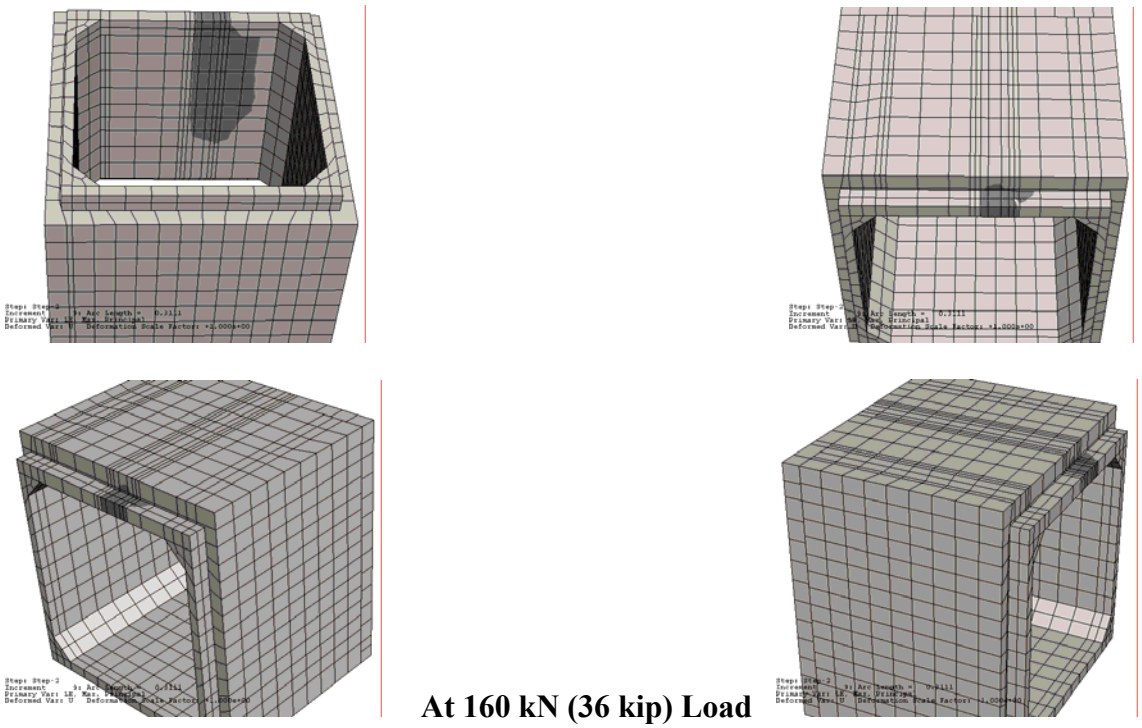

At 160 kN (36 kip) Load

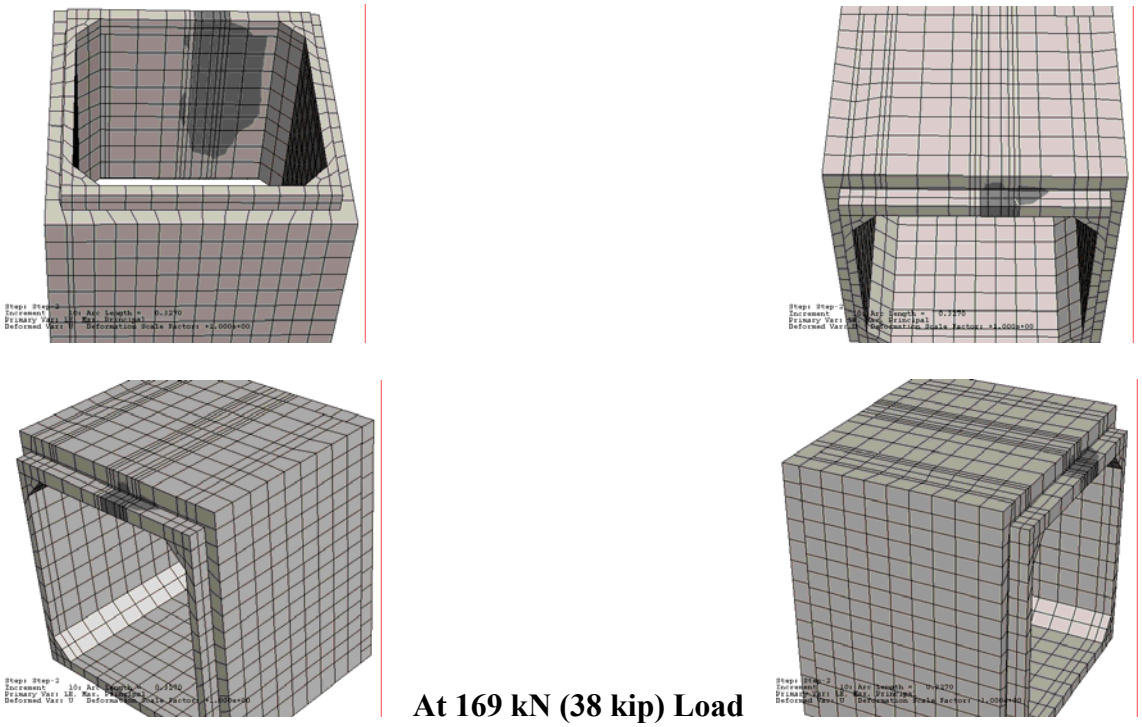

At 169 kN (38 kip) Load

Figure C3 FEM Crack Prediction of Model SP_122-122-122_N_d (SP_4-4-4_N_d)

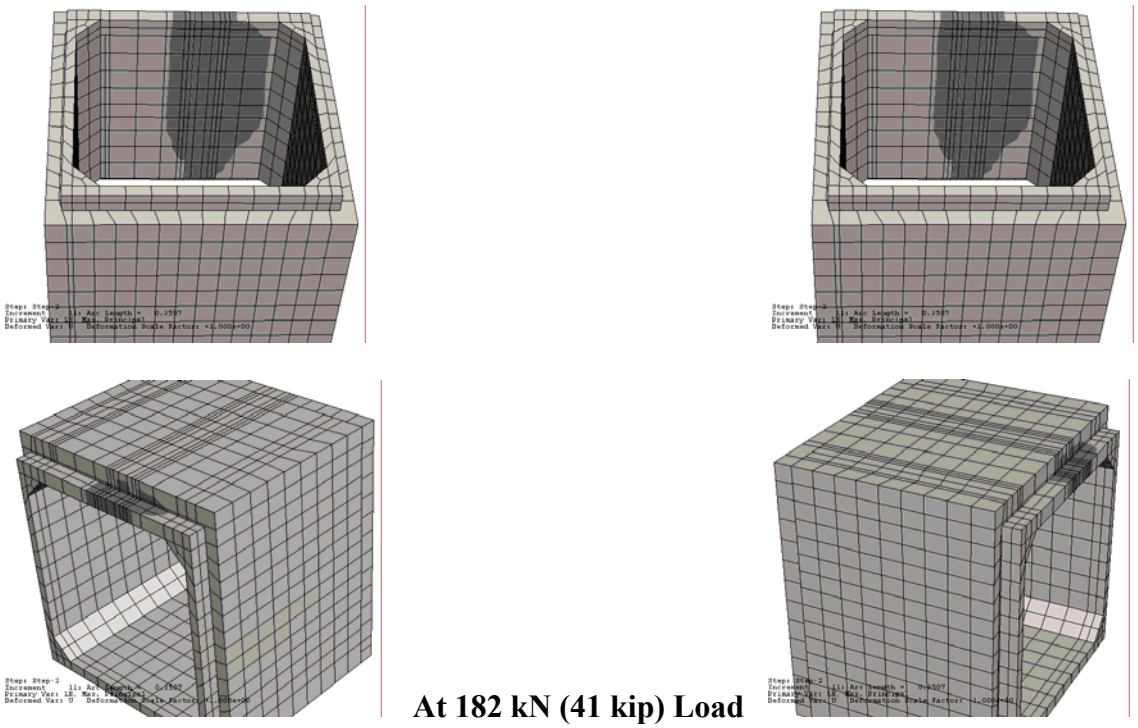

At 182 kN (41 kip) Load

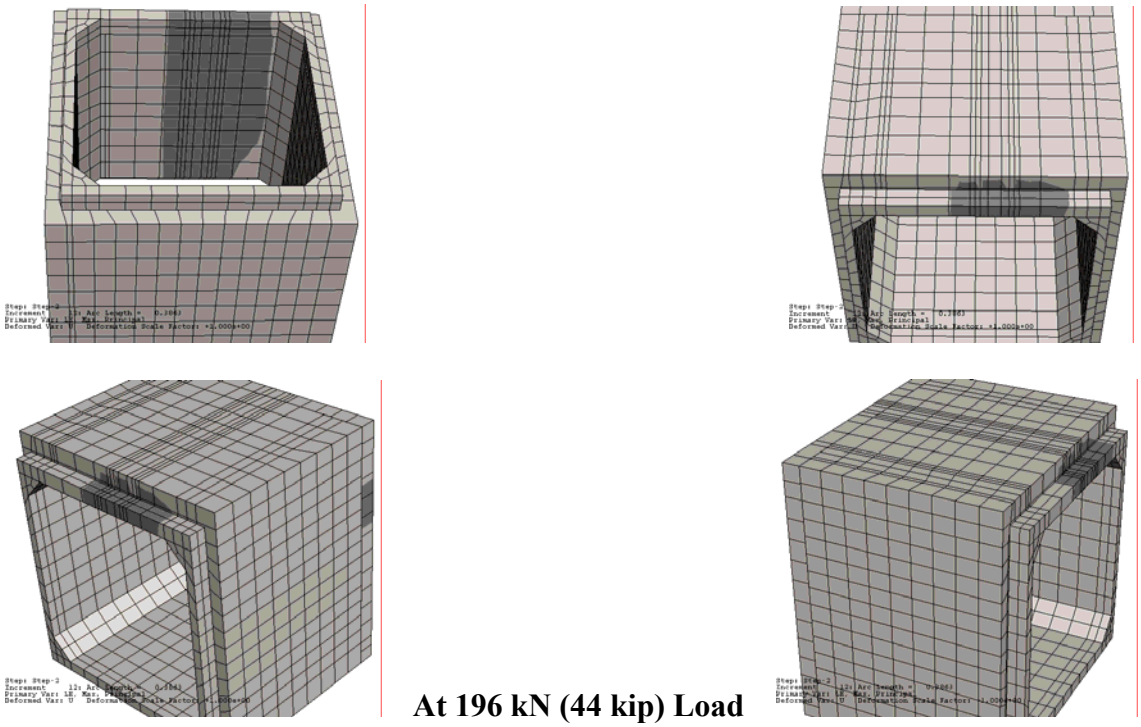

At 196 kN (44 kip) Load

Figure C4 FEM Crack Prediction of Model SP_122-122-122_N_d (SP_4-4-4_N_d)

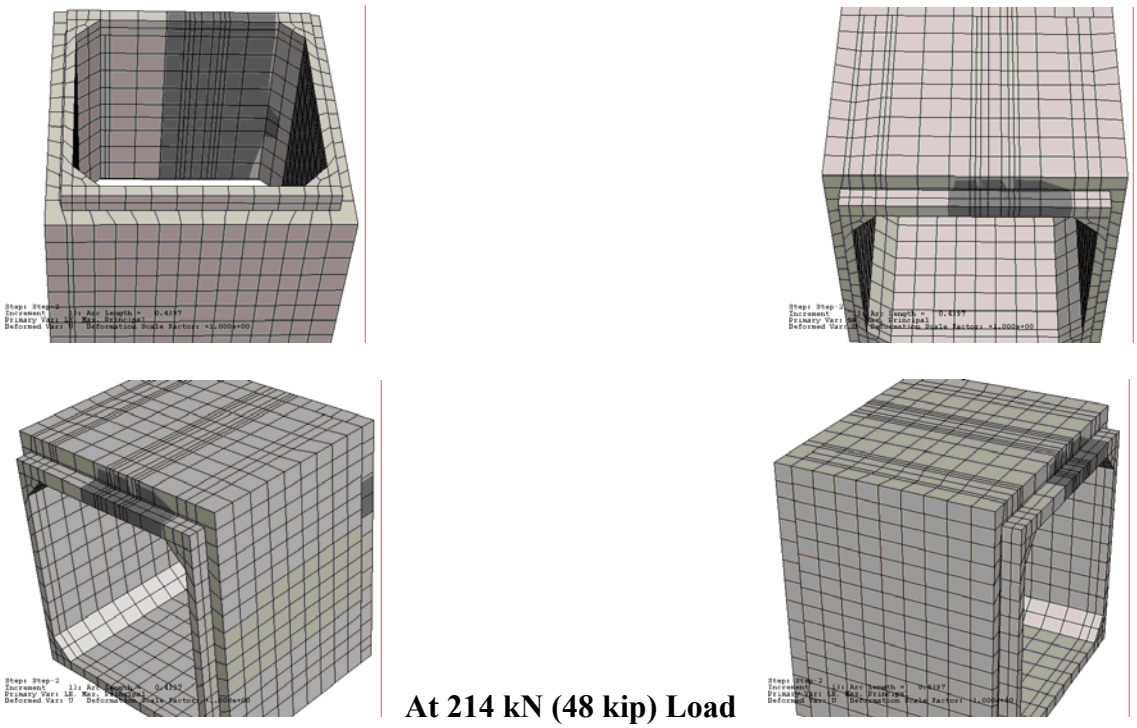

At 214 kN (48 kip) Load

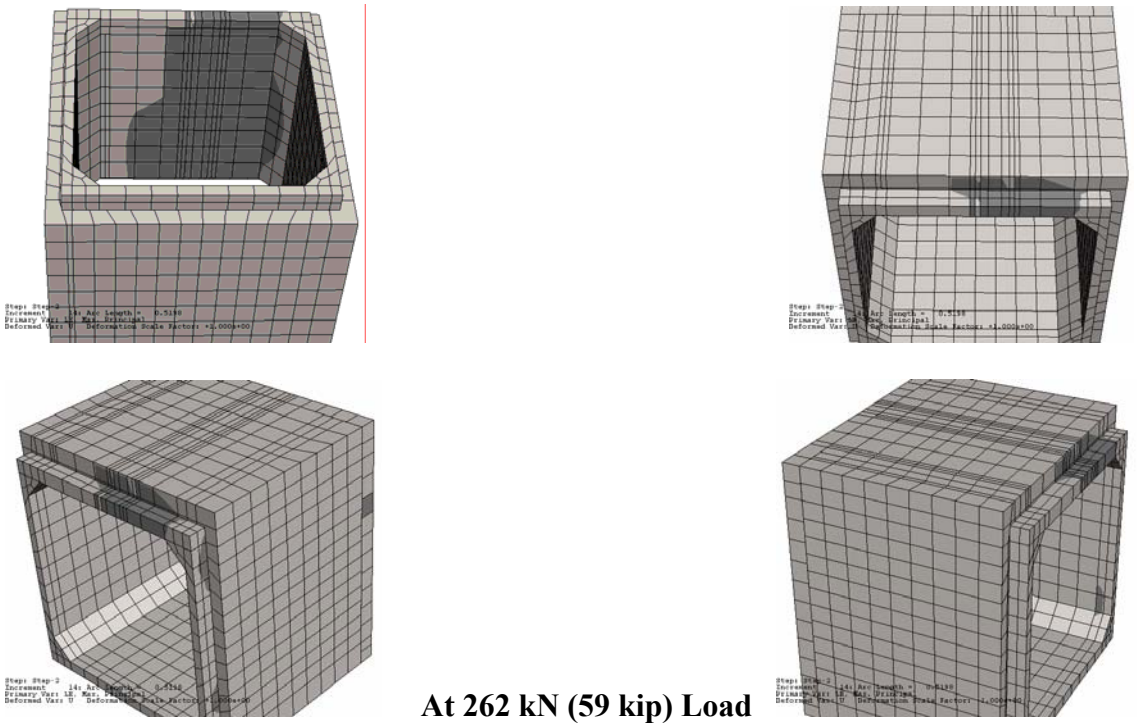

At 262 kN (59 kip) Load

Figure C5 FEM Crack Prediction of Model SP_122-122-122_N_d (SP_4-4-4_N_d)

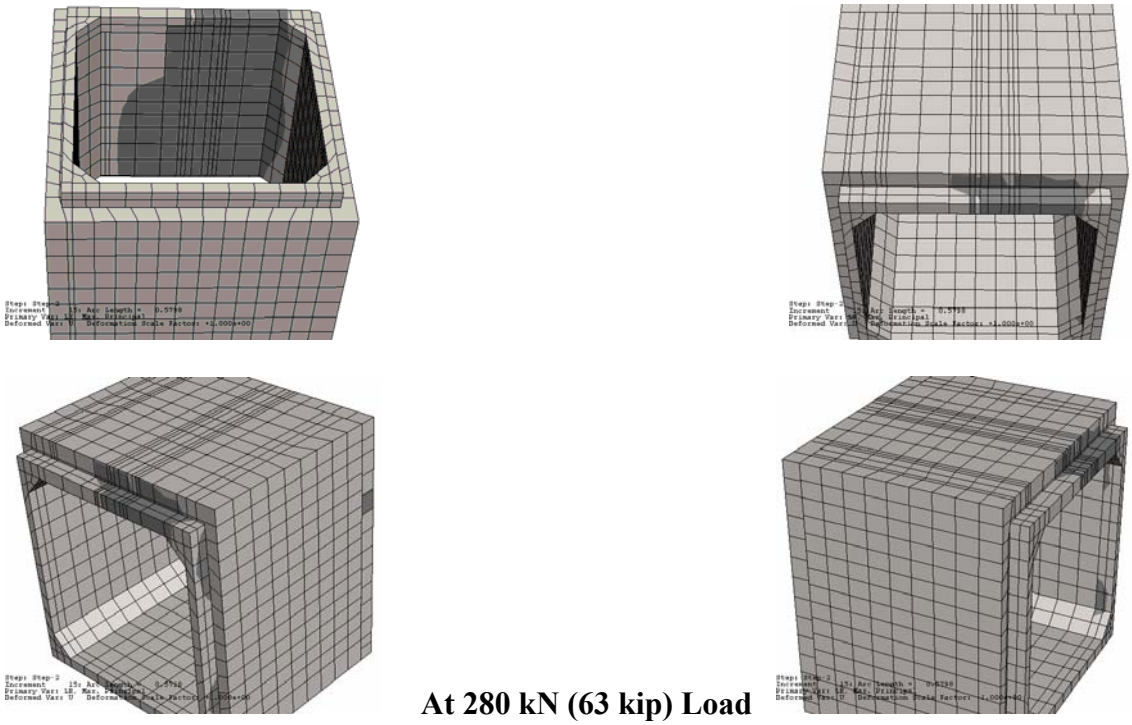

At 280 kN (63 kip) Load

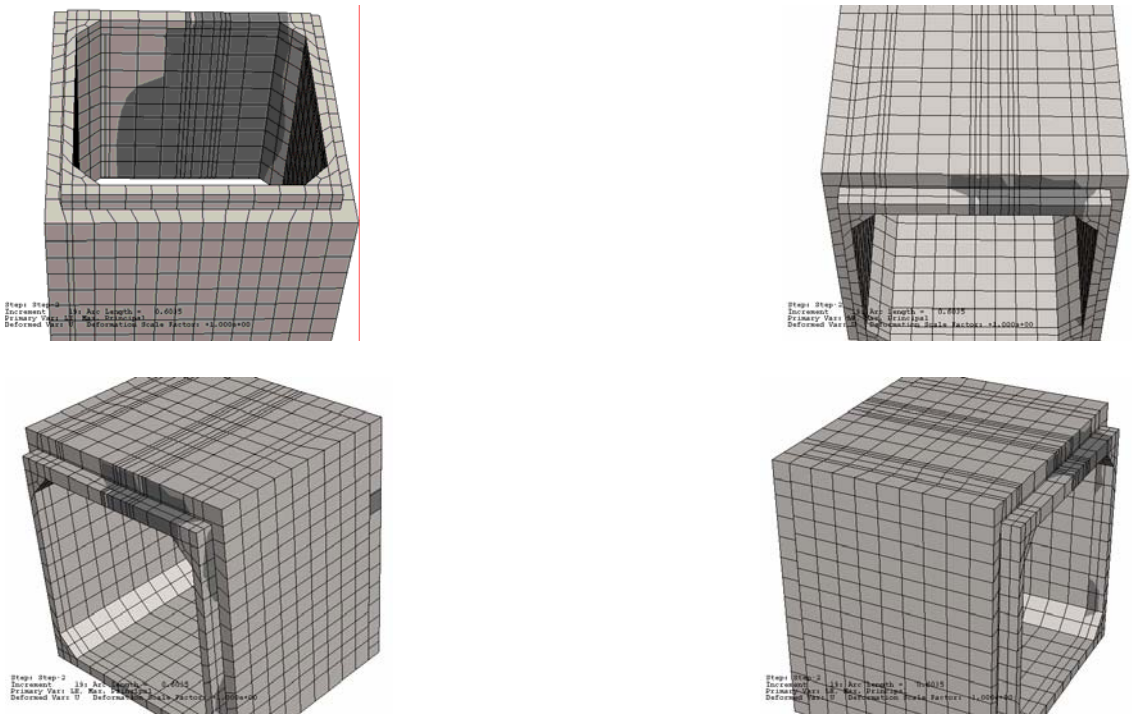

At 285 kN (64 kip) Load

Figure C6 FEM Crack Prediction of Model SP_122-122-122_N_d (SP_4-4-4_N_d)

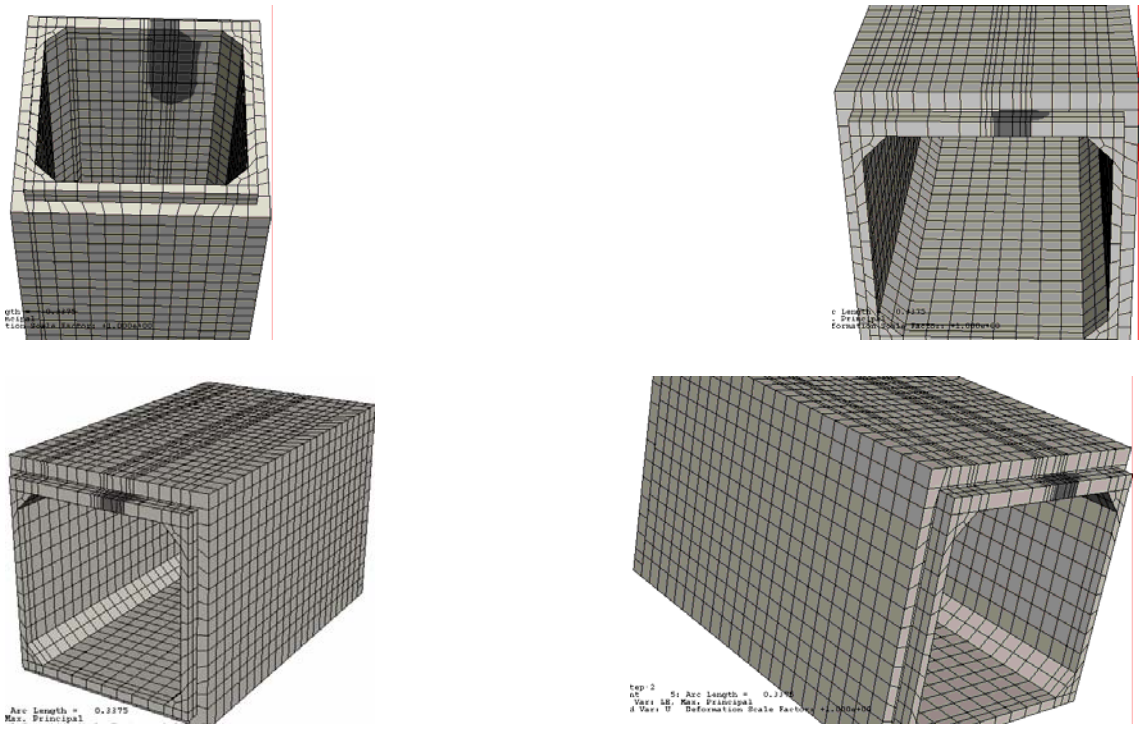

At 125 kN (28 kip) Load

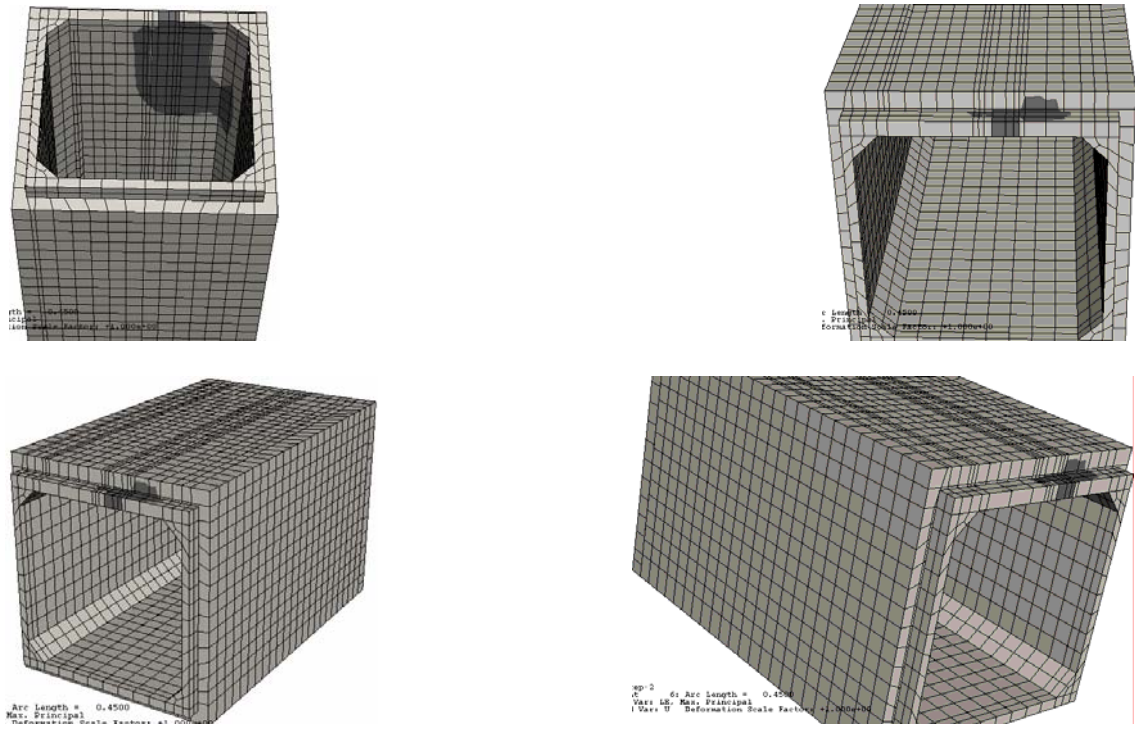

At 151 kN (34 kip) Load

Figure C7 FEM Crack Prediction of Model SP_122-122-244_N_d (SP_4-4-8_N_d)

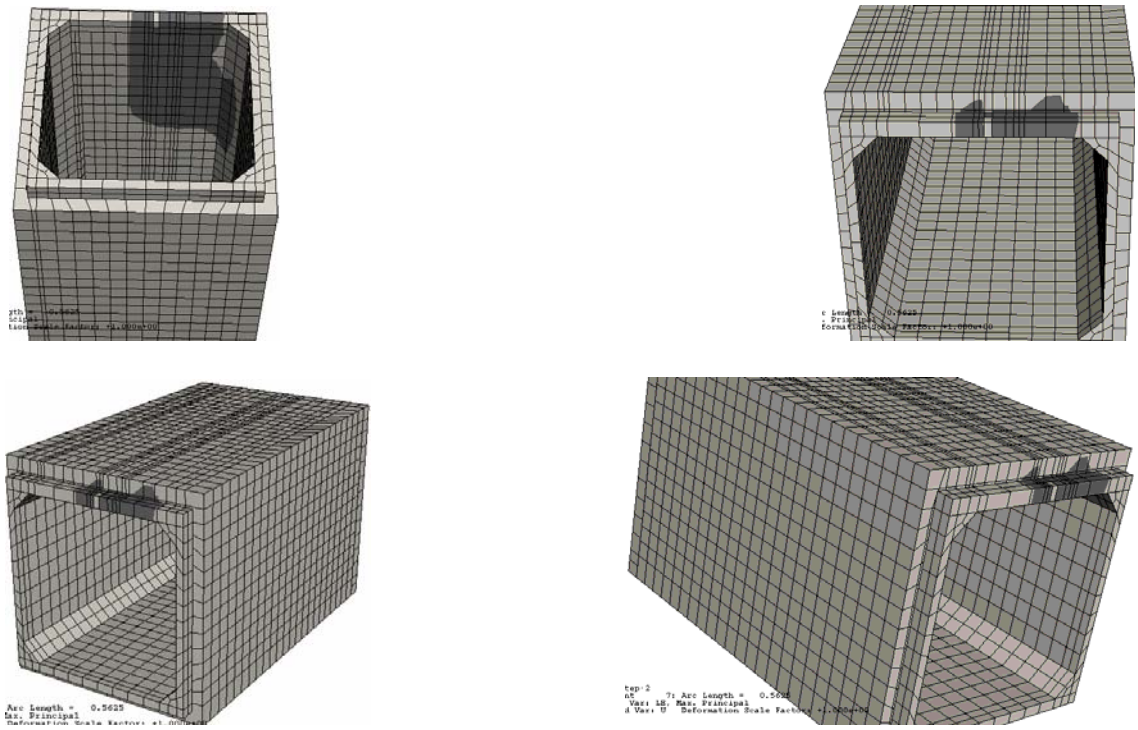

At 173 kN (39 kip) Load

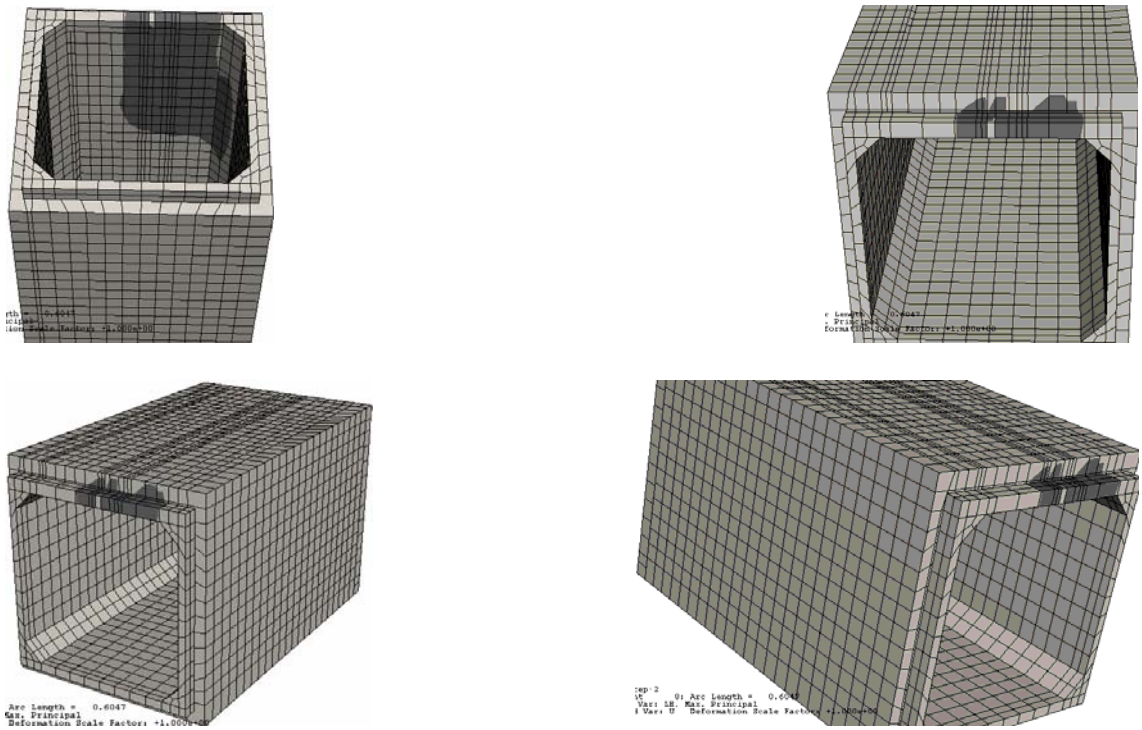

At 187 kN (42 kip) Load

Figure C8 FEM Crack Prediction of Model SP_122-122-244_N_d (SP_4-4-8_N_d)

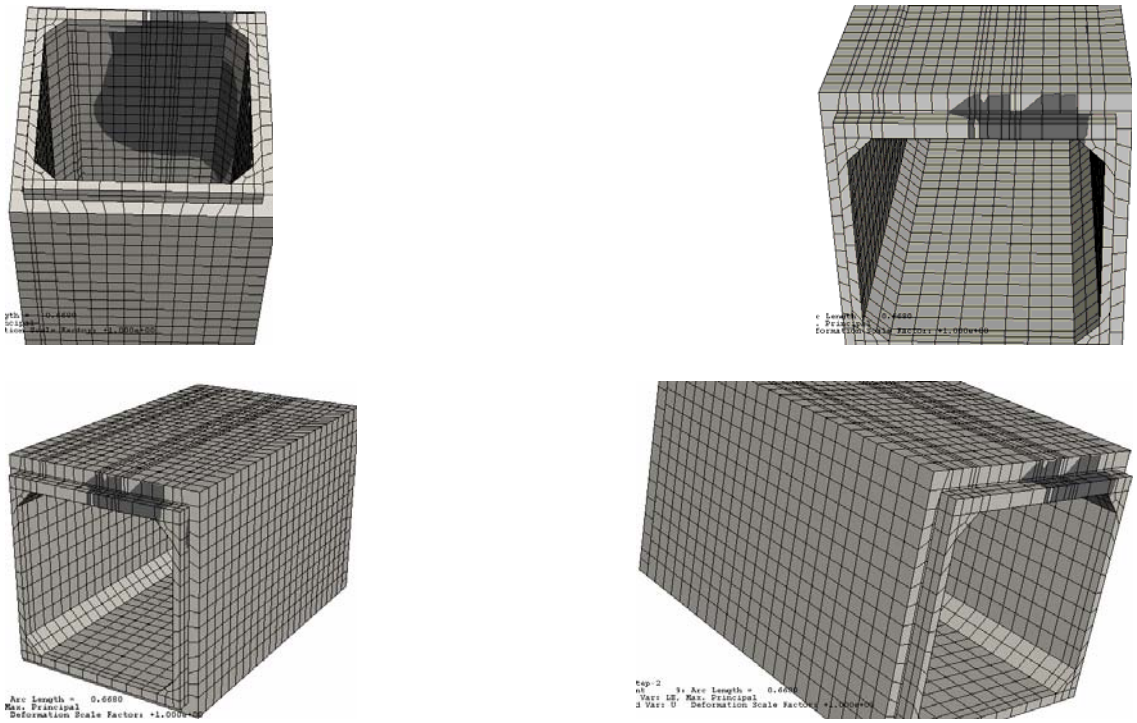

At 231 kN (52 kip) Load

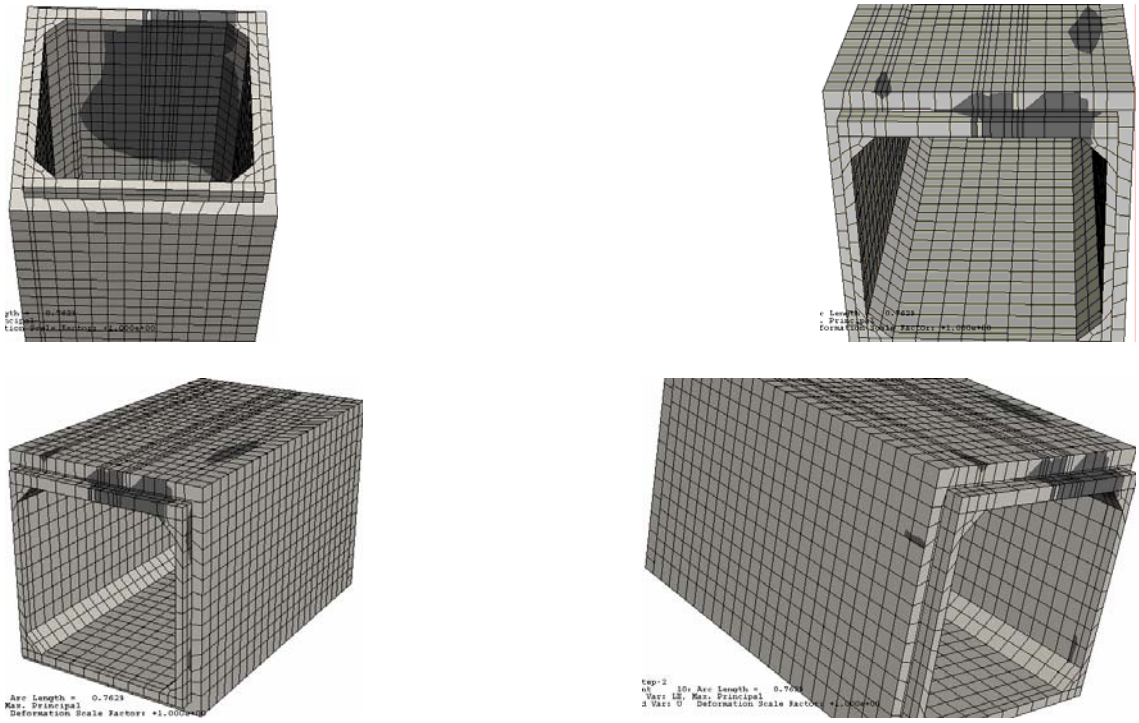

At 258 kN (58 kip) Load

Figure C9 FEM Crack Prediction of Model SP_122-122-244_N_d (SP_4-4-8_N_d)

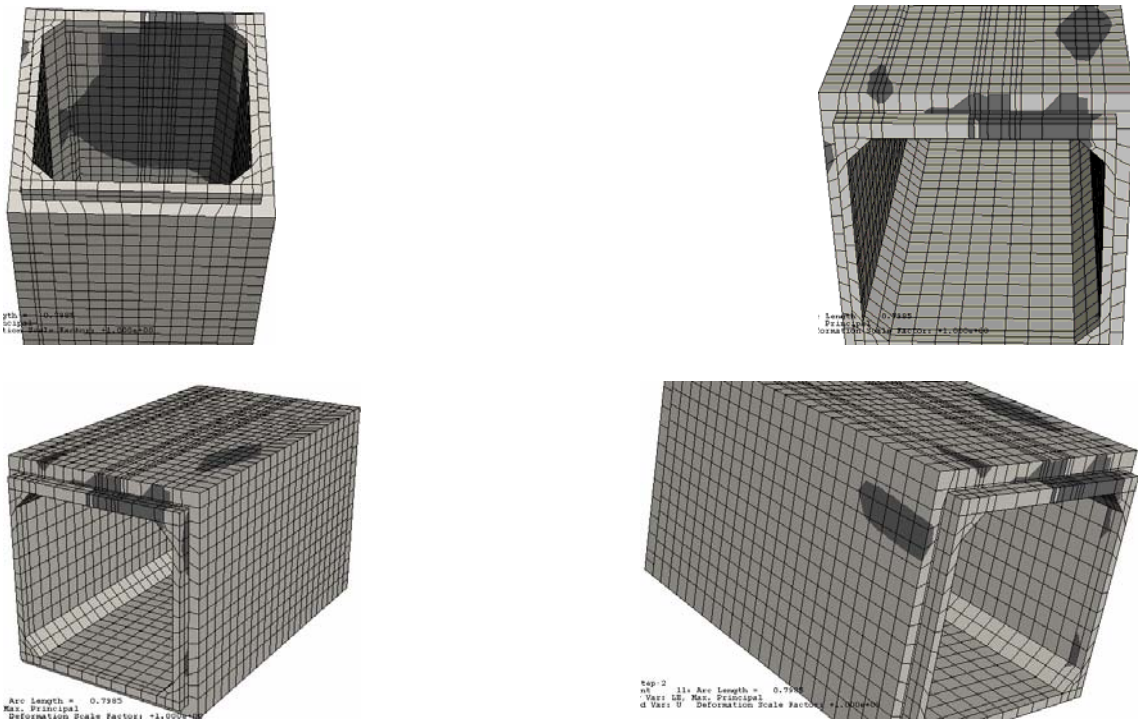

At 267 kN (60 kip) Load

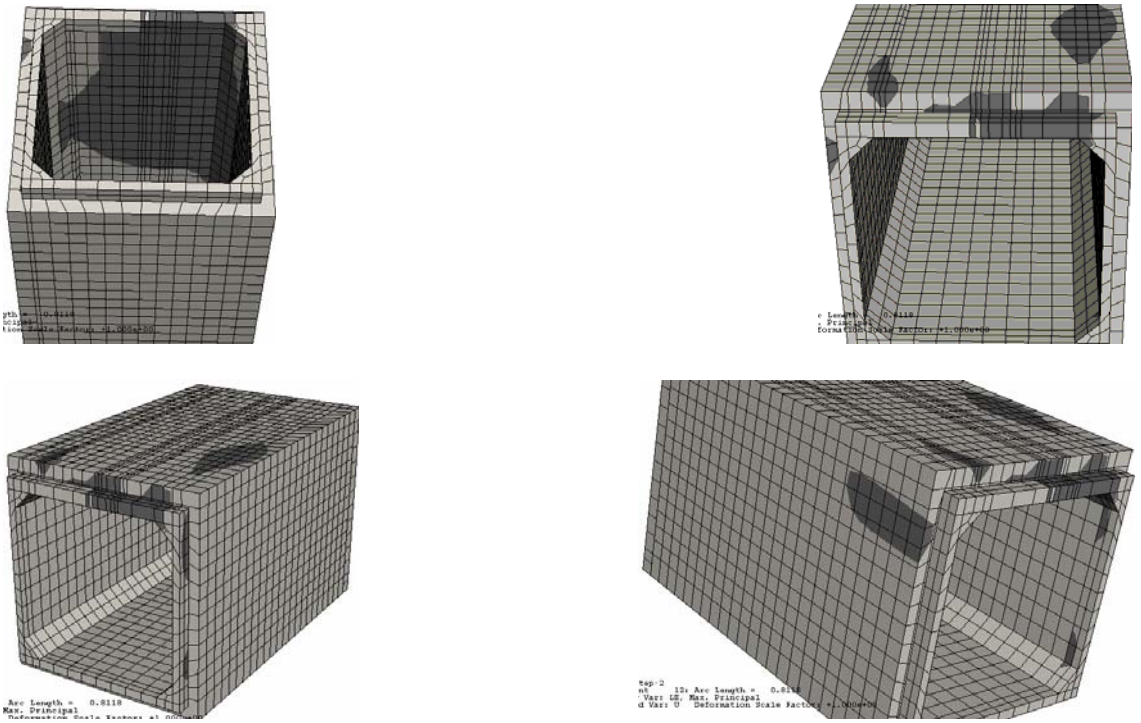

At 276 kN (62 kip) Load

Figure C10 FEM Crack Prediction of Model SP_122-122-244_N_d (SP_4-4-8_N_d)

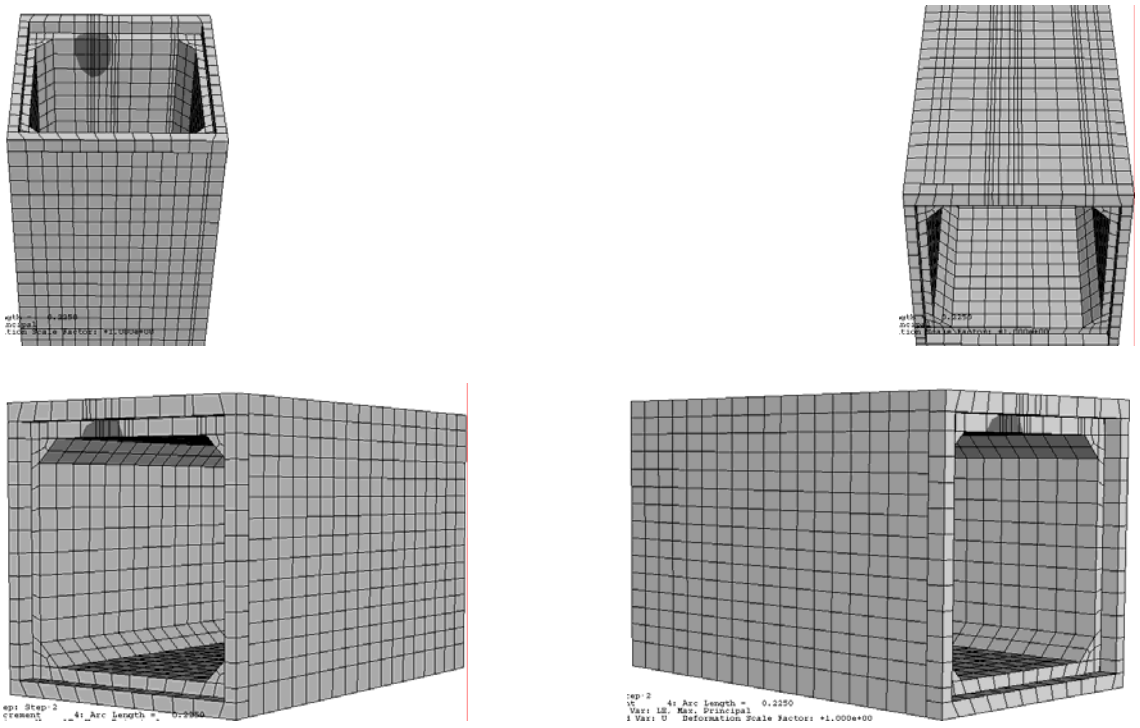

At 76 kN (17 kip) Load

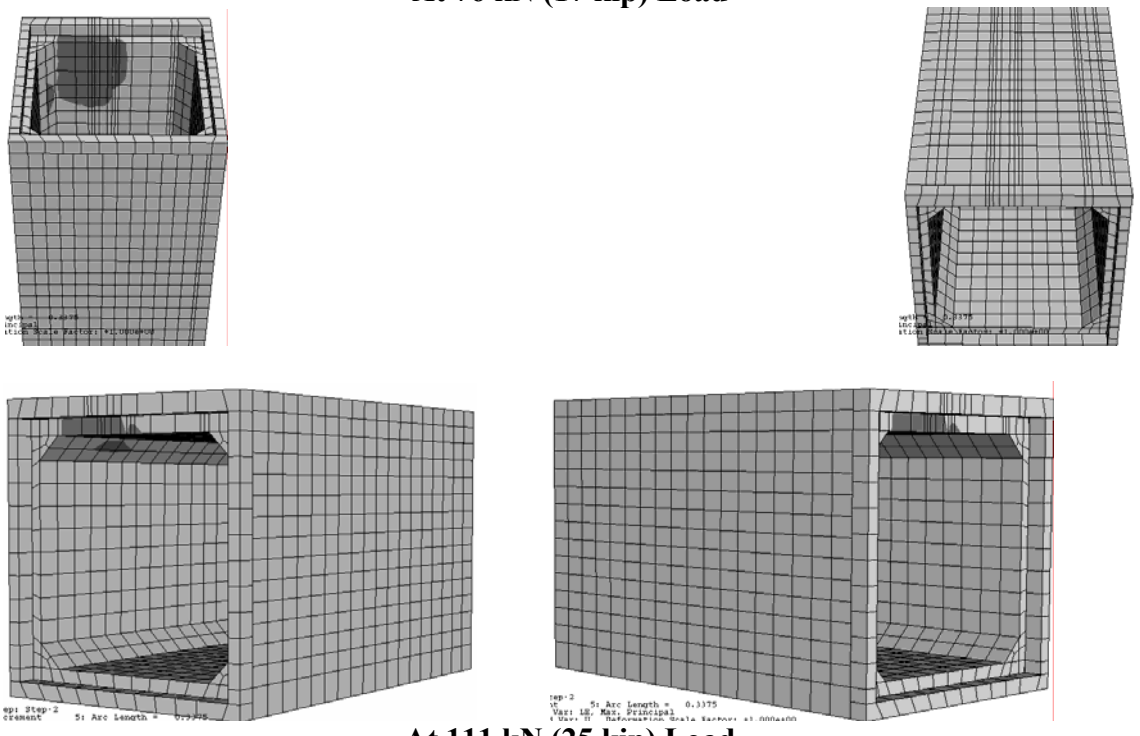

At 111 kN (25 kip) Load

Figure C11 FEM Crack Prediction of Model BL_122-122-244_N_d (BL_4-4-8_N_d)

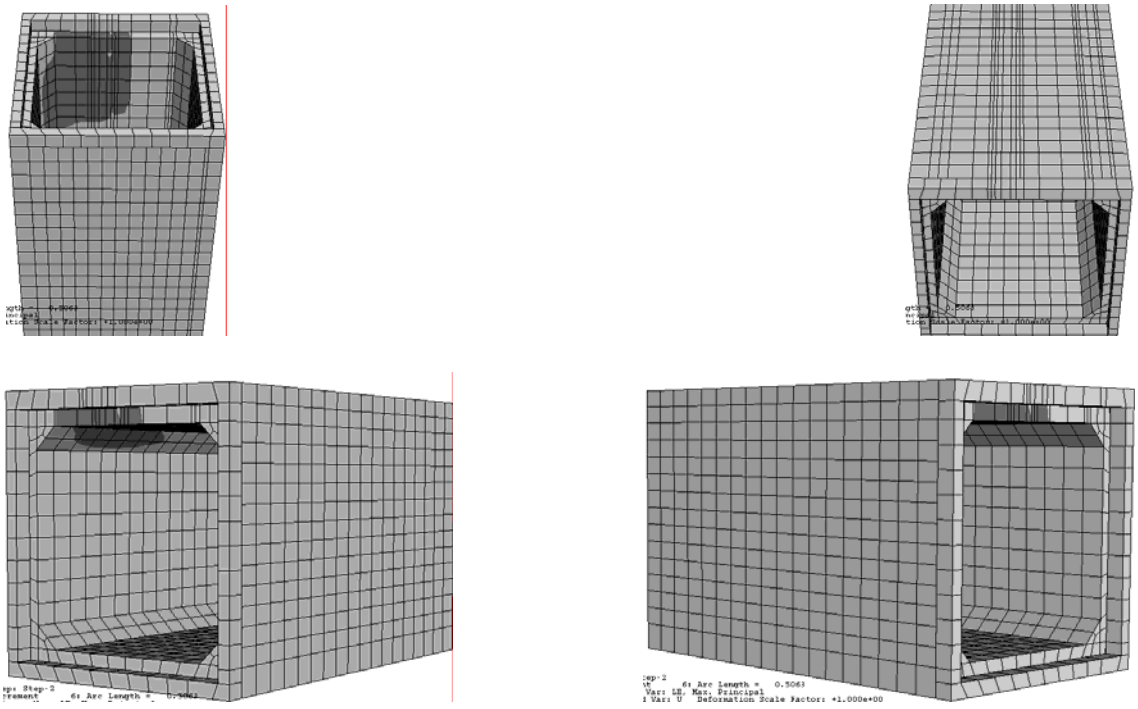

At 147 kN (33 kip) Load

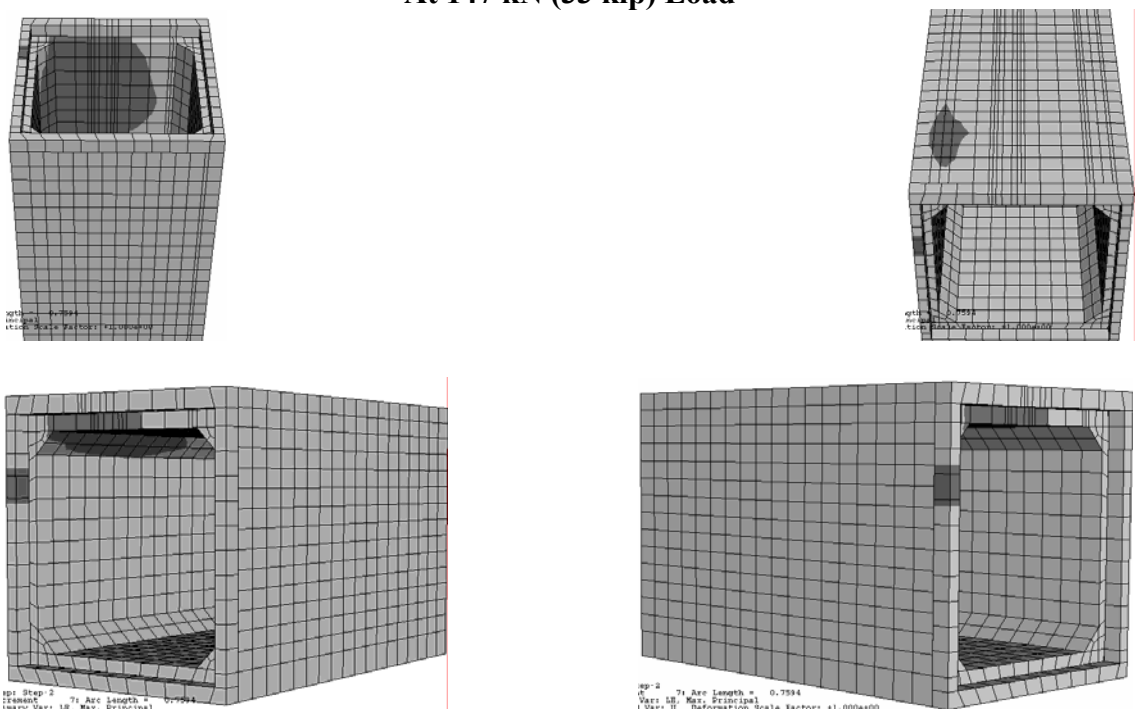

At 147 kN (33 kip) Load

Figure C12 FEM Crack Prediction of Model BL_122-122-244_N_d (BL_4-4-8_N_d)

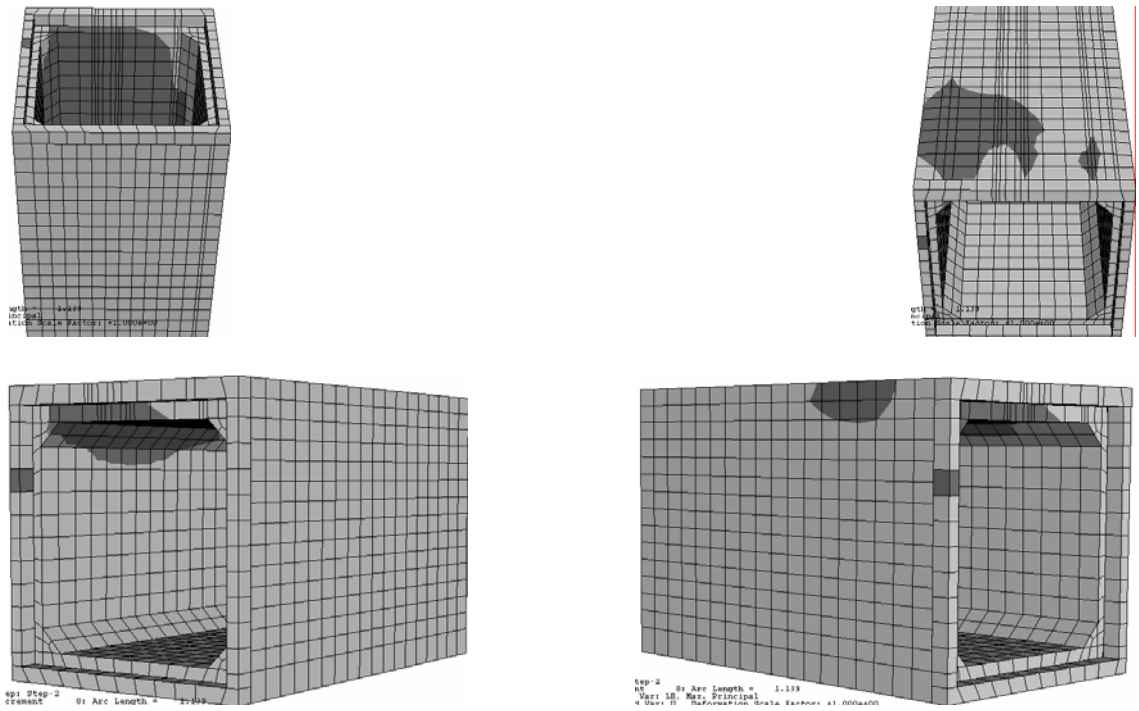

At 231 kN (52 kip) Load

Figure C13 FEM Crack Prediction of Model BL_122-122-244_N_d (BL_4-4-8_N_d)

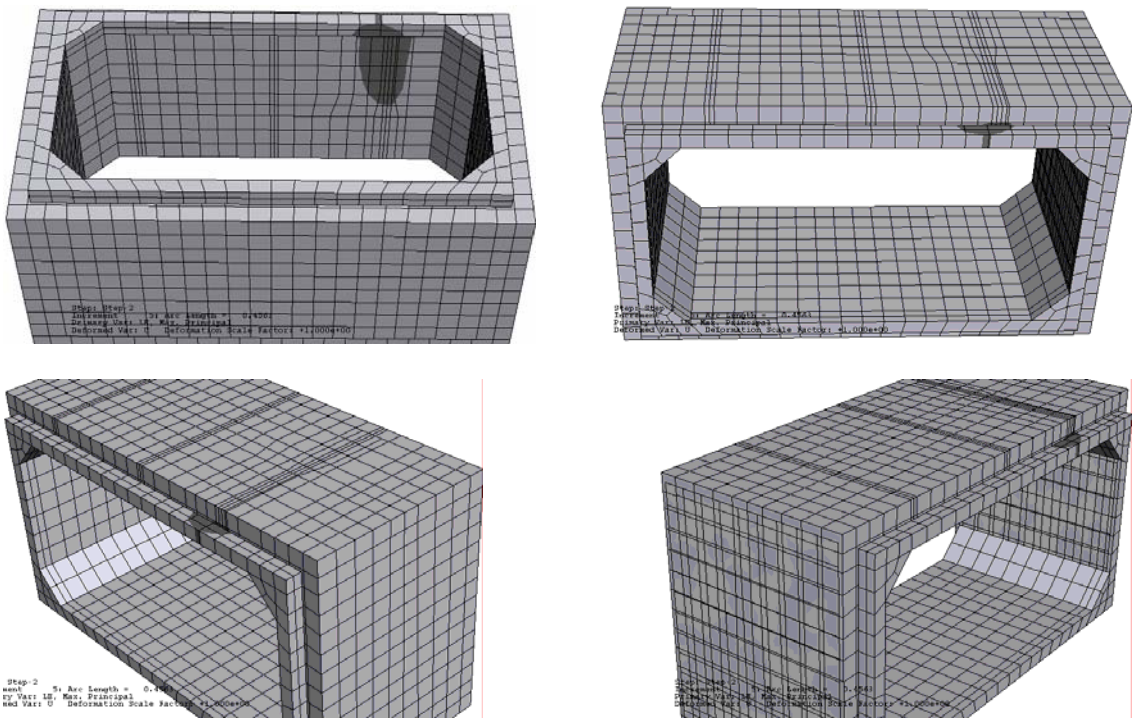

At 169 kN (38 kip) Load

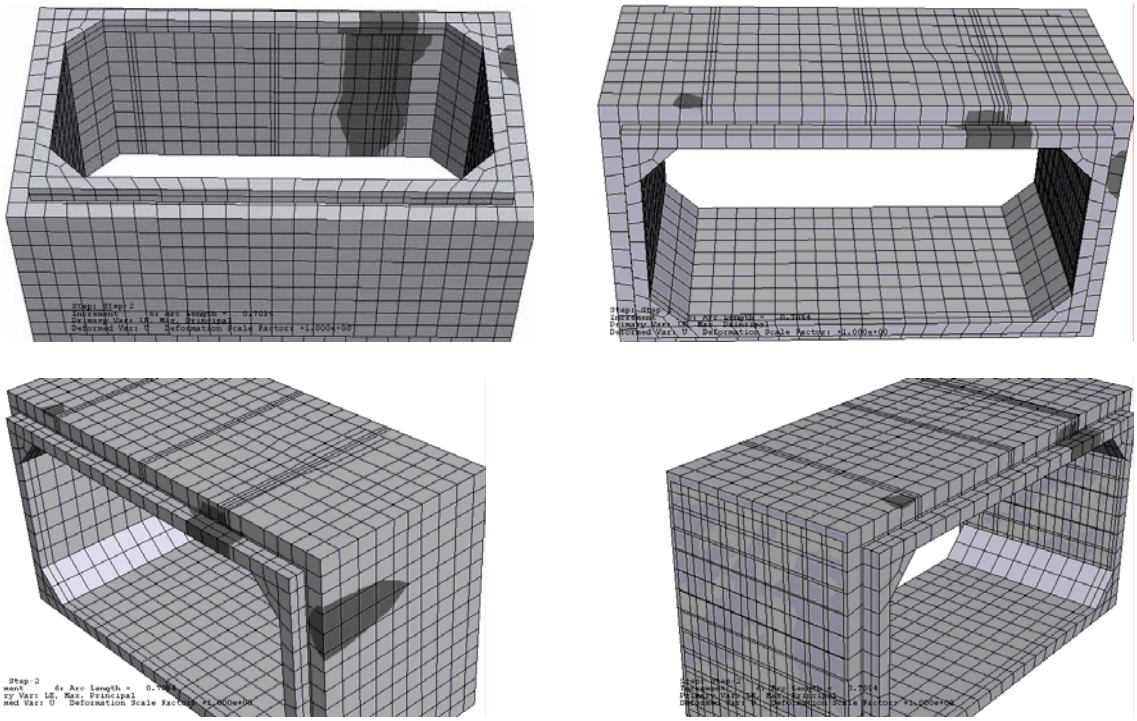

At 222 kN (50 kip) Load

Figure C14 FEM Crack Prediction of Model SP_244-122-122_N_d (SP_8-4-4_N_d)

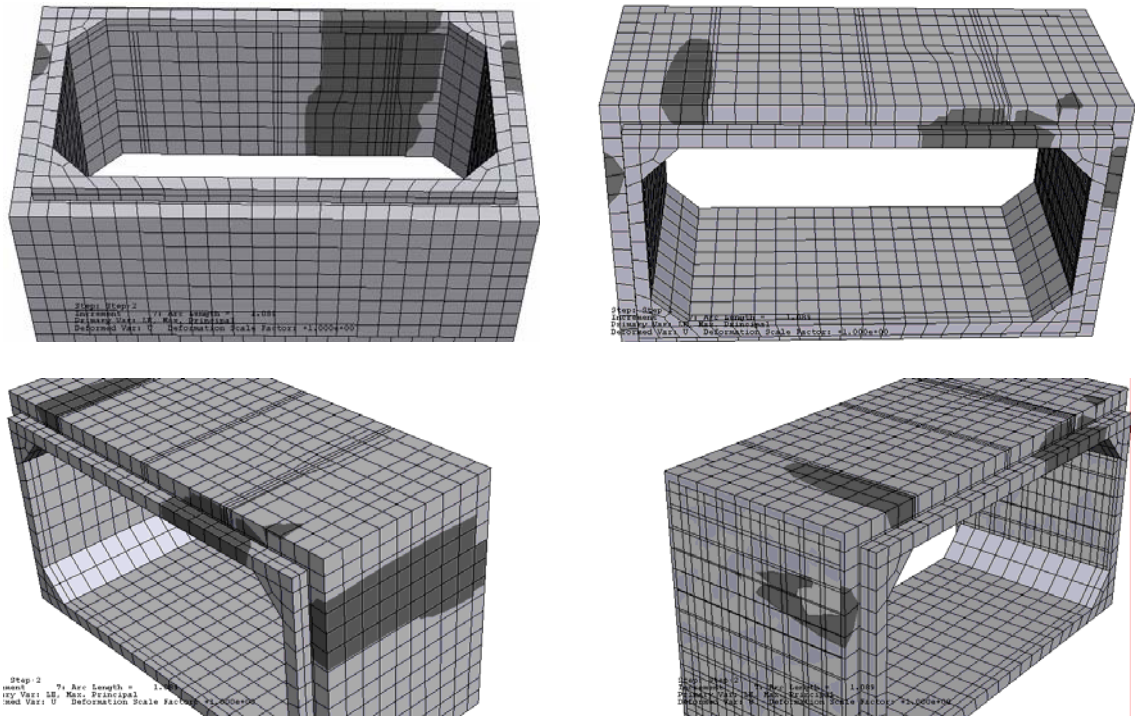

At 276 kN (62 kip) Load

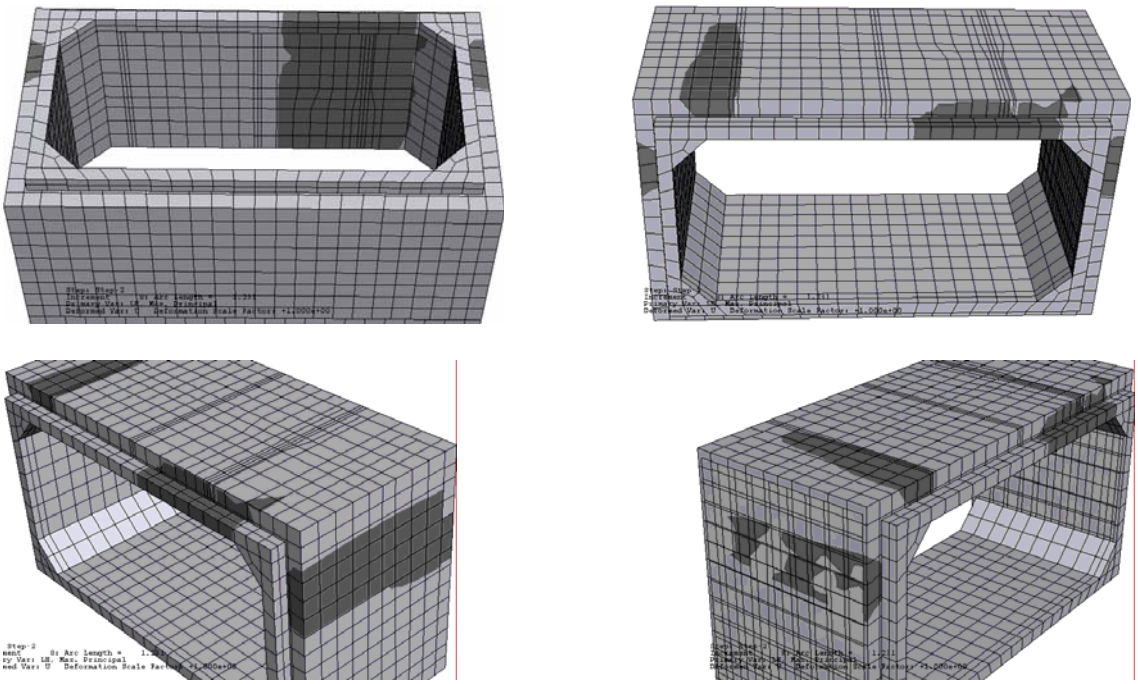

At 294 kN (66 kip) Load

Figure C15 FEM Crack Prediction of Model SP_244-122-122_N_d (SP_8-4-4_N_d)

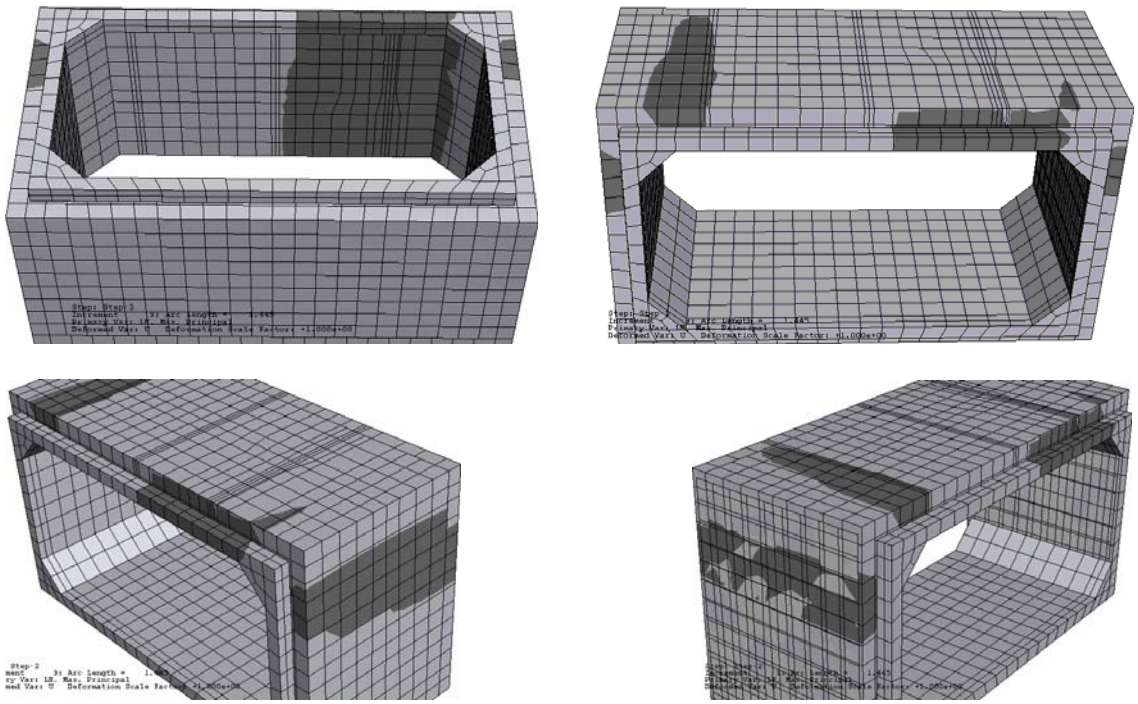

At 320 kN (72 kip) Load

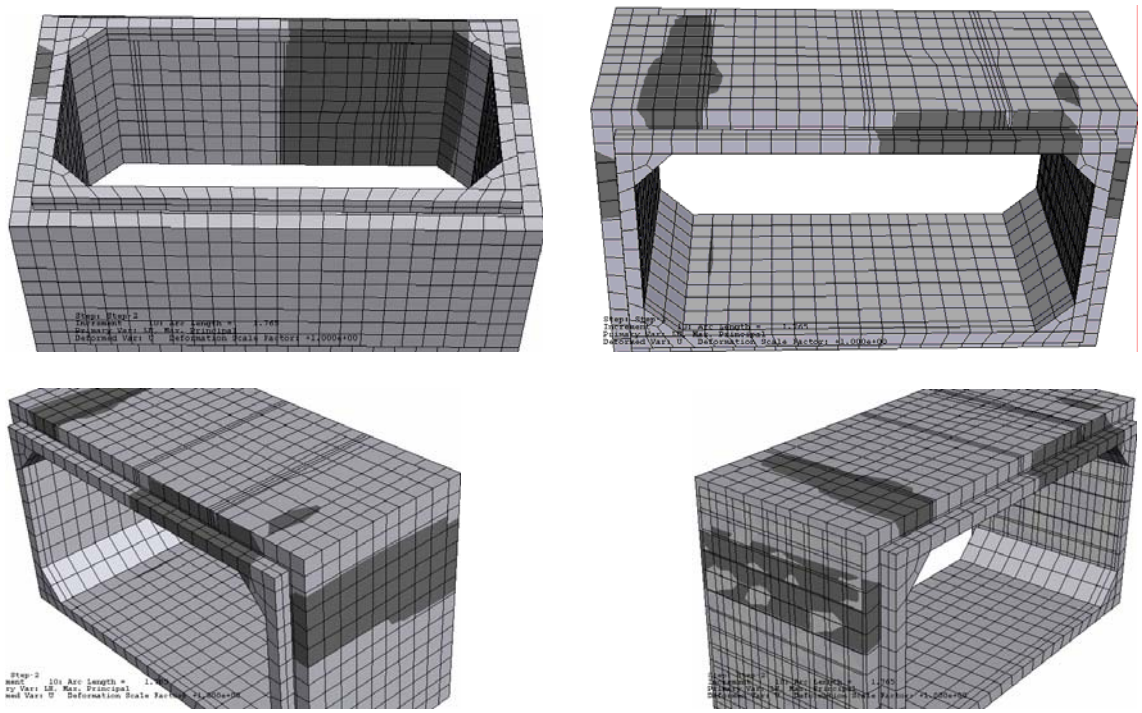

At 351 kN (79 kip) Load

Figure C16 FEM Crack Prediction of Model SP_244-122-122_N_d (SP_8-4-4_N_d)

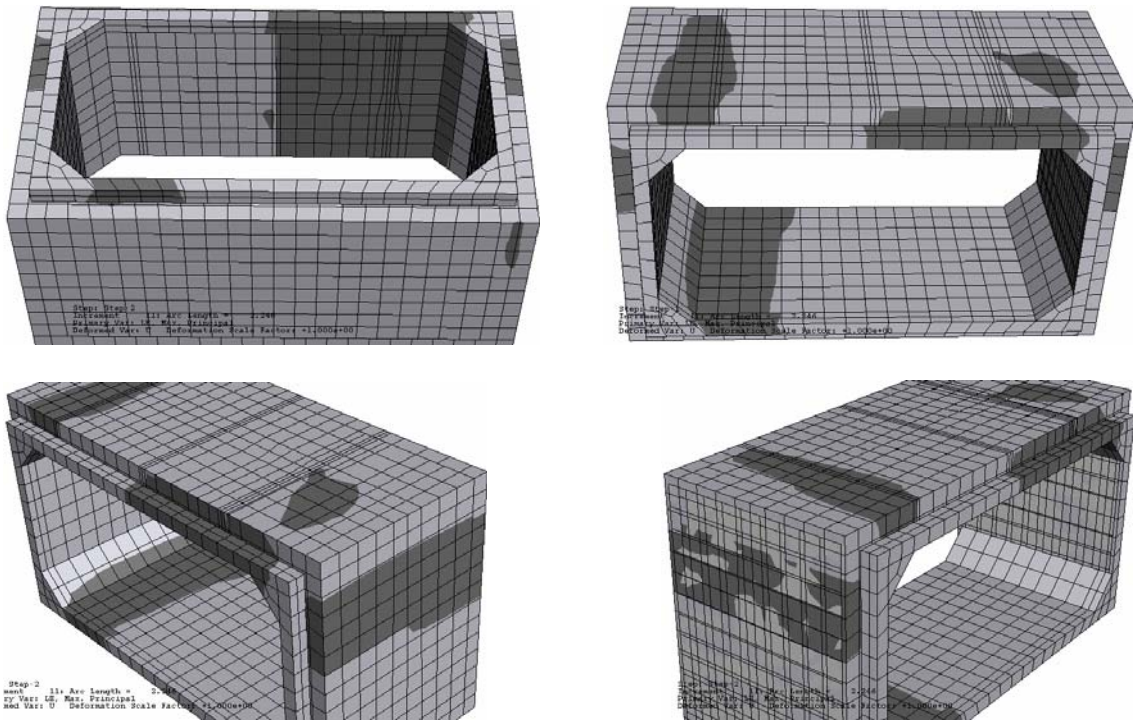

At 383 kN (86 kip) Load

Figure C17 FEM Crack Prediction of Model SP_244-122-122_N_d (SP_8-4-4_N_d)

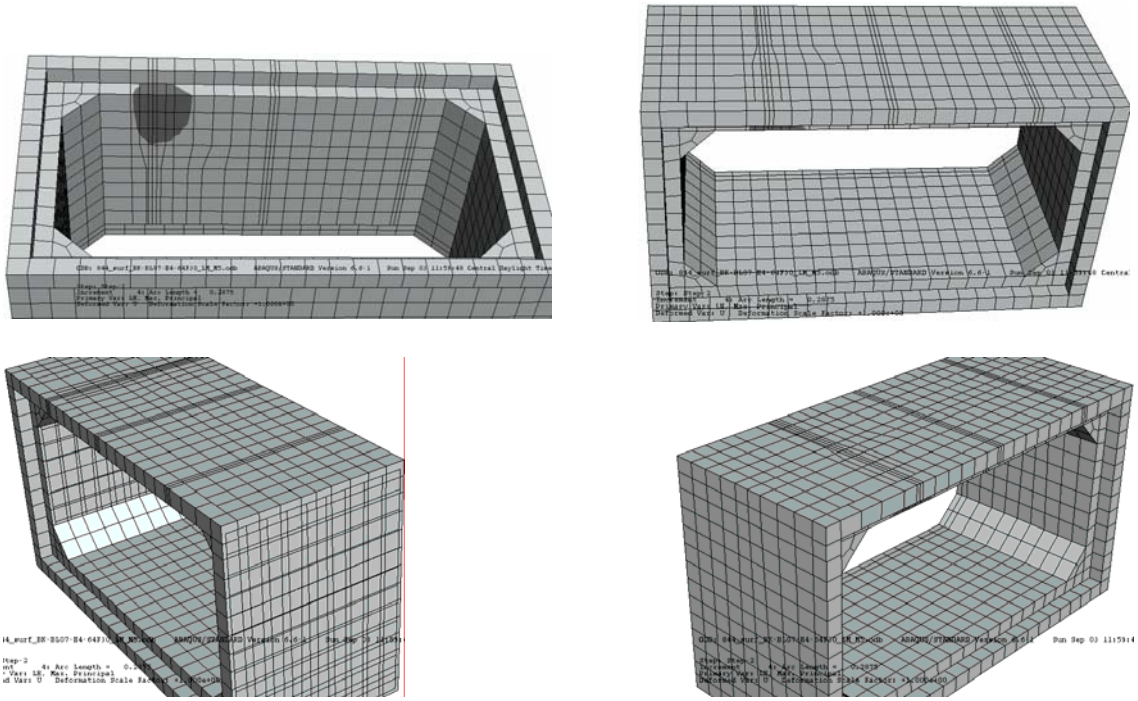

At 102 kN (23 kip) Load

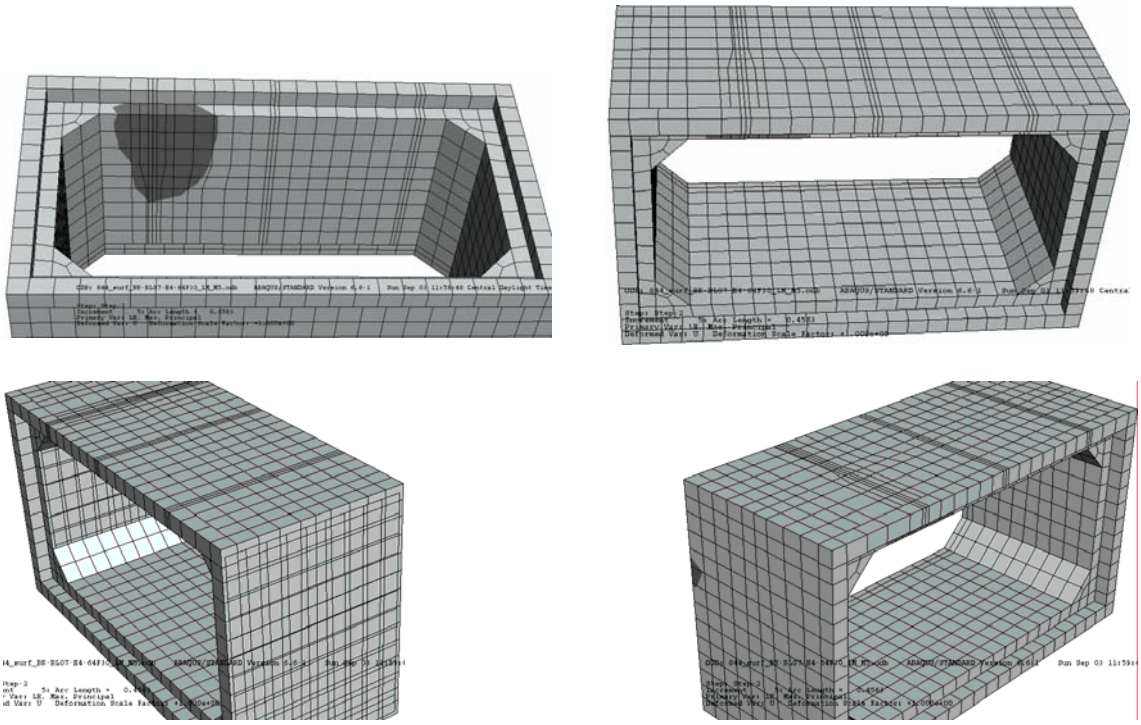

At 156 kN (35 kip) Load

Figure C18 FEM Crack Prediction of Model BL_244-122_122_N_d (BL_8-4-4_N_d)

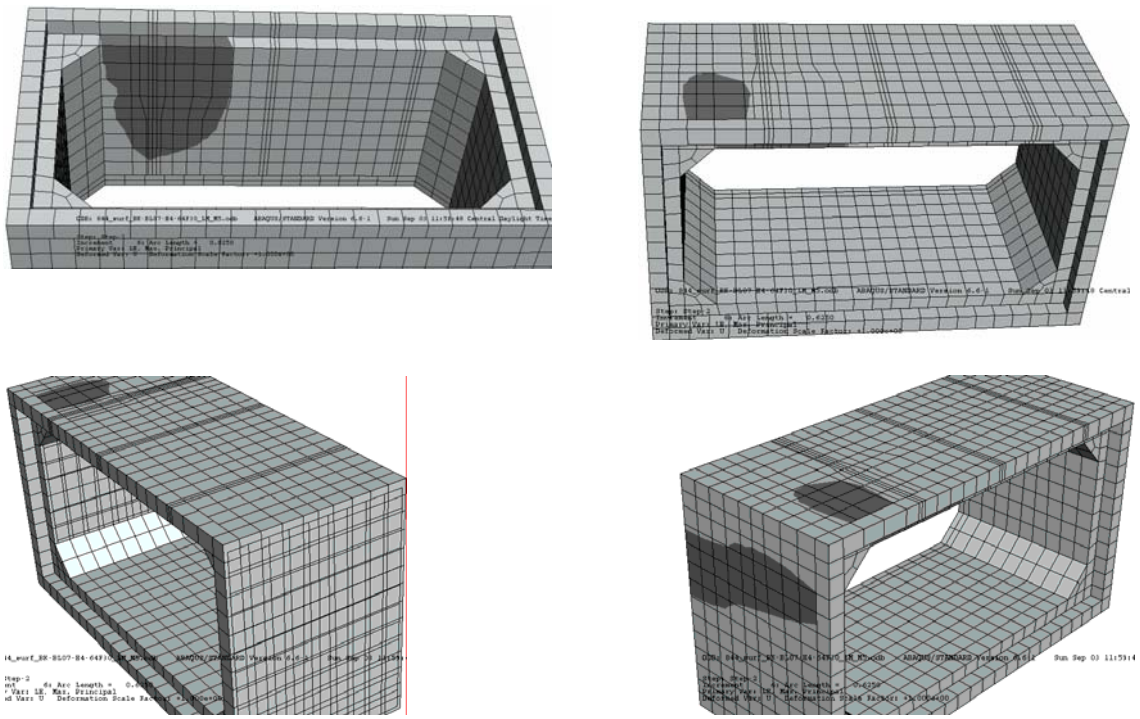

At 196 kN (44 kip) Load

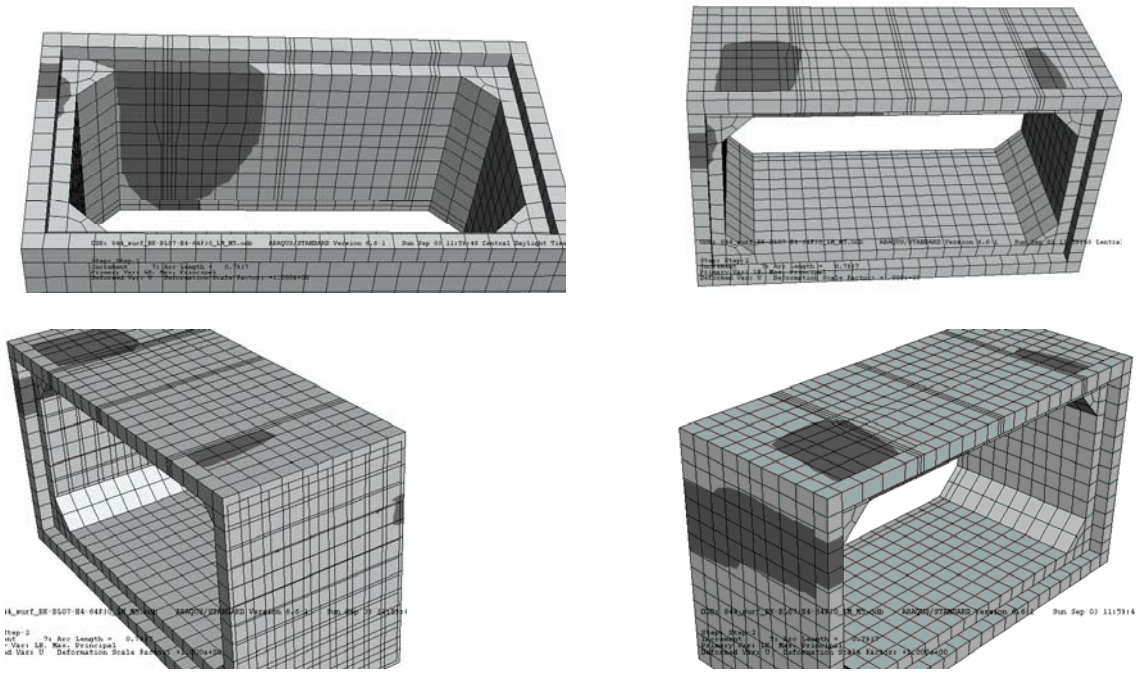

At 227 kN (51 kip) Load

Figure C19 FEM Crack Prediction of Model BL_244-122_122_N_d (BL_8-4-4_N_d)

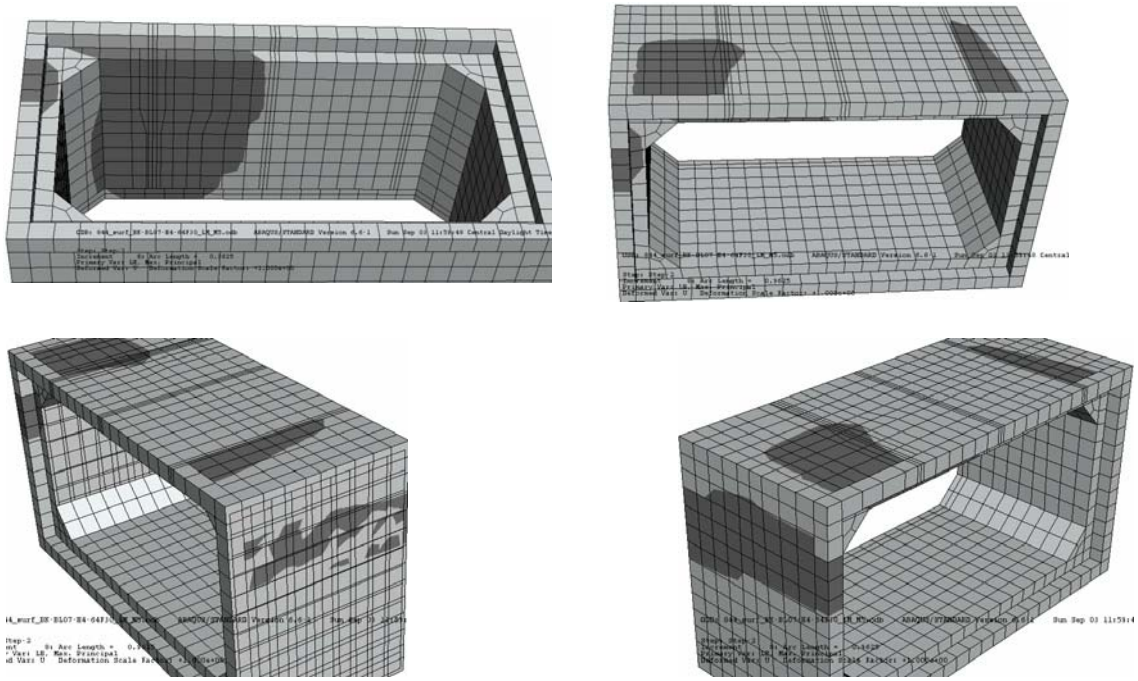

At 245 kN (55 kip) Load

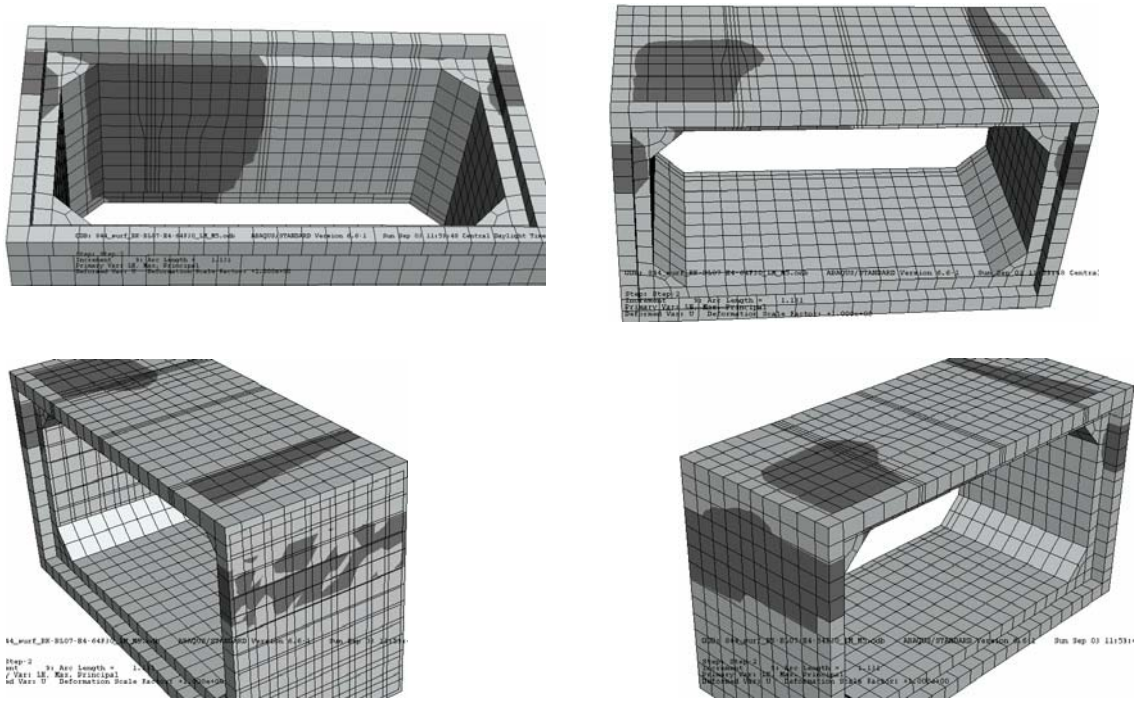

At 262 kN (59 kip) Load

Figure C20 FEM Crack Prediction of Model BL_244-122_122_N_d (BL_8-4-4_N_d)

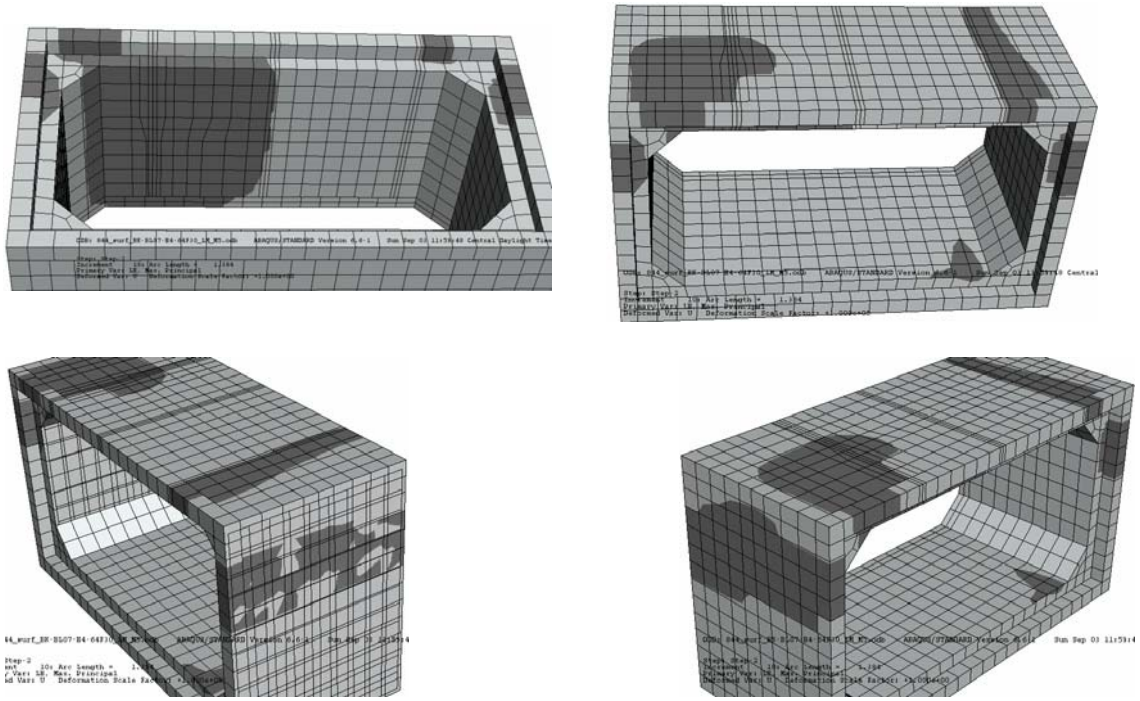

At 276 kN (62 kip) Load

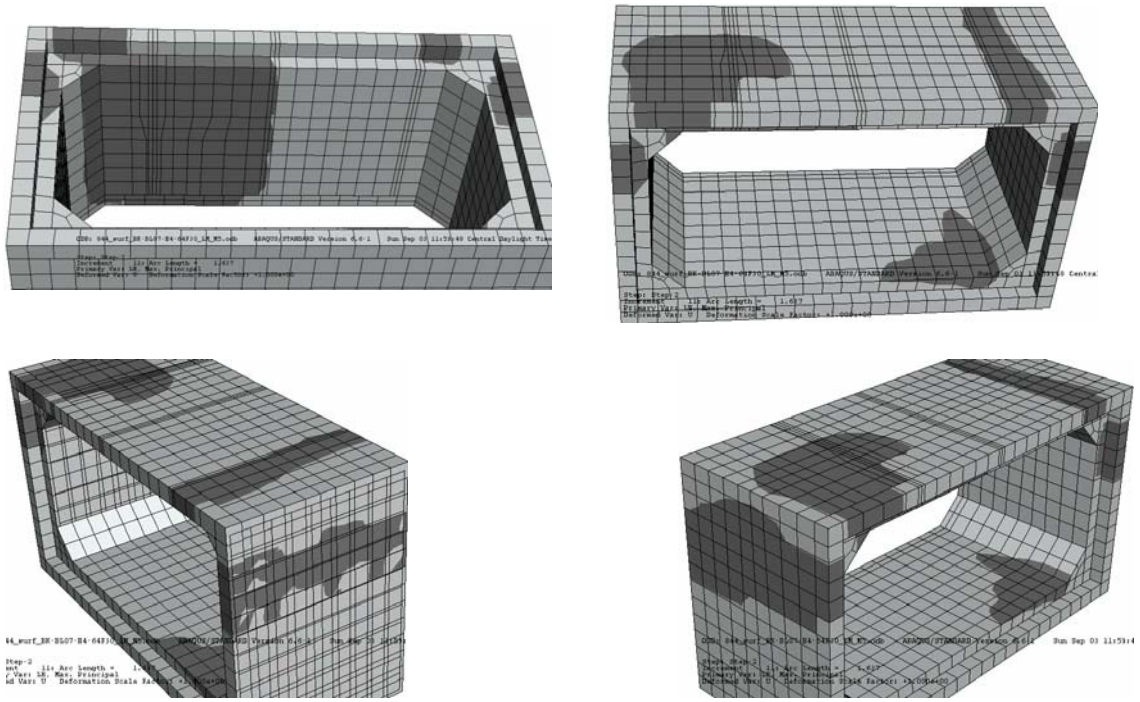

At 294 kN (66 kip) Load

Figure C21 FEM Crack Prediction of Model BL_244-122_122_N_d (BL_8-4-4_N_d)

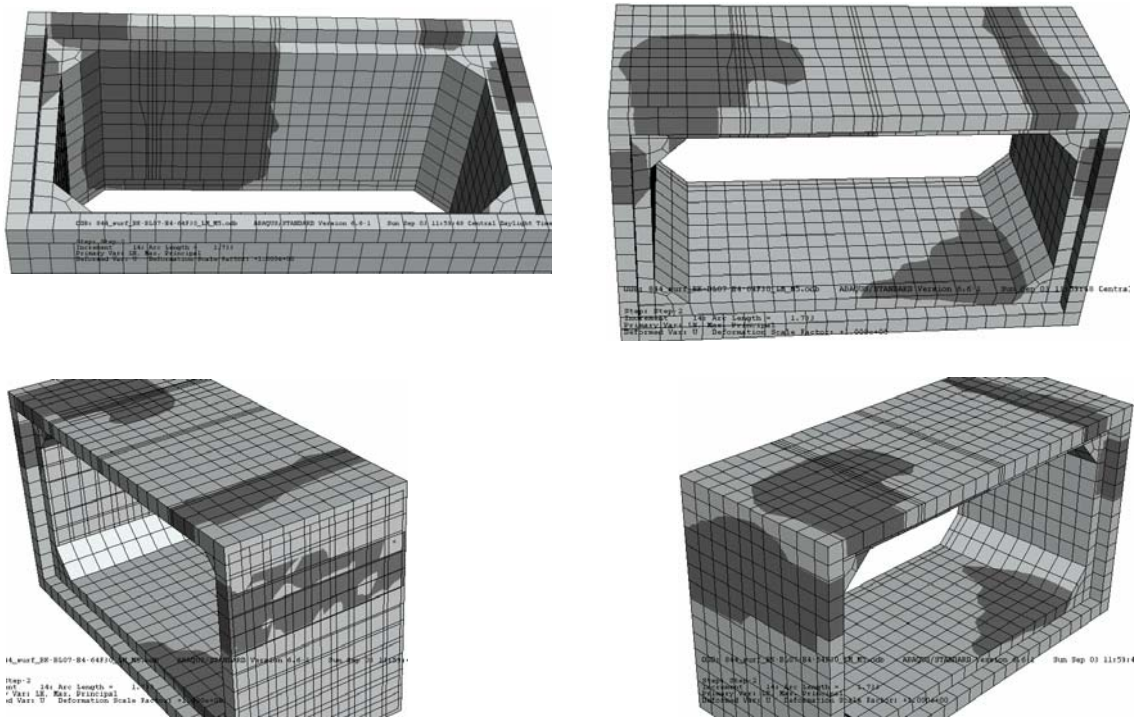

At 298 kN (67 kip) Load

Figure C22 FEM Crack Prediction of Model BL_244-122_122_N_d (BL_8-4-4_N_d)

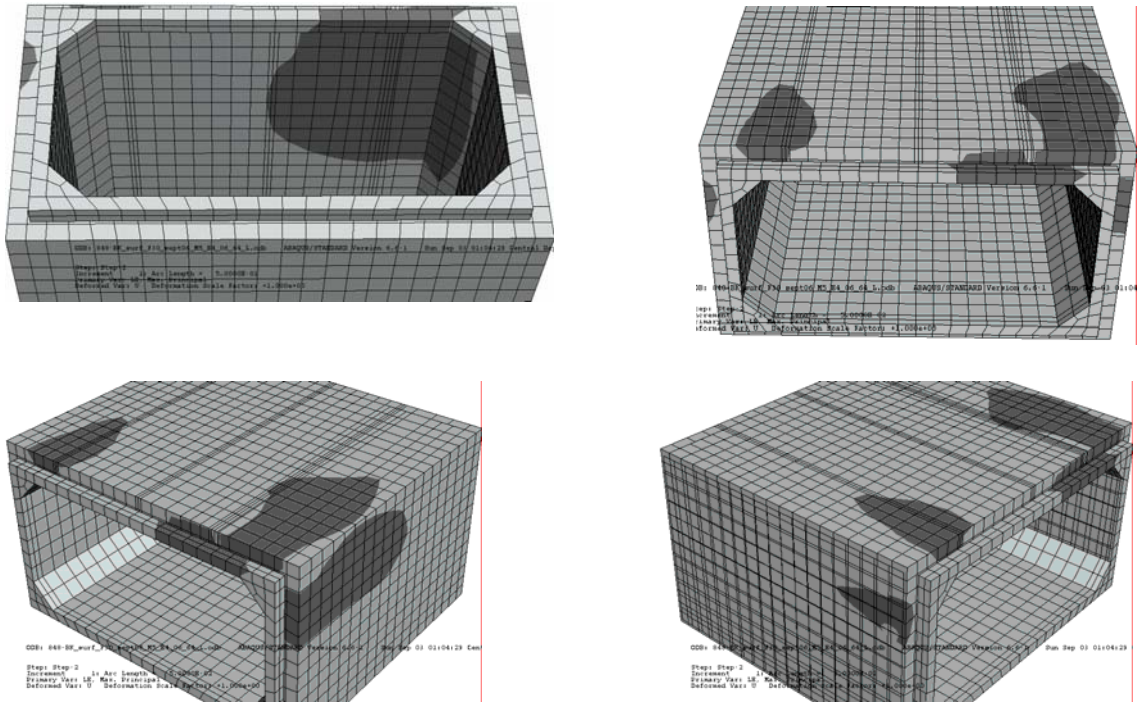

At 307 kN (69 kip) Load

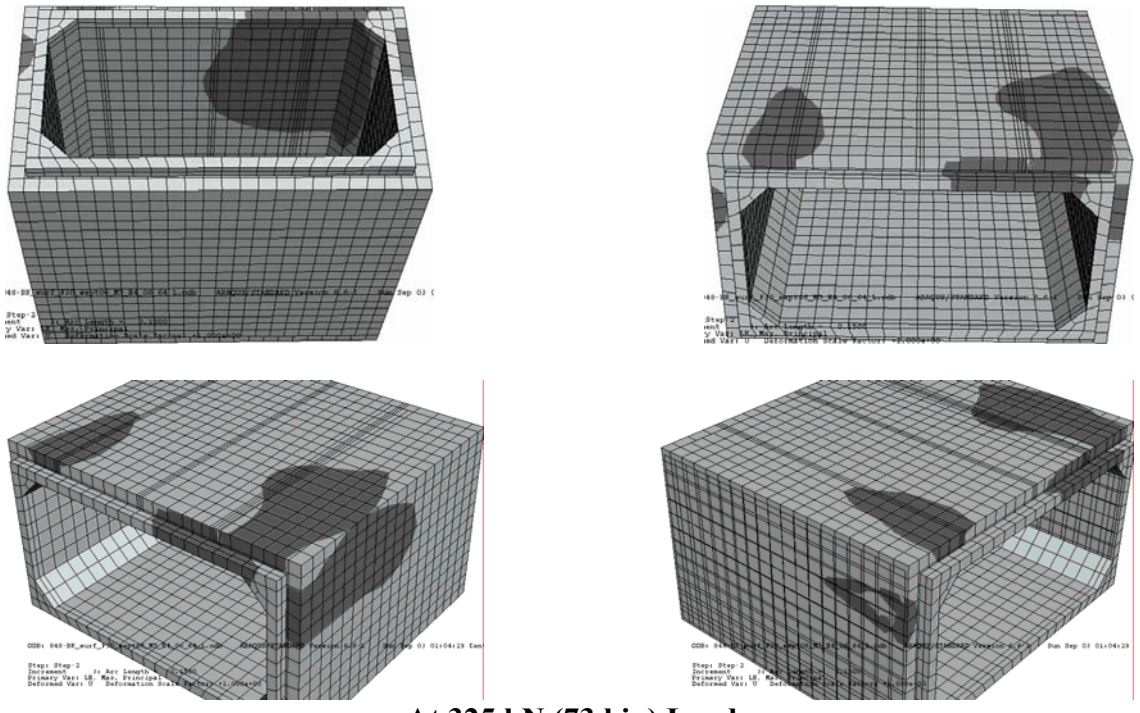

At 325 kN (73 kip) Load

Figure C23 FEM Crack Prediction of Model SP_244-122_244_N_d (SP_8-4-8_N_d)

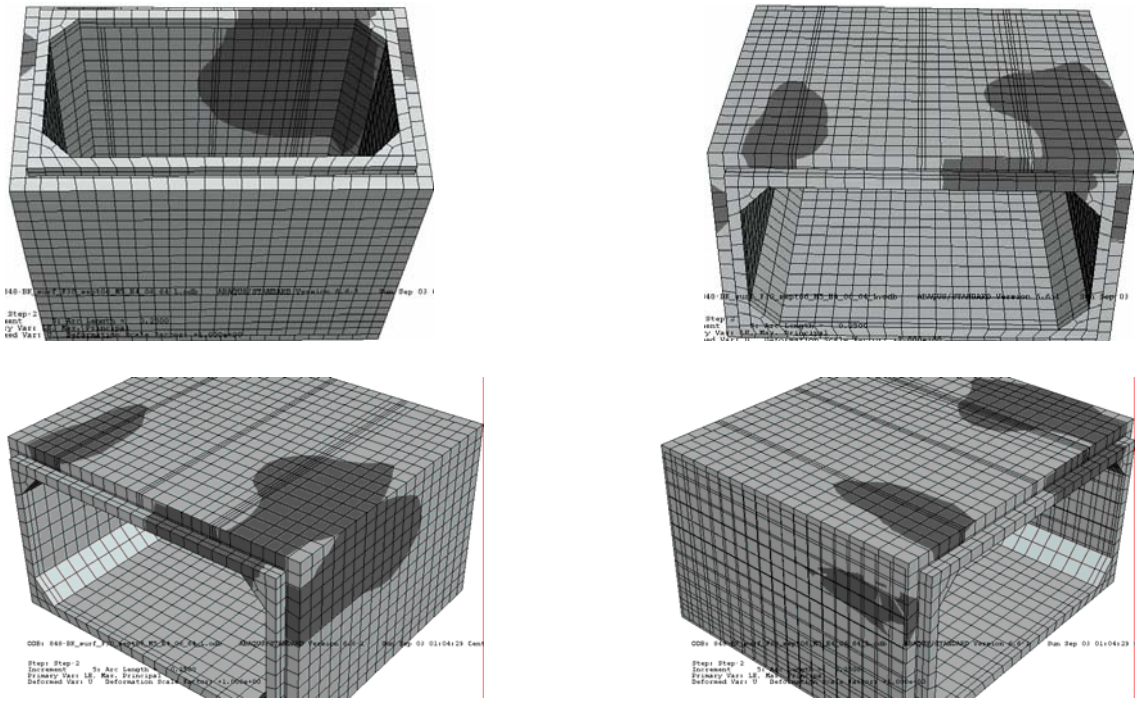

At 343 kN (77 kip) Load

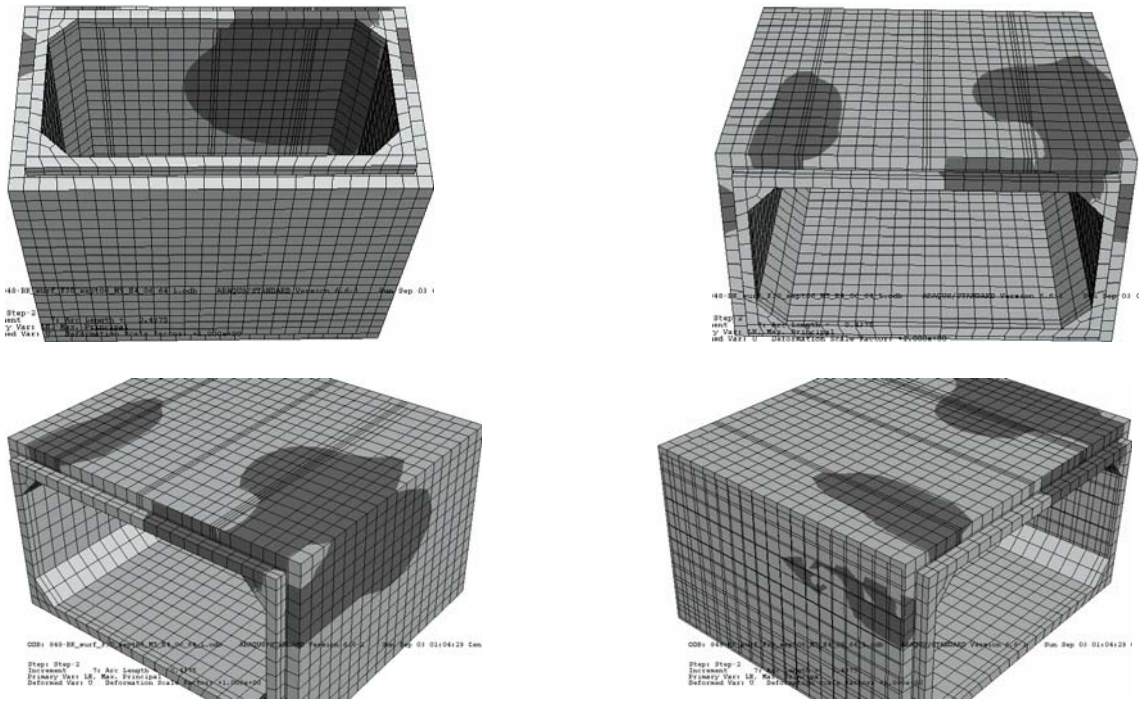

At 374 kN (84 kip) Load

Figure C24 FEM Crack Prediction of Model SP_244-122_244_N_d (SP_8-4-8_N_d)

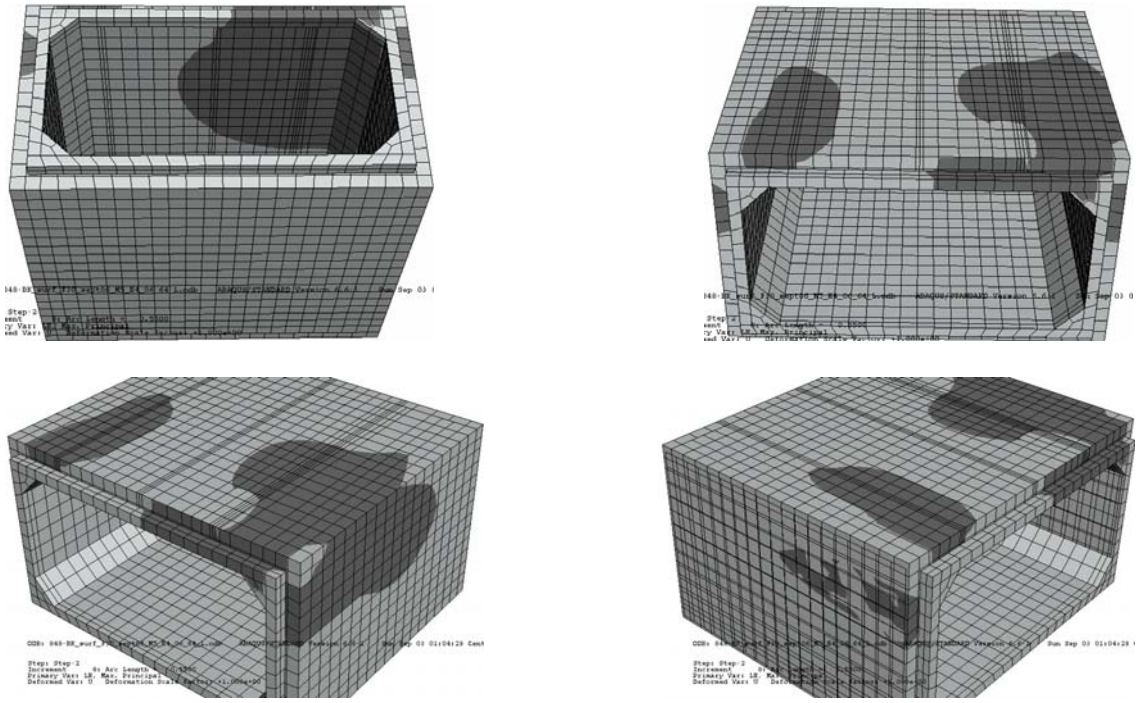

At 400 kN (90 kip) Load

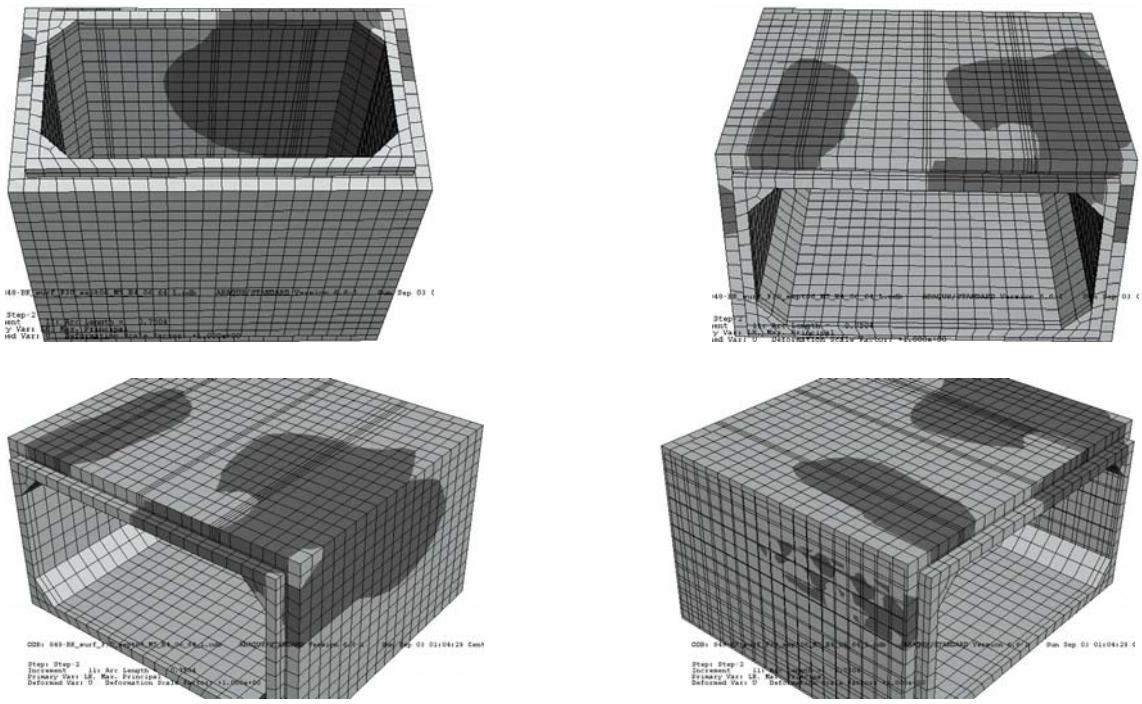

At 418 kN (94 kip) Load

Figure C25 FEM Crack Prediction of Model SP_244-122_244_N_d (SP_8-4-8_N_d)

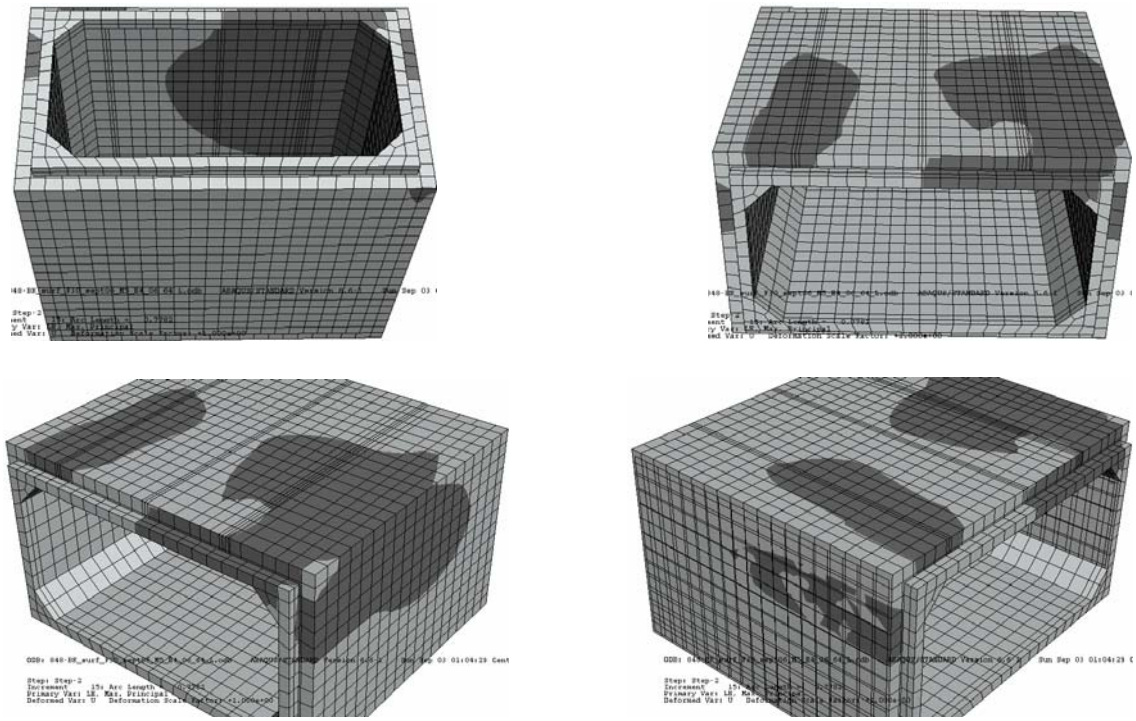

At 427 kN (96 kip) Load

Figure C26 FEM Crack Prediction of Model SP_244-122_244_N_d (SP_8-4-8_N_d)

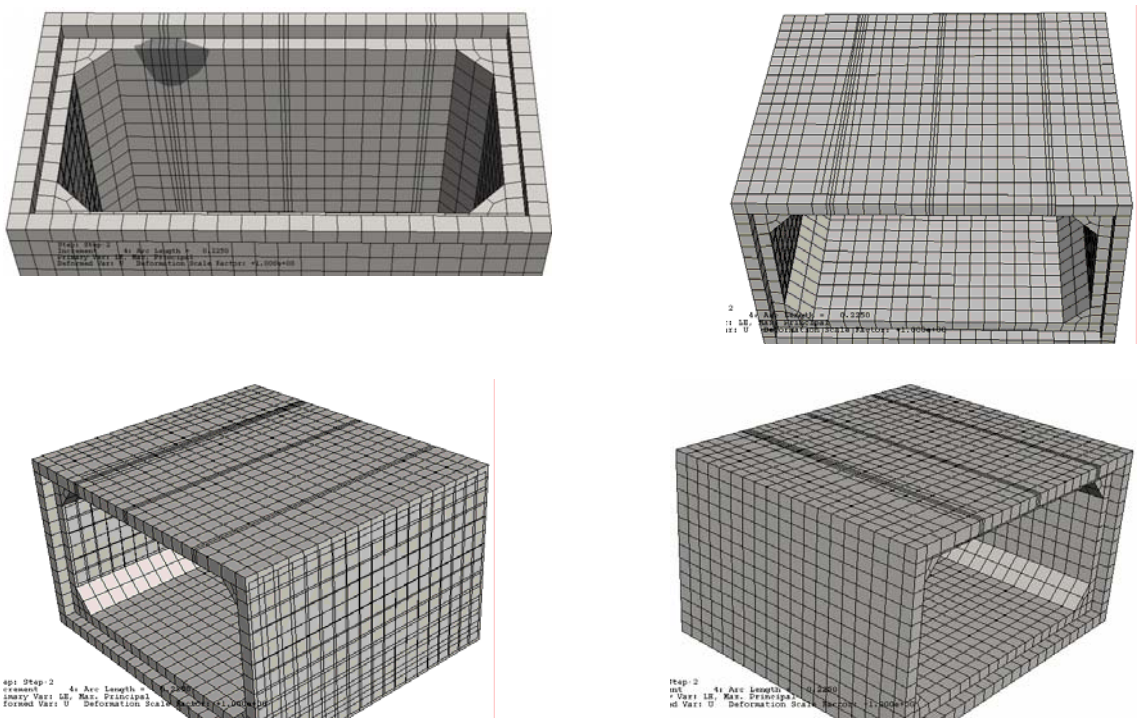

At 76 kN (17 kip) Load

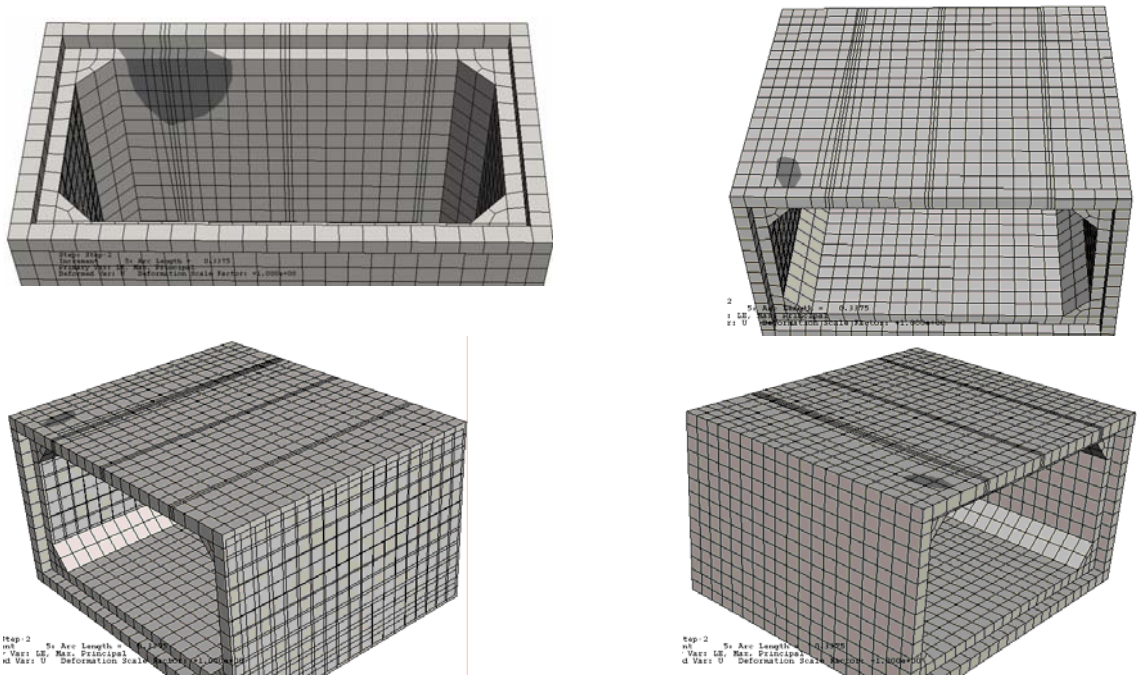

At 108 kN (24 kip) Load

Figure C27 FEM Crack Prediction of Model BL_244-122_244_N_d (BL_8-4-8_N_d)

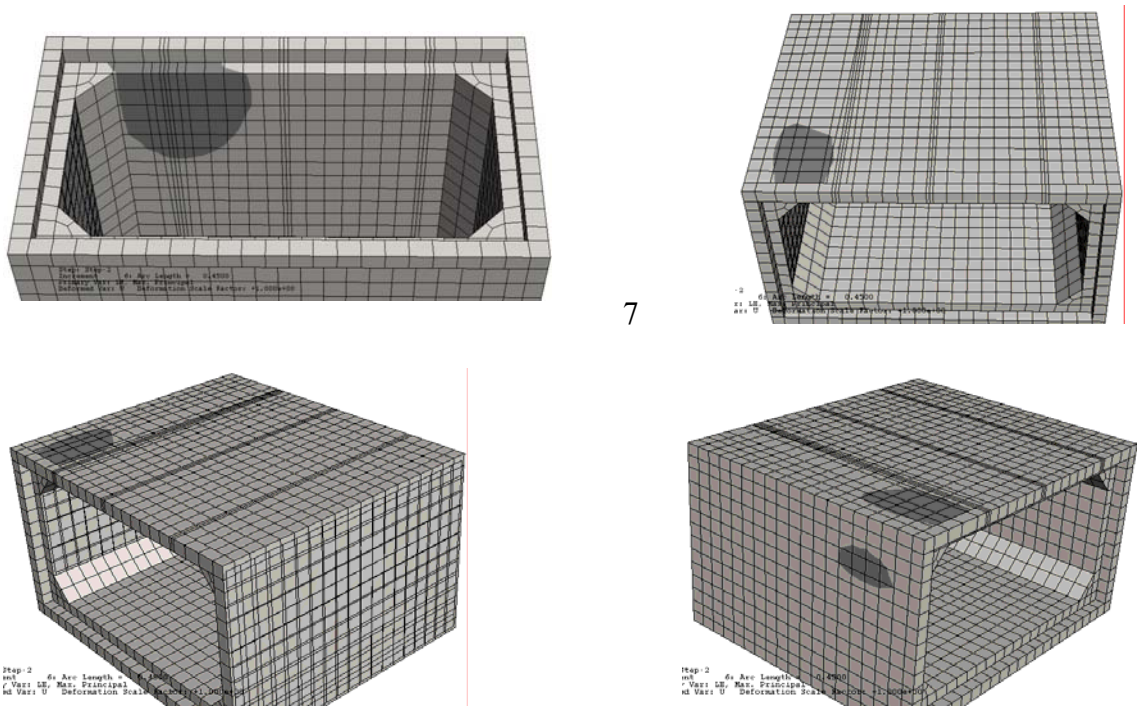

7

At 138 kN (31 kip) Load

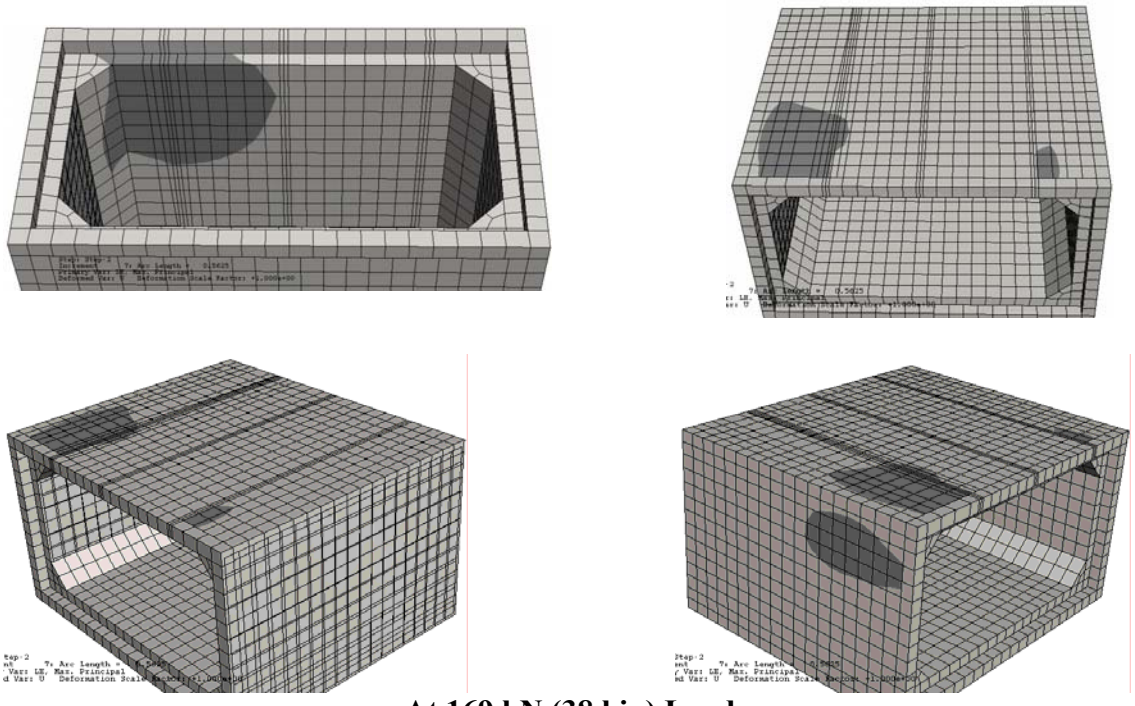

At 169 kN (38 kip) Load

Figure C28 FEM Crack Prediction of Model BL_244-122_244_N_d (BL_8-4-8_N_d)

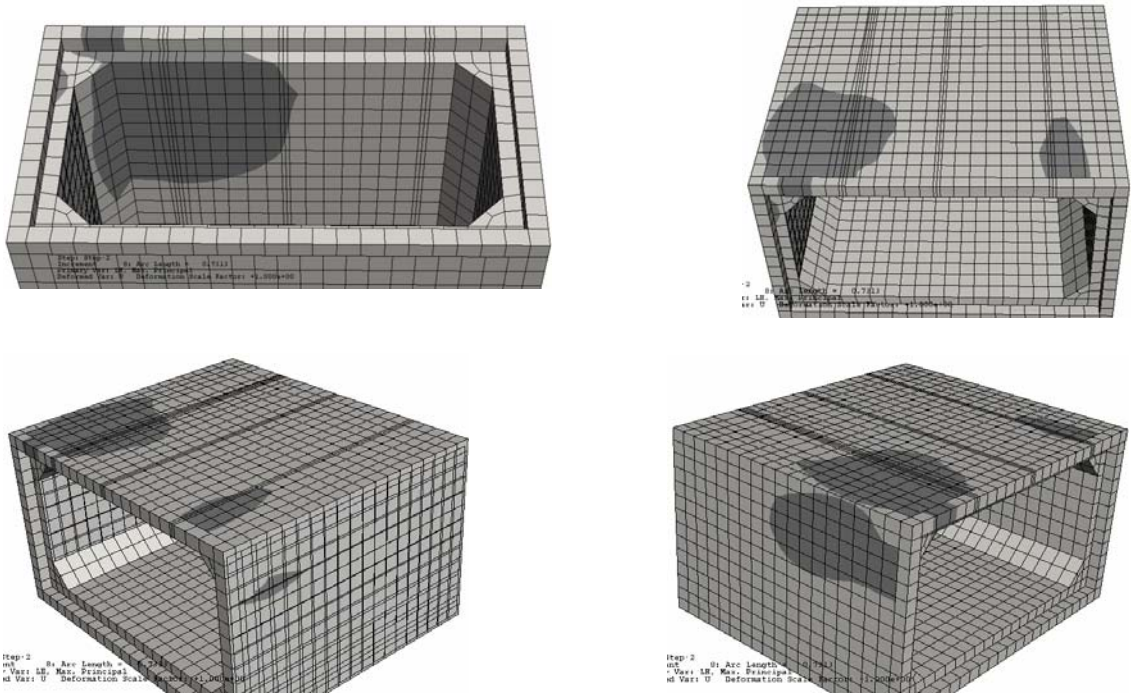

At 214 kN (48 kip) Load

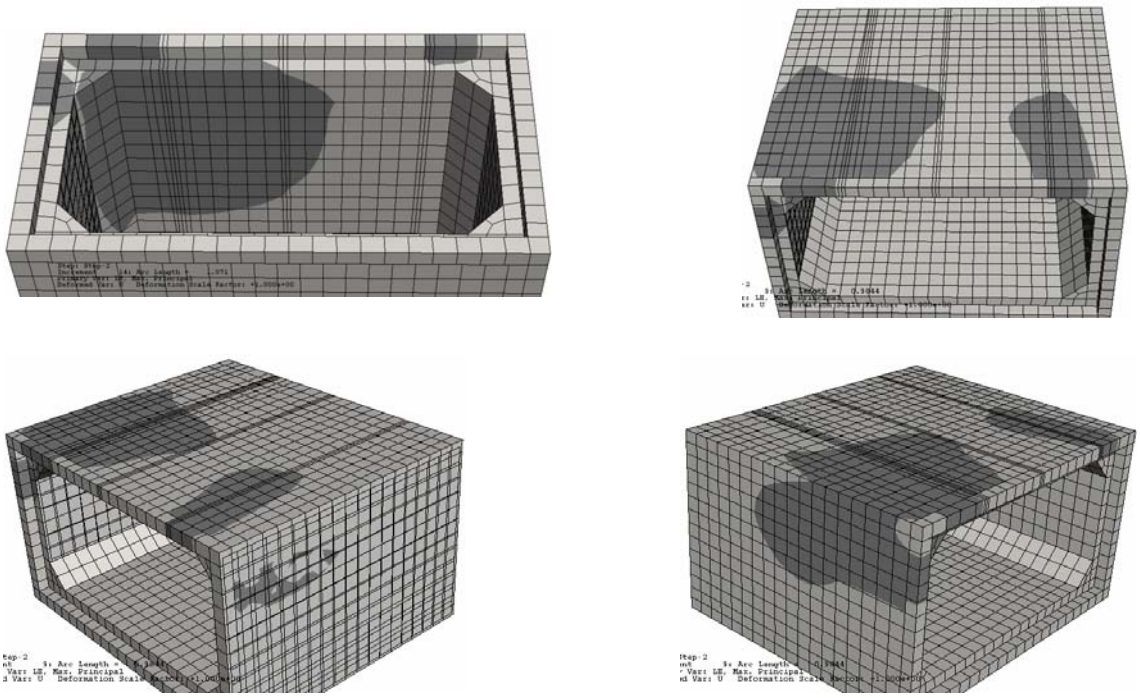

At 258 kN (58 kip) Load

Figure C29 FEM Crack Prediction of Model BL_244-122_244_N_d (BL_8-4-8_N_d)

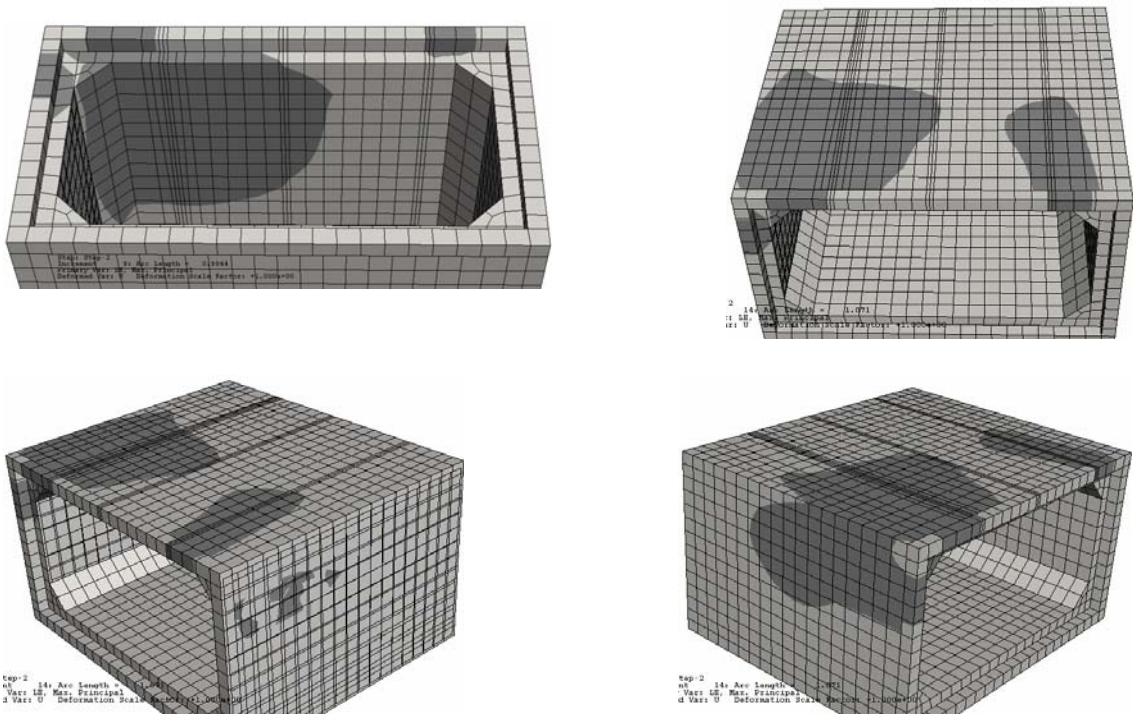

At 262 kN (59 kip) Load

Figure C30 FEM Crack Prediction of Model BL_244-122_244_N_d (BL_8-4-8_N_d)

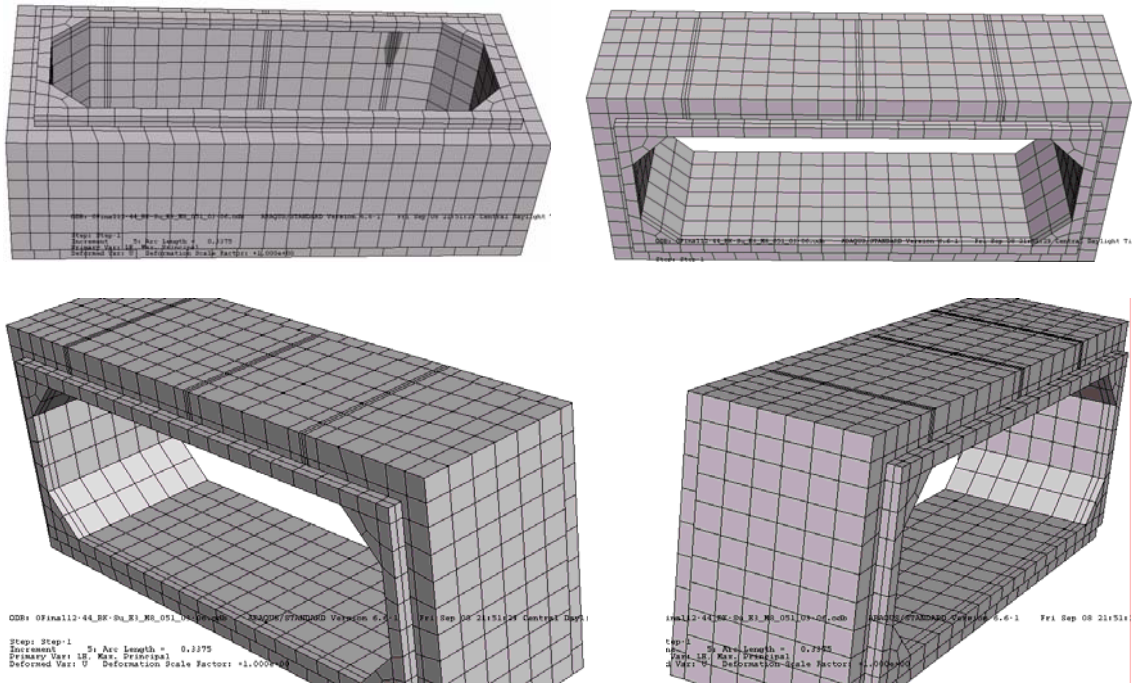

At 120 kN (27 kip) Load

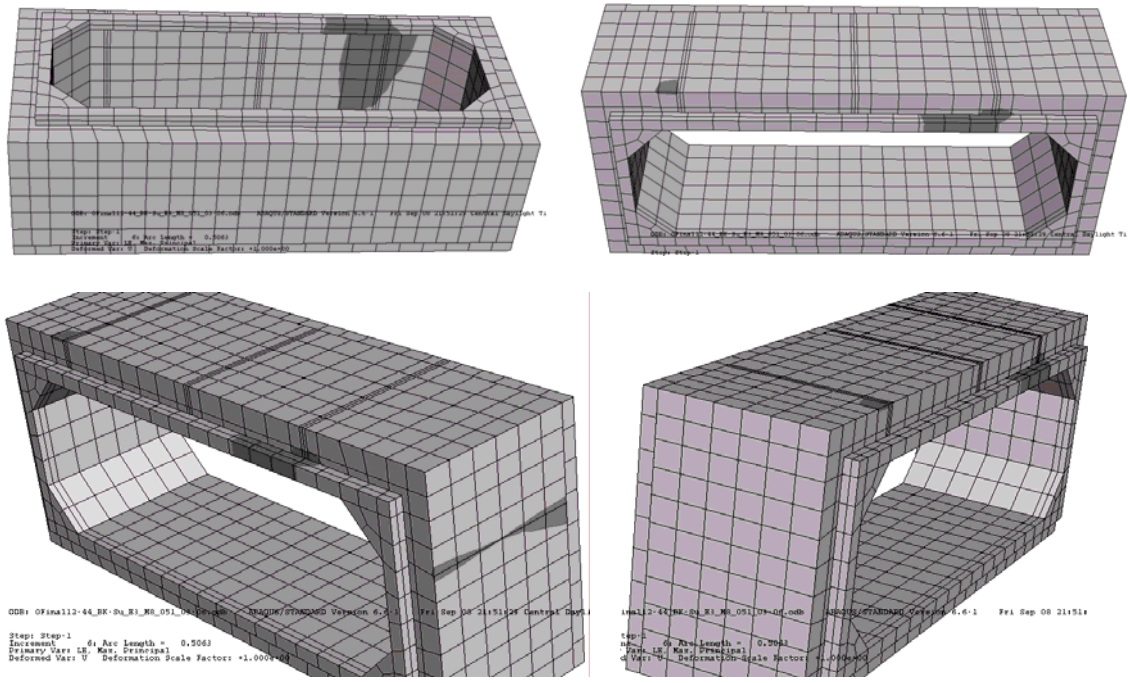

At 178 kN (40 kip) Load

Figure C31 FEM Crack Prediction of Model SP_366-122_122_N_d (SP_12-4-4_N_d)

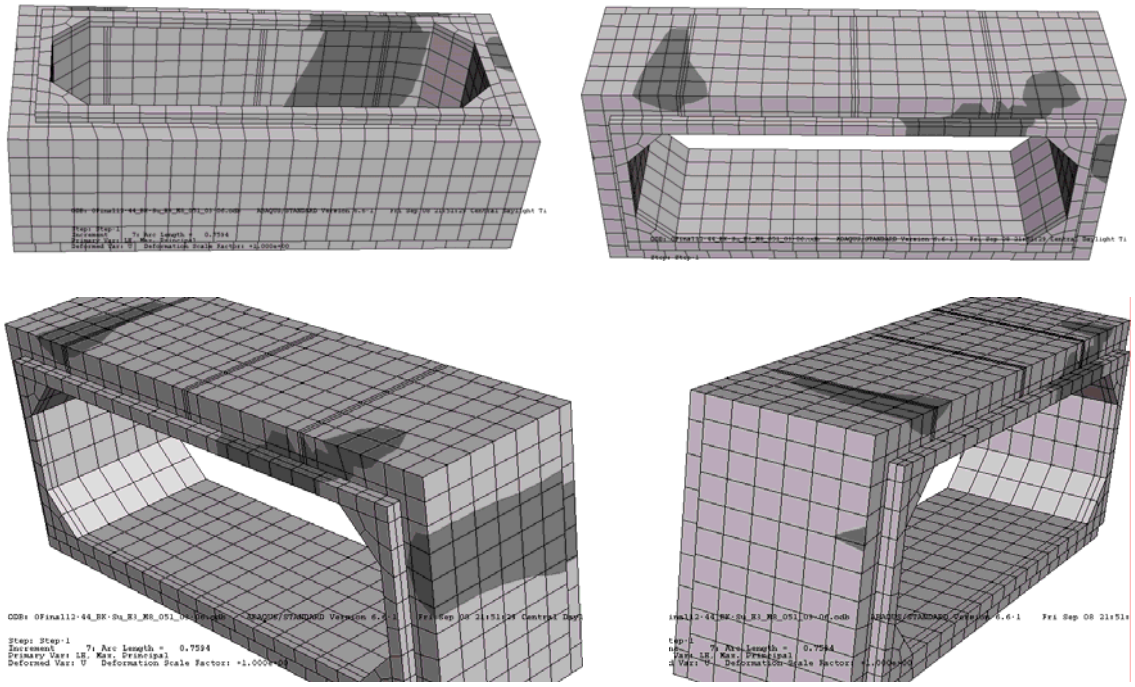

At 254 kN (57 kip) Load

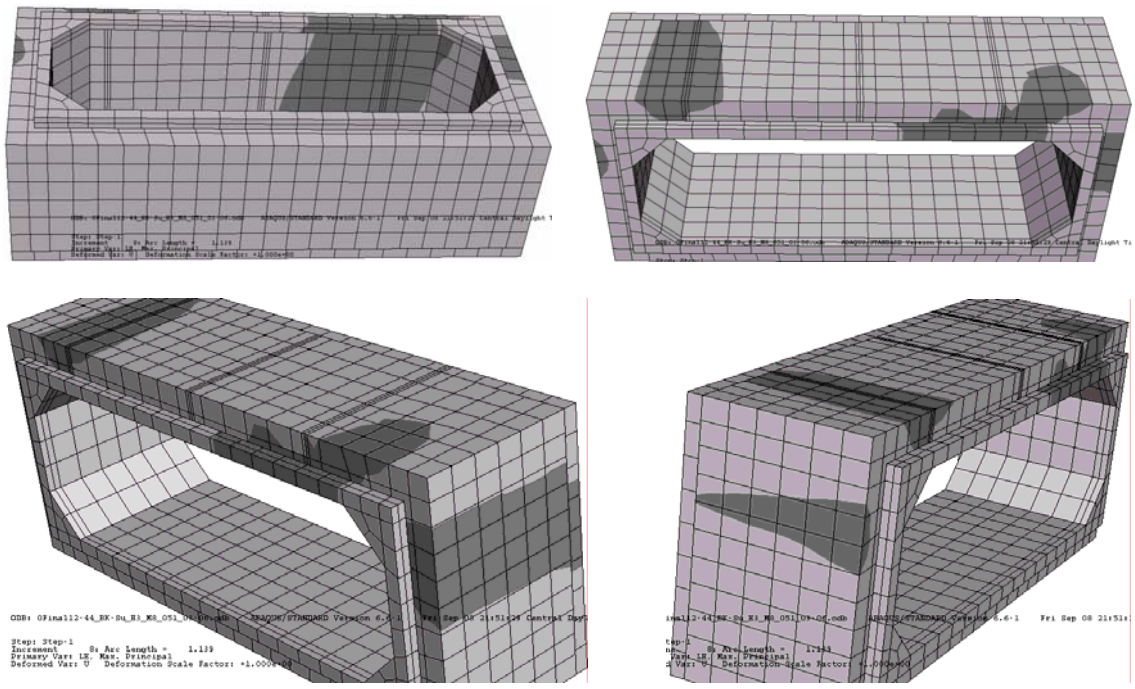

At 307 kN (69 kip) Load

Figure C32 FEM Crack Prediction of Model SP_366-122_122_N_d (SP_12-4-4_N_d)

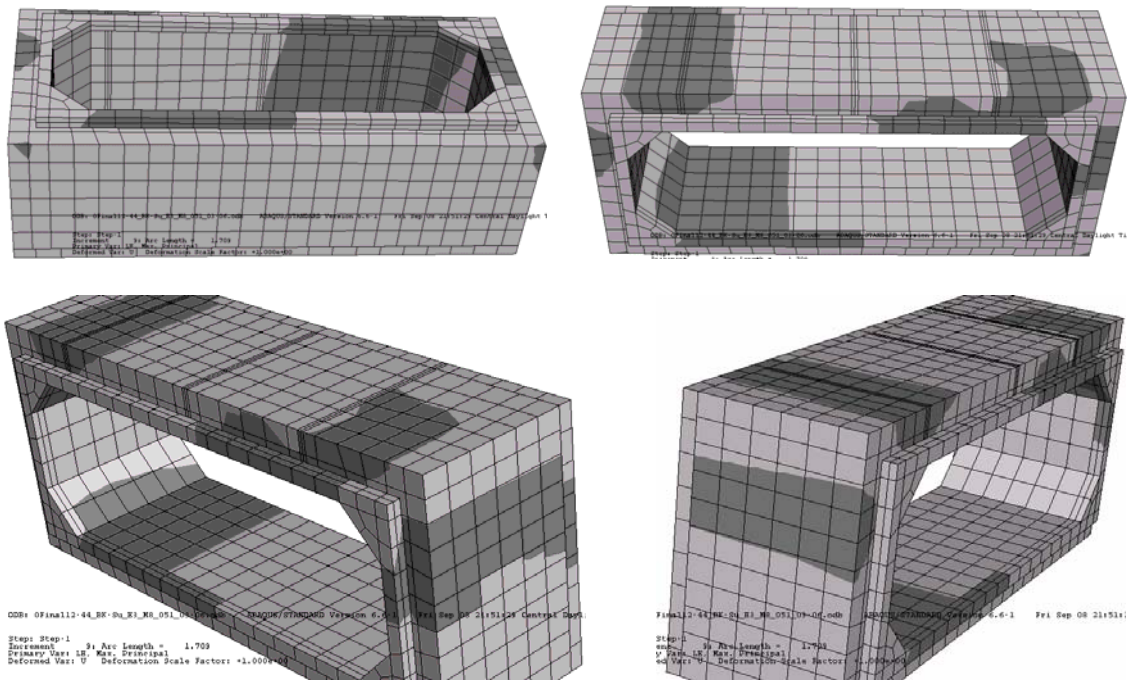

At 369 kN (83 kip) Load

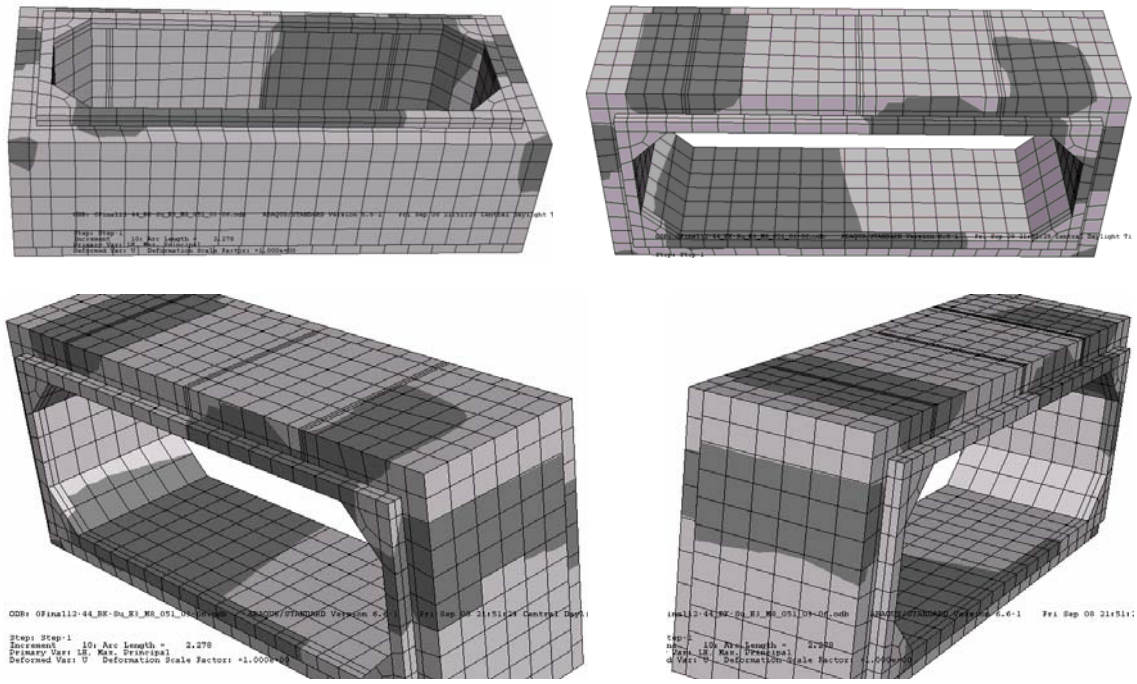

At 405 kN (91 kip) Load

Figure C33 FEM Crack Prediction of Model SP_366-122_122_N_d (SP_12-4-4_N_d)

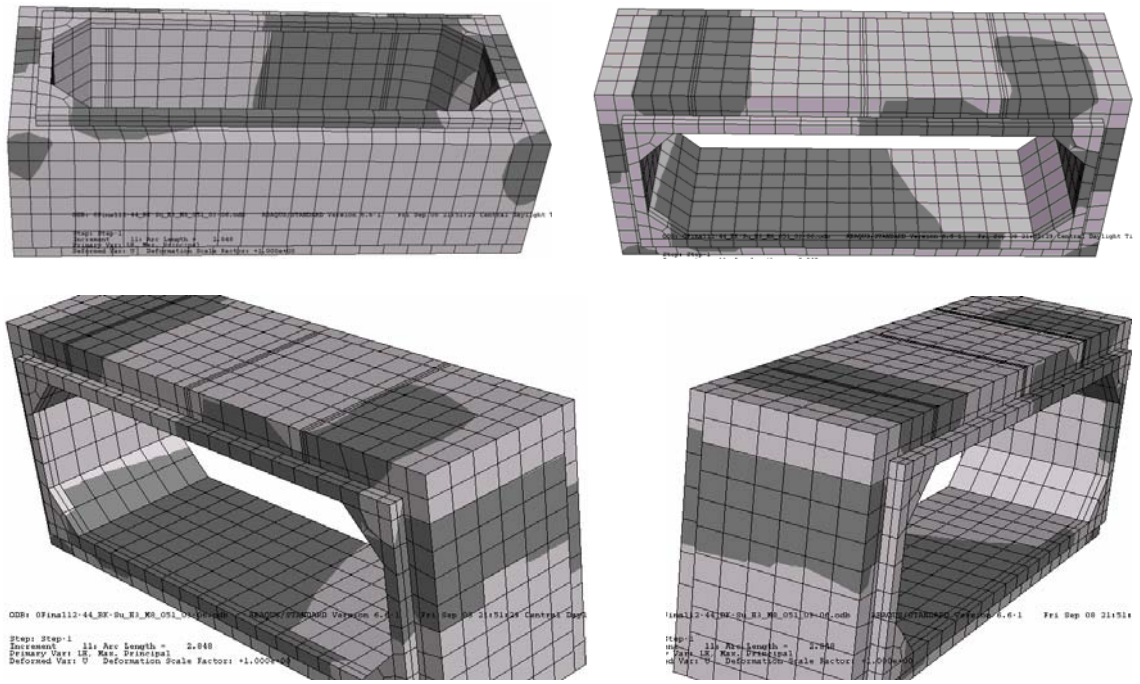

At 436 kN (98 kip) Load

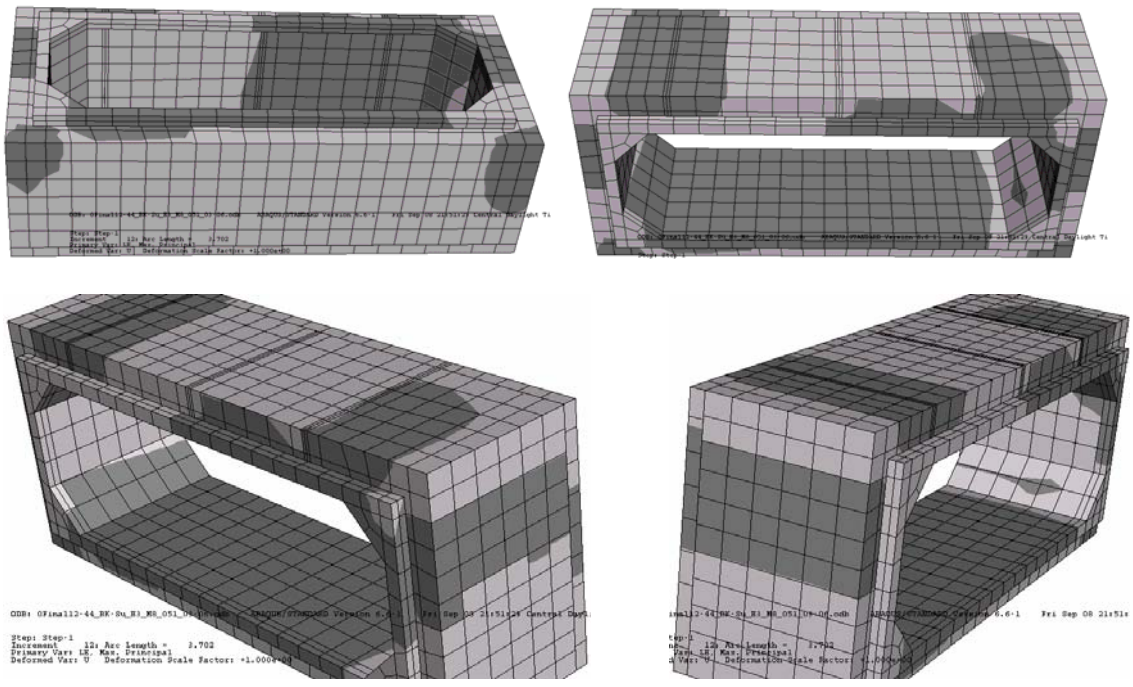

At 467 kN (105 kip) Load

Figure C34 FEM Crack Prediction of Model SP_366-122_122_N_d (SP_12-4-4_N_d)

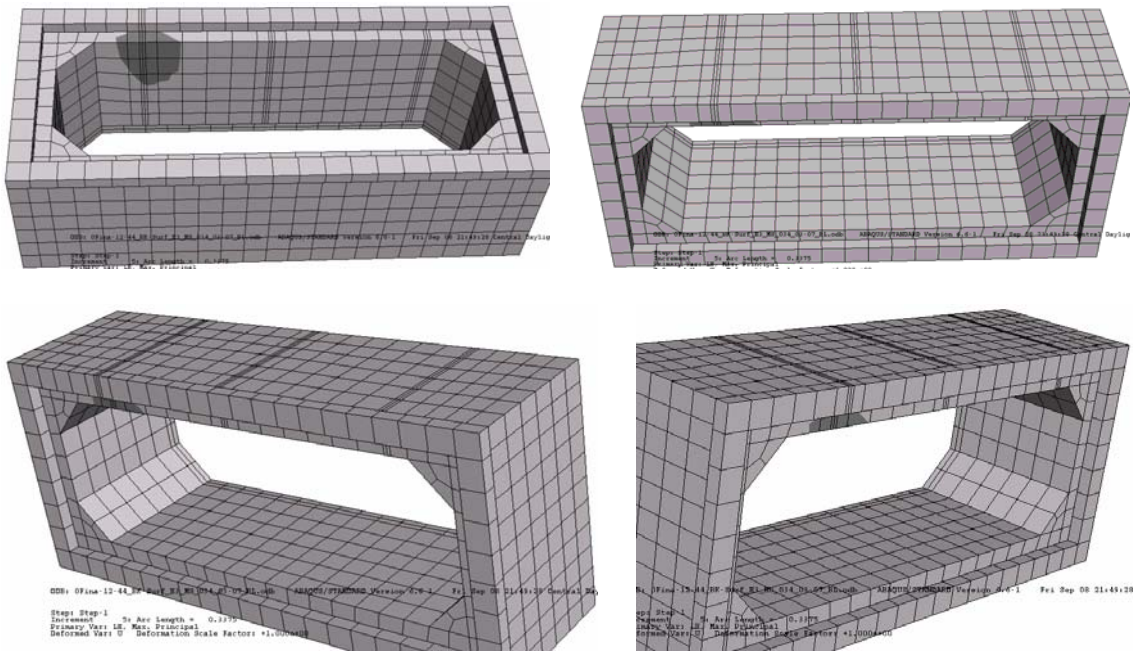

At 116 kN (26 kip) Load

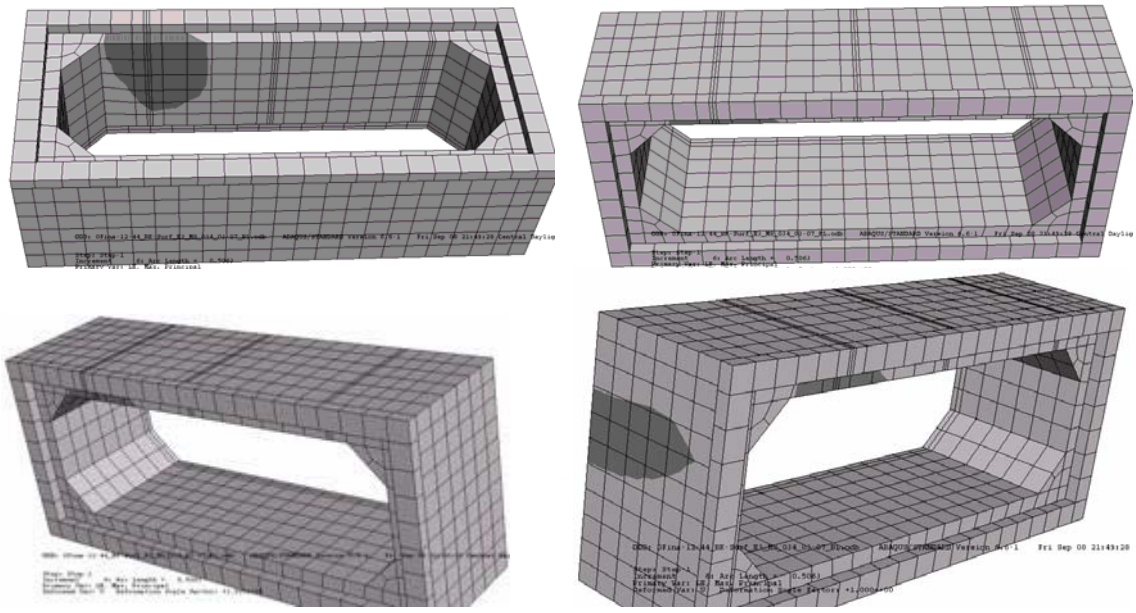

At 160 kN (36 kip) Load

Figure C35 FEM Crack Prediction of Model BL_366-122_122_N_d (BL_12-4-4_N_d)

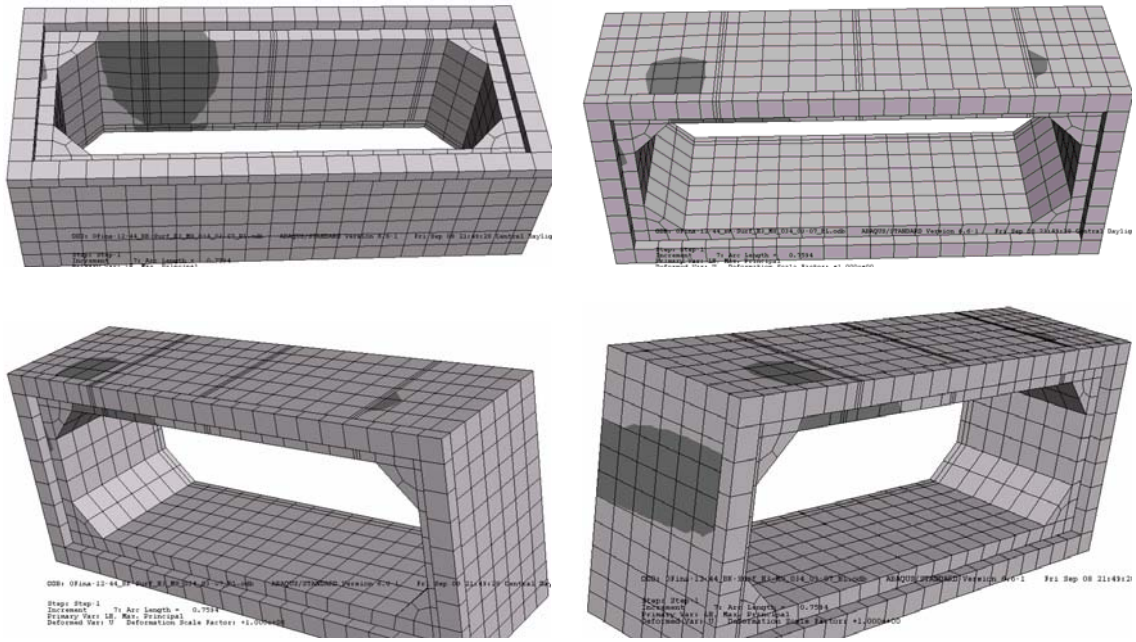

At 191 kN (43 kip) Load

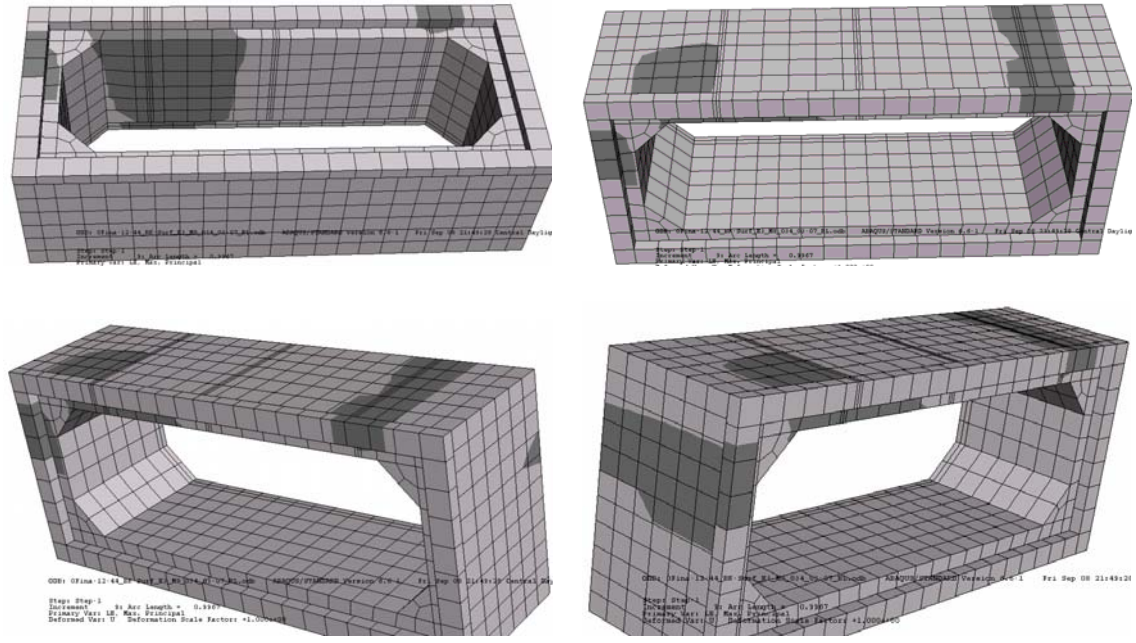

At 222 kN (50 kip) Load

Figure C36 FEM Crack Prediction of Model BL_366-122_122_N_d (BL_12-4-4_N_d)

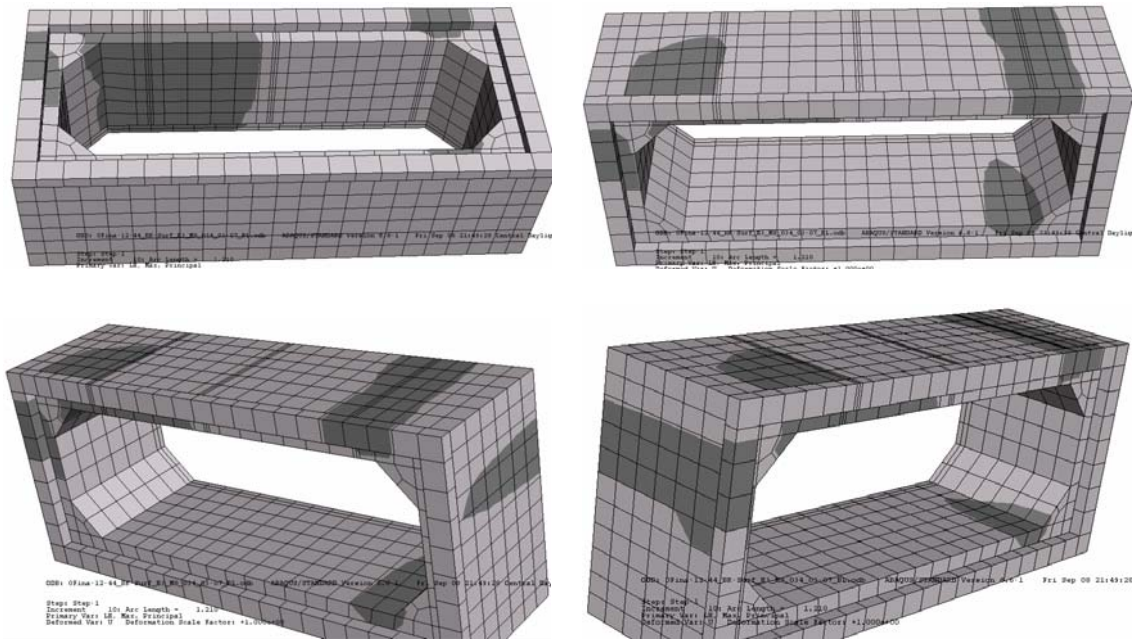

At 249 kN (56 kip) Load

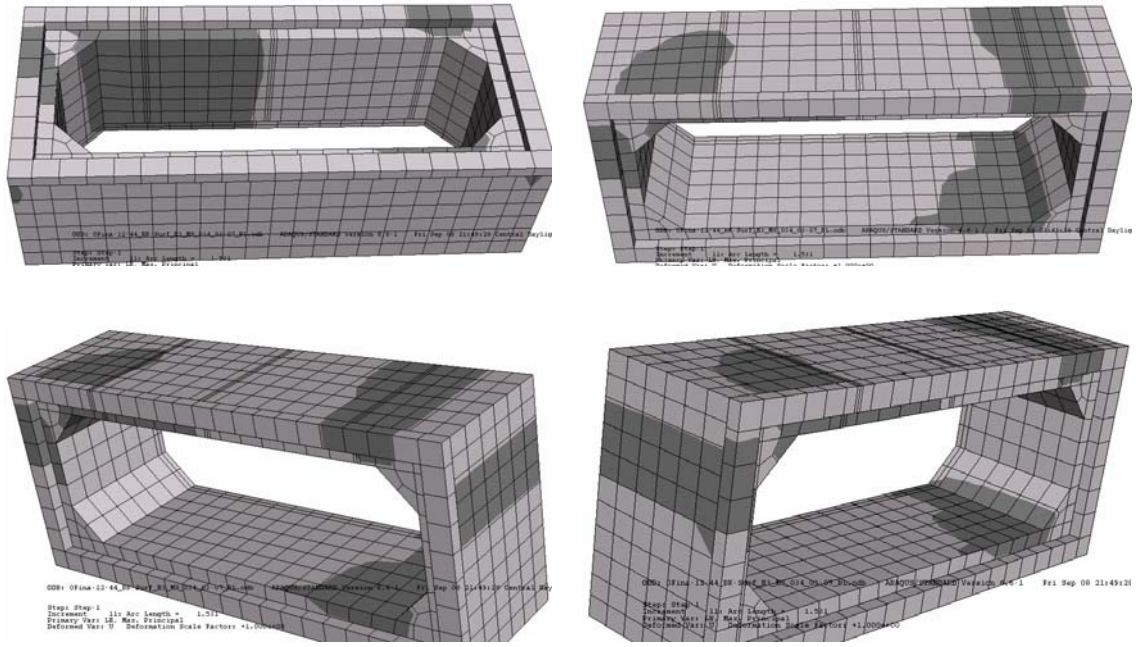

At 276 kN (62 kip) Load

Figure C37 FEM Crack Prediction of Model BL_366-122_122_N_d (BL_12-4-4_N_d)

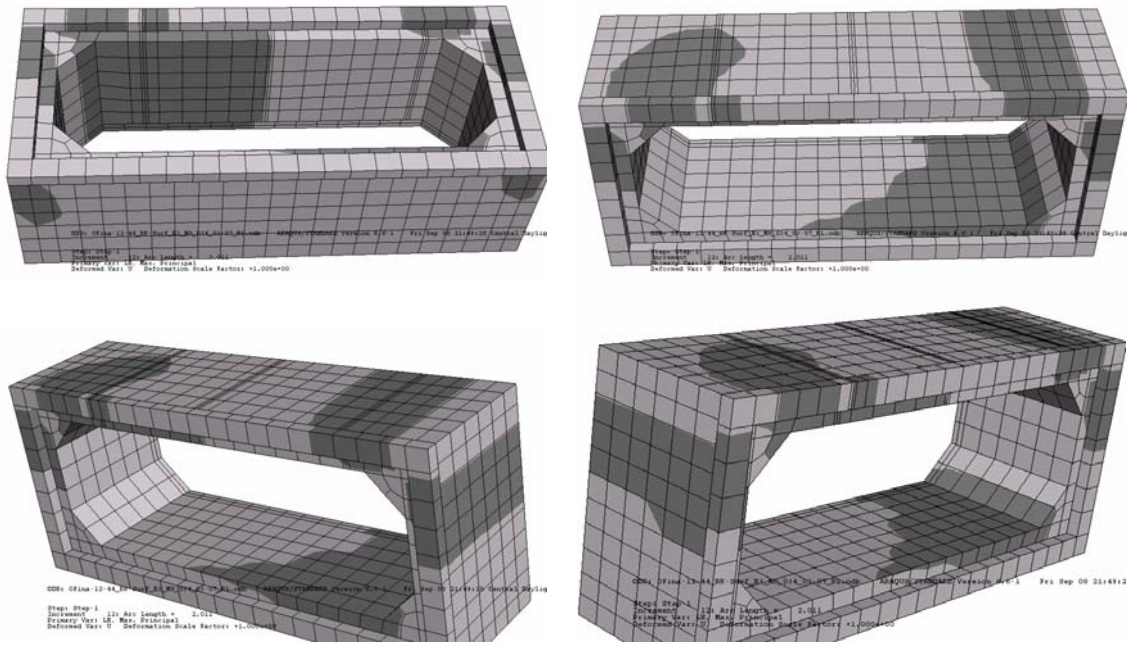

At 307 kN (69 kip) Load

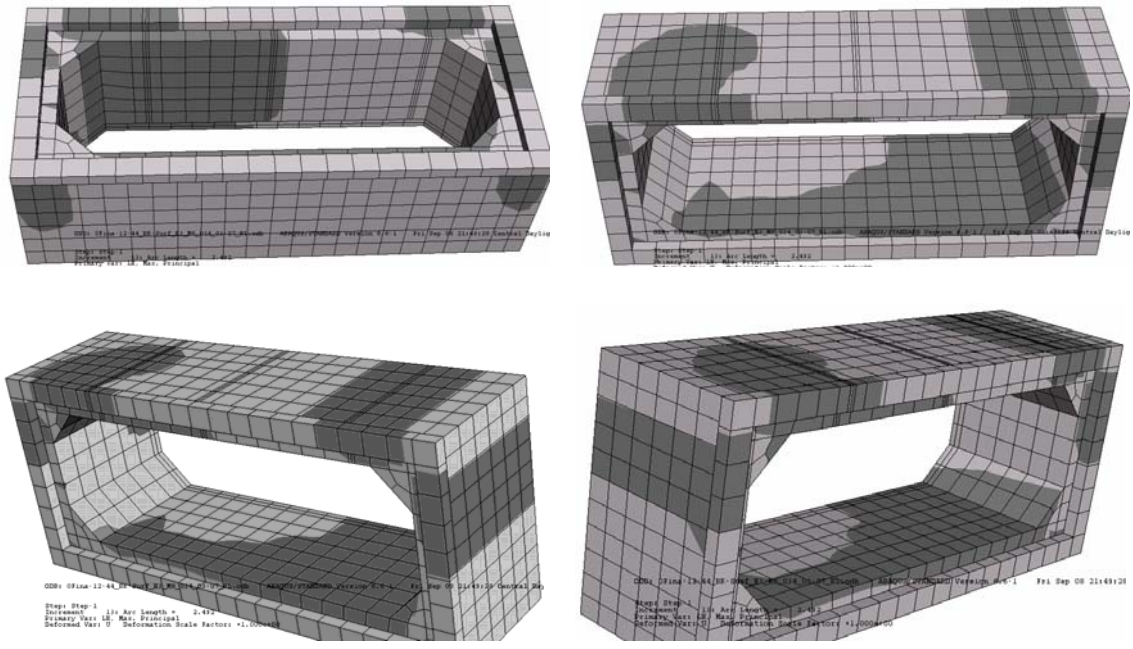

At 334 kN (75 kip) Load

Figure C38 FEM Crack Prediction of Model BL_366-122_122_N_d (BL_12-4-4_N_d)

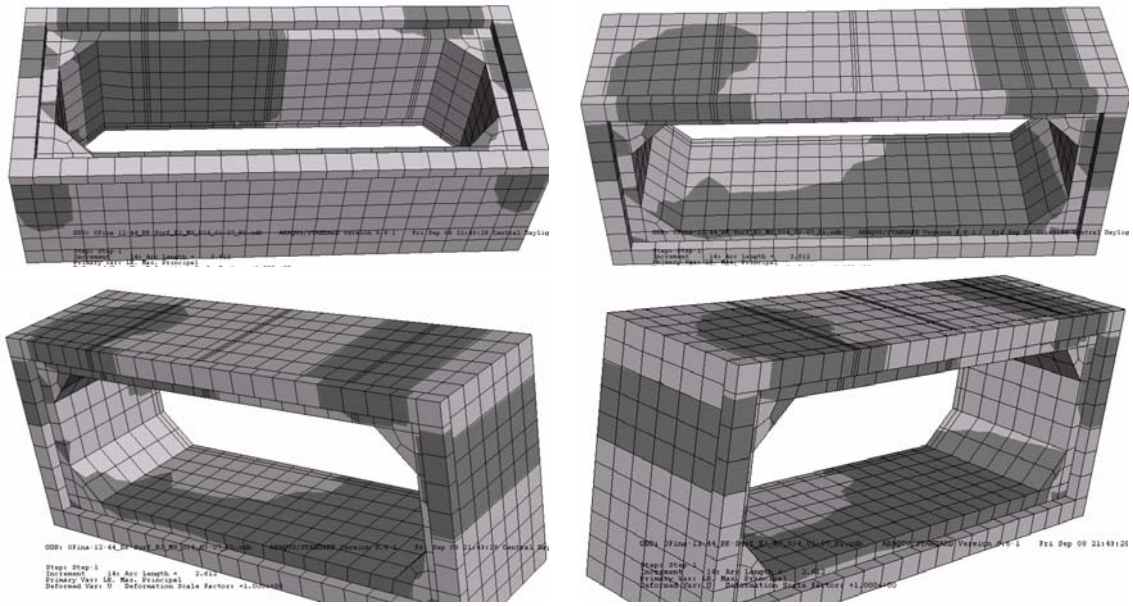

At 343 kN (77 kip) Load

Figure C39 FEM Crack Prediction of Model BL_366-122_122_N_d (BL_12-4-4_N_d)

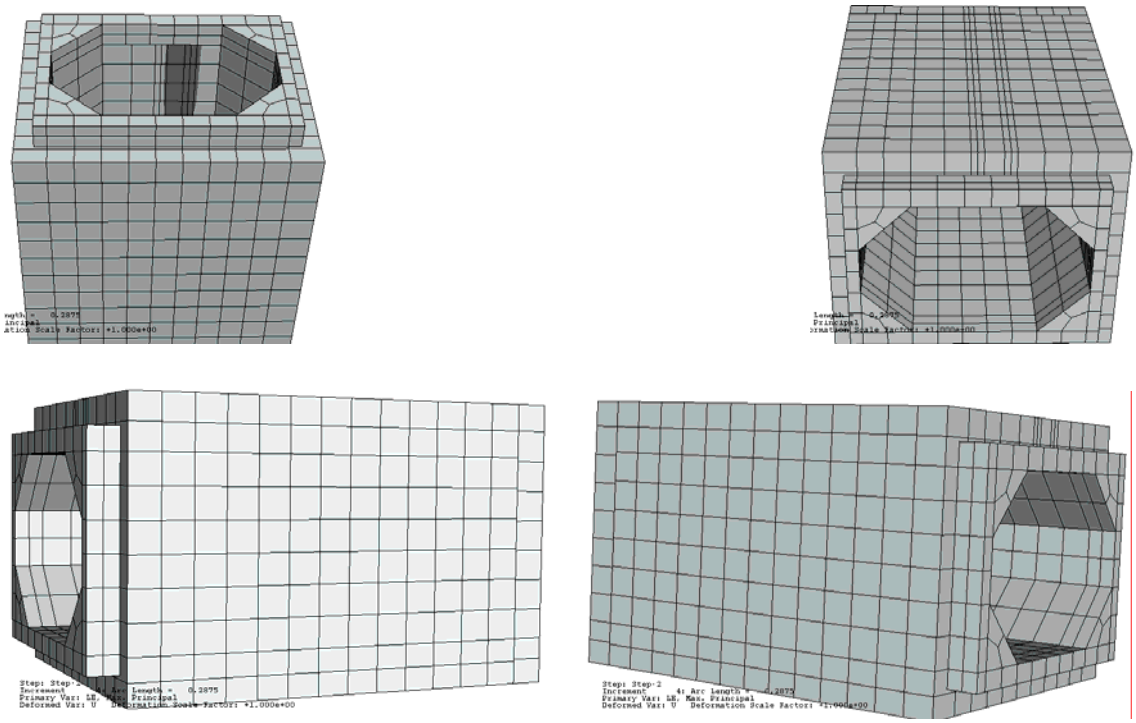

At 116 kN (26 kip) Load

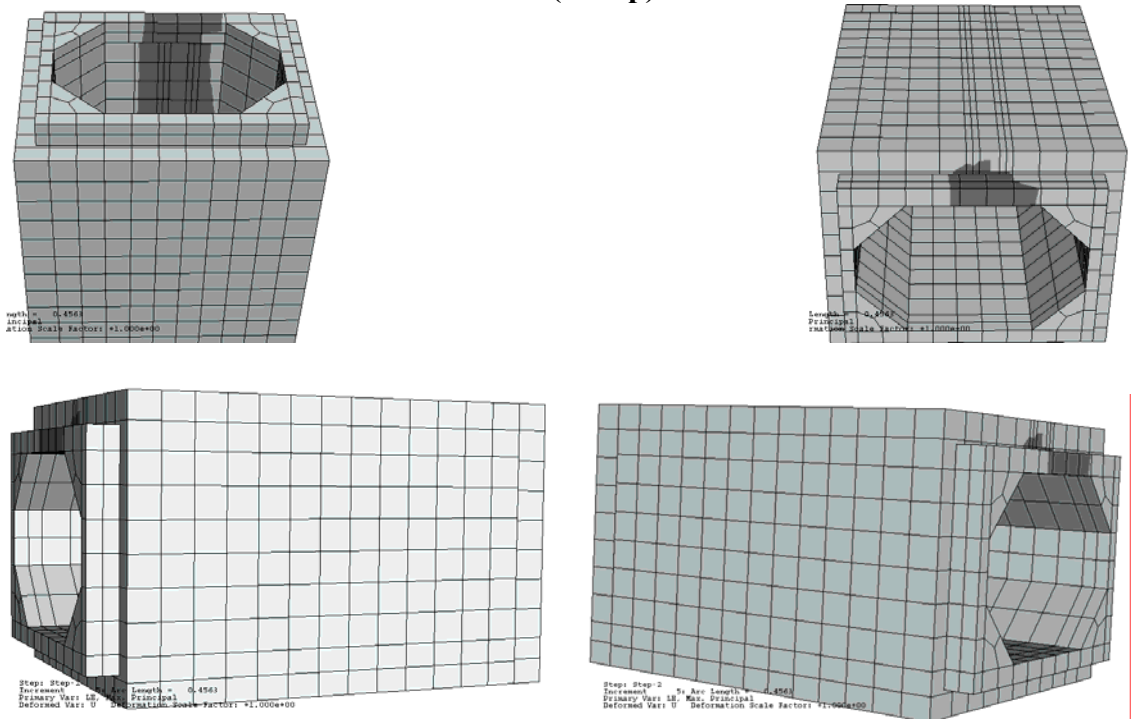

At 165 kN (37 kip) Load

Figure C40 FEM Crack Prediction of Model SP_91-61_145_N_0 (SP_3-2-4.75_N_0)

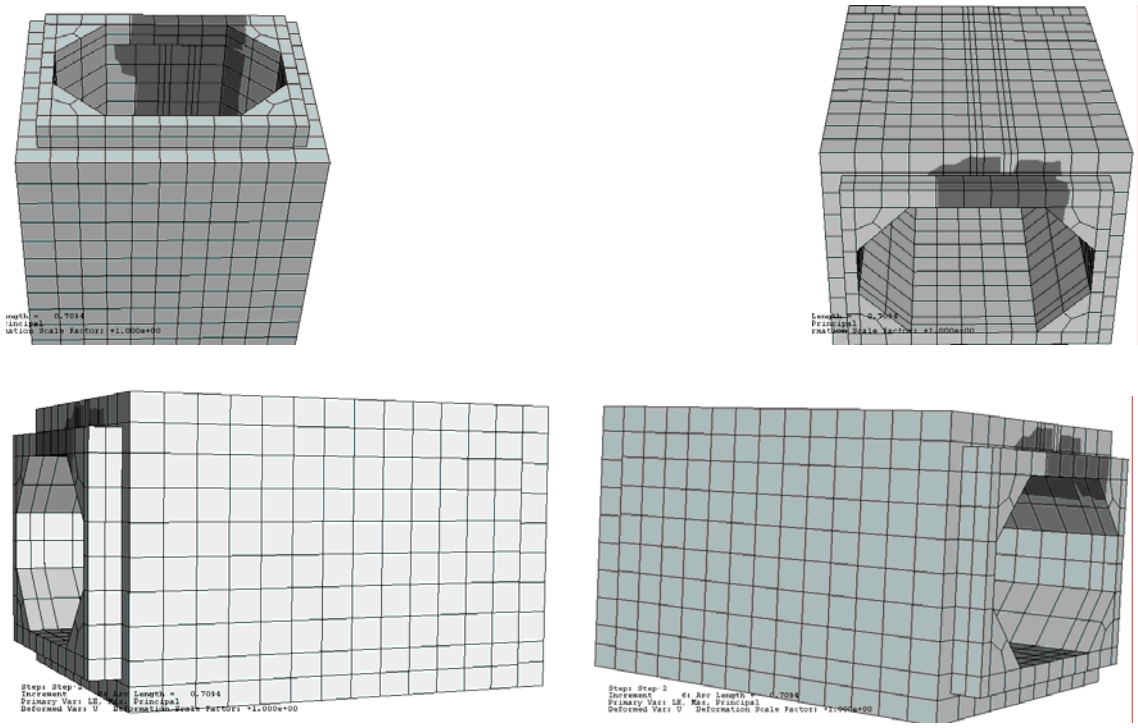

At 222 kN (50 kip) Load

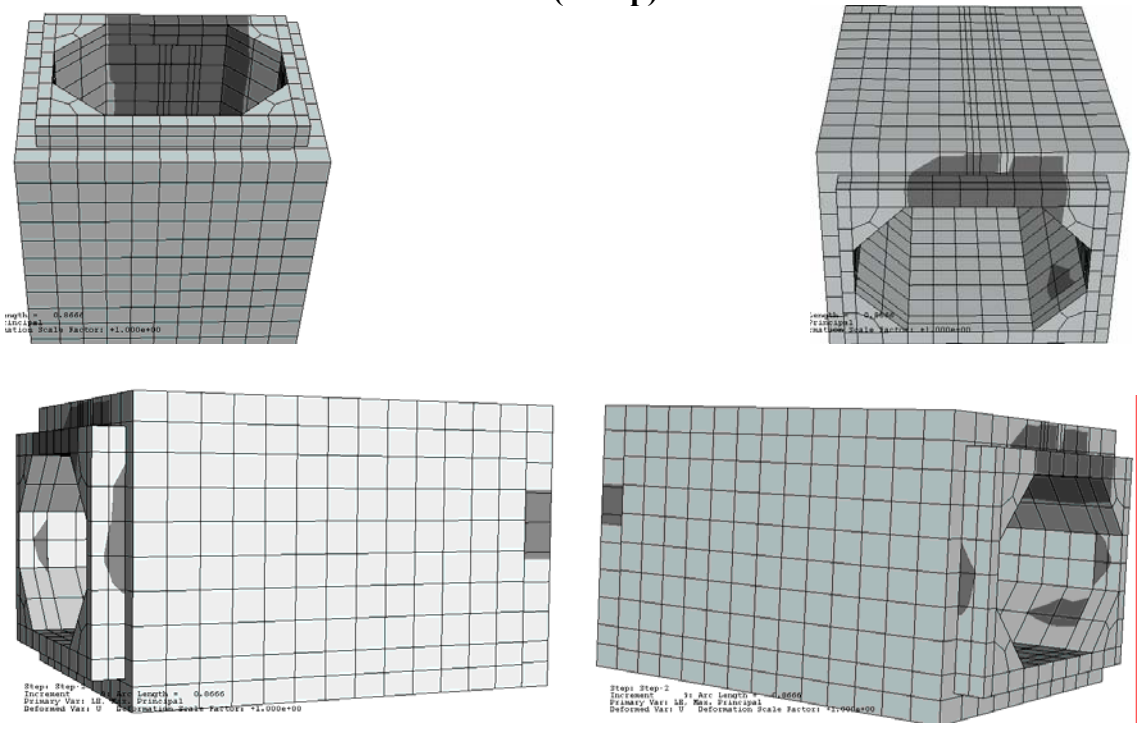

At 276 kN (62 kip) Load

Figure C41 FEM Crack Prediction of Model SP_91-61_145_N_0 (SP_3-2-4.75_N_0)

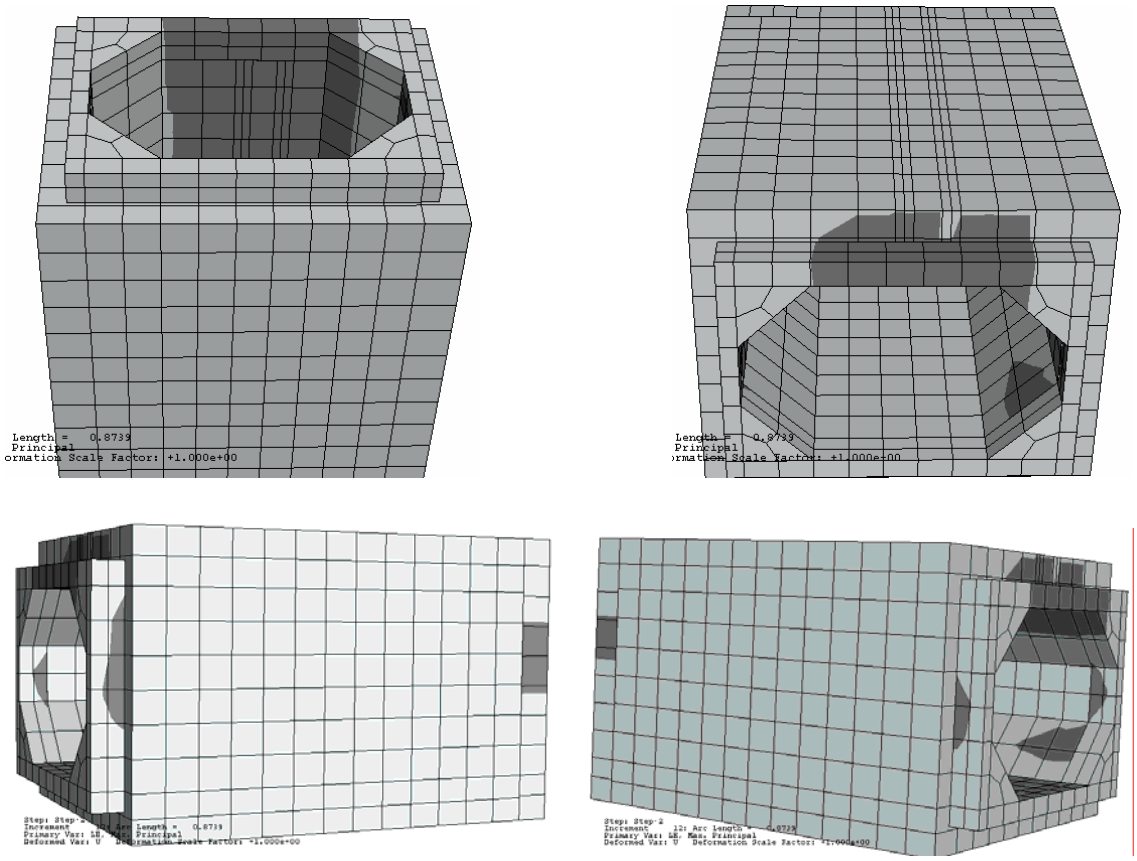

At 280 kN (63 kip) Load

Figure C42 FEM Crack Prediction of Model SP_91-61_145_N_0 (SP_3-2-4.75_N_0)

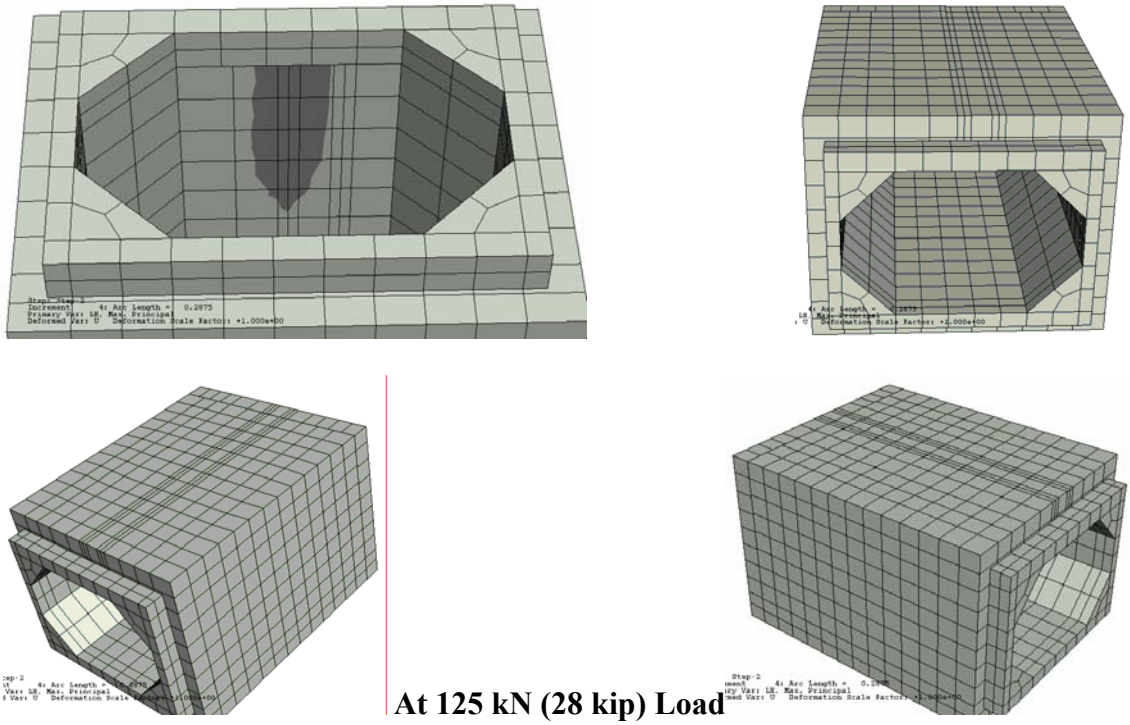

At 125 kN (28 kip) Load

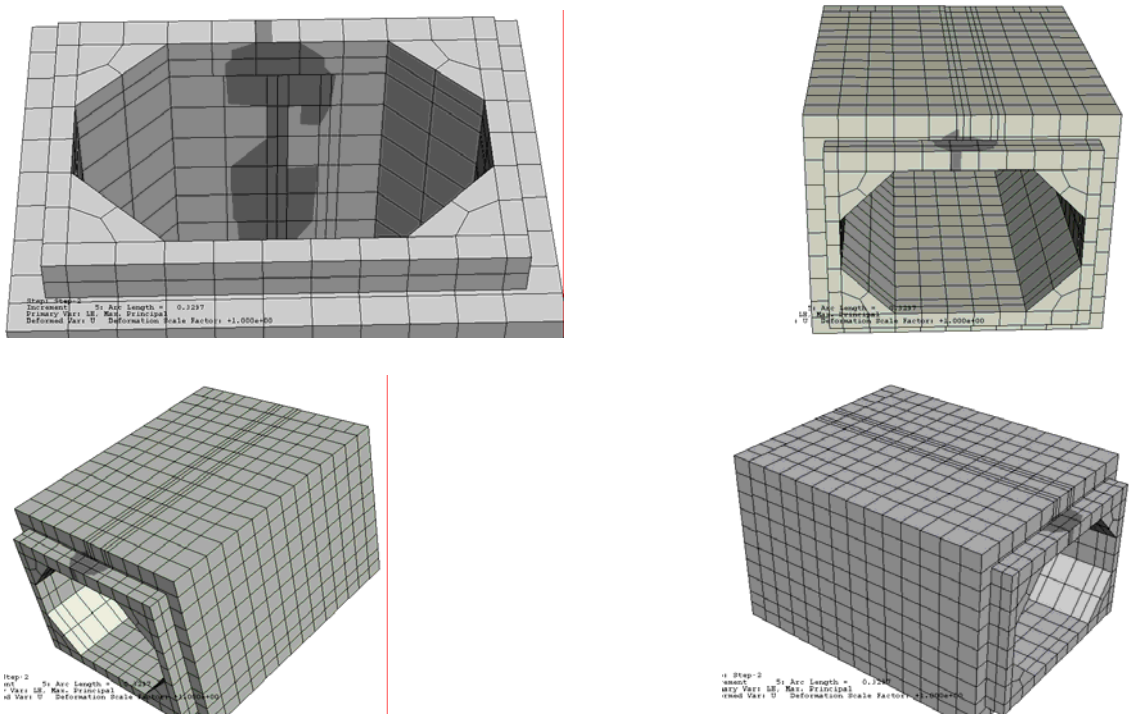

At 151 kN (34 kip) Load

Figure C43 FEM Crack Prediction of Model SP_91-61_145_0.83d (SP_3-2-4.75_N_0.83d)

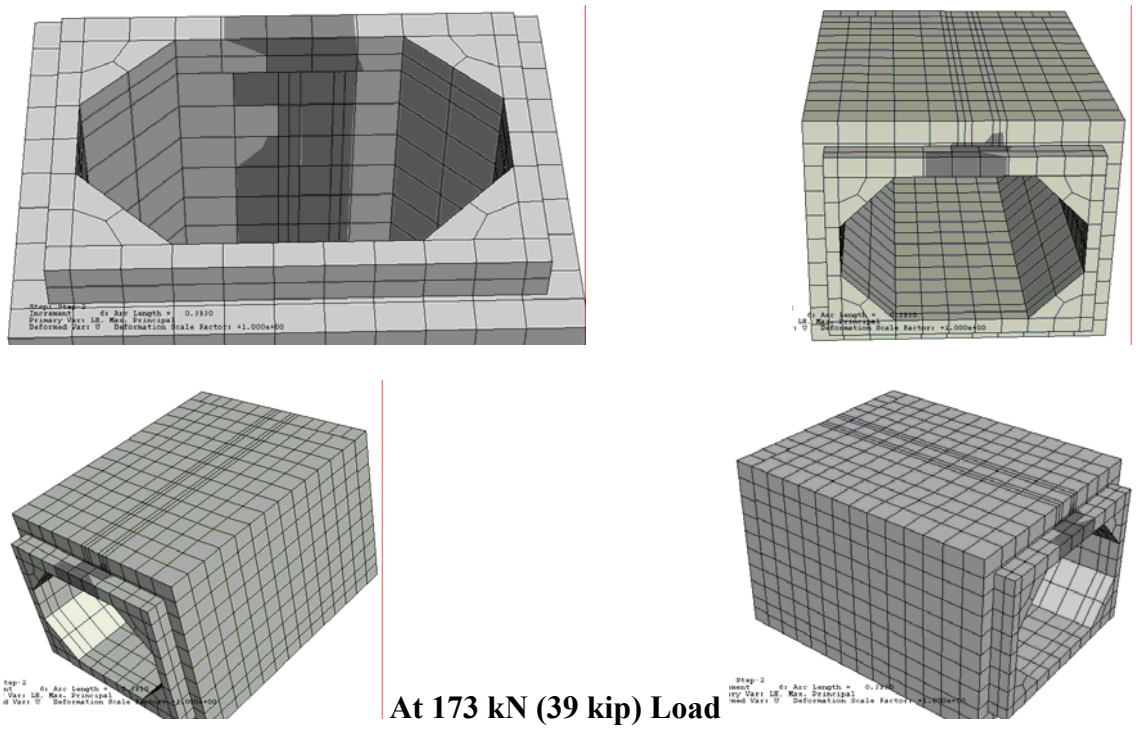

Figure C44 FEM Crack Prediction of Model SP_91-61_145_0.83d (SP_3-2-4.75_N_0.83d)

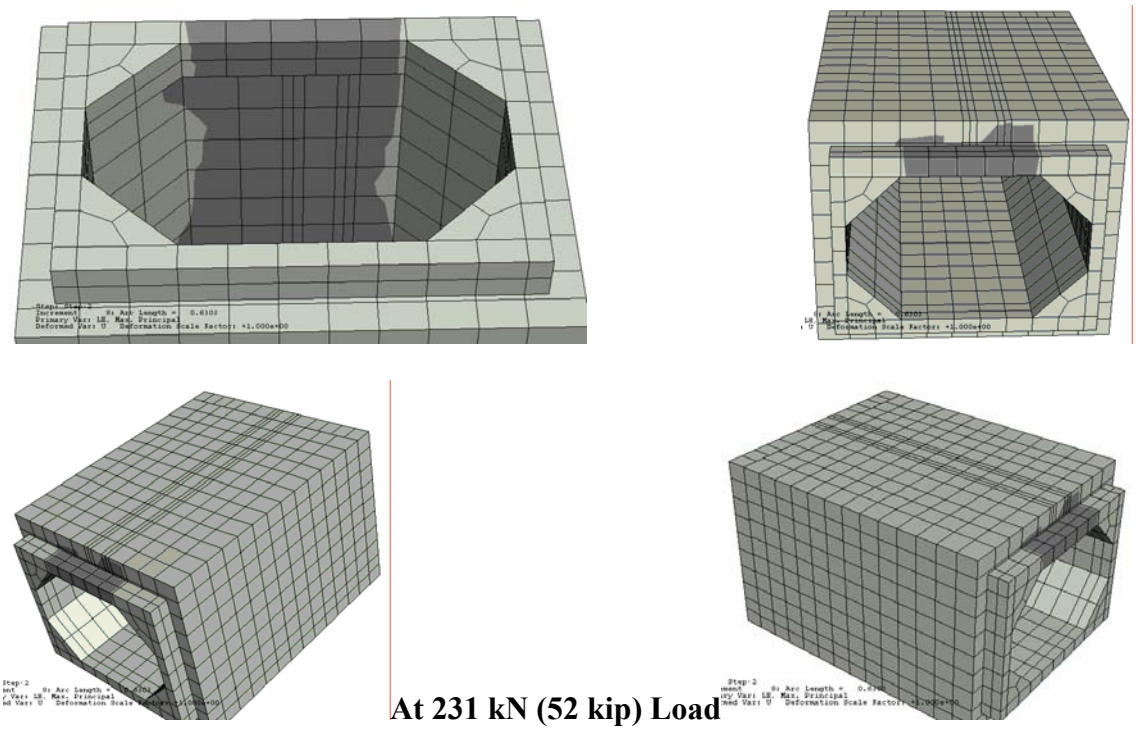

At 231 kN (52 kip) Load

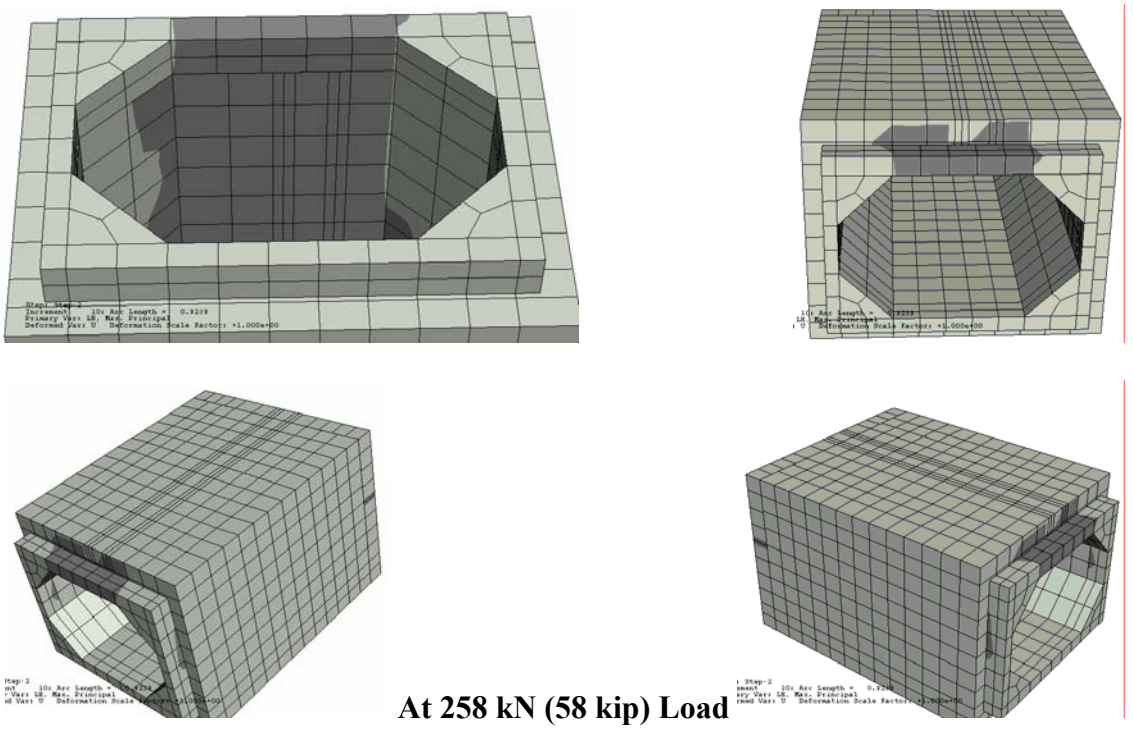

At 258 kN (58 kip) Load

Figure C45 FEM Crack Prediction of Model SP_91-61_145_0.83d (SP_3-2-4.75_N_0.83d)

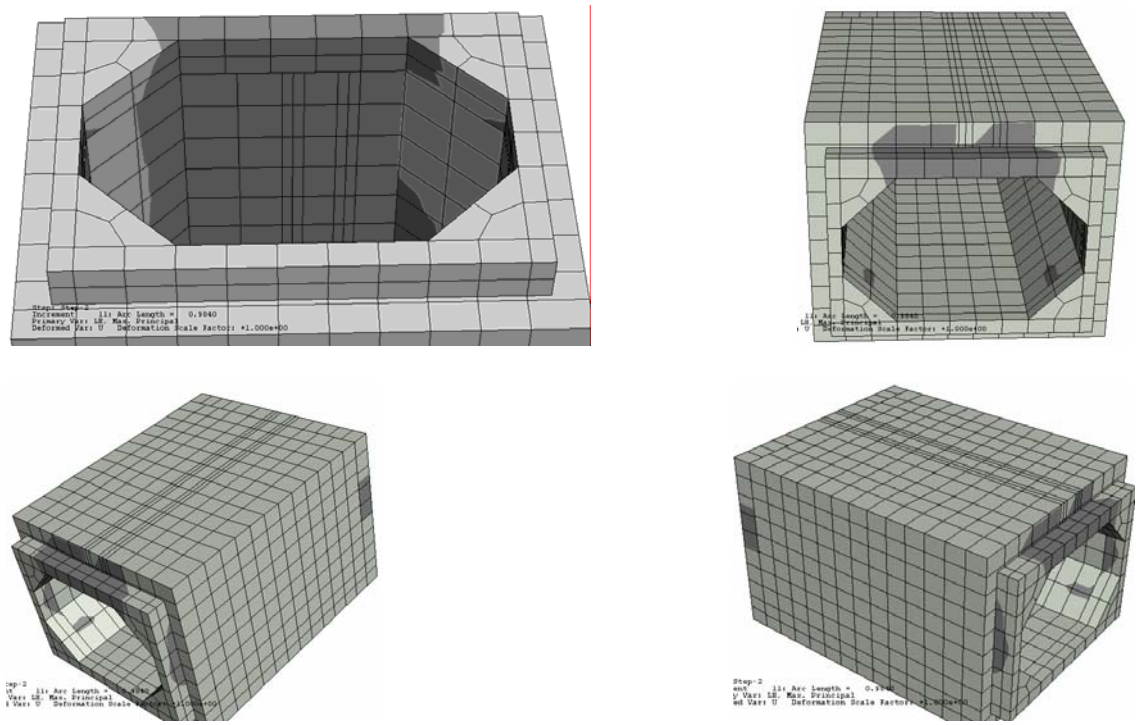

At 267 kN (60 kip) Load

Figure C46 FEM Crack Prediction of Model SP_91-61_145_0.83d (SP_3-2-4.75_N_0.83d)

APPENDIX D

CORE TEST RESULTS

Table D1 Cored Samples Test Results

Test Box	Core Strength N/mm^2 (psi)	
SP_122-122-244_Y_d (SP_4-4-8_Y_d)	58.1 43.0 45.8	8425 6241 6649
BL_122-122-244_Y_d (BL_4-4-8_Y_d)	45.0 44.4 43.5	6522 6441 6314
SP_244-122-122_N_d (SP_8-4-4_N_d)	33.3 37.0 33.3	4824 5360 4833
SP_244-122-122_Y_d (SP_8-4-4_Y_d)	32.9 35.7 33.6	4771 5176 4868
BL_244-122-122_N_d (BL_8-4-4_N_d)	34.0 45.3 51.3	4936 6573 7434
BL_244-122-122_Y_d (BL_8-4-4_Y_d)	34.2 26.5 38.3	4965 3849 5553
SP_244-122-122_Y_1.5d (SP_8-4-4_Y_1.5d)	39.6 35.5 34.7	5747 5149 5026
SP_244-122-122_Y_2d (SP_8-4-4_Y_2d)	34.2 26.5 38.3	4956 3849 5553
SP_244-122-244_Y_d (SP_8-4-8_Y_d)	63.1 62.2 58.2	9156 9015 8444
SP_244-122-244_N_d (SP_8-4-8_N_d)	70.8 69.5 70.0	10272 10087 10149
BL_244-122-244_Y_d (BL_8-4-8_Y_d)	71.2 76.8 73.9	10333 11142 10720
BL_244-122-244_N_d (BL_8-4-8_N_d)	67.3 71.6 61.9	9762 10386 8980
SP_366-122-122_Y_d (SP_12-4-4_Y_d)	42.5 43.5 44.8	6168 6309 6494

Table D1 - *continued*

Test Box	Core Strength (psi)	Core Strength N/mm^2
SP_366-122-122_N_d (SP_12-4-4_N_d)	51.7 53.8 51.1	7501 7809 7410
BL_366-122-122_Y_d (BL_12-4-4_Y_d)	39.1 35.0 41.3	5671 5082 5997
BL_366-122-122_N_d (BL_12-4-4_N_d)	45.1 42.4 45.4	6538 6148 6581

REFERENCES

AASHTO (1998). AASHTO LRFD Bridge Design Specifications, 2nd Edition. with interim specifications through 2002, American Association of State Highway and Transportation Officials, Washington, D.C.

AASHTO (2002). AASHTO Standard Specifications for Highway Bridges, 17th Edition. American Association of State Highway and Transportation Officials, Washington, D.C.

AASHTO (2005). interim AASHTO LRFD Bridge Design Specifications, 3rd Edition, American Association of State Highway and Transportation Officials, Washington, D.C.; 3.4.2.2 p 3.14; 12.14.3, p 12.80.

Abolmaali, Ali, and Garg, Anil K. (2006). "Effect of Wheel Live Load on Shear Behavior of Precast Reinforced Concrete Box Culverts." *ASCE Journal of Bridge Engineering,* under review.

Abolmaali, Ali, and Garg, Anil K. (2006). "Failure Mode for Precast Concrete Box Culverts Subjected to Wheel Live Load." *Transportation Research Board 86th Annual meeting*, Washington D.C., under review.

ASTM (2001). American Society for Testing and Materials (ASTM) International. "A185-(2001): Standard Specification for Steel Welded Wire Reinforcement, Plain, for Concrete." ASTM International, West Conshohocken, PA.

ASTM (2001). American Society for Testing and Materials (ASTM) International. "A497-(2001): Standard Specification for Steel Welded Wire Reinforcement, Deformed, for Concrete." ASTM International, West Conshohocken, PA.

ASTM (2003). American Society for Testing and Materials (ASTM) International. "C1433-03: Standard Specification for Precast Reinforced Concrete Box Sections for Culverts, Storm Drains, and Sewers." ASTM International, West Conshohocken, PA.

Biggs, R. Michael, Barton, Furman W., Gomez, Jose P., Massarelli, Peter J., and McKeel, Wallace T. Jr. (2000). "Finite Element Modeling and Analysis of Reinforced-Concrete Bridge Decks." *Virginia Transportation Research Counci*l. Federal Highway Administration, September 2000, VTRC 01-R4 pp 1-23.

Crisfield, M.A. (1986). "Snap- Through and Snap- Back Response in Concrete Structures and the Dangers of Under-Integration." *International Journal for Numerical Methods in Engineering,* Vol. 22, pp 751-767.

Federick, G.R., Ardis, C.V., Tarhini, K.M., and Koo, B. (1988). "Investigation of The Structural Adequacy Of C 850 Box Culverts," *Transportation Research Record 1191*, Transportation Research Board, National Research council, Washington D.C., pp 73-80.

Garg, Anil K, Abolmaali, Ali, and Fernandez, Raul (2006). "Experimental Investigation of Shear Capacity of Precast Reinforced Concrete Box Culverts." *ASCE Journal of Bridge Engineering,* In Press.

Garg, Anil K, and Abolmaali, Ali. (2006). "Shear Behavior of Small Span Single and Double Precast Reinforced Concrete Box Culverts." *Proceedings of the ASCE Pipeline Division Specialty Conference "Pipelines 2006 Service to the Owne*r", Chicago, Illinois, on CD Rom.

Hu, Hsuan-The, and Liang, Jiin-Iuan Liang (2000). "Ultimate Analysis of BWR Mark III Reinforced Concrete Containment Subjected to Internal Pressure." *Nuclear Engineering and Design*. 195 (1), pp 1-11.

James, Ray W. (1984). "Behavior of ASTM C 850 Concrete Box Culverts Without Shear Connectors." *Transportation Research Record 1001*, Transportation Research Board, National Research council, Washington D.C., pp 104-111.

Kwak, H.G., and Filippou, Filip C. (1990). "Finite Element Analysis of Reinforced Concrete Structures under Monotonic Loads." Structural Engineering, Mechanics and Materials, Department of Civil Engineering, University of California, Berkeley.

Mabsout, M., Tarhini, K., Jabakhanji, R., and Awwad, E. (2004). "Wheel Load Distribution in I-Girder Highway Bridges" *ASCE Journal of Bridge Engineering*, March-April, pp 147-155.

Marzouk, H., Osman, M., and Hussein, A. (2002). "Punching Shear of Slabs: Crack Size and Size Effects." *Magazine of Concrete Research.* 54 (1), pp 13-21.

McGrath, Timothy J., Liepins, Atis A., Beaver, Jesse L., and Strohman, Bryan P. (2004). "Live Load Distribution Widths for Reinforced Concrete Box Culverts." A study for the Pennsylvania Department of Transportation, Simpson Gumpertz & Heger Inc, Boston.

Modjeski and Masters (2003). Memorandum-Background of the deck strip width equations in the AASHTO-LRFD specifications, September 2003, Modjeski & masters, Inc.

Polak, Maria Anna (2005). "Shell Finite Element Analysis of RC Plates Supported on Columns for Punching Shear and Flexure." *International Journal for Computer-Aided Engineering and Software.* 22 (4) 409-428.

Rots, J.G., and Blaauwendraad, J. (1989). "Crack Models for Concrete: Discrete or Smeared? Fixed, Multi-Directional or Rotating?" *Heron*. 34 (1).

Razavi, Hadi (2004). " Kinematic Hardening Cyclic Plasticity-Based Semi-Meshless Finite Element Algorithm for Contact and Bolted Problems in Computational Mechanics." Ph.D. Dissertation submitted as partial fulfillment for degree of Doctor of Philosophy, Department of Civil and Environmental Engineering, University of Texas at Arlington, Arlington, Texas.

Smeltzer, Paul, and Bentz, Evans (2004). "Research Suggests Conservative Design of Concrete Box Culverts." Environmental Science & Engineering Magazine, <http://www.esemag.com> May.

Sonnenberg, A. M. C., Al-Mahaidi, R., and Taplin,G. (2003). "Behavior of Concrete Under Shear and Normal Stresses." *Magazine of Concrete Research.* 55 (4) 367-372.

Torres, Li, Lopez-Almansa, F., Bozzo, L.M. (2004). "Tension-Stiffening Model for Cracked Flexural Concrete Members." *Journal of Structural Engineering.* 1242-1251.

Yee, R.A., Bentz, E.C., Collins, and M.P. (2004). "Shear Behaviour of Concrete Box Culverts: A Preliminary Study", Department of Civil Engineering, University of Toronto, Toronto, Canada.

BIOGRAPHICAL INFORMATION

Anil K Garg was born in 1965 in Delhi, the capital of India. He earned his Associate Membership of The Institution of Engineers (India) in Civil Engineering and designated as "Chartered Engineer (Civil)" in September 1986. After that, he earned his M.B.A. from Indira Gandhi National Open University [IGNOU] (New Delhi, India) with the specialization in "Operation Management" in June 1998. He achieved his Master of Technology from the Indian Institute of Technology, Delhi [IIT Delhi] (New Delhi, India) in December 2000. Then, he was admitted to the Ph.D. program in structural Engineering and Mechanics at the University of Texas at Arlington (Texas, USA) in the fall of 2004, and he received his Ph.D. in the fall of 2006. He also earned his license as a professional engineer (P.E.) in the state of Texas in the spring of 2006.

He is a fellow of the Indian Council of Arbitration (ICA), and a member of the Indian Building Congress (IBC), The Institution of Engineers [India] (IE(I)) and the Indian Road Congress (IRC). He is also Student Member of the ASCE, ASTM, TRB, AISC and ACI. He is also member of the Engineering Honor Society-Tau Beta Pi.

He has several years of teaching experience in the field of civil engineering. He has prior experience in the infrastructure development, industrial, commercial, educational, institutional, and residential structures in the field of design, contract, execution, maintenance and rehabilitation.